Stephen, R.A., Kasahara, J., Acton, G.D., et al., 2003
Proceedings of the Ocean Drilling Program, Initial Reports Volume 200

4. SITE 1224[1]

Shipboard Scientific Party[2]

PRELIMINARY RESULTS

Borehole Seismic Installation

The primary objective of Leg 200 was to prepare a borehole in basaltic crust for the installation of a broadband borehole seismometer that will be connected to the Hawaii-2 Observatory (H2O) for continuous, real-time data transmission to the University of Hawaii. From Hawaii the data will be made available to seismologists worldwide through the IRIS (Incorporated Research Institutions for Seismology) Data Management Center in Seattle.

Proposed Site H2O-5 (27°53.363′N, 141°58.758′W) (Fig. F1) was selected for the seismometer installation. This site is 1.48 km northeast (a bearing of 056°) of the H2O junction box location. The bearing was chosen so that regional earthquake events from the Island of Hawaii would be on the same great circle path to both the shallow buried seismometer at the junction box and to the borehole seismometer to be installed at Site 1224. The range was chosen as a compromise between being sufficiently far away to not disturb other experiments at the junction box but still close enough to conveniently run a cable from the borehole to the junction box. The bathymetry slopes smoothly downward ~6 m from the junction box to Site 1224, and the two sites appear to be on the same crustal block in a relatively flat abyssal plain environment.

Preliminary drilling and coring at the site showed that the sedimentary layer above basaltic basement was much thinner (only 28–30 m) than estimated from precruise seismic surveys. This meant that there was little sediment to support the bottom-hole assembly (BHA) for drilling into basement. The drillers needed to take more care and started the hole in basement with less weight on the bit than they would otherwise use. The sediment was sufficiently thin (~30 m) that the basement con-

F1. Locations of Site 1224, H2O, and proposed sites, p. 67.

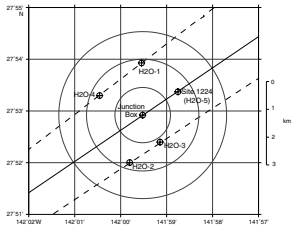

[1]Examples of how to reference the whole or part of this volume.
[2]Shipboard Scientific Party addresses.

Ms 200IR-104

tact could occasionally be imaged on 3.5-kHz echo sounding records (Fig. F2). All H2O drilling activities took place within a 20 m × 20 m area at the site (Fig. F3).

Hole 1224D (27°53.370′N, 141°58.753′W; 4967 m water depth) has a reentry cone and 58.5 m of 10.75-in casing, which was cemented into a 30-m-thick well-consolidated massive basalt flow underlying 28 m of soft, red clay (Figs. F4, F5). After cementing, the hole was washed to a depth of 5036 meters below rig floor (mbrf) (58 meters below seafloor [mbsf] or 30 m into basaltic basement). On reentering for the wiper trip, we noticed that the cone had settled ~1.7 m into the sediment.

After setting the reentry cone and casing in Hole 1224D, we drilled a single-bit hole, 1224F, to 174.5 mbsf to acquire sediment and basalt samples for shipboard and shore-based analysis as well as to run a logging program. Hole 1224F is <20 m to the southeast of Hole 1224D, and measurements in Hole 1224F can be used to infer the structure surrounding the seismometer hole. We dropped a free-fall funnel (FFF) in Hole 1224F so that future borehole experiments using wireline reentry technology can be conducted (Figs. F6, F7). For example, this would be a good site to compare measurements in a sealed hole in basement (1224D) to measurements in an open hole in basement (1224F).

Lithology

Sedimentary Section

The top 6.53 m of Site 1224 (Hole 1224C) is massive brown clay that gradually changes color to very dark brown. Radiolarian spicules are present throughout the section but increase with depth and are common at the bottom of the unit. Sponge spicules are not found near the top of the section but are common below 4.50 m. Core recovery from Holes 1224A and 1224B was not significant enough to characterize the sediments. One significant discovery, however, was the recovery of light-colored noneffervescing granules and pebbles from a depth of between 6 and 15.6 mbsf from Hole 1224A. These are fossil worm burrows made of zeolite. The total sediment depth at Site 1224 is 28 m.

Paleontological analysis of calcareous nannofossils indicates that essentially the whole sedimentary sequence was deposited within a few million years of the crustal age of ~46 Ma (on the transition between marine magnetic Anomalies 20R and 21N).

Hard Rock Section

The lithostratigraphy of basalts at Site 1224 is divided into three units. Unit 3, the deepest, is intermixed pillows and flows of no more than a few meters thickness each. At least two, and probably more, eruptive events are represented. Overlying Unit 3, Unit 2 is a succession of thin flows and pillows. Chemical analyses of these rocks are very similar, indicating that they are of one eruptive composition. Two thick lava flows from Unit 1 cap the underlying units. The lower of these has the same composition as the basalts of Unit 2. These two flows may have accumulated in a structural depression or pond that formed, probably by faulting, after eruption of the last thin flows or pillows of Unit 2.

Apart from the interiors of the massive flows, the lava sequence was pervasively altered under conditions with variable oxygen fugacity. Hydrous fluids carrying dissolved metals flowed through cracks, cavities,

F2. 3.5-kHz echo sounder recording, p. 68.

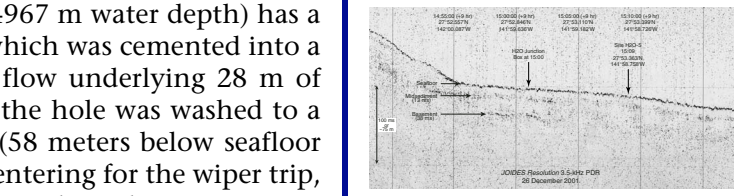

F3. Significant locations at Site 1224, p. 69.

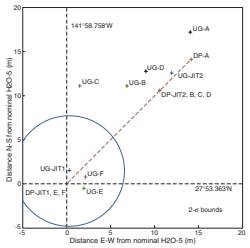

F4. Reentry cone and casing deployed in Hole 1224D, p. 70.

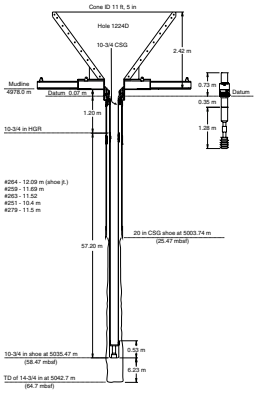

F5. Reentry cone in Hole 1224D, p. 71.

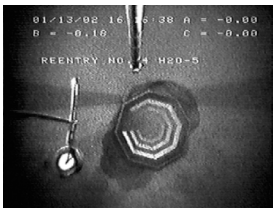

and fractures in the formation and deposited iron oxyhydroxides and sulfide minerals in this porosity structure. The fluids penetrated several centimeters into the rock adjacent to the fractures and impregnated microfractures with the same material that was deposited in the larger veins. Later, carbonate-saturated fluids coursed through the same fractures depositing calcite. Except for the interiors of the two upper massive lavas, most of the rock was at least partially transformed to secondary minerals by this process. Eventually, enough calcite precipitated to cement the originally fragile iron oxyhydroxides and sulfide minerals. The calcite cementing contributed to higher core recovery of basalts above ~60 mbsf at Site 1224.

It is too early to say how warm the fluids might have been, although calcite and aragonite are the ideal minerals to use for oxygen isotope determinations and to estimate temperatures for the cementation portion of these processes. Iron oxyhydroxides are a principal component of hydrothermal sediments deposited on volcanically active ridge axes near, but not at, high-temperature vents. Elsewhere on the flanks of the East Pacific Rise, basalt coring has not been successful in crust as old as Miocene, largely because of the absence of calcite vein cement. Thus, the carbonate-lined veins in the Eocene rocks at Site 1224 may be evidence for sustained fluid flow at low temperature and far off axis. There is only a thin layer of sediment at Site 1224, insufficient to seal off fluids circulating in the crust. Interaction of those fluids with oxygenated bottom water may be why most of the section cored exhibits mainly oxidative alteration. The exception to this is the massive basalts at the top. In those, fractures may have been so few and widely spaced that fluid flow was restricted. The oxygen fugacity of the small quantity of fluids moving along them was consequently reduced by reaction with adjacent wall rock, allowing pyrite to precipitate.

Petrography

Thin section examination of volcanic basement at Site 1224 (Holes 1224A, 1224D, 1224E, and 1224F) evidenced a relatively homogeneous mineral paragenesis. The main phases are plagioclase, clinopyroxene, opaque minerals, and rare pigeonite; therefore, the rocks can be classified as tholeiitic basalts. Olivine is rare, and only a few small iddingsitized euhedral to anhedral groundmass crystals were found. Iddingsite is a typical alteration of olivine and is composed of a mixture of goethite and layer silicates (e.g., smectite). The majority of the basalt is holocrystalline (almost 100% crystals) to hypocrystalline (glass concentration <50%) and can be ascribed to lava flows. With increasing depth of coring, hypohyaline textures and volcanic glass contents >90% become common and indicate the presence of pillow fragments with chilled margins. The deepest samples recovered (~153 mbsf) also show textural features of holocrystalline massive lava flows. With regard to their granularity, the basalts range from aphanitic (difficult to distinguish the crystals in the groundmass with the naked eye) to aphyric (absence of phenocrysts), though rare plagioclase or plagioclase-clinopyroxene sparsely phyric basalts (phenocryst content <2%) have been also found. The relative size of the crystals in the groundmass is equigranular, and their distribution is isotropic. The groundmass is hypidiomorphic with the presence of euhedral- to anhedral-shaped crystals. The texture of the massive lava flow basalts is intergranular (with clinopyroxene in interstitial relationships with plagioclase) to subophitic (with plagioclase laths partially enclosed in clinopyroxene) and,

F6. FFF deployed in Hole 1224F, p. 72.

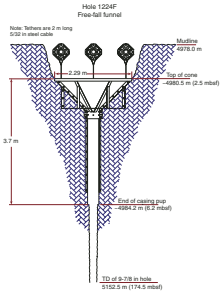

F7. Free-fall funnel in Hole 1224F, p. 73.

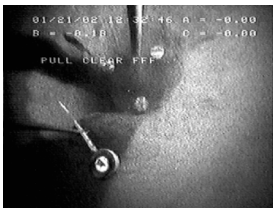

more rarely, intersertal (with microcrystalline to glassy material between plagioclase). Hyalopilitic (with plagioclase laths and clinopyroxene crystals in a glassy matrix) to, more rarely, intersertal textures have been found in the pillow lavas. The grain size of the groundmass ranges from very fine grained (0.001–0.5 mm) to fine grained (0.5–1 mm).

Geochemistry

Inductively coupled plasma–atomic emission spectroscopy (ICP-AES) data for basalts were obtained late during Leg 200. Only partial analyses are available for plotting on samples obtained from Holes 1224D, 1224E, and 1224F. The discussion here is based on contents of K_2O, TiO_2, MgO, Ba, Zr, and loss on ignition (LOI) from the ICP-AES data.

The basalts range from differentiated to very differentiated normal mid-ocean-ridge basalt (N-MORB) (4–7 wt% MgO and 2–3.5 wt% TiO_2). The highly differentiated (4 wt% MgO and 3.5 wt% TiO_2) basalts plot at the most differentiated end of the N-MORB data array. The samples selected for analysis from Hole 1224D are fairly fresh and have LOI values ranging from 0 to 0.45 wt%. Concentrations of K_2O (0.11–0.27 wt%) may be slightly elevated (>0.2 wt%) in three of the ten samples analyzed. All the basalts have Ba concentrations (9–18 ppm) that are consistently lower than many comparably differentiated MORB glasses from the East Pacific Rise. This may indicate a greater than average depletion of the mantle sources in the basalts from Hole 1224D. Alternatively, the rocks may have experienced a slight nonoxidative alteration as these components were partially removed from the rock.

The samples from Hole 1224D can be divided into two groups based on their TiO_2 concentrations. These geochemical groups correspond to (1) the lithologic Unit 1 upper flow (>2.3 wt% TiO_2) and (2) the lithologic Unit 1 lower flow (<2.3 wt% TiO_2). Interestingly, lithologic Unit 2 pillow lavas have TiO_2 concentrations similar to the lower flow basalts from Unit 1. The lithologic Unit 3 pillow lavas have TiO_2 concentrations >3.1 wt%. Therefore, the geochemical divisions (based on TiO_2 contents) do not correlate directly with the lithologic units.

The topmost flow in Unit 1 was also sampled in Holes 1224E and 1224F, and the lower flow in Unit 1 was also sampled in Hole 1224F. Samples of lithologic Unit 2 have TiO_2 contents similar to those of the lower flow of Unit 1. Apparently accumulation of this chemically uniform basalt at the site began with thin flows. These were capped with a thick flow of the same material. The samples of Holes 1224E and 1224F from Unit 2, however, are more greatly altered than those of the capping flow at the base of Unit 1, usually having as much as two to three times the amount of K_2O present in samples of Hole 1224D and in one case having >1 wt% K_2O. This is in accordance with the strong contrast in extent of alteration noted between holes only 15 m apart in the core descriptions.

Samples of lithologic Unit 3 have TiO_2 contents greater than in any of the basalts from the thick flows or pillows of lithologic Units 1 and 2. Based on TiO_2 contents, these are among the most differentiated basalts sampled thus far from the flanks or axis of the East Pacific Rise. Their compositions are at or about the point where oxide minerals join the liquidus, causing TiO_2 contents to drop as MgO decreases and producing andesitic and ultimately rhyodacitic residual liquids.

Secondary minerals found in altered layers and fractures at Site 1224 were analyzed by X-ray diffraction (XRD). XRD analysis was carried out

on one clayey pebble from the sediment and twenty-five vein materials within the basalt. Five distinct vein types were documented by XRD analysis: clay, carbonate, zeolite, quartz, and calcite/smectite (Fig. F48) (see "X-Ray Diffraction Investigation of Secondary Minerals," p. 37, in "Geochemistry"). Many vein minerals in the basement at Site 1224 are stable at low temperature and pressure (i.e., zeolite). Phillipsite, the principal zeolite present at Site 1224, is a low-temperature member of the zeolite group (Miyashiro, 1973). Smectite is also commonly found as a product of the alteration of volcanic ash and rocks from the seafloor and is present in most of the low-grade metamorphic terranes in the world.

Four of the vein types observed at Site 1224—clay (smectite-illite), carbonate (calcite-aragonite), quartz, and zeolite—are similar to veins observed at Sites 896 and 504 near the Costa Rica Rift (Alt, Kinoshita, Stokking et al., 1993). These minerals are present in relatively lower temperature hydrothermal assemblages (probably <100°C) at these sites (Laverne et al., 1996). Truly high-temperature vein assemblages, such as the actinolite and epidote veins found deeper than 2000 mbsf at Site 504, were not found at Site 1224. The mineral laumontite in the illite veins indicates a high-temperature zeolite facies assemblage (Miyashiro, 1973). Aragonite generally forms at a higher temperature than calcite. These minerals indicate the local influence of warm hydrothermal fluids.

Tartarotti et al. (1996) considered the sequence of secondary mineralization in open fractures based on studies of Hole 896A in the Costa Rica Rift. They suggested a general sequence of vein formation from oldest to youngest as follows:

1. Fe oxyhydroxide,
2. Smectite with spheroidal texture,
3. Calcium carbonate with blocky crystal shape,
4. Smectite with fibrous texture, and
5. Calcium carbonate with fibrous texture.

Visual and macroscope observations together with XRD analysis of veins suggest that this sequence also is present at Site 1224 (e.g., many thick calcite veins have distinct inner calcite and outer green smectite zones; fibrous smectite is present only in thick veins; many quartz veins have associated outer green smectite; and most vein surfaces of host rocks show greenish [smectite] or black [oxyhydroxide] colors).

Tartarotti et al. (1996) characterized clay-lined veins at Site 896 into two types: nonfibrous and fibrous veins. Nonfibrous veins are thought to represent fractures filled by minerals crystallizing in open cavities where fluid-filled spaces were available for crystal growth. Fibrous veins are interpreted as crack-seal veins in which narrow cracks propagated and then were cemented. According to this model, thin and deposit-poor veins record hydrothermal activity, whereas thick crystallized veins reflect hydrothermal activity together with shear stress in the flow unit. Veins are thicker in pillows than massive flows. Perhaps this is because pillows are more fractured, sheared, and therefore more permeable to hydrothermal fluids than massive flows.

Many vein minerals in basement at Site 1224 are stable at low temperature and pressure conditions (e.g., zeolite). Phillipsite, the main zeolite present at Site 1224, is a low-temperature member of the zeolite group (e.g., Miyashiro, 1973). Smectite is also commonly found as a product of the alteration of volcanic ashes and rocks from the seafloor.

Smectite is present in most low-grade metamorphic terranes around the world.

Paleomagnetism

We used progressive alternating-field (AF) demagnetization of archive-half sections, one whole-core section, one working-half section, and discrete samples to characterize the paleomagnetic signal and resolve the magnetization components recorded in the recovered core. An unambiguous magnetostratigraphy could not be obtained from the only undisturbed core (Core 200-1224C-1H) that was recovered in the sedimentary section; the other sediment cores were extremely disturbed by drilling. Based on postcruise analysis of calcareous nannofossils in the sediments, it appears that nearly the entire sedimentary section is middle Eocene in age. During the cruise, we only had time for a cursory interpretation of the magnetization of the basaltic units, although fairly detailed demagnetization experiments were conducted on split cores and discrete samples.

Given that 58 m of basalt core was recovered (see **"Igneous Petrology,"** p. 26, in "Lithology") that may span enough time to average geomagnetic secular variation, the magnetization of the basalts should provide a valuable paleolatitude estimate for the Pacific plate at ~45 Ma. This age corresponds to the Pacific plate's abrupt change in motion relative to the hotspots as marked by the kink in the Hawaiian-Emperor hotspot track. A cusp in the Pacific plate apparent polar wander path (APWP) may also occur at this age, marking a change in the motion of the Pacific plate relative to the spin axis. The Pacific APWP and hotspot tracks together provide key constraints on estimates of the size of motions between hotspots, ultimately extending our understanding of mantle dynamics (Acton and Gordon, 1994). Additionally, the age also lies within the period (39–57 Ma) when the Hawaiian hotspot has been shown to have moved rapidly southward relative to the spin axis (Petronotis et al., 1994). If geomagnetic secular variation has been averaged by the basalt units and if secondary overprints caused by alteration do not mask the primary magnetization, then we should be able to obtain an accurate paleolatitude. Finally, rock magnetic studies of the basalts should help refine our understanding of the magnetization of the upper oceanic crust and its role in generating lineated marine magnetic anomalies.

Microbiology

Samples of different sediment types and samples from basaltic rock were collected at Site 1224 for aerobic and anaerobic cultivation, for deoxyribonucleic acid (DNA) extraction and analysis, for phylogenetic characterization, for total cell counts, and for determination of the live/dead ratio of indigenous microbial communities. Sediment suspensions and ground basalt material were used under oxygen depleted conditions in the anaerobic chamber for the establishment of enrichment cultures. Aerobic cultivation was carried out using both seawater-based media and commercial Zobell's medium (Difco). Anaerobic cultures were based on reduced mineral media.

To evaluate the microbial background at Site 1224, ambient seawater samples were collected at 1 m below sea surface upwind of the *JOIDES Resolution*. The microscopically enumerated total cell counts in the surface water at Site 1224 were 1.4×10^4 cells/mL.

Sediment samples from Holes 1224C, 1224D, and 1224E were obtained from different depths ranging from the near-surface layer down to 24.9 mbsf. Bacteria were present in all sediment samples taken to 24.9 mbsf.

The amount of active bacteria was assessed in two representative sediment samples taken from the near-surface layer (Sample 200-1224C-1H-1, 0–5 cm) and from a depth of 25 mbsf (Sample 200-1224E-2R-5, 143–150 cm). As indicated by fluorescent signals after hybridization with the Bacteria-specific probe EUB338, the amount of metabolically active bacteria ranged in these sediment layers from 62% to 41% of the total cell counts, respectively.

Microscopic investigation of thin sections revealed the first survey of the presence of eukaryotic microorganisms that are counted among the kingdom of fungi within basement of the North Pacific Ocean. Hyphae have been found within cavities, small fractures, and veins filled with $CaCO_3$. These fungal structures were viewed by transmitted light microscopy, in which they appear with a brownish tinge. A net of fungal hyphae shown in Figure **F63** filled the complete space spanning from the basalt/calcite boundary to the center of the cavity (see **"Microbiology,"** p. 43). The cross-sectional dimension of the hyphal network is 5–10 µm with a length ranging from 50 to several hundred micrometers. The hyphae are typically interrupted at irregular intervals by cross-walls, so-called septa, which divide the entire fungal hyphae into single distinctive cells. Our results provide strong evidence for eukaryotic life in addition to bacteria in deep subsurface environments.

Physical Properties

In Hole 1224A, *P*-wave velocities of aphyric basalt from Cores 200-1224A-5X and 6N are ~5900 and ~5800 m/s, respectively.

In Hole 1224C, the gamma ray attenuation (GRA) densities of sediments gradually decrease with increasing depth between 0 and 6.4 mbsf, corresponding to a color change from light brown to dark brown. Similarly, we observed an unusual trend for bulk and dry densities in Hole 1224C that decreases from ~1.52 to ~1.36 g/cm³ and from ~0.8 to 0.54 g/cm³, respectively. Porosities in Hole 1224C gradually increase from ~71% to ~80%. *P*-wave velocities (as measured with the *P*-wave logger [PWL]), however, show a small increase from ~1460 to ~1500 m/s with depth between 0 and 6.4 mbsf. *P*-wave velocities (as measured with the *P*-wave velocity sensor [PWS] contact probe) between Cores 200-1224C-1H and 4H (between 0 and ~5.70 mbsf) range from ~1525 to ~1535 m/s. The *P*-wave velocity in Core 200-1224C-5H is ~1555 m/s, which is greater than other sections. Grain densities for Hole 1224C show a small increase from 2.782 to 2.831 g/cm³ for depths shallower than ~2 mbsf. Between ~2 and ~6 mbsf, grain densities remain fairly constant—between ~2.70 and ~2.74 g/cm³.

In Core 200-1224D-2R, bulk and dry densities increase from 2.7 to 2.9 g/cm³ and 2.6 to 2.8 g/cm³, respectively. In Core 200-1224D-3R, bulk and dry densities decrease from 2.9 to 2.8 g/cm³ and from 2.8 to 2.7 g/cm³, respectively. In Cores 200-1224D-4R and 5R, they also decrease from 2.85 to 2.80 g/cm³ and from 2.8 to 2.7 g/cm³, respectively. Porosities remain at low values and range from 4% to 9%. PWS velocities range from 4200 to 6500 m/s. Compressional wave velocity anisotropy for each sample is ~2%–10%. PWS velocities have a sinusoidal depth variation. They decrease between 25 and 35 mbsf, increase be-

tween 35 and 45 mbsf, and decrease again between 45 and 55 mbsf. This sinusoidal depth variation is also identified for Hole 1224F.

Between 25 and 60 mbsf, PWS velocities in Holes 1224E and 1224F have a similar trend to Hole 1224D. PWS velocities have a strong depth dependence. Compressional velocities separate into seven depth zones (Fig. F71) (see "Hole 1224D," p. 47, in "Physical Properties"):

1. 30–38 mbsf: 5500–6000 m/s,
2. 38–41 mbsf: 4200–5500 m/s,
3. 41–61 mbsf: 5000–6000 m/s,
4. 61–100 mbsf: 4500–5000 m/s,
5. 100–138 mbsf: 4700–6000 m/s,
6. 138–147 mbsf: 4000–4700 m/s, and
7. below 147 mbsf: 5500 m/s.

Zones 1–3 may be characterized as rather uniform basalt flow zones with a thin low velocity (fractured) layer. Zone 4 has a slightly lower velocity than the zones above and below it. Velocities of zone 5 are higher than those for zones 4 and 6. Zone 6 is highly fractured and characterized by the lowest velocities. Zone 7 corresponds to more uniform basalt layers.

P-wave velocities have a scattered correlation with increasing bulk density. Compressional wave velocity vs. porosity, however, has a good inverse correlation, as *P*-wave velocity decreases with increasing porosity. These two relations imply that compressional velocities are not controlled by bulk densities, but are well controlled by porosities. Large porosities are associated with more fractured zones. If this is true, zones 2 and 6 are intensively fractured.

3.5-kHz Deep-Source Experiment

A long-standing problem in the red clay province of the eastern Pacific Ocean is how to adequately resolve chert layers and basement in the presence of sediments <50 m thick. By lowering a battery-powered, free-running 3.5-kHz pinger to the seafloor on the vibration isolated television (VIT) sled and recording the pulse on the ship's 3.5-kHz acquisition system, we hoped to increase the sound level incident on the seafloor, improve the penetration into the subbottom, reduce the footprint of the sound on the seafloor, and increase the received signal levels. The deep-source 3.5-kHz experiment was conducted whenever the VIT camera was lowered to the seafloor either for reconnaissance surveys or reentries.

Examination of the deep-source 3.5-kHz records shows two prominent reflections at 13 and 38 ms below the seafloor. Depending on the sound velocities in the seabed, these reflectors would be 10–13 m and 28–38 m deep, respectively. The continuity of these reflectors varies with time throughout the survey, although the ship moved only a few meters. The first subseafloor reflection at 13 ms (10–13 m) is the most continuous. Another faint reflector was identified just above 30 ms (22–30 m). This may indicate a local heterogeneity or the irregular surface of pillow lava flows.

Recording during significant portions of the seafloor survey was degraded by the wash from thruster 3 across the ship's hull-mounted 3.5-kHz transducer pod. The wash increased as the ship responded to gradually increasing wind on the port side. The battery-powered pinger ran for the entire 16 hr of the lowering.

Our preliminary interpretation had been that the 13-ms reflection is present at an intermittent chert layer. The first jet-in test stopped abruptly at 13 m. Although chert layers within the sediments have been encountered at other drill sites in the eastern Pacific Ocean, nowhere at Site 1224 did we sample chert. Basalt cores were regularly acquired at 28–30 m depth, corresponding to the 38-ms reflector.

In summary, the deep-source 3.5-kHz experiment identified a second reflector at 38 ms below the seafloor that was neither observed in the traditional 3.5-kHz survey conducted in 1997 nor in the shipboard 3.5-kHz survey acquired while coming on site (Fig. **F2**). This deeper reflector, however, was observed beneath the junction box. It was shown by drilling that this is the sediment/basalt contact. Data from the deep-source 3.5-kHz experiment were digitized and are available for post-cruise processing.

Logging

Based on shipboard preliminary log analysis at this site during Leg 200, we conclude that basement in Hole 1224F consists of at least five distinctive units (see Fig. **F80** and the discussion in **"Lithostratigraphy,"** p. 54, in "Downhole Measurements") with unit contacts at roughly 45, 63, 103, and 142 mbsf. These layered formations can be distinguished using the continuous electrical resistivity, density, sonic, neutron porosity, magnetic field, and possibly spectral gamma ray logs. The existence of a conduit or large-scale fracture between 138 and 142 mbsf was detected by all the log tools including the temperature tool. In addition, the temperature tool reveals that the "warmer" fluid had a temperature of 4.6°C at the time of the logging. The vicinity of this conduit is much more highly altered than other rocks penetrated by the hole, as indicated by the gamma ray logs. Because of the relative position of the tools located in the tool strings, some tools can resolve the top logged intervals like gamma ray, porosity, density, and sonic logs. On the other hand, the resistivity tools and Formation MicroScanner (FMS) placed at the bottom of the tool string can resolve the formation properties near the bottom of the hole. The values of the magnetic fields calculated from the three-component inclinometer tool are invalid near the bottom of the pipe (~35 mbsf). In the logged intervals where all the tools overlapped, they provide consistent information to support the layered structural units based on these geophysical properties.

Broadband Seismic Observations during the Leg

Drilling at the H2O provides a unique opportunity to observe drilling-related noise from the *JOIDES Resolution* on a seafloor seismometer in the frequency band 0.1–80 Hz. See the **"Leg 200 Summary"** chapter for background material on the H2O and the retired American Telephone and Telegraph (AT&T) oceanic cable that is used to provide continuous, real-time data transmission back to the Makaha cable station on Oahu.

The University of Hawaii operates a Guralp CMG-3T three-component broadband seafloor seismometer and a conventional three-axis geophone at the H2O. Data are acquired continuously and are made available to scientists worldwide through the IRIS Data Management Center in Seattle. During the cruise, Jim Jolly and Fred Duennebier at the University of Hawaii relayed sample data files to the *JOIDES Resolution* by file transfer protocol (FTP) over the shipboard telephone. We

were then able to process data and study correlations with on-site activities and weather. The University of Hawaii also maintained a World Wide Web site showing seismic data from the H2O during the cruise (www.soest.Hawaii.edu/H2O/).

Seismic signal level variation could be associated with wind speed, sea state, shear resonance effects in the sediments, whales, water gun shooting, earthquakes, passing ships, and drilling-related activities such as bit noise and running pipe.

Core, Physical Properties, Logging, and Seismic Correlation

Four different kinds of data were compared. All data show four to six distinct units. In contrast to the seven zones identified by physical properties (given above), logging data give five distinct units in basement: 28–45 mbsf (I), 45–63 mbsf (II), 63–103 mbsf (III), 103–142 mbsf (IV), and deeper than 142 mbsf (V). Units I and II are between 28 and 63 mbsf and are characterized by massive basalts with thin fractured zones around 40 mbsf. Unit III (63–103 mbsf) was characterized by fractured basalt layers. Many small fractures were also identified by the FMS/Dipole Sonic Imager (DSI) logging tool. The calcite veins were found in this unit. Unit IV (103–142 mbsf) is characterized by stacks of small pieces of pillow lavas. Porosities by logging data, however, show highly porous zones for this unit. This unit also indicates the presence of smectite veins. Just below Unit IV, sudden large variations are present on the caliper log, resistivity log, compressional and shear velocity logs, U and Th content, and temperature log. Physical property measurements also indicate that this unit is highly fractured. The presence of high U and Th contents suggests that this unit is a highly altered zone. In Unit V, below ~142 mbsf, basalt sheet flows are found. Although we could not drill below this depth, the single-channel seismic (SCS) data suggest that this is the top of a massive basalt unit. In comparing the above units to the SCS records, these unit boundaries extend many kilometers away from the site. With further analysis it should be possible to understand the nature of oceanic Layers 2A and 2B and their relationship to lithologic boundaries in ~45-Ma fast-spreading oceanic crust.

BACKGROUND AND OBJECTIVES

The long-term H2O site satisfies three scientific objectives of crustal drilling: (1) it is located in one of the high-priority regions for the Ocean Seismic Network (OSN); (2) its proximity to the Hawaii-2 cable and H2O junction box make it a unique site for real-time, continuous monitoring of geophysical and geochemical experiments in the crust; and (3) it is on fast-spreading Pacific crust (71 mm/yr, half rate), which represents one end-member for models of crustal generation and evolution as well as crust/mantle interaction.

This site primarily represents the interests of the Joint Oceanographic Institutions (JOI)/IRIS Steering Committee for Scientific Use of Submarine Cables (Chave et al., 1990), OSN group (Purdy, 1995), and the International Ocean Network (ION) group (Montagner and Lancelot, 1995). Drilling at the H2O site will also provide useful background information for the Borehole Observatories, Laboratories, and Experiments (BOREHOLE) group (Carson et al., 1996), the deep biosphere mi-

crobiology community, and the oceanic lithospheric processes community (Dick and Mével, 1996).

One reentry hole within 2 km of the H2O junction box in the eastern Pacific Ocean at 27°52.916′N, 141°59.504′W in 4979 m water depth (Figs. F8, F9, F10) (Butler, 1995a) was proposed. The site is roughly halfway between California and Hawaii. A limited geophysical survey of the cable, including SCS, was carried out from the *Revelle* in August 1997 (Stephen et al., 1997).

Background

H2O

The Hawaii-2 submarine cable system is a retired AT&T telephone cable system that originally connected San Luis Obispo, California, and Makaha, on Oahu, Hawaii (Fig. F8). The cable system was originally laid in 1964. IRIS installed a long-term seafloor observatory about halfway along the cable (Fig. F11). The cable was cut and terminated with a seafloor junction box. The location of the junction box defines the H2O seafloor observatory. The junction box has eight underwater make-break connections. About 500 W of power is available from the junction box, and there is ample capacity for two-way real-time communications with seafloor instruments. Data channels from the seafloor can be monitored continuously via the Oahu end of the cable to any laboratory in the world. (The California end of the cable cannot be used because it was cut and removed from the continental shelf.) There is a shallow buried broadband seismometer operating at the site (Duennebier et al., 2000, 2002). Other seafloor observatories, such as a geomagnetic observatory (Chave et al., 1995), a hydrothermal observatory (Davis et al., 1992; Foucher et al., 1995), or a broadband borehole seismic observatory (Orcutt and Stephen, 1993) can be installed at the site as funding becomes available.

Within the Ocean Drilling Program (ODP) and the marine geology and geophysics communities, there has been considerable interest in the past few years in long-term seafloor observatories that include a borehole installation. Prototype long-term borehole and seafloor experiments almost exclusively use battery power and internal recording. The data are only available after a recovery cruise. One exception to this is the Columbia-Point Arena ocean-bottom seismic station (OBSS), which was deployed on an offshore cable by Sutton and others in the 1960s (Sutton et al., 1965; Sutton and Barstow, 1990). For the foreseeable future, the most practical method for acquiring real-time, continuous data from the seafloor will be over cables (Chave et al., 1990). The H2O project provides this opportunity.

Geological Setting

The Hawaii-2 cable runs south of the Moonless Mountains between the Murray and Molokai Fracture Zones (Fig. F8) (Mammerickx, 1989). Between 140° and 143°W, water depths along the cable track are typical for the deep ocean (4250–5000 m); the crustal age varies from 45 to 50 Ma (Eocene); and the sediment thickness to within the available resolution is ~100 m or less. Prior to our cable survey cruise in August 1997, sediment thickness in particular was not well resolved along the track (Winterer, 1989).

F8. Site 1224, H2O, repeater locations, major fracture zones, and previous drill sites, p. 74.

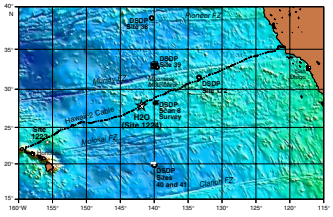

F9. Hydrosweep bathymetry around the H2O area, p. 75.

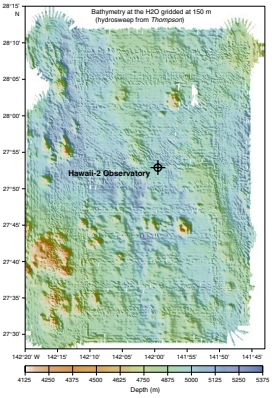

F10. Location of the H2O junction box shown on SeaBeam bathymetry, p. 76.

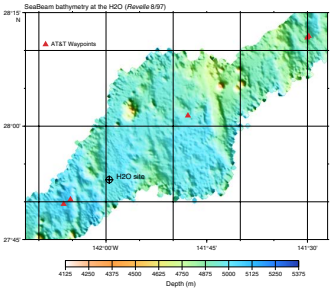

F11. Artist's conception of the H2O, p. 77.

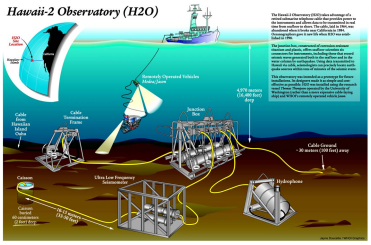

Tectonically, the cable runs across the "disturbed zone" south of the Murray Fracture Zone between magnetic isochrons 13 and 19 (Atwater 1989; Atwater and Severinghaus, 1989). In the disturbed zone, substantial pieces of the Farallon plate were captured by the Pacific plate in three discrete ridge jumps and several propagating rifts. To avoid this tectonically complicated region and to be well away from the fracture zone to the south of the disturbed zone, the H2O site was situated west of isochron 20 (45 Ma) at ~140°W.

The crust west of 140°W was formed between the Pacific and Farallon plates under "normal" spreading conditions. The average half-rate quoted by Malahoff and Handschumacher (1971) in this region for Anomalies 18–31 is 49 mm/yr. However, a careful analysis of spreading rate based on the magnetic anomalies of Atwater and Severinghaus (1989) and the ages reported by Cande and Kent (1992, 1995) give a half-rate of 71 mm/yr for Anomalies 18–22 (38.5–48.9 Ma), ~49 mm/yr for Anomalies 22–25, and ~35 mm/yr for Anomalies 25–30 (Fig. **F12**). At the time this crust was formed, the Farallon plate had not split into the Cocos and Nazca plates, and the ridge that formed this crust was the same as the present-day East Pacific Rise.

F12. Spreading rate and crustal age, p. 78.

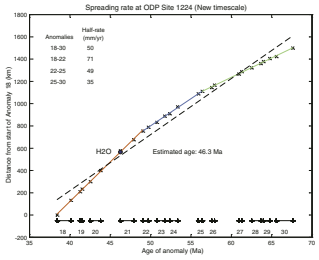

Between 140° and 143°W, the Hawaii-2 cable lies in the pelagic clay province of the North Pacific Ocean (Leinen, 1989). The sediments here are eolian in origin, consisting primarily of dust blown from Asia. They are unfossiliferous red clays. Deep Sea Drilling Project (DSDP) Leg 5 drilled a transect of holes in the pelagic clay province along longitude 140°W (McManus, Burns, et al., 1970). Site 39 is north of the cable at latitude 32°48.28′N with an age of 60 Ma (Fig. **F8**). It has a sediment thickness of only 17 m. Sites 40 and 41 are near the same latitude at 19°50′N with an age of ~67 Ma. Site 40 was drilled in an area of ponded sediments at the base of a large abyssal hill. Basement was not reached, and drilling terminated at a chert bed at 156 m. Acoustic basement, the deepest horizon identified on the seismic reflection profiles at Site 40, corresponded to the chert beds. Site 41 was drilled 15 km from Site 40 but was considered to be more representative of the sediments in the general area. Basaltic basement was encountered at 34 mbsf, but there were no cherts. Site 39 is north of the Murray Fracture Zone, and Sites 40 and 41 are south of the Molokai Fracture Zone. The actual "ribbon" of crust on which the cable lies is between the two fracture zones and was not drilled during DSDP Leg 5.

Site 172 was drilled during DSDP Leg 18 between the Molokai and Murray Fracture Zones but east of 140°W in the "disturbed" zone (31°32.23′N, 133°22.36′W), which has an estimated crustal age of 35 Ma (Kulm, von Huene, et al., 1973). Sediment thickness above the basaltic basement was 24 m. The sediment thickness from seismic reflection profiles had been interpreted as 90–105 m. The discrepancy was attributed to "reverberations and thin sediment cover."

Cable Survey Cruise in August 1997

In August 1997, a survey of the Hawaii-2 cable between 140° and 143°W was carried out (Stephen et al., 1997). The survey strategy consisted of two phases. First, we collected SeaBeam bathymetry, magnetics, and SCS along the cable track starting at 140°W and heading west. Our site criteria were to have 100 m of sediment thickness for setting the reentry cone, to be in relatively undisturbed "normal" crust in a plate tectonic sense, and to optimize drilling penetration by selecting sites with well-consolidated basement, not rubble or highly altered

zones. As a second phase, we carried out a survey in a 20 km × 20 km area around each of three proposed drill sites to map bathymetry, sediment thickness, basement morphology, and magnetics in the vicinity (e.g., Fig. **F13**).

Figure **F14** shows the H2O junction box location with respect to the track lines for the *Revelle* during the site survey in 1997. The actual site is to the southwest of a well-surveyed block but is bracketed by two parallel SCS lines. Figures **F15** and **F16** show the track lines, annotated in SCS shot numbers and Julian time, respectively, for the SCS and 3.5-kHz data. Circles at 1, 2, and 3 km radius from the site and the originally proposed drill locations are also indicated. Although cross-tie seismic lines are not available, the parallel seismic lines are sufficiently close together that contiguous structure can be identified across the lines.

Figures **F17** and **F18** are the 3.5-kHz lines north and south, respectively, of the H2O area. These 3.5-kHz data were acquired on the *Revelle* in August 1997 at the same time as the SCS data. Unmigrated and migrated SCS profiles from this site are shown in Figures **F19** and **F20,** respectively, for the north line and in Figures **F21** and **F22,** respectively, for the south line. A tenth of a second two-way traveltime corresponds to ~75 m in the water column.

Prior to drilling, we suspected that there were chert layers in this part of the Pacific Ocean from earlier drilling during DSDP Legs 5 and 18. On these 3.5-kHz records, there is a clean single pulse followed 10 ms later by a diffuse event. Our interpretation was that the clean event was the seafloor and that the diffuse event was the "chert layer." Ten milliseconds of two-way traveltime corresponds to ~8 m thickness of soft sediments. These 3.5-kHz data show nothing coherent below the "chert layer," but some inconclusive, subtle arrivals do appear occasionally near the 38-ms depth (Fig. **F18**). This was also the experience in the 1960 surveys where "acoustic basement" turned out to be chert.

We had interpreted a continuous mid-sediment reflector at ~0.03 s, or ~25 m depth, in the SCS records, which did not correspond to the "chert layer" identified on the 3.5-kHz records. Futhermore, we interpreted the diffraction events at ~0.06 s in the SCS data as occurring at the sediment-basement boundary, and we estimated a very uniform sediment thickness of ~50 m (Figs. **F19, F20, F21, F22**). As discussed in **"3.5-kHz Deep-Source Experiment,"** p. 55, and **"Core, Physical Properties, Logging, and Seismic Correlation,"** p. 57, the horizon at ~8 mbsf is a mid-sediment reflector but is not chert. The subtle arrivals at ~25–30 mbsf are basaltic basement, not a mid-sediment reflector. The diffraction events at ~50–60 mbsf could be originating from the interface between lithologic Units 1 and 2.

Scientific Objectives

Drilling at the H2O site directly addresses the second of three initiatives outlined in the ODP Long Range Plan (JOIDES Planning Committee, 1996): "In situ monitoring of geological processes" (pp. 49–51). It also represents an initial step in accomplishing the oceanic crustal component of the third initiative: "Exploring the deep structure of continental margins and oceanic crust" (pp. 52–54). The drilling is intimately tied to the use of "seafloor observatories" (p. 63) and represents the partnership of ODP with the OSN, ION, and BOREHOLE (p. 74). (Page numbers refer to pages in the Long Range Plan.)

F13. Track lines during the 1997 site survey cruise, p. 79.

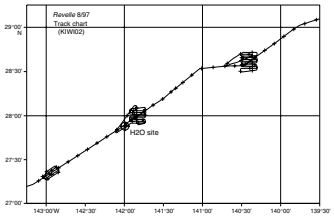

F14. Track chart showing the H2O junction box position, p. 80.

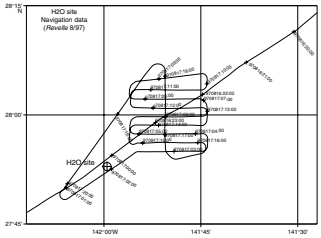

F15. 1997 survey track lines annotated with SCS shot numbers, p. 81.

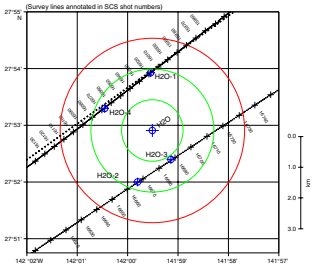

F16. 1997 survey track lines annotated with Julian day and time, p. 82.

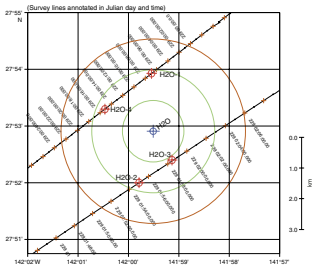

Basement Drilling on the Pacific Plate

Prior to Leg 200, there was only one deep borehole (>100 m) in the normal Pacific plate, the largest modern tectonic plate. Table T1 summarizes the boreholes drilled on "normal" crust on the Pacific plate that have >10 m of basement penetration and with crustal ages <100 Ma during past DSDP and ODP drillings. Holes in seamounts, plateaus, aseismic ridges, and fracture zones were not included. Holes with crustal ages >100 Ma were also not included because they would have been affected by the mid-Cretaceous superplume event (Pringle et al., 1993). Prior to Leg 200, in 30 yr of deep ocean drilling and in more than 1000 holes worldwide, there were only 13 holes with >10 m penetration into "normal" igneous Pacific plate: only one hole during ODP, only one hole with >100 m penetration, and no holes in crust with ages between 29 and 72 Ma. Furthermore, there were no boreholes off axis in "very fast" spreading crust. At the latitude and age of the H2O area, the spreading rate was 142 mm/yr (full rate). Having a reference station in "normal" (45–50 Ma) ocean crust would constrain geochemical and hydrothermal models of crustal evolution.

Although fast-spreading ridges represent only ~20% of the global ridge system, they produce more than half of the ocean crust on the surface of the planet—almost all of it along the East Pacific Rise. Most ocean crust currently being recycled back into the mantle at subduction zones was produced at a fast-spreading ridge. If we wish to understand the Wilson cycle in its most typical and geodynamically significant form, we need to examine ocean crust produced at fast-spreading ridges. We have also known for >40 yr that fast-spreading crust is both simple and uniform, certainly so in terms of seismic structure (Raitt, 1963; Menard, 1964). Successful deep drilling of such crust at any single location is thus likely to provide fundamental information that can be extrapolated to a significant fraction of the Earth's surface.

Ocean Seismic Network

Drilling at the H2O area would address both teleseismic, whole-Earth seismic studies, and regional studies. The site is located in a region on the Earth's surface where there is no land within a 1700-km radius. For uniform coverage of seismic stations on the surface of the planet, which is necessary for whole-Earth tomographic studies, seafloor seismic observatories are required. This site is one of three high-priority prototype observatories for the OSN (Butler, 1995a, 1995b; Purdy, 1995). Global seismic tomography provides three-dimensional images of the lateral heterogeneity in the Earth and is essential in addressing fundamental problems in subdisciplines of geodynamics such as mantle convection, mineral physics, long-wavelength gravimetry, geochemistry of ridge systems, geomagnetism, and geodesy. Specific problems include the characteristic spectrum of lateral heterogeneity as a function of depth, the anisotropy of the inner core, the structure of the core/mantle boundary, the role of oceanic plates and plumes in deep mantle circulation, and the source rupture processes of Southern Hemisphere earthquakes that are among the world's largest (Forsyth et al., 1995).

The culturally important earthquakes in California are only observed at regional distances on land stations in North America that restrict the azimuthal information to an arc spanning ~180°. To observe California earthquakes at regional distances to the west requires seafloor stations. Regional observations are used in constraining earthquake source

F17. 3.5-kHz data for the line north of Site 1224, p. 83.

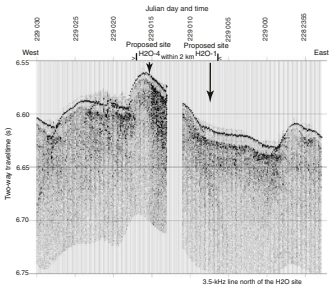

F18. 3.5-kHz data for the line south of Site 1224, p. 84.

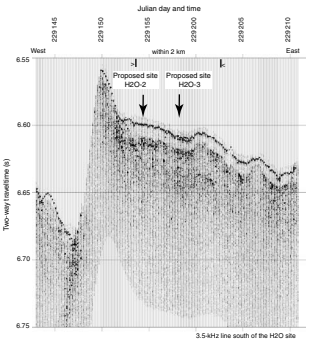

F19. Unmigrated SCS line north of Site 1224, p. 85.

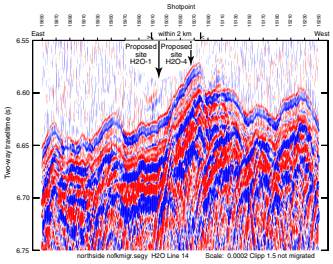

F20. Migrated SCS line north of Site 1224, p. 86.

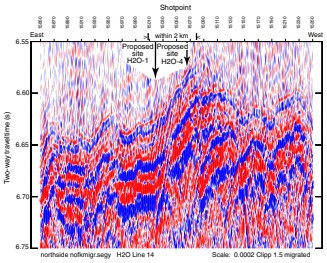

mechanisms. Since the H2O site data will be available in real time, data will be incorporated into focal mechanism determinations within minutes of California earthquake events. Other problems that can be addressed with regional data from Californian and Hawaiian earthquakes are the structure of the 400-km, 525-km, and 670-km discontinuities in the northeastern Pacific Ocean and the variability of elastic and anelastic structure in the Pacific lithosphere from P_o and S_o and pure-path oceanic surface wave studies (Butler, 1995a, 1995b).

At the OSN pilot experiment site in 1998, we deployed seafloor, buried, and borehole broadband seismometers in order to compare the performance of different styles of installation (Fig. **F23**). Figures **F24** and **F25** summarize for vertical and horizontal component data, respectively, the improvement that we expect to see in ambient seismic noise on placing a sensor in basement rather than on or in the sediments. Above 0.3 Hz, the seafloor, buried, and borehole spectra at the OSN-1 site show the borehole to be 10 dB quieter on vertical components and 30 dB quieter on horizontal components (Collins et al., 2001). Shear wave resonances (or Scholte modes) are the physical mechanism responsible for the higher noise levels in or on the sediment. The resonance peaks are particularly distinct and strong at the H2O site. (Note the 15-dB peak on vertical and the 35-dB peak on horizontal near 1 Hz on the H2O spectra.) By placing a borehole seismometer in basement at H2O, we expect to eliminate these high ambient noise levels.

There are three important characteristics for a broadband borehole seismic installation:

1. The hole should penetrate well below the sediment/basement contact so that true basement vibration is observed. The OSN pilot experiment hole was cased only ~20 m into basement, and after installation the top of the sonde was still protruding out of the sediment. Therefore, it is difficult to say conclusively that the seismometer was responding to true basement motion.
2. The sides and bottom of the hole must be sealed to prevent hydrothermal circulation within the formation. Water circulation around the sonde generates undesirable "installation noise." If the bottom of the hole is composed of unconsolidated and fractured basalt, this means that the hole must be cased to total depth and sealed at the bottom with a cement plug.
3. To ensure good coupling of the sonde to the Earth, the hole should be in as consolidated a section of basalt as possible and the casing should be cemented to the formation. It is impossible to predict the seismic response of rubble, and it is impossible to couple the sonde and/or casing to rubble. When cementing in poorly consolidated rock, the cement will flow mostly into the formation rather than up the annulus around the casing, so proper coupling of the casing to the formation cannot be obtained.

Our target depth for drilling at the H2O site was 350–400 m into basement. This was a conservative estimate to get into consolidated basalts based on the drilling experience in Hole 504B. In Hole 504B, sonic logs and resistivity measurements indicate poorly consolidated basalt down to 600 m. A hole that penetrated ~400 m into basement would acquire good-quality basalt samples for geochemical studies, provide adequate penetration into oceanic Layer 2 for paleomagnetic analyses, and provide good hole conditions for in situ experiments.

F21. Unmigrated SCS line south of Site 1224, p. 87.

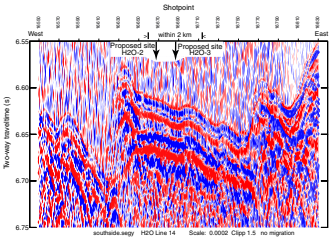

F22. Migrated SCS line south of Site 1224, p. 88.

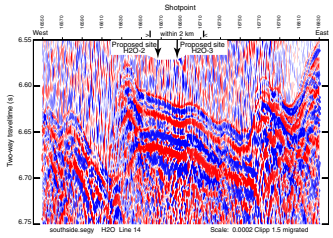

T1. Holes drilled in "normal crust" on the Pacific plate, p. 165.

F23. Locations of OSN-1 and H2O broadband seismic sites, p. 89.

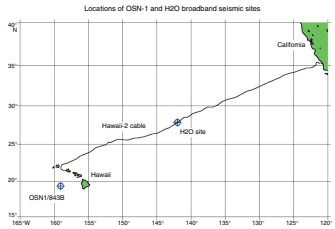

F24. Vertical component spectra, p. 90.

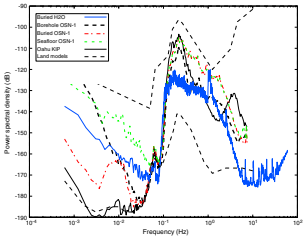

OPERATIONS

Transit to Site 1224

We departed Site 1223 at 0130 hr on 23 December 2001 and arrived at waypoint 1 (27°32.787′N, 142°33.036′W), ~36 nmi southwest of the H2O junction box (27°52.916′N, 141°59.504′W), at 0000 hr on 26 December to begin a seismic and 3.5-kHz echo sounder survey. All times are reported in local ship time, which is Universal Time Coordinated (UTC) – 9 hr at Site 1224. The 766-nmi voyage took 2.9 days at an average speed of 10.9 kt. Summaries of coring results are given in Tables **T2** and **T3,** and an operations synopsis is provided in Table **T4.**

At waypoint 1, the captain set the course to 56° at 6 kt to begin the survey. The water gun located at the stern of the ship was fired every 10 s during the survey as part of a seismic refraction study in which an ocean-bottom seismometer (OBS) located on the seafloor at the H2O was the receiver (see **"Seismic Results from Hawaii-2 Observatory,"** p. 59). We had also intended to conduct a seismic reflection survey, but the single-channel streamer did not function because of an electronic failure. Fortunately, the 3.5-kHz data provided sufficient imaging of the sediment above basement to allow us to select a new primary drilling site (proposed Site H2O-5; 27°53.363′N, 141°58.758′W) that was more ideally positioned relative to the OBS than the other sites previously surveyed. Proposed Site H2O-5 was approved for drilling, subsequently becoming ODP Site 1224.

Following completion of the survey at waypoint 2 (27°54.426′N, 141°56.985′W) at ~0745 hr on 26 December, the *JOIDES Resolution* returned and was positioned on site with Global Positioning System navigation at 0845 hr on 26 December. Operations were then temporarily suspended while waiting on weather (WOW) because of heave, pitch, roll, and wind up to 7.7 m, 5.2°, 4.5°, and 29 kt, respectively. A total of 13.25 hr of WOW time occurred before drilling operations could proceed.

Site 1224

After the weather improved, the drill crew and core technician made up the advanced piston corer (APC)/extended core barrel (XCB)/motor-driven core barrel (MDCB) BHA with an 11 7/16-in Security H87F four-cone button-type drill bit. The bit was dressed with four #16 (½-in) jet nozzles in preparation for a jet-in test. The pipe trip down began at 2200 hr on 26 December. When the bit was at a depth of 3778.94 m, the VIT was launched in order to conduct a camera survey of the site for debris. During the camera survey, we also conducted a survey with an echo sounder attached to the VIT frame to further delineate subsurface layers. The roll and pitch, along with the surge through the moonpool, made it very difficult to launch the VIT with the pipe moving the length of the moonpool. The VIT was fully secured with four tether ropes; the compass was oriented; and the VIT was successfully launched.

The drill string continued to be run to 4963.82 m. The top drive was then picked up, and the drill string was spaced out for performing a dynamically positioned 30-m × 30-m box survey. The survey took 2.0 hr and showed that the site was flat, undisturbed, and free of debris and cables.

F25. Horizontal component spectra, p. 91.

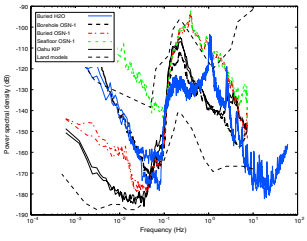

T2. Coring Summary, Site 1224, p. 166.

T3. Expanded coring summary, p. 169.

T4. Operation synopsis, Leg 200, p. 170.

First Jet-In Test

A wash barrel was dropped and the bit was lowered to 4973.47 m for a jet-in test (Fig. F3). The seafloor was tagged at 4966.1 meters below sea level (mbsl) (4977 mbrf) at 1525 hr on 27 December (see Fig. F16, p. 59, in the "Explanatory Notes" chapter for a comparison of depths below rig floor and depths below seafloor). The jet-in test was performed to confirm a refusal depth for jetting in the reentry cone with 20-in casing. Operating parameters for the jet-in test included a range of 4- to 8-klb weight on bit, with a pump output of 50 strokes per minute (spm) utilizing a 6½-in liner (0.123 barrels [bbl] of water per stroke) at up to 1375 psi. At 12 to 13 mbsf, a hard layer was encountered. After about an hour of jetting with pump rates increasing from 50 to 90 spm and with pressure increasing from 600 to 1375 psi, the jet-in test was stopped. Refusal depth was determined to be 4990 mbrf (13 mbsf), although the test was suspect as the ship was experiencing 4- to 5-m heave at the time of the test. The bit cleared the seafloor at 1740 hr on 27 December. The Maritime Hydraulics active heave compensator (AHC) was on during the test.

It took 6.25 hr to pull the VIT to the surface because of insufficient hydraulic fluid volume in the VIT pump. We determined later that this resulted from having two of the hydraulic lines incorrectly connected when the winch hydraulic hoses were rebuilt. The VIT was recovered at 0000 hr on 28 December. While we recovered the VIT, we pulled the bit up to 4944.57 mbrf and retrieved the wash barrel.

During deteriorating weather conditions, the upper guide horn was reinstalled; knobby joints were set across the guide horn; and the string was hung off in a 500-T elevator on the dual elevator stool, with the end of the pipe at 4953.15 mbrf. Maximum heave while WOW at this juncture was 5.8 m, with maximum pitch and roll of 3.8° and 4.1°, respectively. Total WOW before resuming operations was 13.75 hr.

Hole 1224A

At 1345 hr on 28 December, a core barrel was dropped and the drill string was spaced out to 4973.47 m. Because of a 4.6-m heave with a roll of 5°, the decision was made to core with the XCB to avoid the risk of bending the APC core barrel. The seafloor was tagged at 4966.1 mbsl (4977 mbrf), and Hole 1224A was spudded at 1455 hr on 28 December. Core 200-1224A-1X was advanced 6 m downhole with no recovery; hence, we could not establish a precise mudline (Table T2). Recovery in Core 200-1224A-2X consisted of a few gray pebbles, later interpreted to be zeolite pebbles, and recovery in Core 200-1224A-3X was little more than a smear of red clay. Thus, for the first three cores, we had advanced to ~25.2 mbsf and only recovered ~3 cm of core (0.12% recovery). On Core 200-1224A-4X, drilling progress was slow when we got to hard rock, which at the time was thought to be chert or basaltic basement. Recovery of 1.24 m of red clay and pieces of basalt confirmed that we had penetrated basement near the bottom of the 5.5-m interval cored, or at ~28 mbsf. We attempted one more XCB core (200-1224A-5X), before switching to the MDCB for one last short core. We pulled out of the hole and cleared the seafloor at 0530 hr on 29 December, ending Hole 1224A.

Overall, we cored 32.2 m and recovered 1.67 m of core (5.19% recovery), with 32 m cored and 1.45 m recovered (4.53% recovery) with the

XCB and 0.2 m cored and 0.22 m recovered (110% recovery) with the MDCB (Table T2).

Hole 1224B

The bit was set at 4961.1 mbsl (4972 mbrf), and Hole 1224B was spudded with the APC at 0650 hr on 29 December. Core 200-1224A-1H appeared to have suffered from a mechanical shear due to heave, resulting in recovery of only 0.2 m, which was not considered sufficient to establish a valid mudline. The primary goal of APC coring was to establish the mudline; therefore, we offset to spud Hole 1224C. Hole 1224B officially ended at 0745 hr on 29 December after we pulled the bit up to clear the seafloor.

Hole 1224C

The bit was positioned at 4964.1 mbsl (4975 mbrf), and Hole 1224C was spudded with the APC at 0820 hr 29 December. We recovered 6.53 m of core and established the mudline at 4967.1 mbsl (mbsl) (4978.0 mbrf). Having successfully determined the mudline, the bit was pulled clear of the seafloor at 0915 hr on 29 December, marking the end of Hole 1224C.

Second Jet-In Test

Because of deteriorating weather, we pulled the bit up to 4933.6 mbsf (4944.5 mbrf) at 1000 hr on 29 December and hung the drill pipe off the dual elevator stool. Weather at the time included maximum heave, pitch, and roll of 6.3 m, 2.4°, and 8.1°, respectively, with winds up to 44 kt. Total WOW time was 16.0 hr, with operations beginning again at 0115 hr on 30 December.

A second jet-in test was deemed necessary to confirm the depth of penetration for the 20-in surface casing, which would be run with the reentry cone. A wash barrel was dropped, and the BHA was jetted in to 4996.1 mbsl (5007 mbrf; ~29 mbsf) with no obstructions encountered, unlike the first jet-in test. Jetting was done at 20 spm with a water pressure of 170 psi and no rotation of the bit. After 35 min the jet-in test was stopped at 60 spm and 600 psi with 10-klb weight on bit. The drill string was pulled out of the hole, with the bit clearing the seafloor at 0230 hr on 30 December and the rotary table at 1430 hr 30 December.

Hole 1224D

The reentry cone was positioned over the moonpool doors, and the casing string was partially assembled at 1830 hr on 30 December 2001. Poor weather conditions and the associated large heave, roll, and pitch forced us to delay operations until 1715 hr on 1 January 2002—a loss of 46.75 hr.

With weather conditions improving, the reentry cone and ~25 m of 20-in casing were assembled and lowered through the moonpool at 2335 hr on 1 January. Hole 1224D was spudded at 1220 hr on 2 January. It took only 24 min at 40 spm and 200 psi to jet the 20-in casing string down to 5003.47 mbrf (25.47 mbsf) and set the reentry cone. VIT observation of the reentry cone confirmed that it was in a satisfactory position. The bit cleared the seafloor at 1315 hr on 2 January, and the

pipe was tripped back to the rig floor with the jet-in BHA and bit clearing the rotary table at 0200 hr on 3 January.

The rotary core barrel (RCB) BHA was made up and run down to 4388.89 mbrf in preparation for reentry. Hole 1224D was reentered at 1837 hr on 3 January, with coring beginning at 25.5 mbsf. Cores 200-1224D-1R and 2R were taken from standard 9.6-m-long cored intervals, with 43.2% and 50.1% recovery, respectively (Table T2). Core 200-1224D-3R penetrated only 4.6 m in an attempt to see if core recovery improved, which it did to 71.74%. Core 200-1224D-4R was to be run as another short core, which would also allow the kelly to be properly spaced out. Ship heave of 4.8 m and a 4° roll forced us, however, to pull up to 22.69 mbsf or into the casing shoe at 0500 hr on 5 January to wait out the weather after only penetrating 2 m. After 5.75 hr of WOW we returned to Core 200-1224D-5R, but again we were forced to stop coring early because of increasing seas and roll. The bit was pulled into the 20-in casing and set at 24 mbsf.

Sea state continued to increase with two major swell directions. Because of increasing dynamic positioning power requirements with no reserve for unusual loads that could force the ship off the hole, the bit was pulled to 4907.3 mbrf (70.7 m above the seafloor) at 1000 hr on 6 January. We continued WOW, with maximum heave, pitch, roll, and wind at 7.3 m, 4.3°, 10°, and 25 kt, respectively. Total WOW time was 26.0 hr total before operations resumed.

The marine forecast called for continued poor weather for our operating area, with very strong low-pressure systems to the west and north and large swells. Therefore, we decided to prepare to take advantage of any weather window by tripping the drill string and changing to the 14¾-in bit and BHA. This would allow us to open the cored hole when a more appropriate weather window was available and be in position to run 10¾-in casing. At 0045 hr on 7 January, we started to trip the pipe, with the bit clearing the rotary at 1100 hr on 7 January.

Overall, we cored 33.5 m in Hole 1224D and recovered 15.65 m of core (46.72% recovery) with the RCB coring system (Table T2).

Reaming the Hole

Taking advantage of a short interval of reduced ship motion, the crew assembled the 14¾-in bit and BHA, which consisted of an Atlas 14¾-in tricone insert bit (IADC Code 617) with three $^{14}/_{32}$-in jet nozzles. The BHA included a bit sub with float, 11-in × 8¼-in drill collars, one tapered drill collar, six joints of 5½-in (31.5 lb/ft) drill pipe, and two crossover subs for a total BHA length of 170.03 m and a drill string weight of 510,000 lb. The bit was run down to 4790 mbrf at 2345 hr on 7 January.

Operations were then put on hold while WOW, with a maximum heave, pitch, and roll of 7.5 m, 3.8°, and 2.3°, respectively. Total WOW time was 19.00 hr before operations officially resumed. Some of this total time includes operations that were conducted while we were WOW that were required because of changes in the operation plan caused by the weather. For example, during this time the VIT frame was launched and lowered, and Hole 1224D was reentered to return to the state we were in prior to WOW. Operations resumed at 1845 hr on 8 January after Hole 1224D was reentered.

The AHC was turned off at 1515 hr on 9 January, after we had reamed open the hole to a depth of 5021.44 mbrf (43.44 mbsf) because of problems with the AHC aft cylinder gimbal. The AHC remained off

for the rest of the cruise, although the passive heave compensator was in operation.

As the hole was reamed downward, several high-viscosity sepiolite sweeps were made at depths of 5016, 5022, 5030, 5035, and 5037 mbrf to aid in cutting removal while opening the hole. There were no signs of cutting buildup. From 5037 mbrf (59 mbsf), which is the depth where RCB coring had ended, the 14¾-in hole was drilled to 5042.7 mbrf (64.7 mbsf). The 5.7-m-long interval took 16.5 hr of bit rotation for an average penetration rate of 0.35 m/hr. This is significantly slower than the rate of penetration for the RCB bit in the $9^{7}/_{8}$-in hole (0.66 m/hr) and significantly slower than the 14¾-in bit in the previously opened $9^{7}/_{8}$-in hole (0.76 m/hr). A slower drilling rate for a 14¾-in bit in basement is expected because the bit has to grind up a larger area relative to reaming a previously cored hole or even coring the hole.

The rig instrumentation system indicated that excessive bit torque (700 A) occurred between ~2000 and 2100 hr on 10 January at 5040.7 mbrf (62.7 mbsf), possibly because of a lithology change. This is approximately the depth reached in Hole 1224F where the lithology changed downhole from thick basalt flows to fractured basalts and pillows. A mud sweep was then circulated at 5040.7 (2000 hr on 10 January) to clean the hole of cuttings. The hole continued to show excessive torque until 64.2 mbsf, when the torque settled down to 160 A. Drilling of the 14¾-in hole was shut down from 2100 to 2130 hr on 10 January for replacement of a washed out saver sub in the kelly. Operations then resumed with a circulating pressure of 1950 psi. At ~2240 hr on 10 January, the circulating pressure dropped suddenly to 1100 psi. It took ~40 min for the pressure to stabilize at this lower circulating pressure, with a pressure spike occurring before it fell back to 1100 psi. This was assumed to be a jet blowing out on the bit. An additional mud sweep was pumped at 2330 hr on 10 January at 5042.7 mbrf (64.7 mbsf) to see if this would help resolve the hole problems. A third sweep was performed at 0340 hr on 11 January. Because of the ongoing hole problems, potential bit problems, and the fact that we had only planned to drill down to ~67 mbsf, we ceased drilling at 0730 hr on 11 January, for a total depth in Hole 1224D of 64.7 mbsf.

A 30-bbl sepiolite pill was circulated before making a wiper trip up to 4992.19 mbrf (14.19 mbsf) and then back down to the bottom of the hole, where 0.5 m of soft fill was tagged at 64.2 mbsf. Another 30-bbl sepiolite sweep was pumped and followed with 50 bbl of seawater. The hole was then displaced with 35 bbl of sepiolite before the string was tripped to the surface.

When the drill string was pulled to the surface, to the surprise of all, the bit had been left in the hole, thus explaining the drilling difficulties. The BHA cleared the rotary at 2025 hr 11 January.

The bit appeared to have been sheared off, with only the bit's flattened pin end ($7^{5}/_{8}$-in regular threads) still engaged in the box end of the bit sub. None of the experienced drilling staff aboard the ship had ever seen this type of bit failure before, especially with a tricone drilling bit this large.

As noted above, it was observed from the Standpipe Pressure Plot derived from the rig instrumentation system that from 2240 to ~2320 hr on 10 January there was a sustained pressure loss of ~850 psi. This 850-psi pressure loss was first interpreted as a blown jet nozzle but more likely indicated the formation of a crack at the root of the pin. In this scenario, crack propagation ultimately led to failure and loss of the entire bit.

Installation of 10¾-in Casing

Starting at 2030 hr on 11 January, the drill crew began assembling the 10¾-in casing string, which consisted of five joints of 10¾-in (40.5 lb/ft) casing. Because the Dril-Quip casing hanger system is not designed to land a 10¾-in hanger inside of the 20-in hanger, the drill crew modified the 16-in hanger by cutting off the 16-in casing extension ring. They then lifted the 16-in hanger and set it down over top of the 10¾-in casing sitting in the rotary table. The crew then picked up the 10¾-in casing hanger, which had already been made up with the casing hanger running tool, and attached it to the casing, which was sitting on the slips in the rotary table. The 10¾-in casing string and hanger were landed into the 16-in casing hanger and then tack welded together.

The casing string was run down starting at 2355 hr on 11 January. After we deployed and lowered the VIT frame, Hole 1224D was reentered at 1336 hr on 12 January. We noted during reentry that the reentry cone and skirt had settled by ~1.7 m below the original mudline. The casing string was run down and landed with the base at 5036.47 mbrf (58.47 mbsf) on 1515 hr on 12 January. The casing was cemented with 18.8 bbl of 15.5 ppg Class G cement. The first attempt to release from the casing hanger failed and resulted in the 10¾-in casing hanger being pulled up above the reentry cone. The casing hanger was landed again in the 20-in casing hanger, and this time the 10¾-in hanger released at 1715 hr on 12 January. The pipe was tripped up, with the running tool clearing the rotary table at 0530 hr on 13 January.

The BHA was assembled with a $9^{7}/_{8}$-in C-4 RCB bit and run down to 4388.89 mbrf in preparation for coring in Hole 1224E. The VIT camera was also lowered. Because the casing string had been lifted several meters and then relanded during the first attempt to unlatch, we wanted to reenter Hole 1224D to ensure that the casing and cement were properly installed. We tagged the base of the hole and then washed down to a depth of 5036.1 mbrf (58.1 mbsf), confirming that the reentry cone and casing were properly set for future installation of a seismometer (Fig. **F5**). The wash depth also indicated that the reentry cone had settled ~1.75 m below the mudline. The casing was then circulated clean, and operations at Hole 1224D were completed at 1815 on 13 January as the bit cleared seafloor.

Hole 1224E

The *JOIDES Resolution* was offset 15 m to the southwest and Hole 1224E was spudded at 1840 hr on 13 January at 4978 mbrf (Fig. **F3**). We washed down the first 8 m and then took two punch, or push, cores (200-1224E-1R and 2R), which were acquired by lowering the RCB bit through the soft sediments without rotating the bit. Both cores sustained substantial drilling disturbance, but we were able to recover 10.52 m of sediment core in a 19.2-m-long interval from 8.0 to 27.1 mbsf, whereas recovery was virtually absent in the other holes.

Coring penetrated from 27.1 to 36.7 mbsf for Core 200-1224E-3R. Basement was tagged at 27.7 mbsf during coring. Recovery consisted of basaltic basement underlying a 5-cm-thick piece of hyaloclastite into which basalt glass and clay pieces had been incorporated. This likely is the top few centimeters of the basement. After completing coring on Core 200-1224E-3R, the bit was pulled up by one stand of drill pipe to make a connection with another joint of pipe. This placed the bit above the sediment/basement contact. After making the connection, the

driller was unable to reenter the basement hole. After 1 hr of attempting to find the hole at the sediment/basement contact by rotating the bit on bottom, a new hole, Hole 1224F, was started.

Overall, we cored 28.7 m in Hole 1224E and recovered 14.91 m of core (51.95% recovery) with the RCB coring system (Table T2).

Hole 1224F

The start of Hole 1224 F is somewhat of an anomaly in the ODP nomenclature, because the bit never pulled totally out of Hole 1224E, but it did pull out of the hard rock portion of Hole 1224E. The distance between Holes 1224E and 1224F is likely no more than ~1 m. In any case, we began penetrating basement again at 1630 hr on 14 January in Hole 1224F.

For all the bad weather we had previously, we were due a good spell. Thus, coring proceeded without interruption except for the occasional wiper trip and one trip to replace the knobby joints with drill pipe. During the latter trip, which started at 2315 hr on 17 January after recovery of Core 200-1224F-11R, the bit was inadvertently pulled above the basement/sediment contact. The driller worked the drill string up and down with rotation in an attempt to reenter Hole 1224F. Instead, Hole 1224E was reentered five times before the bit finally went back into Hole 1224F. RCB coring proceeded after washing ~11 m of soft fill from the bottom of the hole. Cores continued to be cut at a rate of ~6–8 hr/core, which was roughly twice as fast as cores cut from near the top of the basement. No core was recovered in Core 200-1224F-16R. The bit deplugger was run to remove potential obstructions, but Core 200-1224F-17R also had no recovery. Owing to time limitations, coring in Hole 1224F ended and preparations for logging began.

Overall, in Hole 1224F we penetrated 174.5 m, cored 146.8 m, and recovered 37.7 m of core (25.68% recovery) with the RCB coring system (Table T2).

Logging

The bit was released in the bottom of Hole 1224F at 2320 hr on 19 January. The hole was then displaced with 75 bbl of sepiolite. A FFF was launched at 0442 hr on 20 January to facilitate reentries into Hole 1224F on future scientific experiments.

At 0730 hr on 20 January, the triple combination (triple combo) logging tool (see "Downhole Measurements," p. 49) was prepared to run downhole. The tool reached 5152 mbrf, which is only 0.5 m off the bottom of the hole. The first logging run was completed, and the tool was through the rotary table at 1520 hr on 20 January. Because a new logging cable had been installed during Leg 199 and was not fully stretched, the winch speed was relatively slow, which added ~3 hr to each logging run. For each logging run, the base of the pipe was lowered to 49.9 mbsf initially. As each run was made uphole, the pipe was pulled up from 49.9 mbsf to 34.5 mbsf to increase the open hole interval for logging.

The second logging run was with the FMS/DSI tool. An electrical problem required the tool to be pulled back to surface for repairs. After the tool was checked and it went into the hole ~1000 m, the tool started having power problems. It was brought back to surface, and it was determined that the telemetry cartridge was at fault. The cartridge was changed. The tool was then lowered to bottom with no further

problem. Three passes of this string were run uphole at 275 m/hr from the bottom of the hole to the basement contact (27.7 mbsf). The third logging run was completed, and the tool cleared the rotary table at 0525 on 21 January.

We had planned to test the three-component well seismic tool (WST-3) if time and weather conditions permitted. A 4.92-L (300 in^3) Bolt air gun aboard the *JOIDES Resolution* was used as the source. The gun was suspended from a buoy and tethered to the aft port crane with the gun depth at 5.5 m below the sea surface. When the WST-3 tool was in the drill pipe at a depth of 1057 mbrf, it was clamped to the pipe to conduct a test. The shot time was supposed to be detected by the blast hydrophone suspended 3 m beneath the gun. However, the seismic acquisition tool (SAT) detected no source signals from either the blast hydrophone or the WST-3. Subsequently, three problems were found: a circuit was faulty in the blast hydrophone of the air gun; there was an air leak from the air gun; and the WST-3 telemetry worked intermittently. The experiment was thus terminated because there was insufficient time to attempt to fix these problems and complete the planned shooting and logging program for the WST-3. The time constraint on the logging program was determined by the departure time required to make the San Diego port call. The WST-3 was back through the rotary table at 0945 hr on 21 January.

The VIT was launched starting at 1030 hr 21 January to observe the FFF at the top of Hole 1224F (Fig. **F7**). A large hole was observed in the seafloor from circulating the cuttings out of the hole. As a result, the top of the FFF was observed at ~4980.5 mbrf (2.5 mbsf) with the three buoys just below the mudline, secured to the FFF by $^5/_{32}$-in steel cable. The end of the casing on the FFF is estimated to be at 6.2 mbsf.

The open end of the drill pipe cleared the seafloor and FFF at 1238 hr on 21 January. The VIT was recovered at 1445 hr, and the BHA cleared the rotary table at 2355 hr on 21 January, completing activity at Site 1224.

The vessel was secured to commence a sea voyage by 0030 hr on 22 January. A test of the SCS system was conducted from 0030 hr to 0145 on 22 January prior to leaving the site. Although the system was demonstrated to be working, there was insufficient time to conduct a seismic survey. Pie charts of the time spent on various classes of activities are given in Figure **F7,** p. 41, in the "Leg 200 Summary" chapter.

Sediment Thickness and Depth to Basement

Because a complete sedimentary section was not recovered above basement, we use the drill pipe measurements from the holes and jet-in tests at Site 1224 to estimate the thickness. Undulations in bathymetry and the basement/sediment interface can add to the uncertainty, but these are likely small (±1 m) over the small area encompassed by the six drill holes (see Fig. **F3**), which is roughly 20 m × 20 m. The drill pipe measurement also has an uncertainty of about ±1 m. The constraints are as follows:

1. In Hole 1224A, basaltic basement was encountered in the core catcher of Core 200-1224A-4X, where a ~6-cm chunk of basalt was recovered. The cored interval is from 25.2 to 30.7 mbsf. We also recovered ~117 cm of sediment above this, which places the basement contact somewhere between 25.2 + 1.17 mbsf and 30.7 – 0.06 mbsf, or between 26.37 and 30.64 mbsf. The driller noted

a hard contact, as determined by a change in the weight on bit, at 28.9 mbsf. At this point, we did not have an accurate mudline, so this estimate has a greater uncertainty than those below.
2. The second jet-in test penetrated down to 29 mbsf, which was taken to be the depth to basement. A mudline had been established in Core 200-1224C-1H prior to this test, so basement should be 29 mbsf or deeper in the jet-in hole.
3. In Hole 1224D, the 20-in casing was set at 25.5 mbsf and the first core, which was basalt, was cored from 25.5 to 35.1 mbsf, with 4.15 m of recovery. Thus, the basement is between 25.5 and 35.1 – 4.15 mbsf, or between 25.5 and 30.95 mbsf. A better estimate comes from the driller, who noted a change in the weight on bit at 29.5 mbsf.
4. In Hole 1224E, sediment was recovered in the push, or punch, core that extended to 27.1 mbsf. The next core (Core 200-1224E-3R) recovered 4.39 m of basalt in the interval from 27.1 to 36.7 mbsf. Basement is thus between 27.1 and 36.7 – 4.39 mbsf, or between 27.1 and 32.31 mbsf. In addition, the driller noted that he felt basement from weight on bit at 27.7 mbsf.

We consider the best estimates as 29, 29.5, and 27.7 mbsf, where basement was felt. All three estimates are consistent with the ranges obtained from coring. Basement may thus vary in depth below seafloor by ~2 m or average ~28 or 29 mbsf over the area of operations with the variation related to uncertainties in the drill pipe measurement.

Transit to San Diego

The vessel settled onto a bearing of 78° for San Diego. Weather conditions were excellent aiding in a rapid transit to San Diego. The 1320-nmi trip took 125.26 hr, for an average transit speed of >11 kt. The harbor pilot came on board at 0700 hr on 27 January, and the vessel was tied up at port with the first line ashore at 0820 hr on 27 January, officially ending Leg 200.

LITHOLOGY

Sedimentology

Site 1224 lies in the pelagic clay province of the North Pacific Ocean (Leinen, 1989). The sediments in this part of the Pacific Ocean are eolian in origin, consisting primarily of dust blown eastward from the arid regions of central Asia. This region of the Pacific Ocean is below the calcite compensation depth (~3500 m), and little or no biogenic calcite is thought to reach the seafloor (Leinen, 1989). Nevertheless, calcareous nannofossils are present in Core 200-1224E-2R below 17.5 mbsf. Calcium carbonate was found during DSDP Leg 5 in many of the sites drilled, although in the red clays, carbonate content was low (Vallier, 1970) (Fig. F8). Coccoliths and discoasters were recorded in samples from some of the cores. They were present in all but 34 of the 168 samples collected specifically for this purpose (Bukry and Bramlette, 1970). At Site 172, a calcareous ooze was detected 48 cm below the top of Core 18-172-4. Preservation of the nannofossils was generally poor (Wise, 1973). The overlying 22 m of brown clay was unfossiliferous.

Siliceous biogenic material is rapidly dissolved by the silica-poor bottom waters; nevertheless, some radiolarians are recorded in the sediment column at Site 1224 (see "Site 1224 Smear Slides," p. 63).

Sediments were obtained from four holes drilled at Site 1224. The sediments consist mostly of abyssal clays of varying color. Occasionally coarser horizons are present as are horizons with varying densities of microfossils, both siliceous (radiolarians and sponge spicules) and calcareous (coccoliths and discoasters) (Figs. F26, F27).

Core 200-1224A-1X had zero recovery and Core 2X recovered <0.1 m of pebbles and granules in the core catcher. These do not effervesce in acid and are thought to be infilled burrows. They are <1 cm in diameter, roughly circular in cross section, and some are nearly cylindrical in form. They are indurated but not hard, and XRD analysis indicates the presence of phillipsite (a member of the zeolite group) (see "Geochemistry," p. 36). Core 200-1224A-3X contains only a few grams of soupy, very dark brown clay. Section 200-1224A-4X-1 contains ~117 cm of highly disturbed, soupy red-brown clay along with a 6-cm-long piece of basalt in the base of the core catcher and other related pebbles and granules. Sections 200-1224A-5X-1 and 6N-1 were cored into basaltic basement, and they contain only small amounts of basaltic granules and pebbles mixed in with clay that is likely to have been washed downhole. Radiolarians are found in varying abundance throughout the sediments. Sponge spicules are much less common.

Core 200-1224B-1H contains only ~20 cm of homogenous brown clay. Radiolarians are rare.

A single piston core was collected in Hole 1224C. It contained massive clay throughout the entire 6.53 m recovered. Sections 200-1224C-1H-1 and 1H-2 are massive homogenous brown pelagic clay. Section 200-1224C-1H-3 is also massive pelagic clay, but it gradually darkens in color from brown at the top to dark brown at 70 cm to very dark brown at 147 cm. Sections 200-1224C-1H-4, 1H-5, and 1H-CC are also very dark brown massive clay. Radiolarians and sponge spicules are common in Sections 200-1224C-1H-4, 1H-5, and 1H-CC.

In Hole 1224D, only basalt was cored.

The cored sediment interval in Hole 1224E was 27.1 m thick, and we recovered 10.52 m of highly disturbed massive clay. The sediments were acquired by punch cores using the RCB bit and coring system but without rotating. The clay varies in color between dark brown, very dark brown, black, and dark yellowish brown. The high disturbance due to the punch coring process causes the colors to be streaked and mottled throughout the hole. Most color changes are gradual. Some are sharp, however, especially in the lower part of the core. Light-colored granules and pebbles are found in the top few centimeters of Core 200-1224E-1R (~8 mbsf). Like the burrows in Hole 1224A, they do not effervesce and are thought to be infilled burrows. These sediments also contain small manganese nodules. They are as wide as 2 mm and are irregular or elongated in shape. The surface is either relatively smooth or is mammillated on a very small scale. Radiolarians are abundant at the top of Core 200-1224E-1R (~8 mbsf) and occur less frequently throughout the rest of the hole. Calcium carbonate fossils such as coccoliths and discoasters are present below 17.5 mbsf.

Samples taken at regularly spaced intervals (except the interval from 8.0 to 8.8 mbsf) from Hole 1224E effervesce with acid. Smear slides from samples taken along the core did not indicate a uniform presence of coccoliths and discoasters.

In Hole 1224F, no sediments were cored.

F26. Discoasters, p. 92.

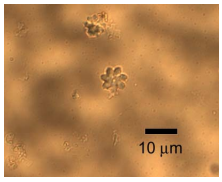

F27. Coccoliths and discoasters, p. 93.

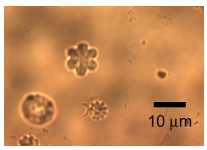

Igneous Petrology

Visual Description

Basalts were recovered in Holes 1224A, 1224D, 1224E, and 1224F. Basaltic basement was tagged with the XCB in Hole 1224A (Core 200-1224A-4X), and two additional short cores were taken with the MDCB (Core 200-1224A-6N). Basalt was rotary cored for 31 m in reentry Hole 1224D. Hole 1224E was intended as a single-bit follow-up ~20 m southwest of Hole 1224D (Fig. F3). It was also rotary cored, but, because of equipment malfunction, it was cored without the advantage of AHC. After one core's length was drilled into basalts, the pipe was pulled out of basement but not above the mudline in order to change out some pipe at the top of the string. Upon lowering the drill bit back into basaltic basement, however, the driller was unable to reenter the hole into basalt because (1) the short section of soft sediments was insufficient to support the end of the drill string laterally and (2) the diameter of the hole through the sediment had widened.

The top of the basalts was cored again in Hole 1224F, probably <1 m away from Hole 1224E. The new hole was cored for 146.4 m into basalts. Site 1224 thus accomplished a novel, if inadvertent, experiment—sampling the top of the same basaltic section three times within ~20 m. However, unlike triple piston coring in sediments, which is deliberately done to recover duplicate sections, the result was to discover substantial lateral variability in the basalts over a very short distance.

The general attributes of the cores with basalts are summarized in Table T5 and Figure F28. In Figure F28, except for the uppermost cores into basement, all depths of recovered rock are based on the assumption, by ODP convention, that the top of a core is assigned to the top of the cored interval, as measured from drill string length and reported in the Janus database.

We assume that the top of basaltic basement lies at a constant depth of 28 mbsf for all four holes. The basement depth of 28 mbsf is probably uncertain by about a meter, and there may be some slight relief to the top of basalts as well. But this method avoids assigning basalt recovery to depths that actually are above the point where basement was touched by the drill string. Drilling in all four holes cored into the same fairly massive basalt flow. The recovered basalt is placed at this fixed depth of 28 mbsf for Holes 1224A and 1224E from which a glassy flow top was recovered. The basalt contact was not cored in Holes 1224D and 1224F, and an uncertain but arbitrarily small gap of ~30 cm is shown between sediments and the top of basalts for these two holes.

In Hole 1224D, a second substantial flow was encountered at 50.7 mbsf, near the base of the hole (Unit 2, lower flow). This lower flow was not reached in the short 8.7 m of coring into basalt below 28 mbsf in Hole 1224E. Based on chemical analyses (see "Geochemistry," p. 36), it almost certainly was reached and drilled completely through in Hole 1224F. Hole 1224F was cored for 146.5 m below the presumed top of basement at 28 mbsf. The massive Unit 1 basalts extend for 34.7 m (62.7 mbsf) in Hole 1224D. Below 62.7 mbsf, the percentage of recovery dropped off sharply. This may be related to the change in morphology to thinner flows and pillows that are more intensely fractured and altered from the massive rocks sampled above. Somewhat thicker flows were encountered again at 133.5 mbsf (Core 200-1224F-13R). Core 200-1224F-15R reached a depth of 161.8 mbsf and was the last core in which basalt was recovered. The following two cores were empty, prob-

T5. Summary of cooling units and alteration, Site 1224, p. 173.

F28. Lithologic summary of basalts, p. 94.

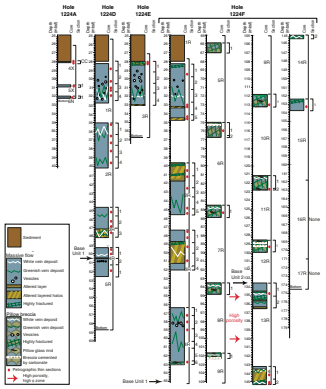

ably because of a jammed bit. We cannot say this for sure, because the bit was released in the hole in preparation for logging after Core 200-1224F-17R. The total penetration in Hole 1224F was 174.5 m; we cored 146.5 m into basement, making it the deepest hole cored into basaltic basement of the Pacific plate younger than 100 Ma since DSDP Leg 65. For all holes, we recovered a total of ~58.14 m of core from ~191 m of penetration.

Based on morphology, physical properties, and downhole log correlations, the basalts recovered from Site 1224 are divided into three lithologic units:

- Unit 1 (28–62.7 mbsf): two massive basalt flows. This unit includes all the basalt cores from Holes 1224A, 1224D, and 1224E and cores down to 62.7 mbsf in Hole 1224F. The thickness of Unit 1 in Hole 1224F is curated as 34.7 m. Recovery in Unit 1 was 52.6% for all four holes. The two flows have different compositions (see **"Geochemistry,"** p. 36).
- Unit 2 (62.7–133.5 mbsf): thin flows and pillows. This unit extends from interval 200-1224F-4R-6 (top of Piece 2, 10 cm) to 200-1224F-12R-1 (Piece 15, 129 cm). The base of the unit is curated at 133.5 mbsf, and its thickness as curated is 70.7 m. Recovery in Unit 2 was 14.6%. These basalts are chemically similar to the lower of the two massive flows in Unit 1.
- Unit 3 (133.5–161.7 mbsf): basalt flows of intermediate thickness alternating with thin flows and pillows. This unit includes Core 200-1224F-13R through the end of Core 15R. The base of the unit is taken to be the bottom of Core 200-1224F-15R at 161.7 mbsf, and its curated thickness is 28.1 m. Recovery in Unit 3 was 21.4%. The rocks are ferrobasalts, the most strongly differentiated of any rocks cored at the site.

Based on downhole logs, the base of Unit 1 corresponds to a change in porosity and density at 63 mbsf. This is almost exactly the curated depth (62.7 mbsf). The base of Unit 2 in the logs is less precise, but probably deeper than the curated depth of 133.5 mbsf. A zone of very high porosity (high ϕ) is present between 135 and 140 mbsf (see **"Downhole Measurements,"** p. 49) (shown as large, red arrows on Fig. **F28**). The temperature in the hole also increased at 136 mbsf (see **"Downhole Measurements,"** p. 49) (Fig. **F80**), suggesting that seawater flowed down the hole or was introduced by drilling operations. A permeability barrier was probably encountered at this depth. The relatively massive rock in Core 200-1224F-13R is unlikely to have been cored above this depth. In the formation, then, the base of Unit 2 appears to be ~2–4 m deeper than the curated depth.

Detailed descriptions of these units are given below. Locations of cooling unit boundaries are inferred from the presence of glass, changes in grain size, fractures, vein presence, and alteration.

Unit 1

For Unit 1, the descriptions are based mainly upon observations on cores from Holes 1224D and 1224F, but they apply to all four holes. The Unit 1 basalt is fresh, massive, and fine grained, but grain size coarsens slightly in the middle of flows. The Unit 1 basalt of Hole 1224D is unusually fresh, with only incipient local alteration. Based on variations in grain size, Unit 1 consists of two flows. The upper flow of Unit 1 is

22.7 m thick in Hole 1224D and 35.2 m thick in Hole 1224F. The bottom of the second flow was not reached in ~8 m of coring in Hole 1224D, but it was reached after 13.6 m of coring in Hole 1224F. These thicknesses are based on cores with incomplete recovery. The actual thicknesses of the flows are somewhat greater.

In Hole 1224A, the glassy top of the upper flow is a rim on a small piece of basalt. In Hole 1224E, it consists of a thin flow-top palagonitized hyaloclastite breccia. The rocks are slightly vesicular, and the vesicles are small, irregularly distributed, usually round, and widely spaced. Some entire 1.5-m sections are nearly without vesicles. Many vesicles are segregation vesicles, with macroscopically visible linings of darker basaltic material. The vesicles are usually lined or filled with bluish gray clays, and some are filled with calcite (Fig. F29). There are several gas pipes contained in coarser-grained basalt that have segregation vesicles filled with calcite (Fig. F30) near the top of the deeper flow in Unit 1.

Pieces of continuously cored basalt approximately several tens of centimeters long with few fractures were recovered from Unit 1. The few fractures are generally straight and at high angles to the core. Some are vertical and may be columnar-type contraction fractures. A few are irregular vein networks. Almost all fractures in Unit 1 of Hole 1224D and many in Hole 1224F are lined with dark-green clays, calcite, and pyrite. These have only narrow zones of ~1 cm width of darker, slightly altered basalt adjacent to them.

Whereas basalts of Unit 1 from Hole 1224D are quite fresh, a substantial proportion of Unit 1 basalts from Hole 1224F are moderately to strongly altered (Fig. F28). The alteration is present in two forms. The first is prominent dark-gray to light reddish brown or orange-brown alteration zones. The second alteration manifestations are halos that are either adjacent to iron oxyhydroxides and calcite-lined fractures or are located on the edges of pieces that once had fractures but were lost during coring (Fig. F31). Where the fracture fillings are intact, broken bits of iron oxyhydroxides can be seen embedded in calcite lining the same veins (Fig. F32). The iron oxyhydroxides thus lined the fractures first, and the calcite came later. Cores, tens of centimeters to meters in length, are veined and altered in this way (Fig. F28). Even interiors of some pieces of rock with prominent alteration halos are affected, being light tan rather than dark gray in color. Plagioclase crystals, especially, are bleached in contrast to their appearance in equally coarse-grained but darker fresh basalt at the immediate edge of the altered zone. In such bleached rock the halos branch in intricate swirls into the centers of the pieces (Fig. F33), evidently following microfractures. In the cores from Hole 1224D, however, the only basalts altered to this extent are fine grained at the base of the uppermost thick flow (Fig. F28).

Unit 2

Ascertaining the character of the basalts in Unit 2 was hindered by the poor recovery. Few of the rocks were obtained in pieces in which the original orientation could be determined. Many of the smallpieces retain almost circumferential alteration halos (Fig. F34) and were thus not significantly rounded by churning in rubble broken from the hole by the bit. They entered the core barrel at about their original size and shape, which was often smaller than the diameter of the core. As in Unit 1, the halos are presumed to have formed next to fractures lined with iron oxyhydroxides, but few pieces were recovered with fractures.

F29. Clay-lined and calcite-filled vesicles, p. 95.

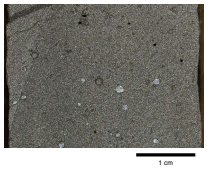

F30. Gas pipe structure, p. 96.

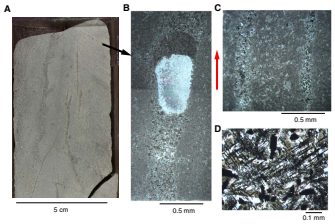

F31. Wide oxidation halo, p. 97.

F32. Subvertical fractures lined with iron oxyhydroxides and calcite, p. 98.

We hypothesize that the host formation was highly jointed or fractured and laced with veins.

Several pieces still retain fresh or altered glass. Ten cooling-unit boundaries were defined on the basis of glass presence in Unit 2 (Hole 1224F) (Table T5). Unit 2 probably contains dozens of small pillows and flows. Two hyaloclastites were recovered. One is cemented by clays and is entirely palagonitized. Interestingly, the other is cemented by calcite (Fig. F35). In the latter, angular glass chips are partially altered to orange palagonite.

The basalts are either nonvesicular or they have only tiny pinhole-sized vesicles, partially filled with clays (dark specks in Fig. F34) or iron oxyhydroxides. The usually dark-gray color of the basalts has been dulled by pervasive minor oxidative alteration.

Unit 3

Unit 3 basalts combine attributes from Units 1 and 2 in that they are fairly coarse grained and have alteration halos adjacent to inclined fracture networks that alternate with small pieces of fine-grained basalt with circumferential alteration halos. Portions of at least two cooling units were recovered through Unit 3 (Table T5). There is a small percentage of vesicles that are filled with secondary minerals. Fracturing and alteration are similar to those of Unit 1. Reddish brown stains are present as either halos on small pieces, or, in larger pieces, the stains are parallel to fractures lined with iron oxyhydroxides and calcite. Vein calcite intergrown with zeolite is present in thin section. One rock has a spectacular closely spaced parallel set of fractures (Fig. F36) lined with iron oxyhydroxides and subsequent calcite. The same sequence is present in crossing fractures in some of the finer-grained basalts of Unit 3 (Fig. F37).

Petrography

Basalts from Holes 1224A, 1224D, 1224E, and 1224F have a relatively homogeneous mineral paragenesis, but with subtle distinctions in crystal morphologies between basalts of different composition, especially in the quickly quenched margins of pillows and flows. The main phases are plagioclase, clinopyroxene, two oxide minerals, ilmenite and magnetite, globular sulfides, and rare pigeonite. Based on the presence of the pigeonite in the coarsest-grained basalts, the rocks can be classified as tholeiitic basalts. Olivine is rare, and only a few small iddingsitized euhedral to anhedral groundmass crystals in fine-grained rocks have been found. Iddingsite is a typical alteration product of olivine and is made up of a mixture of goethite and layer-lattice silicates (e.g., smectite). The massive basalts are holocrystalline (almost 100% crystals) to hypocrystalline (crystals >50%) and can be described as Unit 1 lava flows. Below the two upper massive flows, Unit 2 basalts have hypohyaline (crystals <50% and glass >50%) texture and volcanic glass contents >90% are common. The increase in glass content indicates the presence of chilled pillow margins. The Unit 3 basalts (~153 mbsf) are holocrystalline massive lava flows. The basalts range from aphanitic (difficult to distinguish the crystals in the groundmass with the naked eye) to aphyric (absence of phenocrysts). Rare plagioclase or plagioclase-clinopyroxene sparsely phyric (<2% phenocrysts) basalts are also present. The crystals in the groundmass are equigranular and are euhedral to anhedral. The texture of the massive basalts of Unit 1 is intergranular (with clino-

F33. Sharp alteration zones in medium-grained basalt, p. 99.

F34. Nearly circumferential alteration halos in fine-grained basalt, p. 100.

F35. Flow-top hyaloclastite cemented by calcite, p. 101.

pyroxene in interstitial relationships with plagioclase) to subophitic (with plagioclase laths partially enclosed in clinopyroxene) and, more rarely, intersertal (with microcrystalline to glassy material between plagioclase). Rare vermicular structures in the groundmass between plagioclase laths can be considered as myrmekitic intergrowths of sodic plagioclase and quartz. The presence of segregation vesicles has been commonly reported. Hyalopilitic (with plagioclase laths and clinopyroxene crystals in a glassy matrix) to, more rarely, intersertal textures are found in the pillow lavas of Unit 2. The grain size of the groundmass ranges from very fine grained (0.001–0.5 mm) to fine grained (0.5–1 mm).

Hole 1224A

In Hole 1224A, basement was encountered at 28 mbsf, and a total length of <1 m was recovered (see **"Site 1224 Visual Core Descriptions,"** p. 1). This represents the quenched and fine-grained top of the upper massive flow of Unit 1. Six thin sections (15, 24, 25, 26, 52, and 59) have been examined for this hole. The topmost thin section (Sample 200-1224A-4X-CC, 16–21 cm) is made up of plagioclase-clinopyroxene sparsely phyric basalt with <3% phenocrysts (Fig. **F38A**). Typical phenocrysts are (1) fresh euhedral bytownite (percent An = ~80) with columnar habit and a maximum length of 1.2 mm and (2) partially fractured pale-yellow euhedral Ca- and Mg-rich clinopyroxene (Augite; c^γ = ~46°), with prismatic and pseudo-octagonal habit and a maximum size of 3 mm. The clinopyroxene is usually intergrown with smaller, tabular plagioclase crystals. These rare phenocrysts are embedded in an intersertal, intergranular, and rarely subophitic groundmass of plagioclase, clinopyroxene, and opaque minerals (Fig. **F38B**). The groundmass plagioclase is often skeletal, whereas the clinopyroxene is anhedral and equant. Opaque minerals (Fig. **F38C**) include acicular, skeletal or equant, and globular sulfide (pyrrhotite). Noteworthy is the variable amount of partially devitrified brownish volcanic glass in the groundmass (generally >50%). Abundant tiny, acicular plagioclase spherulites are present in the glassy matrix. Alteration is generally <6%. The secondary mineralogy is composed of clay minerals and iron oxyhydroxides, the latter replacing olivine. Vesicles are ~2% and in some cases are partially filled with an unidentified yellowish globular, highly birefringent clay.

Brownish to yellowish palagonitized volcanic glass from chilled pillow margins is present in >90% of the two thin sections (15 and 24) from Core 200-1224A-4X. There are a few (~1%) fresh, euhedral, and tabular plagioclase microphenocrysts (maximum size = ~0.5 mm) present in thin section 59 (taken 2 cm below thin section 24). Vesicles filled by brownish to yellowish clay minerals are present in minor amounts (~1%). Reddish granules (~4%), some with rhombic shape, may be olivines replaced by iddingsite.

We recovered aphyric basalts with <1% plagioclase microphenocrysts (maximum size = ~1.1 mm) from Hole 1224A (Cores 200-1224A-5X and 6N). The groundmass is composed of plagioclase, clinopyroxene, and opaques but is only 60% in volume. The remainder is mainly made up of segregation vesicles (Fig. **F38D, F38E**). These are brown to black and show acicular to skeletal plagioclase, anhedral equant clinopyroxene, and tiny elongate opaque minerals (ilmenite?) in a devitrified glassy matrix. These vesicles represent late-stage interstitial melt. The skeletal and acicular shape of plagioclase and opaques is a result of rapid cool-

F36. Oblique fractures lined with iron oxyhydroxides and calcite, p. 102.

F37. Fine-grained basalt cut by two generations of fractures, p. 103.

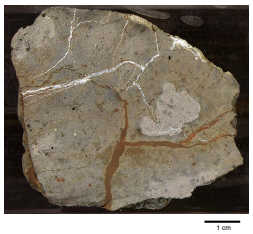

F38. Petrographic features of basalt, p. 104.

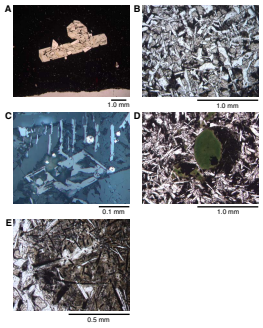

ing. Approximately 5% of glass and clinopyroxene is replaced by brownish clay minerals that are often associated with segregation vesicles. A green nontronite (clay mineral) is present (~1%) as cavity and vesicle filling in the bottom of Section 200-1224A-5X-1 (thin section 25) (Fig. F38D). Nontronite is distinguished from chlorite by its color and higher birefringence and from glauconite by weaker pleochroism (green to pale yellow). Cavities are always <3% of the total volume. They are either empty (~60%), partially filled (~15%), or totally filled (~25%). The filling material is either (1) nontronite; (2) a microlitic intergrowth of plagioclase, clinopyroxene, and opaques, all <0.1 mm (segregation cavity); (3) a sulfide mineral (pyrite?); or (4) combinations of all three. Microlitic intergrowths that partially fill some of the cavities are the same material as the segregation vesicles and may represent late-stage magmatic melts. In one case, a large pyrite crystal (~1 mm) almost entirely fills one such cavity.

Hole 1224D

In Hole 1224D, a total of 15.65 m of basalt was recovered in 31 m of coring (see "Site 1224 Visual Core Descriptions," p. 1). Eighteen thin sections (34–51) were examined for this hole. Only the massive basalts of Unit 1 were recovered, reaching into the top few meters of the lower flow. Approximately 55% of the recovered rocks are aphanitic, aphyric basalts. The average dimension of the groundmass crystals is <0.5 mm; ~15% are clinopyroxene-plagioclase sparsely phyric (<2% phenocrysts) basalts (average crystal dimension = <0.5 mm), and the remaining 30% are fine-grained (average crystal dimension = ~0.5 mm) basalts. All but one of the thin sections are holocrystalline with hypidiomorphic, equigranular, and isotropic textures (Fig. F39A, F39B, F39C). Petrographic textures are typical for relatively thick lava flows. An alteration zone at 47–48 mbsf (in Section 200-1224D-3R-3) (Fig. F28) is the transition zone between the two cooling units. Unfortunately, the contact between these two flows was not recovered.

The rare phenocrysts are pale-yellow subhedral, equant, partially fractured clinopyroxenes (maximum size = ~1.5 mm), and/or euhedral tabular to anhedral bytownitic plagioclase (maximum size = ~3 mm). Glomerocrysts of plagioclase and clinopyroxene with two mineral intergrowths are present in thin sections 36, 48, and 50. The groundmass is composed of plagioclase, clinopyroxene, and opaque oxide minerals for all Hole 1224D basalts. Pigeonite, Ca-poor clinopyroxene, is characteristically found in subalkaline volcanic rocks (Fig. F39D). It is present in the groundmass in only two thin sections (44, 45). These thin sections were taken from the upper flow in lithologic Unit 1 (Samples 200-1224-D-3R-1, 50–53 cm, and 3R-1, 54–57 cm). Plagioclase with tabular to acicular habit has intergranular to subophitic textures with anhedral pale-yellow clinopyroxene (augite; 2V γ = ~60°) and euhedral to anhedral equant or skeletal opaque minerals (Fig. F39E, F39F). In some cases, plagioclase is skeletal and the voids are filled by microlites of clinopyroxene and skeletal opaque minerals. Pigeonite is a clinopyroxene characteristic of subalkaline volcanic rocks, and its presence confirms the petrographic classification of tholeiitic basalts. It is distinguished from Ca-rich clinopyroxene mainly on the basis of its pseudomonoassic character (2V γ = ~0°) and its euhedral shape. Plagioclase and pyroxenes are usually fresh with only minor signs of alteration. The plagioclase, clinopyroxene, opaques, and pigeonite groundmass ranges from 40% to 90% in volume and is generally >70%. The presence of "open" plagio-

F39. Textural and mineralogical features of the upper massive flow, p. 105.

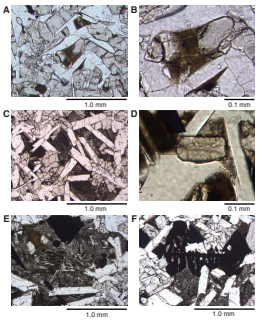

clase spherulites in fine-grained interstitial patches in the groundmass is relatively common (Fig. F39E). These are composed of columnar to acicular plagioclase radiating from a center. The space between each plagioclase lath is occupied by smaller clinopyroxene and plagioclase spherulites. Many interstitial patches contain one or more large euhedral or skeletal titanomagnetite crystals (Fig. F39E, F39F) suggesting crystallization from very iron-rich late-stage in situ liquids. Some also contain round sulfide globules that segregated immiscibly from such liquids (Fig. F39E).

The second most abundant feature is irregular segregation vesicles similar to those already described in basalts from Hole 1224A (~5% to 40% but generally >25%). These are crystallization products of late-stage melts that leaked into ruptured vesicles. The segregation vesicles have acicular to skeletal plagioclase, subhedral to anhedral, equant to prismatic clinopyroxene, and needlelike or trellised iron titanium oxides in a devitrified glassy matrix. Plagioclase and clinopyroxene are smaller in the segregation vesicles than in the groundmass, but the oxide minerals can be much coarser. The following features are present in only some thin sections or are present in association with only one segregation vesicle: (1) a tiny elongated, often acicular (i.e., needlelike) opaque mineral (ilmenite?); (2) a large (up to 0.6 mm) equant, skeletal, opaque mineral (Ti magnetite?); (3) small (~0.1 mm) spherical drops of a sulfide mineral (pyrrhotite?); (4) an acicular low-birefringent mineral with roughly parallel extinction, 2V = ~90°, and rosette texture (albite-oligoclase?); and (5) a high-birefringent mineral with a columnar habit (epidote?). Segregation vesicles (variable from ~5% to 50% but generally <30%) are altered to brownish to yellowish clay minerals and iron oxyhydroxides. Interstitial volcanic glass is easily altered to clays. Alteration only affects the glass in the segregation vesicles, not the plagioclase and clinopyroxene. There are also patches of a brownish clay mineral that is not related to the segregation vesicles. Here, the clay minerals have an interstitial relationship with the groundmass plagioclase and are possibly a result of clinopyroxene or interstitial glass alteration.

Vesicularity is variable in the basalts. Both virtually vesicle-free zones (e.g., Core 200-1224D-2R; ~5 m thick with much less than 1% cavities) and relatively vesicle-free zones (e.g., Core 200-1224D-1R; ~4.4 m thick, with cavities ranging from 3% to 6%) are present. Generally, the percentage of vesicles decreases with depth above ~60 mbsf, and vesicles are concentrated mainly in the first 5 m of the cored basement, although the number of cavities increases in the deeper part of Hole 1224F. The cavities are either empty (5%–50%), partially filled (35%–60%), or completely filled (20%–100%). All three types of vesicles with subspherical shape often coexist in the same thin section. The filling material may be (1) brownish clay minerals; (2) microlitic intergrowth of plagioclase, clinopyroxene, acicular opaques, plus possibly glass and clay minerals; (3) chalcedony?; (4) aragonite; (5) calcite; (6) brownish to pale greenish clay minerals; (7) sulfide minerals (pyrite?); or (8) a combination. The border of the cavities is often made of plagioclase or elongated opaque minerals tangent to the outer surface. In a few cases, vermicular structures are associated with carbonate-filled cavities. These have been interpreted as possible evidence of biological processes (see "Microbiology," p. 43).

There are only a few thin sections of veined basalts (36, 39, 41, 48, 50). The filling material ranges from Ca carbonate (either calcite or aragonite) to anhedral to cubic euhedral sulfide minerals (pyrite?), low-

birefringent minerals (zeolites?), iron oxyhydroxides, acicular colorless minerals with high birefringence and parallel extinction (lawsonite?), chlorite, and clay minerals. In hand specimen, the iron oxyhydroxide–filled cavities have a pale brownish halo ~1.5 cm wide on both sides of the vein. This halo is due to the presence of a brownish film (iron oxyhydroxide?) coating the groundmass minerals.

The top of the lower lava flow in Unit 1 (Section 200-1224D-4R-1) has textures typical of gas pipes (Fig. F30); vertical bands (Fig. F30A) have the same minerals as the groundmass but with coarser size (maximum plagioclase size = ~0.6 mm). Some of them contain their own internal segregation vesicles (Fig. F30B). The gas pipes are preferential escape routes for volcanic gases (Fig. F30C). Their segregation vesicles contain plagioclase, brown clinopyroxene, and trellised iron titanium oxides.

Hole 1224E

In Hole 1224E, ~4.4 m of basalt was recovered over a total cored section of ~9.6 m (~46% recovery) (see "Site 1224 Visual Core Descriptions," p. 1). Three thin sections (53–55) of volcanic rocks were examined from Hole 1224E. In two of the thin sections (53 and 54) we observed hyaloclastitic breccias composed of variably sized (0.5 to 3 cm) subangular to subrounded glass clasts set in carbonate cement. The glass clasts are almost always altered and have an orange palagonite rim of variable thickness (Fig. F40A, F40B). The palagonite is embayed into the glass along fractures (Fig. F40A) and has alternating dark- and light-orange bands concentric to the surfaces of the glass, with which it forms a sharp contact (Fig. F40B). It penetrates into the glass along small microfractures (Fig. F40C).

The carbonate cementing the glass shards is fine to very fine grained, but larger crystals (~0.3 mm) are present at the contact with the glass clasts. A colorless biaxial mineral with low relief, extremely low birefringence, a rhombic to prismatic habit, and multiple twins is only present in the carbonate veins and where it is in contact with the glass clasts. This mineral may be either tridymite or one of the zeolite-group minerals. Alternatively, the mineral may be a zeolite.

The hyaloclastite flow top is the only portion of the upper flow in Unit 1 to reveal the quench mineralogy of the flow. Quench crystals include rare prismatic, tabular, and equant plagioclase microphenocrysts ~0.1 to 0.3 mm in length (Fig. F40C). The sections also contain numerous smaller acicular plagioclase crystals <0.1 mm in width, similarly tiny euhedra of clinopyroxene, and these two minerals intergrown (Fig. F40C, F40D, F40E). In some larger shards, these minerals are coated with dark-brown plagioclase spherulites set in pale-brown glass (Fig. F40D). In some palagonitized glass, there are rare skeletal olivine crystals ~0.1 mm long (Fig. F40F). These are altered to iddingsite (clays plus iron oxyhydroxides).

The third thin section (55) from Hole 1224E is from an aphyric holocrystalline basalt with hypidiomorphic texture and <1% plagioclase phenocrysts (maximum size = ~2.2 mm). The groundmass and texture are similar to the basalts from Holes 1224A and 1224D. Cavities compose ~5% of the rock, and they are almost totally filled. The material infilling the cavities is mainly calcite. Microlitic intergrowth of plagioclase, opaque minerals, and clinopyroxene (segregation material) fills ~30% of the cavities; rarely (~2%–3%) the cavities are filled by a brownish clay mineral.

F40. Features of hyaloclastite, p. 106.

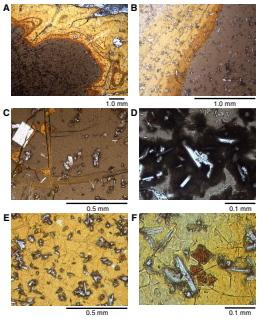

Hole 1224F

In Hole 1224F, a total of 37.7 m of basalt was recovered from a cored section of 147 m (recovery ~25%) (see "Site 1224 Visual Core Descriptions," p. 1). The low recovery of this hole is related to the morphology of the volcanic rocks that, below Core 200-1224F-4R (63 mbsf), are mainly pebble-sized pillow lava fragments with a few thin massive lava flows near the bottom of the hole. Twenty-seven thin sections (56–60, 62, 64–69, and 71–85) were examined from Hole 1224F. There are pillow basalts (74, 76, and 78) (10% have glassy chilled margins), volcanic breccias (65 and 66), and hyaloclastites (79 and 80). Seventy percent of the rock recovered is aphanitic, aphyric massive lava flows. Sixty-five percent of the massive lavas are designated as very fine grained (<0.5 mm), and 35% are defined as fine grained (~0.5 mm). All of the massive basalts are holocrystalline with hypidiomorphic, equigranular, and isotropic textures. Pillow lava fragments were cored from ~62 to ~130 mbsf. They have holocrystalline (with intergranular to subophitic textures) to hypohyaline (with intersertal to hyalopilitic textures and >90% glass) textures.

Massive flows and pillow lavas have subhedral to euhedral skeletal to tabular plagioclase in an intergranular to subophitic relationship with anhedral to subhedral clinopyroxene (possibly augite; 2V γ = ~60°) and subhedral to euhedral equant opaque minerals in the goundmass. A few (<1%) euhedral tabular plagioclase microphenocrysts (maximum size = <1.4 mm) are present. Groundmass minerals compose 55% to 80% of the rock, and the abundance of segregation vesicles is 10% to 30%. These have a paragenesis similar to the segregation vesicles of Holes 1224A and 1224D, with acicular to skeletal plagioclase, anhedral to subhedral equant clinopyroxene, tiny acicular opaques (ilmenite?), and skeletal equant Ti magnetite set in a partially devitrified glassy matrix. Cavities and vesicles are generally rare (all but one sample [81] have <10%) and empty (80%–100%). In a few cases, the cavities are partially (~10%) to totally (100%) filled. The filling materials are brownish clay minerals and possibly iron oxyhydroxides.

Pillow lava fragments cored from ~62 to ~130 mbsf are holocrystalline (with intergranular to subophitic textures) to hypohyaline (with intersertal to hyalopilitic textures and >90% of glass). From Cores 200-1224F-5R to 200-1224F-11R, the rocks have compositions similar to that of the lower flow in Unit 1. Therefore, these rocks reveal the quench mineralogy of the lower massive flow. The quench mineralogy is seen in glassy pillow rims extending into zones of coalesced and sheaf spherulites within ~2 cm of pillow rims (Fig. F41A). The spherulites at the pillow rims are dark-brown globules that coalesce within ~1 cm of wholly glassy rims. The glass itself is light grayish brown except where it has been altered to yellowish palagonite. The most abundant quench mineral is acicular plagioclase, usually present as isolated crystals ~0.5 to 1.0 mm long or as intergrowths with smaller anhedral clinopyroxene (Fig. F41A, F41B). More rarely, small euhedral olivine (Fig. F41C) and zoned euhedral clinopyroxene (Fig. F41D) also are present. Even in palagonite, the plagioclase and clinopyroxene are fresh. Olivine, however, is usually altered to orange-red iron oxyhydroxides and clay minerals (iddingsite).

Pillow fragments show a large textural variation, from virtually holohyaline (glass = >90%) through hypohyaline (crystals = <50%) and hypocrystalline (glass = <50%) to virtually holocrystalline (glass = <10%). The coarser-grained fragments are from the inner parts of the

F41. Quench textures and crystal morphologies of pillow rims, p. 107.

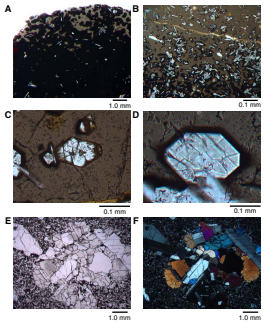

pillows. These experienced a lower undercooling than quenched pillow rims; therefore, they had the possibility to develop larger crystal sizes. Groundmass phases of the pillows are the same as the massive flows, except that large equant opaque minerals, such as those found in segregation vesicles of the massive lavas, are not found here. Plagioclase is often arranged in isolated round or coalesced sheaf and fan spherulites, with fibers of plagioclase becoming coarser in this progression toward pillow interiors. In the more glassy samples, small glomerules of plagioclase and clinopyroxene (average size = <0.5 mm) give the pillow rims a spotted appearance.

In a few cases, gabbroic clots or xenoliths ~1 cm in diameter (Sample 200-1224F-3R-1, 90–92 cm) also are present (Fig. **F41E, F41F**). These indicate scavenging of phases that crystallized in the lower gabbroic portion of the ocean crust. The mineralogy of the xenoliths is similar to the rare phenocrysts—subhedral to euhedral tabular plagioclase and anhedral to euhedral equant prismatic clinopyroxene. Absence of the magmatic oxides, ilmenite and magnetite, is a characteristic of gabbroic cumulates from the ocean crust (e.g., Natland and Dick, 1996).

The increase in size and morphology of plagioclase spherulites from the pillow rims to their interiors is associated with the disappearance of fresh olivine in the pillow interiors. The mineral evidently was better preserved in nearly impermeable glass. The chilled margins vary from vesicle-free to slightly vesicular (~3%); vesicles and cavities are generally partially filled with calcium carbonates.

Two hyaloclastite breccias were recovered at 102 and 129 mbsf, both lying within the interval of ferrobasaltic pillows and flows comprising Unit 3. These consist of subangular glassy shards of variable size from 0.5 to ~3 cm set in a calcitic cement (Fig. **F42A, F42B, F42D**). In some places, the cement can also be reddish to dark-brown iron oxyhydroxides. The glassy fragments are almost always altered with a thin to thick orange palagonite rim. The glassy shards of the sample at 102 mbsf (Sample 200-1224F-12R-1, 61–64 cm) are almost totally glassy, with the percentage of plagioclase, clinopyroxene, and olivine crystallites even in the most crystalline shards <2%. This aspect is quite different from the chilled margins of the pillow fragments of Unit 2 and the glass flow top of the upper flow of Unit 2, which always have several percent of plagioclase crystallites, dark spherulitic rims to those crystals, and a few microphenocrysts of plagioclase, clinopyroxene, and olivine (Figs. **F40C, F41A, F41B**). The more numerous small crystallites in the pillow rims thus nucleated and grew after eruption at a smaller undercooling than was experienced by the purely glassy hyaloclastites.

The calcitic cement is fine to very fine grained. Larger calcite crystals (average size = ~0.3 mm) formed only at the contact with the glassy shards. A colorless mineral with low relief and extremely low birefringence, rhombic to prismatic habit, and multiple twinning (possibly tridymite or zeolite) is intergrown with the calcite in the veins at the contact with the glassy shards.

The partly crystalline glass shards in the Unit 3 hyaloclastite have crystals of olivine, plagioclase, and clinopyroxene that are at once smaller and more numerous than the most comparable glassy portions of pillow rims of Units 1 and 2 (Fig. **F42D, F42E**). Near the pale-yellow palagonitized glassy rims of these shards, short prismatic to acicular and partially skeletal plagioclase crystallites and stellate intergrowths of plagioclase and clinopyroxene are set in the altered glass (Fig. **F42D**). This photomicrograph also shows two small, skeletal olivine crystals altered to orange secondary minerals. Farther away from the glassiest

F42. Textures of hyaloclastites and glass shards, p. 108.

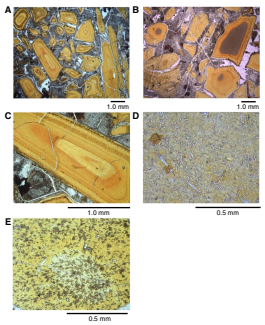

rims, many of the crystallites and stellate intergrowths are coated with brown fibrous spherulitic material (Fig. F42E). All of these crystallites and crystal fibers formed after eruption at high undercooling during quenching of the glass.

There are no larger tabular plagioclases or well-formed clinopyroxene microphenocrysts. These basalts therefore arrived at the seafloor as almost completely aphyric magma, in contrast to the basalts of Units 1 and 2. However, the nucleation density of plagioclase nearest the quenched edges of the shards was greater (compare Fig. F42D, F42E to Figs. F40, F41A, F41B, F41C, F41D). This probably reflects the more differentiated composition and accordingly higher viscosity of the ferrobasaltic liquids when they were so suddenly and strongly cooled.

The interiors of pillows and flows of this basalt show a mineral paragenesis similar to that of the two upper flows of Unit 1. The differences are (1) these portions of the rocks are coarser grained (average dimension of the crystals = >0.5 mm), (2) these have a higher proportion of segregation vesicles (~50%), (3) the acicular opaque minerals in the segregation vesicles are much longer (up to 0.6 mm), and (4) they are more altered to brownish clay minerals (~7%–10%).

All the petrographic features of volcanic basement at Site 1224 can be found in eight Microsoft PowerPoint files (see the "Supplementary Materials" contents list). The first four files (IA to ID) deal mainly with petrographic definitions and the classification of the massive lava flows (phenocrysts and groundmass); the fifth and sixth files (IIA and IIB) deal with pillow-related features; and the seventh and eighth files (IIIA and IIIB) deal mainly with alteration. Tables with detailed petrographic descriptions (of which there are 52 samples) are available in the "Site 1224 Thin Sections," p. 64.

GEOCHEMISTRY

Chemical Analyses

ICP-AES data for basalts were obtained late during Leg 200. The data were only partially reduced and calibrated to standards before the ship reached San Diego, and some data from the second of two runs for Site 1224 could not be used. Thus, only partial analyses are available for plotting on samples obtained from Holes 1224D, 1224E, and 1224F. The basalts were assigned to units based on lithology because geochemical data were not available. The three lithologic units are

Unit 1 (28–62.7 mbsf): massive fresh and altered basalt recovered near the top of the hole,
Unit 2 (62.7–133.5 mbsf): very fine grained pillows with and without glass rims and sheet flows, and
Unit 3 (133.5–161.7 mbsf): somewhat massive flows.

The discussion here is based on contents of K_2O, TiO_2, MgO, Ba, Zr, and LOI from the ICP-AES data. Two diagrams (Figs. F43, F44) contain additional data obtained by postcruise X-ray fluorescence analysis on samples from 133 to 155 mbsf (S. Haraguchi, pers. comm., 2002).

The basalts range from differentiated to very differentiated N-MORB (4–7 wt% MgO and 2–3.5 wt% TiO_2) (Fig. F43). The highly differentiated (4 wt% MgO and 3.5 wt% TiO_2) basalts plot at the most differentiated end of the N-MORB data array. The samples selected for analysis

F43. MgO vs. TiO_2 for basalts, p. 109.

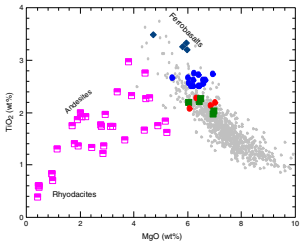

F44. Chemical compositions vs. depth for basalts, p. 110.

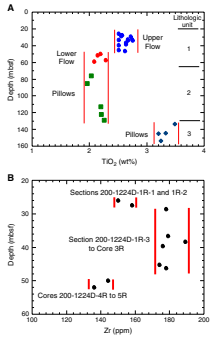

from Hole 1224D are fairly fresh and have LOI values ranging from 0 to 0.45 wt% (Fig. F45). For comparison, the palagonitized crystal vitric tuffs, siltstones, and claystones have much higher LOI values; therefore, they are more altered. Concentrations of K_2O (0.11–0.27 wt%) may be slightly elevated (>0.2 wt%) in three of the ten samples analyzed (Fig. F46). All the basalts have Ba concentrations (9–18 ppm) that are consistently lower than many comparably differentiated MORB glasses from the East Pacific Rise (Fig. F47). This may indicate a greater than average depletion of the mantle sources in the basalts from Hole 1224D. Alternatively, the rocks may have experienced a slight nonoxidative alteration as these components were partially removed from the rock.

The samples from Hole 1224D can be divided into two groups based on their TiO_2 concentrations. These geochemical groups correspond to (1) the lithologic Unit 1 upper flow (>2.3 wt% TiO_2) and (2) the lithologic Unit 1 lower flow (<2.3 wt% TiO_2). Interestingly, lithologic Unit 2 pillow lavas have TiO_2 concentrations similar to the lower flow basalts from Unit 1. The lithologic Unit 3 pillow lavas have TiO_2 concentrations >3.1 wt% TiO_2. Therefore, the geochemical divisions (based on TiO_2 contents) do not correlate directly with the lithologic units.

Analyses from Holes 1224E and 1224F indicate that the topmost flow was sampled in both holes, and the second flow was also sampled in Hole 1224F. These belong to lithologic Unit 1. Samples of lithologic Unit 2 have TiO_2 contents similar to those of the lower flow of Unit 1. Apparently accumulation of this chemically uniform basalt at the site began with thin flows. These were capped with a thick flow of the same material. The samples of Holes 1224E and 1224F from Unit 2, however, are more greatly altered than those of this capping flow at the base of Unit 1, usually having as much as two to three times the amount of K_2O present in samples of Hole 1224D, and in one case having >1 wt% K_2O. This is in accordance with the strong contrast in extent of alteration noted in the core descriptions between holes only 15 m apart.

Samples of lithologic Unit 3 have TiO_2 contents greater than in any of the basalts from the thick flows or pillows of lithologic Units 1 and 2 (Fig. F44A). Based on TiO_2 contents, these are among the most differentiated basalts sampled thus far from the flanks or axis of the East Pacific Rise. Their compositions are at or about the point where oxide minerals join the liquidus, causing TiO_2 contents to drop as MgO decreases and producing andesitic and ultimately rhyodacitic residual liquids (Fig. F43).

X-Ray Diffraction Investigation of Secondary Minerals

At Site 1224, reddish dark-brown clay (Core 200-1224C-1H; <28 mbsf) and basalt (Holes 1224D, 1224E, and 1224F; >28 mbsf) were cored. Some white clayey pebbles were recovered in Core 200-1224A-2X. Massive basalt, present in the upper 35 m of basement, has some altered layers and fractures. Some fractures have green clay or white carbonate deposits. They were analyzed by XRD. The samples analyzed include one clayey pebble and 25 vein materials in the basalt.

Veins

Veins are classified in hand specimen according to color: dark green, light green, dark reddish brown, light reddish brown, white, and color-

F45. LOI plotted vs. depth, p. 111.

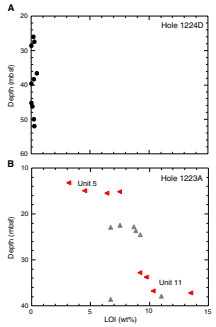

F46. MgO vs. K_2O with N-MORB glass compositions, p. 112.

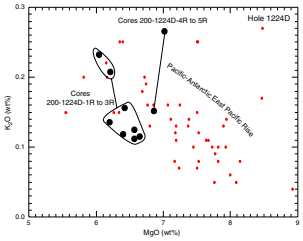

F47. MgO vs. Ba compared to fresh glasses, p. 113.

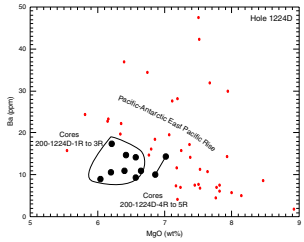

less, and also by degree of crystallization: muddy (clay vein) and consolidated (crystallized).

Five distinct vein types are documented by XRD analysis: clay, carbonate, zeolite, quartz, and smectite + calcite. The samples analyzed and results are shown in Table T6. Sampling points and identification are shown in Figure F48.

Pyrite and black to reddish iron oxyhydroxides were identified in many veins by visual observation, but their volumes were too small for XRD analysis.

Clay Veins

Clay veins are the most abundant vein type in the basement at Site 1224. Most are dark green and <1 mm thick. Some thick veins, which reach nearly 2 mm in thickness, are filled with light-green fibrous clays.

The clay veins are smectite and illite rich. The smectite is characterized by a ~13- to 14-Å peak with additional peaks of montmorillonite and saponite (Fig. F49A). Illite veins have a 10-Å peak (characteristic of the mica group) (Fig. F49B). Other peaks are for montmorillonite, a smectite-group mineral, and laumontite, a zeolite-group mineral. Smectite veins are more abundant than illite veins, based on XRD identification. Only one pure illite vein was found among analyzed samples (interval 200-1224D-3R-3, 90–92 cm). Some veins have both smectite and illite characteristics in their XRD patterns.

Carbonate Veins

The carbonate veins are mainly white and crystallized. Many are lined with green clay and have carbonate in the middle. Many veins in massive flows are <1 mm thick. However, those in pillows and breccias are thicker than those in the massive flows and may reach 1 cm in width. Some veins contain fragments of altered basalt. Sample 200-1224F-6R-1, 29–34 cm, is a hyaloclastite in which altered glass fragments are cemented by calcite.

The XRD patterns of these veins have characteristic calcite peaks (Fig. F50A) and lesser peaks of smectite. Smectite peaks (in the XRD pattern) are a result of the influence of the outer clay layer. Some samples also have minor phillipsite peaks.

Some carbonate deposits have poorly consolidated clays associated with them. These are present as voids in highly fragmented pillows and in cemented brecciated altered pillow fragments.

Fibrous, colorless aragonite is present in one sample (200-1224F-4R-5, 43–47 cm) (Fig. F50B).

Zeolite Veins

One sample (200-1224F-9R-1, 55–57 cm), in a poorly consolidated white vein from a highly fractured pillow, contains cemented fine altered fragments of the host rock. The XRD pattern is characterized by many phillipsite peaks. Some low-intensity peaks are those of smectite. This appears to be an altered fragment of host rock (Fig. F51).

Quartz Veins

Some thin veins in the upper massive basalt are well crystallized and dark green. They are similar to calcite-clay veins but are <1 mm thick and show dark inner cores. These are dominated by quartz with accessory smectite (Fig. F52).

T6. XRD analysis samples and identified minerals, p. 175.

F48. Identification of the main secondary minerals in basement, p. 114.

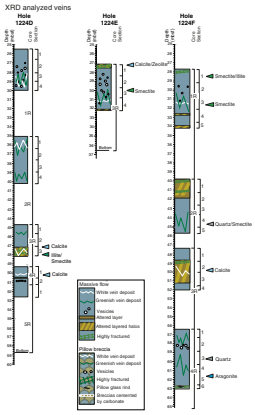

F49. XRD results for smectite and illite veins, p. 116.

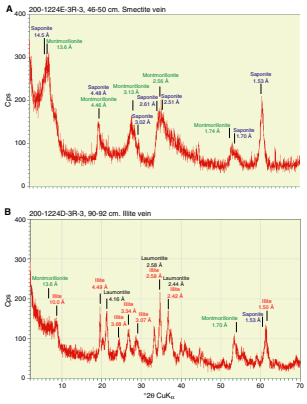

F50. XRD results for calcite and aragonite vein, p. 117.

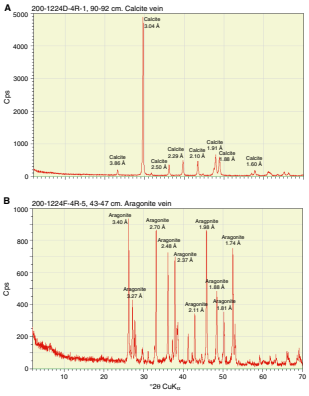

Calcite/Smectite Veins

Some veins combine light-green clay and white carbonate and are nearly 2 mm thick. This vein material is not well consolidated. The XRD patterns have prominent calcite peaks and low smectite peaks (Fig. F53). Based on calcite and smectite XRD patterns and visual observation, the ratio of calcite and smectite in these veins is lower than that in consolidated and layered calcite veins. There is <30% calcite in these veins.

Clayey Pebbles

Clayey pebbles were recovered from the sediments of Hole 1224A. They are light brown and shaped like coral. They produce the complex XRD patterns of phillipsite, a zeolite-group mineral (Fig. F54). The depth of the sample may correspond to a seismic reflection at 10 mbsf (see "Core, Physical Properties, Logging, and Seismic Correlations," p. 57) (Fig. F2).

Discussion

Sequence of Vein Deposit Growth

Tartarotti et al. (1996) considered the sequence of secondary mineralization in open fractures based on studies of Hole 896A in the Costa Rica Rift. They suggested a general sequence of vein formation from oldest to youngest as follows:

1. Fe oxyhydroxide,
2. Smectite with spheroidal texture,
3. Calcium carbonate with blocky crystal shape,
4. Smectite with fibrous texture, and
5. Calcium carbonate with fibrous texture.

Visual and macroscope observations together with XRD analysis of veins suggest that this sequence also is present at Site 1224 (e.g., many thick calcite veins have distinct inner calcite and outer green smectite zones; fibrous smectite is present only in thick veins; many quartz veins have associated outer green smectite; and most vein surfaces of host rocks show greenish [smectite] or black [oxyhydroxide] colors).

Tartarotti et al. (1996) characterized clay-lined veins at Site 896 into two types: nonfibrous and fibrous veins. Nonfibrous veins are thought to represent fractures filled by minerals crystallizing in open cavities where fluid-filled spaces were available for crystal growth. Fibrous veins are interpreted as crack-seal veins in which narrow cracks propagated and then were cemented. According to this model, thin and deposit-poor veins record hydrothermal activity, whereas thick crystallized veins reflect hydrothermal activity together with shear stress in the flow unit. Veins are thicker in pillows than massive flows. Perhaps this is because pillows are more fractured, sheared, and therefore more permeable to hydrothermal fluids than massive flows.

Stable Condition of Mineral Assemblages in Veins

Many vein minerals in basement at Site 1224 are stable at low temperature and pressure conditions (e.g., zeolite). Phillipsite, the main zeolite present at Site 1224, is a low-temperature member of the zeolite group (e.g., Miyashiro, 1973). Smectite is also commonly found as a

F51. XRD result for a zeolite vein, p. 118.

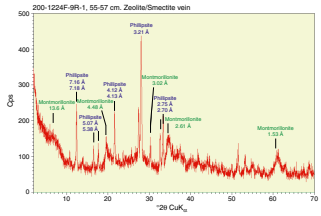

F52. XRD result for a quartz vein, p. 119.

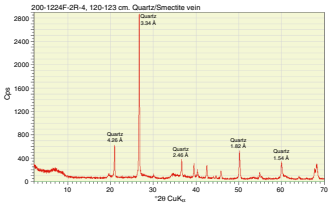

F53. XRD result of a mixed calcite and smectite vein, p. 120.

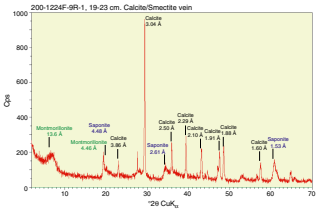

F54. XRD result of zeolite pebbles in a sediment layer, p. 121.

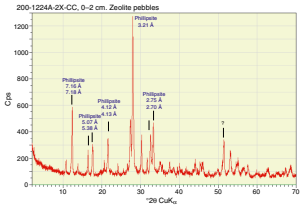

product of the alteration of volcanic ashes and rocks from the seafloor. Smectite is present in most low-grade metamorphic terranes around the world.

Four vein types, smectite-illite, calcite-aragonite, quartz, and zeolite, at Site 1224 are similar to those at Site 896 at the Costa Rica Rift. Quartz veins are not present at Site 896 but are found deeper at nearby Site 504B (Alt, Kinoshita, Stokking, et al., 1993). These minerals are present in relatively lower temperature hydrothermal assemblages (probably <100°C; Laverne et al., 1996).

Truly high temperature vein assemblages, such as the actinolite and epidote veins found deeper than 2000 mbsf in Hole 504B (Alt, Kinoshita, Stokking, et al., 1993), are not present at Site 1224. The mineral laumontite in the illite vein indicates a higher zeolite facies (Miyashiro, 1973). Aragonite generally forms at a higher temperature than calcite. These minerals indicate the local influences of warm hydrothermal fluids.

BIOSTRATIGRAPHY[3]

Because the focus of Leg 200 was on basement drilling, we did not have a paleontologist on board. John Firth, from ODP-TAMU (Texas A&M University), analyzed the calcareous nannofossils in the sediment cores postcruise and wrote a first draft of the following report. A graphical summary of smear slides analyzed for fossils from the sediments cored at Site 1224 is shown in Figure **F55.**

Smear slides were made from Cores 200-1224A-2X and 4X, 200-1224C-1H, and 200-1224E-2R for initial analysis of calcareous nannofossils. The highest and lowest occurrences of nannofossils were compared with those reported in Bralower and Mutterlose (1995) and with the zonation of Okada and Bukry (1980) and correlated to the geologic timescale of Berggren et al. (1995).

Sample 200-1224A-2X-CC was barren of nannofossils. Sample 200-1224A-4X-1, 78 cm, contains rare, poorly preserved nannofossils, including *Chiasmolithus grandis, Coccolithus pelagicus,* and *Campylosphaera dela.* The highest occurrence (HO) of *C. grandis* marks the top of Subzone CP14b of Okada and Bukry (1980), and the HO of *C. dela* falls within Subzone CP14b (according to Bralower and Mutterlose, 1995). Sample 200-1224A-4X-CC contains rare, poorly to moderately preserved nannofossils, including *Reticulofenestra umbilicus, Discoaster barbadiensis, C. pelagicus, Coccolithus formosus, C. grandis,* and *Sphenolithus spiniger.* The lowest occurrence (LO) of *R. umbilicus* marks the base of Subzone CP14a, and the HO of *C. grandis* marks the top of Subzone CP14b. Thus, Core 200-1224A-4X can be constrained to Zone CP14 (~37–43 Ma), of late middle Eocene age. Zone CP14 corresponds in time to polarity Chrons C17N to C20N.

Sample 200-1224C-1H-1, 40 cm, contains very rare, poorly to well preserved nannofossils including *Reticulofenestra bisecta, Reticulofenestra dictyoda,* and *C. dela.* The ranges of *R. bisecta* and *C. dela* overlap within Subzone CP14b (~37–40 Ma); thus, this sample is constrained to that subzone. Sample 200-1224C-1H-4, 27 cm, had very rare, very poorly preserved and unidentifiable nannofossils. Samples 200-1224C-1H-5, 52 cm, and 1H-CC, 5 cm, are barren of nannofossils.

Sample 200-1224E-2R-1, 45 cm, contains abundant, diverse, moderately preserved nannofossils, including *C. grandis, Chiasmolithus solitus, Chiasmolithus gigas, C. pelagicus, C. dela, Sphenolithus furcatolithoides,*

F55. Summary of sediments cored at Site 1224, p. 122.

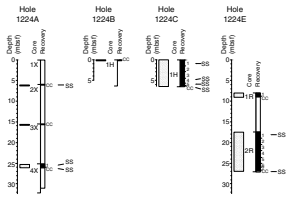

[3] This section was written by John Firth, Ocean Drilling Program, Texas A&M University, 1000 Discovery Drive, College Station TX 78745-9547, USA
firth@odpemail.tamu.edu

and *Braarudosphaera* sp. Sample 200-1224E-2R-CC, 11 cm, contains abundant, moderately to well-preserved nannofossils, including *C. grandis, C. gigas, Chiasmolithus nitidus, C. dela,* and *C. pelagicus*. The presence of *C. gigas* in both samples from Core 200-1224E-2R constrains this core to be within Subzone CP13b (~44–46 Ma) of Okada and Bukry (1980), of middle Eocene age. Subzone CP13b corresponds in time to Chrons C20R and C21.

Sediments from the core catcher of Core 200-1224-2R are within 2 m of the sediment/basement contact. Marine magnetic anomalies over the basement at Site 1224 indicate the age of basement is near the Chron C20R/C21N contact. Thus, the paleontological age of the oldest sediments is consistent with the basement age. Surprisingly, nearly the entire sedimentary section appears to be middle Eocene in age.

PALEOMAGNETISM

We used progressive AF demagnetization of archive-half sections, one whole-core section, one working-half section, and discrete samples to characterize the paleomagnetic signal and resolve the magnetization components recorded in the recovered core. An unambiguous magnetostratigraphy could not be obtained from the only undisturbed core (Core 200-1224C-1H) that was recovered in the sedimentary section; the other sediment cores were extremely disturbed by drilling. In addition, we had time for only a cursory interpretation of the magnetization of the basaltic units, although fairly detailed demagnetization experiments were conducted on split cores and discrete samples.

Given that a number of basalt units were recovered (see **"Igneous Petrology,"** p. 26, in "Lithology") (Table **T5**), the magnetization of the basalts should provide a valuable paleolatitude estimate for the Pacific plate at ~45 Ma. This age corresponds to the Pacific plate's abrupt change in motion relative to the hotspots as marked by the kink in the Hawaiian-Emperor hotspot track. A cusp in the Pacific plate APWP may also occur at this age, marking a change in the motion of the Pacific plate relative to the spin axis. The Pacific APWP and hotspot tracks together provide key constraints on estimates of the size of motions between hotspots, ultimately extending our understanding of mantle dynamics (Acton and Gordon, 1994). Additionally, the age also lies within the period (39–57 Ma) when the Hawaiian hotspot has been shown to have moved rapidly southward relative to the spin axis (Petronotis et al., 1994). If geomagnetic secular variation has been averaged by the basalt units and if secondary overprints caused by alteration do not mask the primary magnetization, then we should be able to obtain an accurate paleolatitude. Finally, rock magnetic studies of the basalts should help refine our understanding of the magnetization of the upper oceanic crust and its role in generating lineated marine magnetic anomalies.

Measurements

We made 88,384 remanent magnetization measurements along the split-core sections and along a whole-core section from Site 1224. Measurements were made every 1 cm before and after AF demagnetization. All sections were progressively demagnetized in steps of 1–5 mT up to peak fields of between 35 and 40 mT, with a few sections measured at higher fields. Sedimentary core sections that were disturbed by coring,

short basalt sections (<30 cm), or basalt sections with only multiple small pieces (<10 cm) were not measured. We also measured remanence, before and after AF demagnetization up to 70–80 mT, on 72 discrete samples. Magnetic susceptibility was measured on whole-core sections every 1 cm (Fig. F56). Both remanence and susceptibility data are available from the ODP Janus database.

Analysis and Results

Unlike at Site 1223, we have not attempted to remove those measurements made near the ends of the core, the ends of basalt pieces, or in gaps as this would have required a substantial amount of time that was not available during the leg. Gaps between basalt pieces are common, so the raw data should be used with care.

All split-core and discrete samples have a drilling overprint. Unlike Site 1223, the steep component was not just directed downward but in some cases pointed upward, as was the case for the XCB and MDCB cores from Hole 1224A. The radial-horizontal component that points toward the center of the core was also present as is evident in the bias in the declinations of the split-cores toward 0° prior to AF demagnetization (Fig. F56). Initial natural remanent magnetization measurements are thus characterized by inclinations greater than +40° and declinations of ~0°. The drilling overprint was much less severe in the basalts at Site 1224 than in the vitric tuffs at Site 1223, which may be related to different acquisition mechanisms, magnetic grain sizes, and, less likely, magnetic mineralogy. In general, ~10-mT AF demagnetization removed the drilling overprint for the basalts, whereas >30 mT was needed for the tuffs.

Results from the sediments were perplexing. Only one core was recovered without a high level of drilling disturbance (Core 200-1224C-1H). We measured the remanence before and after AF demagnetization up to 30 mT on the whole-round section (200-1224C-1H-3). We then compared the result with the archive and working halves. After repeating the 30-mT demagnetization, both halves were measured twice to ensure that any viscous magnetization components that might have been acquired during splitting and handling were removed. Surprisingly, there were large differences in the inclinations of the whole round, archive half, and working half (Fig. F57). To add to the mystery, discrete samples gave inclinations that disagree with the split-core measurements over the 6.5-m interval recovered in Core 200-1224C-1H. We are unsure why such complexity is observed, although deformation caused by splitting or sampling, weak magnetization, or drilling overprints may play a role. We plan to investigate this further postcruise.

The basalt samples display both simple and complex demagnetization paths on orthogonal demagnetization plots. After removing the drilling overprint by ~10 mT, many samples gave linear demagnetization paths that decay to the origin of the plot (Fig. F58). After removing the drilling overprint, other samples gave linear demagnetization paths, but they did not decay directly to the origin. In several cases, multiple components were recorded in a single sample, with the components sometimes being nearly antipodal (Fig. F59). Some level of secondary overprinting is not unexpected given that we recovered altered basalt as well as fresh.

F56. Inclination, declination, and intensity prior to AF demagnetization, p. 123.

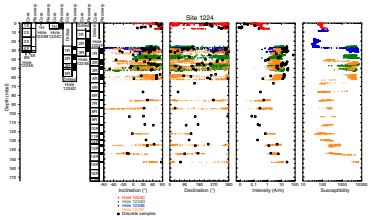

F57. Inclination and intensity, Hole 1224C, p. 124.

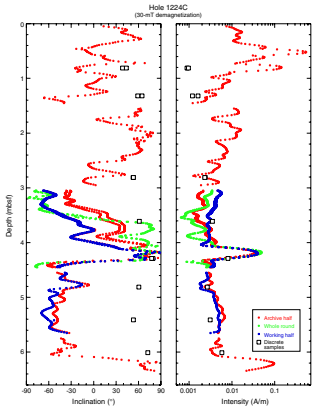

F58. AF demagnetization results from Sample 200-1224A-5X-1, 17 cm, p. 125.

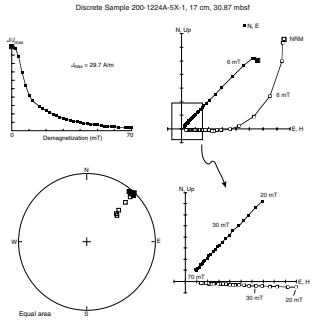

MICROBIOLOGY

Results at Site 1224

Deep drilling into 45-Ma oceanic basaltic crust in a deepwater (~5000 m) environment provided a promising opportunity to explore the bacterial deep biosphere using a comprehensive multiphase experimental approach.

At Site 1224, 25 samples were taken at various depths, ranging from near-surface sediments to hard rock samples of basaltic basement down to 154 mbsf. Sediment samples from Holes 1224C, 1224D, and 1224E were obtained from different depths ranging from the upper surface layer down to 24.9 mbsf, which was almost the bottom of the sediment coverage at this particular site. The sediment samples consist of light-brown to dark red-brown clay. Five sediment samples were taken over the whole color range near the surface (0.05 mbsf) at 1.45, 3.91, 5.63, 6.28 and 24.93 mbsf.

Ambient seawater samples were collected at 1 m below sea surface, upwind of the *JOIDES Resolution,* to evaluate the microbial background at Site 1224. The microscopically enumerated total cell counts in the surface water at Site 1224 were 1.4×10^4 cells/mL.

As shown by a comparative determination of total cell counts using the nucleic acid stains SYTO 9 and SYBR Green I and SYTO 62, bacteria were present in all sediment samples taken from Site 1224 down to 24.9 mbsf. As shown for Site 1223, the highest total count was determined in near-surface sediments (Sample 200-1224C-1H-1, 0–5 cm) with 3.8×10^{10} cells per gram of wet sediment. This was followed by a slow decline in total cell counts to 1.1×10^{10} within the sediment layer located at 1.45 mbsf (Sample 200-1224C-1H-1, 145–150 cm). About 4 m downhole (at 5.63 mbsf; Sample 200-1224C-1H-4, 113–118 cm), the number of total cell counts decreased more rapidly by two orders of magnitude to 2.4×10^8 cells per gram of wet sediment. At a depth of 24.93 mbsf (Sample 200-1224E-2R-5, 143–150 cm), bacterial total cell counts slightly increased to 7.3×10^8 cells per gram of wet sediment.

The amount of metabolically active bacteria within the bacterial communities was assessed by fluorescent in situ hybridization (FISH) in two representative sediment samples taken from an upper sediment layer at a depth of 1.45 mbsf (Sample 200-1224C-1H-4, 145–150 cm) and from a depth of 25 mbsf (Sample 200-1224E-2R-5, 143–150 cm). As indicated by fluorescent signals after hybridization with the Bacteria-specific probe EUB338, the amount of metabolically active bacteria ranged in these sediment layers from 41% to 62% of the total cell counts, respectively (Fig. F60). The FISH-based assessment of bacteria with apparent physiological potential was conducted as described in Manz et al. (2001).

Most probable number assays from both sediment samples and rock suspensions from ground tholeiitic basaltic rocks were conducted for both sulfate-reducing bacteria and fermentative bacteria.

Whole-round cores of basement rocks, including glass samples, were collected and transferred within 5 min into an anaerobic chamber. The rock samples were subsequently manually cracked open with sterile chisels, and only pieces from the inner core were used to establish anaerobic and aerobic cultures.

Suspensions obtained from ground rock material were successfully cultivated at various temperatures under both aerobic and anaerobic

F59. AF demagnetization results from Sample 200-1224F-2R-1, 91 cm, p. 126.

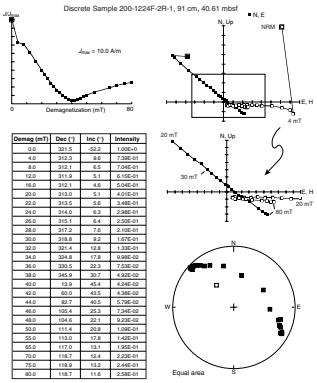

Demag (mT)	Dec (°)	Inc (°)	Intensity
0.0	321.5	62.2	1.00E+0
4.0	312.3	9.6	7.39E-01
8.0	312.1	6.5	7.04E-01
12.0	311.9	5.1	6.15E-01
16.0	312.1	4.6	5.04E-01
20.0	313.0	5.1	4.01E-01
22.0	313.5	5.6	3.48E-01
24.0	314.0	6.3	2.98E-01
26.0	315.1	6.4	2.50E-01
28.0	317.2	7.6	2.10E-01
30.0	318.8	9.2	1.67E-01
32.0	321.4	12.8	1.33E-01
34.0	324.8	17.8	9.99E-02
36.0	330.5	22.3	7.53E-02
38.0	345.9	30.7	4.92E-02
40.0	13.9	45.4	4.24E-02
42.0	60.0	43.5	4.38E-02
44.0	92.7	40.5	5.79E-02
46.0	105.4	25.3	7.34E-02
48.0	104.6	20.1	9.23E-02
50.0	111.4	20.8	1.09E-01
55.0	113.0	17.8	1.42E-01
65.0	117.0	13.1	1.95E-01
70.0	118.7	12.4	2.23E-01
75.0	118.9	13.2	2.44E-01
80.0	118.7	11.6	2.58E-01

F60. Bacterial cells after DAPI staining and hybridization with the CY3-labeled probe EUB338, p. 127.

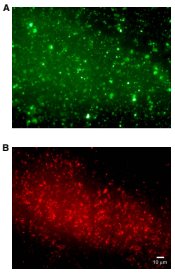

conditions. Ground rock material obtained from rock samples taken at 27 mbsf (Sample 200-1224D-1R-2, 10–15 cm) and 31.5 mbsf (Sample 200-1224E-3R-4, 82.5–87.5 cm) were cultivated under aerobic conditions in an artificial seawater medium. Preliminary microscopic determination of bacterial colonies gave a strong indication of the presence of Fe^{2+}-oxidizing bacteria (Fig. F61).

The microscopic investigation of a thin section of the massive tholeiitic lava flow unit located at 50.9 mbsf showed unique tubular filamentous structures within $CaCO_3$ cavities, which resembled, with regard to shape and dimension, fungal hyphae including cell walls and dichotomous branches. The cross-sectional dimension of the hyphal network is 5–10 µm with a length ranging from 50 to several hundred micrometers. The hyphae are typically interrupted at irregular intervals by cross walls, or septa, which divide the entire fungal hyphae into single distinctive cells (see arrow in Fig. F62). The diameter of the cavities ranges from 0.5 to 3 mm with a filling matrix of calcite and/or aragonite. In our opinion, these cavities are part of a complex pore-channel system that developed as gas pipes during the cooling process of magma. The net of fungal hyphae shown in Figure F63 filled the entire space spanning from the basalt/carbonate boundary to the center of the cavity.

Pyrite was commonly observed as euhedral crystals within the cavities and outside as framboidal pyrite. Iron oxyhydroxides were never observed adjacent to the cavities' faces. Anaerobic conditions were apparently maintained within the cavities for the remainder of the mineralization process. All cavities where fungi were found were completely filled by secondary phases. At present the question of whether the microbial life reported here grew before, after, or at the same time as the formation of $CaCO_3$ remains open.

A completely different situation is given in fractures and veins where we also detected fungal growth. Here again, the hyphae were detected within a carbonate matrix. Because of the encrustation with iron oxyhydroxide, caused by the contact with seawater, morphological traits of the hyphae are not so well preserved (Fig. F64). This surprising discovery provides strong evidence for eukaryotic life in deep subsurface environments in addition to bacteria.

Discussion

The number of near-surface bacterial populations shown for Site 1224 is similar to those at Site 1223, with similar overlying water depth. The most abundant bacterial community was seen in the near-surface sediments. This was followed by a slow decrease of the total cell counts down to 1.45 mbsf and a more rapid reduction in cell numbers at a depth of 5.6 mbsf. Interestingly, within sediments obtained from a depth of 25 mbsf, the bacterial cell counts slightly increased again. The application of high-quantum-yield fluorochromes resulted in total cell counts ranging one to two orders of magnitude higher than reported during previous ODP Legs (Cragg et al., 1996).

As a general trend, bacterial population numbers decreased with increasing depth. However, the amount of metabolically active bacteria as revealed for the first time during Leg 200 by FISH, remained remarkably high with 41%–62% of the total cell counts. Both the high total cell counts as well as the amount of bacteria with apparent physiological potential within the sediment layers suggest a higher contribution of sediment bacteria than has been assumed until now. Keeping this in mind, the recently extrapolated contribution of the marine subsurface

F61. Macroscopic image of Fe^{2+}-oxidizing bacterial colony, p. 128.

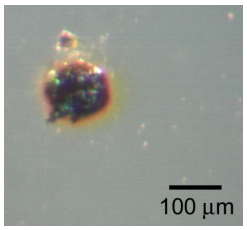

F62. Fungal hyphae divided into distinctive cells by septae, p. 129.

F63. Fungal hyphae in a $CaCO_3$-filled cavity, p. 130.

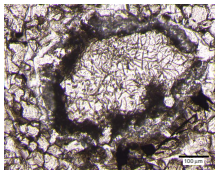

F64. Fe-oxide encrusted fungal hyphae in a carbonate-filled vein, p. 131.

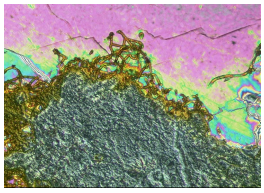

biosphere, ranging from 10% to 30% of the Earth's living biomass (Parkes et al., 2000; Whitman et al., 1998), might be the minimum contribution of bacterial communities.

The successful cultivation of putative Fe^{2+}-oxidizing bacteria and the microscopic indication of further microbial structures within carbonate-filled cavities in basaltic rocks confirm the presence and even activity of microbial life not only in deep marine sediments, but also in old and cold oceanic crust far away from any deep-sea volcanic vent. Both Mn(II) and Fe(II) diffuse upward from reduced sediments and are deposited as oxide layers in the presence of low oxygen contents. Although Fe(II) oxidation is very rapid at neutral pH, filamentous bacteria such as *Gallionella ferruginea* living at the oxic/anoxic interface are known to drive iron oxidation as a mode of energy conservation in freshwater environments. The successful cultivation of aerobic bacteria capable of ferrous iron oxidation in a marine system would be an important contribution to our understanding of the complex biogeochemical iron cycle in marine environments. The phylogenetic affiliation of the obtained cultures will be further investigated by shore-based DNA extraction and characterization, electron microscopy, and biomarker analysis. The detection of fungi within a massive tholeiitic lava flow unit describes eukaryotic life in such a deep-sea environment for the first time. Along with the description of microfossils (fossilized microorganisms) as suggested by McKinley and Stevens (2000), the microbiological characterization of their modern equivalents will result in a more profound knowledge of the biogeochemical processes of the deep biosphere.

In summary, these results constitute further evidence for continuing microbiological activity in the deep subseafloor biosphere environment. The presence of fossilized iron-encrusted bacteria and fungi at interfaces may therefore serve as an indicator of anoxic to dysaerobic conditions in various paleo(micro)environments. Thereby, Leg 200 significantly contributes to the elucidation of the unique but almost unknown deep subseafloor biosphere environment. The secrets that microorganisms associated with the deep-marine component of our biosphere might reveal about the origin and limits of life on Earth are still unspoken and remain to be reported in further investigations.

PHYSICAL PROPERTIES

Physical properties in Hole 1224 were measured on whole cores, split cores, and discrete samples. The multisensor track (MST) was used to perform nondestructive measurements of GRA bulk density, magnetic susceptibility (MS), compressional wave velocity using the *P*-wave logger (PWL), and natural gamma radiation (NGR) on whole cores. Discrete sample measurements were made on sediments and hard rock cores. Compressional wave velocity was measured on split cores using the PWS3 contact probe system in the x-direction for soft sediments and in the x-, y- and z- directions for hard rock cubes. Moisture and density properties, such as bulk density, water content, porosity, and grain density, were measured on discrete samples. The thermal conductivity was measured on whole cores for soft sediments and on discrete samples for hard rock cores.

Hole 1224C

MST Measurements

GRA bulk density and magnetic susceptibility were measured every 1.0 cm. NGR was measured every 10 cm.

Three notable zones were identified in the soft sediment acquired from Hole 1224C by MST measurements (Fig. F65). In the first zone, the GRA densities range from 1.5 to 1.8 g/cm³ between 0 and 2 mbsf (Fig. F65A). In the second zone, the GRA densities continuously decrease from 1.8 to 1.5 g/cm³ with increasing depth between 2 and 4.5 mbsf. In the third zone, the GRA densities are relatively constant at 1.5 g/cm³ from 4.5 to 6 mbsf. In the second zone, magnetic susceptibilities remain constant at ~85 (raw meter SI units) (Fig. F65B); however, in the third zone, they rapidly increase from 86 to 125 between 4.5 and 6.0 mbsf. Natural gamma ray intensities rapidly decrease from 115 to 35 counts per second (cps) within 1 mbsf (Fig. F65C); however, they remain constant at 20–30 cps with increasing depth through all three zones. The decrease in bulk density with increasing depth in the second and third zones is difficult to explain.

Moisture and Density and Thermal Conductivity

Moisture and density properties, such as bulk density, water content, porosity, and grain density, were measured on individual samples. Thermal conductivity was measured on split cores for each section. Bulk density and dry density gradually decrease from 1.53 to 1.36 g/cm³ and from 0.8 to 0.5 g/cm³, respectively (Fig. F66; Table T7). Dry densities have similar tendencies to bulk densities, although dry densities are lower than bulk densities. Grain densities range from 2.7 to 2.8 g/cm³ (Fig. F66C). They remain constant at 2.7 g/cm³ between 2.5 and 5.5 mbsf. Porosities gradually increase from 71% to 80% with increasing depth (Fig. F66D). Thermal conductivity remains fairly constant at 0.8 W/(m·K) except for Section 200-1224C-1H-1 (Fig. F67A; Table T8).

Compressional Wave Velocity

PWL velocities remain constant at 1480 m/s between 0 and 1.5 mbsf (Fig. F67B). They slightly increase from 1480 to 1490 m/s between 2.5 and 4.5 mbsf. Between 4.5 and 5 mbsf, they remain constant at 1480 m/s. Below 5 mbsf they range from 1480 to 1500 m/s with increasing depth. PWS velocities were measured on split cores. PWS velocities are ~40 m/s higher than PWL velocities (Fig. F67B; Table T9), although their trends are somewhat similar. This difference can be explained by moisture lost from the split cores during the measurements. PWS velocities remain between 1525 and 1535 m/s except for Section 200-1224C-1H-5, which has a velocity of 1555 m/s. Figure F68 shows the relation of PWL velocity vs. GRA density. As velocity decreases, bulk density increases. This differs from the general relation between bulk density and compressional wave velocity (e.g., Birch, 1960, 1961; Hamilton, 1976).

Discussion

Most of the physical properties of Hole 1224C show unusual variations with increasing depth. GRA bulk density, PWL velocity, and MS from the MST, and bulk and dry density, porosity, and PWS velocity for

F65. GRA bulk density, MS, and NGR, Hole 1224C, p. 132.

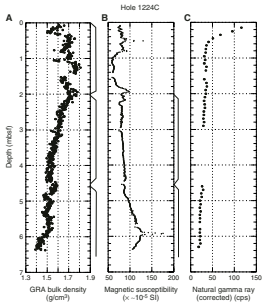

F66. Moisture and density measurements, Hole 1224C, p. 133.

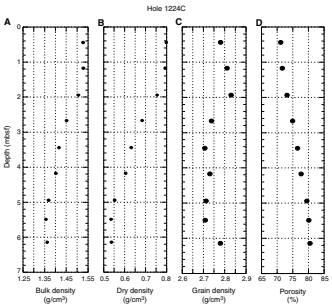

T7. Moisture and density, Site 1224, p. 176.

F67. Thermal conductivity, PWL and PWS, and GRA and bulk density, Hole 1224C, p. 134.

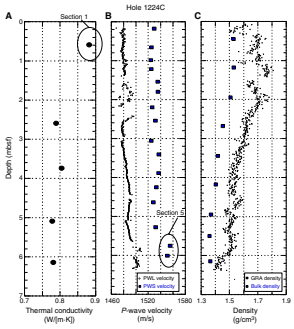

T8. Thermal conductivity measurements, Site 1224, p. 177.

T9. PWS compressional wave velocities, Site 1224, p. 178.

individual samples show strong correlations to each other. Birch (1960, 1961) suggested a positive gradient between velocity and density for most silicates. The GRA density vs. velocity relation for Hole 1224C, however, shows a negative gradient (Fig. F68). Bulk and dry density decrease and porosity increases with increasing depth, suggesting that a large amount of water can be absorbed in the zone between 2 and 4.5 mbsf (Fig. F66).

Hole 1224D

MST Measurements

GRA bulk density and MS were measured every 1.0 cm. NGR was measured every 5.0 cm. The GRA bulk density was not measured for cores obtained from depths shallower than 50 mbsf. GRA densities (between 52 and 55 mbsf) range from 2.5 to 3.1 g/cm³ (Fig. F69A). Although MS and natural gamma radiation intensity were measured for all cores, like the GRA data they may have large errors owing to variations in core diameter and gaps between core pieces. MS also shows large variations (Fig. F69B). Natural gamma radiation intensities are very low values, which is typical for basalt (Fig. F69C).

Moisture and Density and Thermal Conductivity

Figure F70 shows the results of bulk and dry densities, grain densities, porosity, and thermal conductivity for Hole 1224D. Bulk and dry densities increase from 2.7 to 2.9 g/cm³ and 2.6 to 2.8 g/cm³, respectively in Core 200-1224D-2R (Fig. F70A). In Core 200-1224D-3R, bulk and dry densities decrease from 2.9 to 2.8 g/cm³ and from 2.8 to 2.7 g/cm³, respectively. In Cores 200-1224D-4R and 5R, they also decrease from 2.85 to 2.8 g/cm³ and from 2.8 to 2.7 g/cm³. Porosities remain at low values and range from 4% to 9%. Grain densities are fairly constant and range from 2.8 to 3.0 g/cm³. Thermal conductivities for Hole 1224D are scattered and range from 1.65 to 1.85 W/(m·K) (Fig. F70C).

Compressional Wave Velocity

PWS velocity was measured on individual cubic samples. PWS velocities range from 4200 to 6500 m/s (Fig. F71A). Compressional wave velocity anisotropy for each sample is ~2%–10%. PWS velocities have a sinusoidal depth variation. They decrease between ~27 and 35 mbsf, increase between 35 and 45 mbsf, and decrease again between 45 and 52 mbsf. This sinusoidal depth variation is also identified for Hole 1224F (Fig. F71C). A similar variation is also seen in the gamma radiation intensity measurements in the triple combo logging tool (Fig. F87) (see "Core, Physical Properties, Logging, and Seismic Correlation," p. 57).

Discussion

As shown in Figure F72, PWS velocities have positive and negative gradients with bulk densities and porosities, respectively. PWS velocities increase with increasing bulk density, except for two samples. Samples A and B have large anisotropy (Fig. F72A). The velocity of sample B is 4650 m/s for the y-direction and 5100 m/s for the x-direction. PWS velocities decrease with increasing porosity (Fig. F72B). Samples A and B

F68. PWL velocity vs. GRA density, Hole 1224C, p. 135.

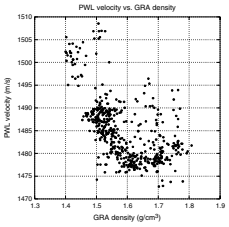

F69. MST measurements of GRA bulk density, MS, and NGR with depth in Hole 1224D, p. 136.

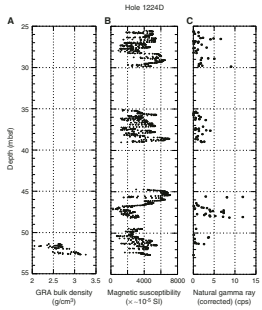

F70. Moisture and density measurements and thermal conductivity measurements with depth, Hole 1224D, p. 137.

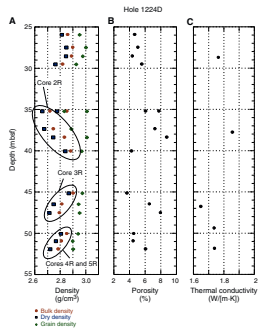

F71. Compressional wave velocity vs. depth, Holes 1224D, 1124E, and 1224F, p. 138.

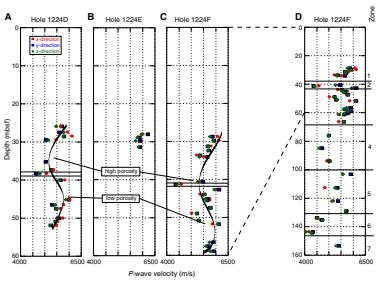

agree with this trend. The porosity of sample B is nearly 9%, and the velocity is low. In contrast to sample B, sample A has medium porosity at 5.6%. The minimum porosity at 3.7% corresponds to a reasonably high velocity of 6000 m/s, which is considered to be representative of unaltered aphyric basalt.

Holes 1224E and 1224F

MST Measurements

In Holes 1224E (Fig. F73) and 1224F (Fig. F74), GRA bulk density and MS were measured every 1.0 cm and NGR was measured every 10 cm.

GRA densities are fairly constant at 1.5 g/cm³ at 8–9 mbsf and 1.65 g/cm³ between 17 and 27 mbsf. This interval corresponds to the soft sediment above basaltic basement (Fig. F73A). Between 27 and 60 mbsf, they remain constant at 2.8 g/cm³ (Figs. F73A, F74A), and below 70 mbsf they are 2.7 g/cm³ (Fig. F74A). Magnetic susceptibilities are ~50 between 5 and 27 mbsf (Fig. F74B). Between 27 and 60 mbsf, they average ~6000–7000 (Figs. F73B, F74B). Between 60 and 140 mbsf, they decrease and remain constant at a low value (Fig. F74B). They rapidly increase, however, below 140 mbsf. Natural gamma radiation intensities decrease between 8 and 9 mbsf, and below 18 mbsf, they remain at fairly constant low values (Figs. F73C, F74C).

Moisture and Density and Thermal Conductivity

Moisture and density properties, such as bulk, dry, and grain densities, water content, and porosity, were measured on individual samples. Bulk densities, grain densities, and porosities are in good agreement between Holes 1224E and 1224F (Figs. F75A, F76A). According to the bulk densities, porosities, and PWS compressional velocities, we divided the combined results into seven depth zones (Fig. F71D): (1) 30–38 mbsf, (2) 38–41 mbsf, (3) 41–61 mbsf, (4) 61–100 mbsf, (5) 100–138 mbsf, (6) 138–147 mbsf, and (7) deeper than 147 mbsf. Porosities for these depth zones are (1) 5%, (2) 10%–15%, (3) 5%, (4) 5%–10%, (5) 5%–10%, (6) 10%–15%, and (7) 5%. The thermal conductivities are constant over the depth range.

Compressional Wave Velocity

PWS velocity was measured on discrete cubic samples. Between 25 and 60 mbsf, PWS velocity on core from Holes 1224E and 1224F has a similar trend to that of Hole 1224D (Fig. F71). PWS velocities have a strong depth dependence. We use the same zoning for compressional velocity as for porosities. Compressional velocities, including seismic velocity anisotropy, in the seven depth zones are (1) 5500–6000 m/s, (2) 4200–5500 m/s, (3) 5000–6000 m/s, (4) 4500–5000 m/s, (5) 4700–6000 m/s, (6) 4000–4700 m/s, and (7) 5500 m/s. Zones 1 through 3 may be characterized as rather uniform basalt flow zones with a thin low velocity (fractured) layer. Zone 4 is characterized by a slightly low velocity zone. Velocities of zone 5 are higher than velocities for zones 4 and 6. Zone 6 is highly fractured, characterized by the lowest velocities. Zone 7 corresponds to more uniform basalt layers.

F72. Compressional wave velocity vs. bulk density and porosity, Hole 1224D, p. 139.

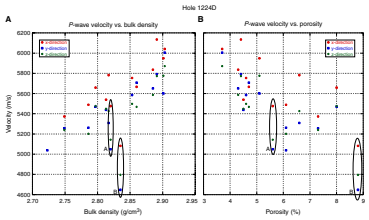

F73. GRA bulk density, MS, and NGR, Hole 1224E, p. 140.

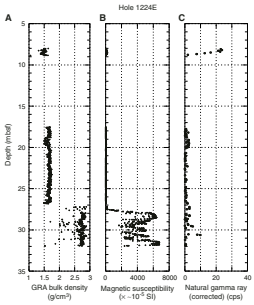

F74. GRA bulk density, MS, and NGR, Hole 1224F, p. 141.

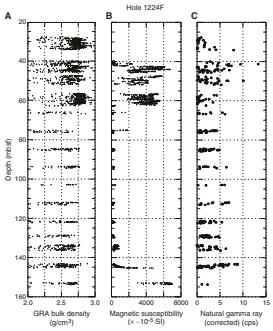

F75. Moisture and density, Hole 1224E, p. 142.

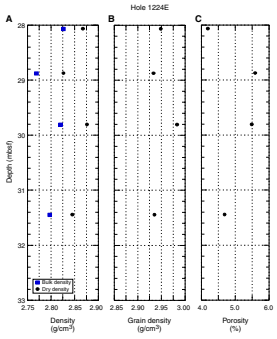

Discussion

Figures F77 and F78 are for Holes 1224E and 1224F, respectively. They show *P*-wave velocity vs. bulk density and *P*-wave velocity vs. porosity. *P*-wave velocities are scattered with increasing bulk density. In general, *P*-wave velocity has a positive correlation with increasing bulk density (e.g., Birch 1960, 1961). *P*-wave velocity vs. porosity, however, has a good inverse correlation, as *P*-wave velocity decreases with increasing porosity. These two relations imply that compressional velocities are less sensitive to bulk density than they are to porosity. Large porosities may be associated with more fractures. If this is true, zones 2 and 6 are intensively fractured.

DOWNHOLE MEASUREMENTS

Operations

Downhole measurements in Hole 1224F (141°58.7567′W, 27°53.3634′N) were made after completion of RCB coring to a total depth (TD) of 174.5 mbsf. The water depth was 4978 mbrf, and sediment thickness was ~28 m in Hole 1224F. Three wireline tool strings were run: the triple combo, the FMS/DSI, and the WST-3 (see **"Downhole Measurements,"** p. 26; Fig. **F14,** p. 57; and Tables **T3,** p. 64, **T4,** p. 65, and **T5,** p. 66, all in the "Explanatory Notes" chapter). For each logging run, the base of the pipe was initially lowered to 49.9 mbsf. As each run was made uphole, the pipe was pulled from 49.9 to 34.5 mbsf to increase the open hole interval for logging. The Lamont-Doherty Earth Observatory (LDEO) Borehole Research Group wireline heave compensator was used for the three logging runs. Prior to logging, Hole 1224F was reamed and flushed of debris. The drill bit was released in the hole, and then the hole was filled with sepiolite mud. The total time used for hole preparation was ~6 hr. Logging operations began at 0530 hr on 20 January and were completed at 1030 hr on 21 January, using a total of 29 hr of rig time.

The first tool string, the triple combo, is 31.5 m long and includes the Hostile Environment Gamma Ray Sonde (HNGS), Accelerator Porosity Sonde (APS), Hostile Environment Litho-Density Tool (HLDT), the Phasor Dual Induction–Spherically Focused Resistivity Tool (DIT-E), and the LDEO Temperature/Acceleration/Pressure (TAP) tool (see **"Downhole Measurements,"** p. 26; Fig. **F14,** p. 57; and Tables **T3,** p. 64, **T4,** p. 65, and **T5,** p. 66, all in the "Explanatory Notes" chapter). The initial depth of the TAP recording was set to start from 4778 mbrf. The depth recording for the TAP tool from the Schlumberger Minimum Configuration Maxis (MCM) system started at 4578 mbrf. Total rig-up time for this run was 2.25 hr. At 1109 hr on 20 January, the bottom of the triple combo tool string reached the mudline at 4978 mbrf and stopped there for 5 min for TAP tool calibration. Then the tool string (TAP tool only) was logged downhole at a speed of 600 m/hr. After the bottom of the hole was reached, the entire tool string was logged uphole at 275 m/hr from TD to the seafloor. The data are of excellent quality, with the exception of one 5-min interval near 138 mbsf where the hole diameter exceeded 17 in and the density and neutron porosity measurements may be unreliable. A shotpoint log was also acquired over the openhole interval. Total rig time for this run was 10.5 hr.

F76. Moisture and density and thermal conductivity, Hole 1224F. p. 143.

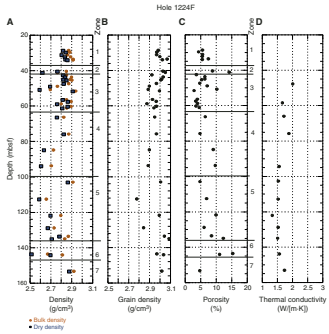

F77. Compressional wave velocity vs. bulk density and porosity, Hole 1224E, p. 144.

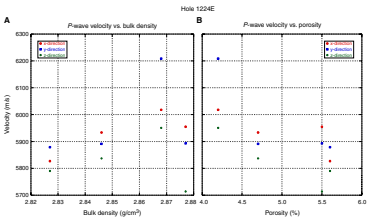

F78. Compressional wave velocity vs. bulk density and porosity, Hole 1224F, p. 145.

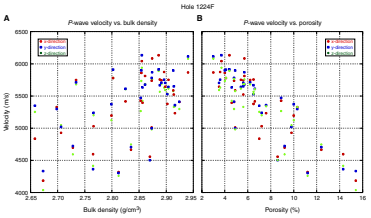

The second tool string, FMS/DSI, includes the DSI, Natural Gamma Ray Spectrometry Tool, and FMS tools and has a total length of 33 m. The FMS/DSI tool string was rigged up starting at 1600 hr on 20 January. When the tool string reached a water depth of ~1000 m, a tool power anomaly occurred and the tool string was immediately brought back to the surface. It was determined that the telemetry cartridge was malfunctional, and a new cartridge was installed. The tool string reached TD at 2320 hr. Three passes of this string were run using the DSI in monopole, dipole, and Stoneley-wave recording modes. Switching between recording modes was accomplished while the tool was downhole. Pass 1 was run uphole at 275 m/hr from TD to the hard rock/sediment interface (27.7 mbsf) to record the data-intensive FMS and DSI lower dipole and monopole *P*-wave and *S*-wave (P&S) modes. Pass 2 was run uphole from TD in open hole, then through the pipe to the hard rock/sediment interface, with the data-intensive cross-dipole mode enabled. Pass 3 was run uphole from TD to the hard rock/sediment interface, with the Stoneley, the upper dipole, and the P&S monopole recording modes enabled. The frequency band is from 80 to 5 kHz for dipole measurements and low-frequency Stoneley acquisition and from 8 to 30 kHz for monopole acquisition. Excellent FMS and compressional and shear waveform data were collected during these three passes. The washout at 138 mbsf apparent on the triple combo caliper reading is not evident on the two FMS caliper readings. A total of 14 hr of rig time was used for the above three passes.

The third tool string is 7 m long and consists of only the WST-3. This was the first test run of the Schlumberger WST-3 in an ODP hole. The WST-3 run was planned to record the zero-offset vertical seismic profiles with a 5-m depth interval between clamping stations. At each receiver station, the WST-3 was to record 6–10 shots with a 1-ms sample interval, a record length of 10 s, and 45 s between shots. A 4.92-L (300 in^3) air gun aboard the *JOIDES Resolution* was used. To maintain a constant depth below the sea surface, the gun was suspended from a buoy and tethered to the aft port crane. Gun depth was set at 5.5 m below the sea surface to obtain the best downward propagating combination of the source and its phase-inverted surface reflection. When the WST-3 tool was in the drill pipe at a water depth of 1057 m, it was clamped to the pipe to conduct a test. The shot time was supposed to be detected by the blast hydrophone suspended 3 m beneath the gun. However, no source signals from either the blast hydrophone or the WST-3 were detected by the SAT. Subsequently, it was found that the blast hydrophone had a faulty circuit; the air gun had a leakage of air; and the WST-3 telemetry was intermittent. The experiment was therefore terminated. The total rig time for this test was 4.5 hr.

Borehole Condition and Log Data Quality

Shipboard analysis of the logs and core descriptions during ODP Leg 200 clearly shows that Hole 1224F consists of definable alternative layers of fresh and fractured and/or altered basalts (breccia and pillows) that correlate to changes in the measured log properties. The logs run during Leg 200 provided high-quality results and can be used to significantly enhance our understanding of the geological settings and the shallow structure of the upper ocean crust at this strategic ODP site in this Pacific region.

A selection of most of the logs acquired in three runs during Leg 200 are presented in Figures **F79, F80, F81, F82,** and **F83.** The interval dis-

F79. Composite log of hole parameters and magnetic field logs, Hole 1224F, p. 146.

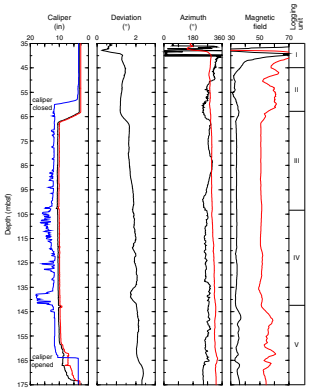

F80. Composite log of temperature, SP, and electrical resistivity logs, Hole 1224F, p. 147.

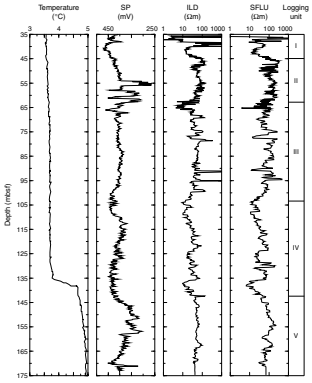

F81. FMS images, Hole 1224F, p. 148.

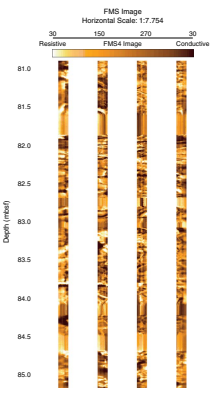

played corresponds to depth in Hole 1224F, from TD (174.5 mbsf) to the base of the pipe (35 mbsf; all in basaltic rocks). The nuclear and sonic logs were also run through the pipe to the seafloor, and repeat passes were made for the FMS/DSI tool string but are not shown. The caliper log from the triple combo run is shown in Figure F79 (Track 1; blue color). The caliper reading changes from 10 to 18 in. However, the measurement of this one-arm caliper is highly nonlinear, and it is directional, generally tracking the major axis of elliptical holes. Two caliper logs from the FMS four pads are also shown in Figure F79 (Track 1; black and red colors) and illustrate two orthogonal dimensions of the borehole as a function of depth. Generally the caliper readings from the FMS tool are much more reliable than the one-arm caliper. The diameter of Hole 1224F varies generally between the bit size ($9^7/_8$ in) and 11 in from the FMS caliper logs. The apparent "washout" or conduit from 138 to 142 mbsf from the directional caliper reading is not identified on the two FMS calipers. The FMS images show that this vertical fracture has a large opening on the northeast part of the borehole wall. The orientation of the calipers with respect to magnetic north (PAZ1 in Track 3) illustrates a relatively constant position of the logging tool as it was pulled uphole. The tool started rotating only when the top of the tool was in the pipe, and the calipers were closed. This is an indication of a very circular borehole without large breakouts, key slots, or elliptical intervals. Small-scale variations in tool rotation are likely related to localized and minor changes in the shape of the borehole.

Figure F79 (Track 2) shows the hole deviation log. In general, Hole 1224F is nearly vertical, having a slightly increasing deviation below the base of the pipe (35 mbsf) to ~2° off vertical at TD. This low angle of hole deviation does not affect the operation of the logging tools. The overall quality of the log data acquired during Leg 200 is excellent.

Magnetic Fields

The three-component acceleration and magnetic field measurements made with the General Purpose Inclinometer Tool (GPIT) of the FMS/DSI tool string are used usually for depth determination and other postcruise log data processing. Both the magnetic field and the magnetic inclination, which are computed from the GPIT log, show elevated values above 67 mbsf and below 142 mbsf (Fig. F79). The boundary at 142 mbsf coincides with the lower boundary of the conduit detected by the triple combo caliper. Both the magnetic intensity and inclination log data between 67 and 103 mbsf and between 103 and 142 mbsf reveal much less variation than those acquired in the upper and lower parts of the hole. The magnetic inclination between 103 and 142 mbsf exhibits a higher variation than that between 67 and 103 mbsf.

Temperature Measurements

The temperature log is presented in Figure F80 (Track 1). The raw temperature data recorded with the LDEO TAP tool (see "Temperature, Acceleration, and Pressure," p. 30, in "Tool Measurement Principles and Applications" in "Downhole Measurements" in the "Explanatory Notes" chapter) are of excellent quality. Although the low-resolution mode was used, it was enough to accurately define the depth (136 mbsf) at which the temperature increased abruptly by ~1°C. The temperature log shows that the temperature between 138 and 142 mbsf remains at a constant temperature of 4.6°C. The temperature steeply de-

F82. Composite log of the density, neutron porosity, and sonic logs, Hole 1224F, p. 149.

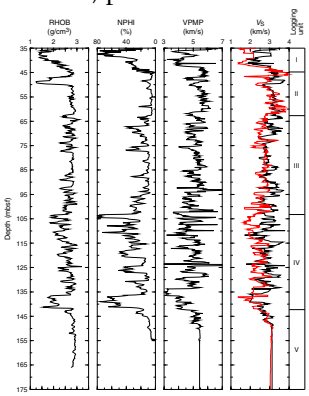

F83. Composite log of the spectral gamma ray logs, Hole 1224F, p. 150.

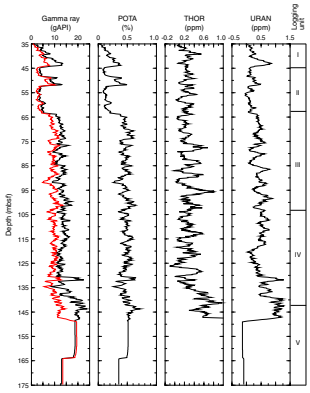

creases to 3.7°C within a 3-m interval from 138 to 135 mbsf, and it then gradually decreases to 3.5°C to the seafloor (only shown up to 35 mbsf). On the other hand, the temperature gradually increases to 5.0°C from 142 mbsf to TD. Combined with the analysis of the caliper logs and the drilling conditions, the temperature log indicates that there is a vertical zone of relatively warm fluid at a temperature of 4.6°C. This vertical zone is 4 m high and corresponds to a vertical fracture oriented in a northeastern direction. Drilling might have enlarged the opening of the fracture (conduit) on the borehole wall. The high-precision GPIT also detected an anomaly at ~142 mbsf. Further analysis is needed to conclude if cool seawater is flowing down Hole 1224F and exiting the borehole through this permeable zone and into the surrounding formation.

The spontaneous potential (SP) log is also shown in Track 2. Although the SP log has been traditionally used to estimate the alternating layers of permeable and impermeable zones, there is no direct relationship between the values of porosity and permeability and the magnitude of the SP deflection. Further analysis will be needed to explain the SP data in Hole 1224F.

Electrical Resistivity Measurements and FMS Images

Electrical resistivity measurements and images were recorded during the first and second logging runs. The deep induction resistivity (IDPH), medium induction resistivity (IMPH), spherically focused log (SFLU), and formation images (FMS) were obtained in Hole 1224F during Leg 200.

Three independent measurements of electrical resistivity were recorded with the DIT-E, which includes the SFLU array. The deep induction resistivity log (ILD) and the SFLU are shown in Figure **F80** (Tracks 3 and 4, respectively). Compared with the resistivity measurements in the oceanic crust in ODP Hole 395A (Shipboard Scientific Party, 1998), the galvanic measurements (SFLU) give readings in the similar range of resistivity for basalts, whereas inductive measurements (IDPH and IMPH) may provide generally lower values, although following closely the same overall profile. This difference is the result of the nature of inductive measurements, where circular current loops are generated in the plane orthogonal to the borehole axis. When used in a vertical hole such as Hole 1224F, the induction tool records the horizontal component of the formation resistivity. In a layered formation, inductive measurements are consequently expected to read lower values than galvanic ones.

The highest values of resistivity correspond to the presence of thin and massive flows at 37, 45, 75, 130, and 155 mbsf, for example. In sections where resistivity values are >100–200 Ωm, the induction measurements may be erroneous because the secondary magnetic field induced by current loops into the rock is not large enough to be picked by the receiving coils. Such erratic measurements are illustrated in the IDPH (ILD) profile at 38, 92, and 95 mbsf in Figure **F80** (Track 3).

The shallow-reaching, centimeter-scale FMS images both lithologic contacts and millimeter-scale fractures (Fig. **F81**). The FMS images show considerably greater resolution of the relative conductivity changes over the interval, and they reflect formation characteristics that are not apparent at the broad scale of the other logs. The alternatively layered structure of fresh and fractured basalts is probably seen on the continuous-image FMS records. For illustration purposes, Figure **F81** shows a 5-m interval of the high-quality FMS images from the entire interval of

Hole 1224F acquired during FMS/DSI Pass 1. Conductive features are imaged with darker color, whereas resistive features are indicated by lighter color. In this figure, for example, sheeted lava flows are between 81.5 and 81.8 mbsf, between 82.6 and 82.8 mbsf, and between 84.4 and 84.6 mbsf.

The FMS record provides continuous structural images of the borehole wall penetrated by Hole 1224F. Above 67 mbsf, the FMS images reveal relatively "smooth" basalts with fewer fractures and fine structures. Core recovery was good (~50%) throughout this interval of massive basalts. Below 67 mbsf and above ~103 mbsf, the FMS images show highly fractured intervals interbedded with sheeted layers 10 cm to 0.5 m thick that have high electrical resistivity values. FMS images between 100 and 142 mbsf show large blocks of electrically resistive fragments against large blocks that are highly conductive and have fewer fractures than the intervals above, which may indicate that this interval mainly consists of less fractured pillow basalts. Below 142 mbsf, rocks become electrically more resistive.

Sonic Measurements

Sonic data were recorded using the DSI during the second logging run with three separate passes of the tool through the open-hole interval. In total, five different modes of the DSI were enabled (see **"Acoustic Velocity,"** p. 31, in "Tool Measurement Principles and Applications" in "Downhole Measurements" in the "Explanatory Notes" chapter) and allowed for acquisition of both compressional and shear waveforms using different acoustic sources. Both high-frequency compressional and shear and dipole shear modes produced excellent quality sonic waveforms. Preliminary data processing for compressional and shear traveltimes was completed on the drill ship using Slowness-Time-Coherence analysis software on the MCM acquisition system (Kimball and Marzetta, 1984). The preliminary results of the compressional wave velocity profile from the monopole source (VPMP) are shown in Figure **F82** (Track 3). The shear wave velocity profiles from the monopole source and the lower dipole are shown in Track 4 (black = monopole and red = lower dipole). The VPMP and dipole shear V_S are raw data converted from the traveltime records. The shear wave velocity data from the monopole that are shown have been edited for the values that are out of the instruments' range. Both the compressional and shear wave velocity data show five logging units: above 45 mbsf (I), 45–63 mbsf (II), 63–103 mbsf (III), 103–142 mbsf (IV), and below 142 mbsf (V). The velocity measurements in the two units above 45 mbsf and from 103 to 142 mbsf have larger variations than the other units. Logging Unit III (63–103 mbsf) has a higher variation than logging Unit II (45–63 mbsf). The average compressional wave velocity is ~4.5, ~5.5, ~5.0, ~4.6, and ~5.4 km/s for the five units from the top to the bottom of the hole, respectively. The average shear wave velocity is ~2.5, ~3.1, ~2.8, ~2.6, and ~3.2 km/s for the five units from the top to the bottom of the hole, respectively. These estimates will be further refined by postcruise studies. Postcruise processing must also be applied to the dipole data to account for dispersion effects. The sonic data from the cross-dipole and the low-frequency Stoneley modes will be further processed postcruise.

Nuclear Measurements

The bulk density (RHOB) of the formation was measured using the HLDT and is displayed in Figure F82 (Track 1). Density values range from 1.25 to ~3.0 g/cm³, and the log shows rapid changes as a function of depth. Low density values are probably related to fractures filled with seawater. The average density value is ~2.0, ~2.8, ~2.6, ~2.5, and ~2.9 g/cm³ for the five logging units from the top to the bottom of the hole, respectively. The differences in RHOB between logging Units II, III, and IV are mainly due to density variations in rocks. The variations increase from logging Units II to IV. Typical values for basalt with no fractures measured on core samples are ~2.95 g/cm³, which are different from the in situ large-scale measurements, especially in breccia and highly fractured rocks. However, the density log readings in Unit V approach typical values.

The APS was used to record the neutron porosity log (NPHI) and is shown in Figure F82 (Track 2). NPHI ranges from 5% to 80%. High values correspond to borehole washouts or fractures and generally correlate with low peaks in the density log. NPHI also exhibits the same overall trends as indicated by density, velocity, and other logs. The average porosity value is ~40%, ~5%, ~15%, ~30%, and ~5% for the five logging units from the top to the bottom of the hole, respectively. The porosity log also shows a transition zone between 95 and 103 mbsf, which is apparent in the velocity logs.

The spectral gamma ray logs (Fig. F83) were measured using the HNGS tool (see "Natural Radioactivity," p. 28, in "Tool Measurement Principles and Applications" in "Downhole Measurements" in the "Explanatory Notes" chapter). The total spectral gamma ray (HSGR; Track 1; black) varies between 2 and 30 gAPI in Hole 1224F. The HSGR, the computed gamma ray (HCGR; Track 1; red), and the potassium content (POTA) also show a strong correlation in the pillow basalts and flows, indicating that most of the natural radioactivity is caused by the potassium rather than the thorium or uranium decay series. Potassium is enriched in oceanic basalts during low-temperature oxidative alteration, thus, HSGR and POTA logs are good indicators of alteration. In the vicinity of the zone of relatively warm fluid between 138 and 142 mbsf, all the natural radioactive elements show elevated values.

Lithostratigraphy

Based on shipboard preliminary log analysis at this site during Leg 200, we conclude that Hole 1224F consists of five distinct logging units: above 45 mbsf (I), 45–63 mbsf (II), 63–103 mbsf (III), 103–142 mbsf (IV), and below 142 mbsf (V). These layered formations can be distinguished using the continuous electrical resistivity, density, sonic, neutron porosity, magnetic field, and possibly spectral gamma ray logs, as presented by the analysis above. The existence of a relatively warm zone or large-scale fracture between 138 and 142 mbsf was detected by all the log tools including the temperature tool. In addition, the temperature tool reveals that the relatively "warm" fluid had a temperature of 4.6°C at the time of the logging. The vicinity of this zone is much more highly altered than other rocks penetrated by the hole, which is indicated by the gamma ray logs. Because of the relative position of the tools located in the tool strings, some tools can resolve the top logged intervals like gamma ray, porosity, density, and sonic logs. On the other hand, the resistivity tools and FMS placed at the bottom of the tool

string can resolve the formation properties near the bottom of the hole. The values of the magnetic fields measured by the GPIT cannot be used for tool orientation near the bottom of the pipe (~35 mbsf) because of the large field produced by the pipe. In the logged intervals where all the tools overlapped, they provide consistent information to support the layered structural units based on these geophysical properties.

3.5-kHz DEEP-SOURCE EXPERIMENT

Objective

Site 1224 has a varying sediment cover draped on basaltic basement. A minimum of 10 m of sediment is needed to set a reentry cone and case a hole. Determining the sediment cover acoustically before spudding-in facilitates the determination of a suitable site.

Reflections from sediment interfaces beneath the seafloor are commonly observed on echo sounder recorders using transducers in the range of 1 to 5 kHz. These returns can come from a variable area depending on the roughness of the seafloor and the acoustic interfaces beneath it. For this reason, in deep water the lateral extent of the subseafloor reflections observed is not definable for soundings made from a ship. To reduce the area insonified, the sounding transducer can be lowered near the seafloor, thereby permitting a better determination of the sediment thickness and the lateral extent of seafloor reflectors at the specific drill site.

Experiment

The *JOIDES Resolution's* VIT frame is used to visually survey the seafloor preparatory to spudding-in and to reenter holes fitted with a reentry cone. To estimate the sediment cover at the sites selected, a pinger was lowered on the VIT frame. The pinger was an ORE Accusonic model 263, consisting of a 4.252-kHz transducer interconnected with a 5-in × 33-in-long pressure housing containing a battery pack, storage capacitor, and electronics. This free-running pinger produced a 2-ms pulse at a repetition rate of one per second. To distinguish it from other sonic devices, each ninth ping was skipped.

The direct water wave arrival and the seafloor reflections were received on the ship's 3.5-kHz echo sounder and displayed ungated on an EPC Labs model 9802 graphic recorder running at a 1-s sweep. During the period when the pinger was within 40 m of the seafloor, a digital recording (12 bit, 12,000 samples per second) was made. The data window was 250 ms beginning with the direct arrival.

Observations

Figure F84 shows deep-source records collected during the installation of the reentry cone and casing in Hole 1224D. The records shown cover the period 2118 to 2215 hr on 2 January. (All times in this section are given in UTC, which equals local time + 9 hr.) Five traces are shown. The upper one is the direct water wave arrival from the pinger to the ship's 3.5-kHz transducer. The second trace is the reflection from the reentry cone that is hung from the drill string. At the start of the recording, the VIT frame and pinger are 19 ms (14 m) above the reentry cone. The third, less intense trace is the seafloor reflection. The reentry cone

F84. Reentry cone and steel casing, Hole 1224D, p. 151.

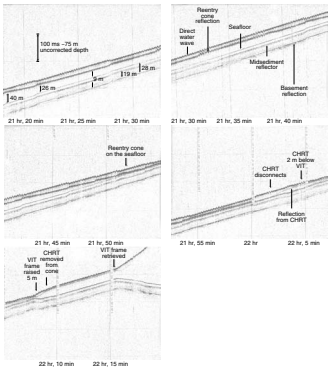

is 40 m above the seafloor. Compared with the measurements made while the VIT frame was farther above the seafloor, the amplitude of the seafloor reflection is reduced, apparently because of the shadowing of the reentry cone. The fourth and fifth traces are reflections from interfaces beneath the seafloor. The first is 12 ms (~9 m, assuming a compressional wave velocity of 1.50 km/s) below the seafloor and of comparable intensity to that of the seafloor reflection. The second is 25 ms beneath the first (or 38 ms below the seafloor) and is more reverberant. Assuming a compressional wave velocity of 1.55 km/s for the material between the two reflections, the third reflection would be an interface ~19 m beneath the first (or 28 mbsf). No deeper reflecting interfaces were identified.

The horizontal lines are 100-ms traveltime marks. The vertical lines are 5-min marks. The clock in the pinger ran 11 ms/min faster than the shipboard recorder resulting in the drift of the traces across the recording. Thrusters 3 and 4, on the port side of the ship, and the 3.5-kHz transducer pod on the keel are abeam of each other at ship frame 43. The discharge of these thrusters when pushing the ship to port crosses the 3.5-kHz transducer pod, creating noise.

At ~2121 hr (Fig. **F84**), the bottom of the casing, 26 m below the cone, touches the seafloor, and the jetting-in begins. The reflections from the reentry cone and the seafloor gradually converge, and at ~2152 hr the two traces merge, indicating that the reentry cone is sitting on the seafloor. At this point, the drill string is rotated, disconnecting the casing hanger running tool (CHRT) from the cone and casing. At 2202 hr, the drill string is raised, lifting the CHRT out of the cone. A weak reflection from the CHRT can be identified. At 2205 hr, the CHRT is raised to 2 m below the VIT frame. At 2208 hr, the VIT frame is raised 5 m, and at 2209 hr, the CHRT is raised the same amount. At 2215 hr, retrieval of the VIT frame begins, and the reflection trace of the CHRT fades as the distance from the VIT frame increases.

Conclusions

Some conclusions based on preliminary analysis are as follows:

1. The deep-source recording shows the emplacement of the reentry cone. It corroborates the video imagery that the placement was as planned.
2. Two subseafloor reflecting interfaces were identified that were subsequently drilled. Based on the changes in acoustic impedance indicated by the two reflections, the following stratigraphic spacing is suggested:
   a. The 13-ms interval between the seafloor and the first subsurface reflection corresponds to the 9 m of unconsolidated yellow to brown clay cored. We assume that the sound velocity of this material is near that of water.
   b. The 25-ms interval between the first and second subseafloor reflectors corresponds to a somewhat more consolidated sedimentary sequence ~19 m thick. There was little core retrieved from this interval.
   c. Basaltic basement is an irregular surface at a depth of ~28 mbsf. Using the 3.5-kHz hull-mounted source, the basement reflector could be identified at the junction box but not at the drill site (Fig. **F2**). At the drill site, the basement reflector was only identified with the deep source.

CORE, PHYSICAL PROPERTIES, LOGGING, AND SEISMIC CORRELATION

Coring was conducted in six holes at Site 1224, with the deepest hole (1224F) being the only hole logged. In Hole 1224F, we penetrated to 174.5 mbsf, cored through 146.8 m, and recovered 37.7 m of core with 25.68% core recovery. With this poor recovery, which is common for oceanic basalts, a detailed correlation among physical properties data, core analysis, logging data, and surface seismic data is required to understand a range of geological and geophysical issues at Site 1224. Basaltic basement at Site 1224 is overlain by ~28 m of soft sediment.

Sedimentary Section

Sediment was recovered from Holes 1224A, 1224B, 1224C, and 1224E with significant recovery only in Holes 1224C and 1224E (Fig. F97). Two distinct shallow reflectors were identified at 13 and 38 ms two-way reflection times by both underway and on-site 3.5-kHz seismic surveys (Fig. F2). Although the deeper reflector corresponds to the top of the basaltic layer at 28 mbsf, the shallower one seems not to be a simple lithologic boundary. If we assume that the compressional velocity of the sedimentary layer is 1500 m/s, the depth of the shallower reflector corresponds to 9.75 mbsf. Based on physical properties measurements on cores, the GRA bulk densities decrease with increasing depth from 1.7 g/cm^3 to 1.3 g/cm^3 between 2 and 6.4 mbsf. The PWL compressional wave velocity is constant at ~1480 m/s in this interval (see **"Compressional Wave Velocity,"** p. 46, in "Hole 1224C" and **"Compressional Wave Velocity,"** p. 48, in "Holes 1224E and 1224F" both in "Physical Properties"). In addition, porosities increase from 70% to 80% between 0.5 and 6.2 mbsf. This result is very different from ordinary velocity vs. density and velocity vs. porosity relations that are positive and negative trends, respectively. The density and porosity should increase and decrease with depth, respectively, if compaction of sediments by overburden pressure is applied. The description of microfossils indicates the presence of abundant radiolarians between 4 and 8–9 mbsf or a little deeper (Fig. F85). The radiolarians are barren in the dark-brown clay/silty clay layer below 8–9 mbsf. Correlating these results and the on-site 3.5-kHz seismic reflection records, a lithologic boundary with a physical property discontinuity is present at 8–9 mbsf. Because of poor core recovery, the depth of 8–9 mbsf can be shifted to a little deeper depth.

In the Barbados accretionary prism, the three-dimensional seismic survey found a seismically bright reflecting plane, which was interpreted as a décollement. During Leg 171, a radiolarian abundant layer with a high pore fluid pressure, a high ratio of smectite/illite, and a large methane concentration was found in the décollement zone (Moore, Klaus, et al., 1998; Moore, 2000). In the Barbados case, the thickness of the décollement was ~20 m. Considering this result, the shallow seismic reflector at 13 ms two-way traveltime (Fig. F2) corresponds to a similar layer with high pore-fluid pressure, although the thicknesses in the two cases are quite different. Phillipsite, which is in the zeolite group, was also found at a depth >6 mbsf in Section 200-1224A-4X-CC and Core 200-1224E-R1. Zeolite is a low-grade metamorphic mineral that may have been deposited in the high pore-fluid pressure zone at 8–9 mbsf. This shallow reflector was also identified at the

F85. Radiolarians, Hole 1224C, p. 152.

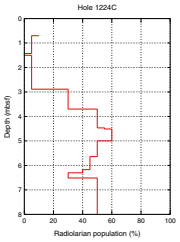

junction box of the H2O Site, 1.5 km from Site 1224 in the 3.5-kHz seismic reflection records (Fig. F2). This suggests a broad distribution of this shallow interface around Site 1224. There are no logging data for the sedimentary layer as usual because the depth is too shallow.

Basaltic Layer

Below 28 mbsf, a basalt layer was drilled in Holes 1224A, 1224D, 1224E, and 1224F. Hole 1224D was drilled for the purpose of installing broadband borehole seismometers in the future. Holes 1224D, 1224E, and 1224F are within a 15-m distance, with Holes 1224E and 1224F being <1 m apart (Fig. F3).

Although the lithologic description identified massive basalt flows and pillow basalts (Fig. F48), one-to-one correlation between logging and physical properties to the petrographical description is difficult because of the differences in the nature of the observations.

The triple combo and FMS/DSI tools were used in logging. We identified five distinct logging units in basement at 28–45 mbsf (Unit I), 45–63 mbsf (Unit II), 63–103 mbsf (Unit III), 103–142 mbsf (Unit IV), and below 142 mbsf (Unit V) by logging with the triple combo tool string, which includes NPHI, RHOB, resistivity, and caliper measurements (Fig. F86). Logging with the triple combo tool string extended uphole to 40 mbsf. Between 40 and 63 mbsf, a low-porosity and uniform layer is identified, although bulk density values are anomalous. In this depth range, porosity is a few percent and bulk density is ~2.75 g/cm^3 with a small variation. The caliper was closed in this depth range. The layer between 63 and 103 mbsf has 2.75 ± 0.25 g/cm^3 bulk density and 10%–30% porosity. Resistivity for this zone varies considerably about the average of ~90 Ωm. The hole size is approximately steady at 12 in. At 136 mbsf, porosity and bulk density logs have a significant variation. Between 103 and 136 mbsf, the hole size changes from place to place. Bulk densities are 2.6 ± 0.4 g/cm^3, which suggest highly heterogeneous layers. The porosities have an extremely large variation between 20% and 80%. The resistivities also vary considerably. All logging parameters indicate highly heterogeneous and/or fractured layers. At the depth range between 136 and 142 mbsf, the hole size reaches to 17 in, corresponding to the maximum extent of the caliper arms. The temperature measurements indicate a sharp change at 136 mbsf (see "Temperature Measurements," p. 51, in "Downhole Measurements"). The temperatures below and above 136 mbsf were 4.9° and 4.0°C, respectively. This suggests that at 136–142 mbsf there is likely to be some kind of boundary such as a highly fractured layer for the fluid flow. Although usually the broadening of the caliper diameter suggests a washed-out hole, this broadening of hole size might be related to lithologic characteristics. Below 142 mbsf, all parameters are quite stable and indicate the presence of a homogeneous hard rock zone.

PWS compressional measurements (Fig. F87) identified seven major physical properties zones: (1) 30–38 mbsf, (2) 38–41 mbsf, (3) 41–61 mbsf, (4) 61–100 mbsf, (5) 100–138 mbsf, (6) 138–147 mbsf, and (7) below 147 mbsf. Zone 2 is very thin. In zones 1 and 3, compressional velocities were ~5700 ± 500 m/s. Zone 2 has velocities as low as 4500 m/s that suggest weak fractures or low porosities. The character of zone 4 is quite different between log and physical properties. Although the PWS velocities for zone 4 are 4600–5100 m/s, suggesting higher porosity or fracturing, logging gives higher bulk densities, indicating less fracturing. Zone 5 also has differences between log and physical properties.

F86. Logging data, Hole 1224F, p. 153.

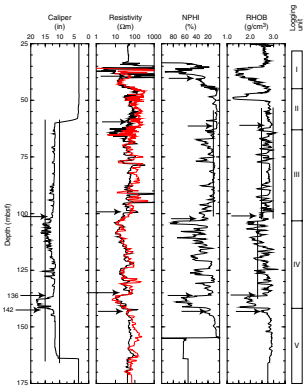

F87. PWS measurements, Hole 1224F, p. 154.

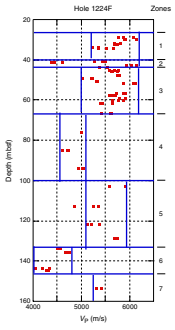

The logging data (Fig. F86) suggest a fractured zone, but the PWS velocity is 5500 ± 500 m/s. The discrepancies can be explained by the scale effect because logging measures at the meter scale and physical properties of rock specimens measure at the centimeter scale. This can be explained by the petrological observation below. The sharp boundary at ~150 mbsf indicates extremely low compressional velocities such as 4000–4700 m/s as measured by the PWS compressional velocity. This zone corresponds to the anomalous caliper zone in the logging. Below 150 mbsf, the PWS compressional velocity increases to 5500 m/s. Using the PWS compressional velocity measurements, a velocity-depth model was generated (Fig. F88).

Physical properties measurements and logging indicate several major lithologic units from the viewpoint of physical parameters. XRD analysis (see "X-Ray Diffraction Investigation of Secondary Minerals," p. 37, in "Geochemistry") indicates five minerals other than ordinary basalt component minerals in veins: calcite, zeolite, smectite, aragonite, and quartz (Fig. F48). Surprisingly, the zones with these minerals are similar to the zones defined by logging and physical properties measurements. Smectite was found in the veins between 28 and 46 mbsf and between 102 and 136 mbsf. Calcite was found in the veins between 50 and 102 mbsf and at 143 mbsf. Zeolite was found at 102 and 143 mbsf, which roughly equals the boundary identified by logging and physical properties measurements. Quartz was identified at 44 mbsf, which is the depth of the smectite extinction and the depth where calcite veins are absent. There are some discrepancies ~45 and 60 mbsf because of sparse sampling intervals. In the depth range from 100 to 140 mbsf, 5- to 10-cm-diameter pieces of rock were recovered. Many of these rocks have chilled margins with glass rims. The small amount of the recovered rocks and the presence of chilled margins suggest that the layer between 100 and 140 mbsf is a pile of small-scale pillow lavas with a minor amount of hyaloclastites. A stack of 10-cm-scale pillows and/or hyaloclastites can explain the observations of high porosity and low bulk density values obtained by logging and the low velocity values obtained by physical properties measurements.

Smectite is stable at temperatures lower than 150°C, and zeolite is a mineral group of low-grade metamorphism. If the layer between 100 and 140 mbsf is highly permeable, seawater can easily flow into this layer and smectite could result from this water flow. The shallowest layer above 136 mbsf may allow the penetration of seawater and low-temperature alteration. The discontinuous temperature change at ~136 mbsf may be explained by the presence of a high–pore fluid layer caused by fractures.

F88. Compressional wave velocity model, p. 155.

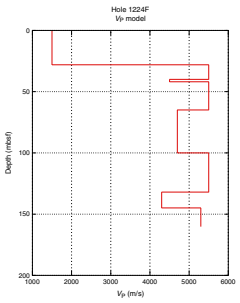

SEISMIC RESULTS FROM THE HAWAII-2 OBSERVATORY

Drilling at the H2O site provides a unique opportunity to observe drilling-related noise from the *JOIDES Resolution* on a seafloor seismometer in the frequency band of 0.1–80 Hz. (See "Hawaii-2 Observatory," p. 2, in the "Leg 200 Summary" chapter for background material on H2O and the retired AT&T oceanic cable that is used to provide continuous, real-time data transmission back to the Makaha cable station on Oahu.)

The University of Hawaii operates an OBSS composed of a Guralp CMG-3T three-component broadband seafloor seismometer and a conventional 4.5-Hz three-axis geophone at H2O (Duennebier et al., 2000, 2002). Data are acquired continuously and are made available to scientists worldwide through the IRIS Data Management Center in Seattle. During the cruise, Jim Jolly and Fred Duennebier at the University of Hawaii relayed sample data files to the *JOIDES Resolution* by FTP via satellite communication. We were then able to process data and study correlations with on-site activities and weather. The University of Hawaii also maintained a Web site showing seismic data from H2O during the cruise (**www.soest.Hawaii.edu/H2O/**).

All of the data we show here are from the conventional 4.5-Hz three-axis geophone in digital counts. Sensitivity and transfer functions to get output in ground motion units were not applied. All times in this section are given in UTC, which is equal to local time + 9 hr. Occasionally days are represented by the Julian day, the consecutive number of the day in the year.

The objective of this report is to present an overview of the seismic behavior and some of the natural and man-made noise sources at the site. For more information on seismic ambient noise levels in the ocean see Webb (1998); for an introduction to earthquake seismology see Lay and Wallace (1995).

Sea State

Figure **F89** shows a vertical component spectrogram for the 1-week period from 22 to 28 December (Julian days 356 to 362). A spectrogram is a display of energy levels as a function of frequency vs. time. In this case the frequency range of interest is 0.1–10 Hz. In this band, sea state (the gravity waves on the surface of the ocean) is the dominant source of ambient noise.

It has been shown that the microseism peak, the broad vertical red band at frequencies from 0.2 to 0.3 Hz, is created by nonlinear wave-wave interaction of surface gravity waves (Longuet-Higgins, 1950). This peak is a ubiquitous feature on all terrestrial seismograms and is observed at stations deep within the continents. It is interesting to note that the amplitude of this peak is not dramatically greater for seafloor stations than for some land stations.

This spectrogram also shows two and a half storm cycles. These are the broad red bands that slope upward to the left from ~1 to 0.2 Hz over 1.5 to 2 days. They terminate at the microseism peak. The model for this phenomenon is a steady wind creating local waves. Imagine the wind blowing steadily over a calm sea. Initially small waves with short wavelengths and relatively high frequencies are generated by the wind. As the wind continues to blow the waves get larger, longer in wavelength, and lower in frequency. Often, the intervals when the *JOIDES Resolution* was WOW correspond to the later times in the evolution of this noise.

Sediment Resonances

The thin, constant-frequency red bands near 1.1 and 2.3 Hz in Figure **F89** correspond to resonances in the thin sediment cover at this site (Zeldenrust and Stephen, 2001). These bands are another ubiquitous feature observed on seafloor seismometers either on or in sediment layers. Their frequency will depend on the sediment thickness and velocity

F89. Ambient noise levels on the vertical component of the H2O seafloor seismometer, p. 156.

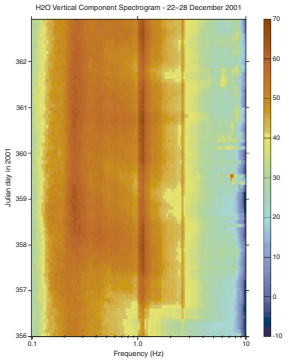

structure local to the station, but for a given station the frequencies are constant. The resonances are observed as bands in the ambient noise field and as ringing after impulsive signals. More resonant frequencies are apparent in the horizontal (x) component spectrogram (Fig. F90). A complete explanation for the frequency and relative amplitude of these resonances is still in progress. The major reason for installing broadband seismometers in boreholes on the seafloor is to attenuate the effects of these sediment resonances. Ambient noise spectra from the OSN pilot experiment (Figs. F24, F25) show that these resonances are much more pronounced on the seafloor and shallow buried sensors than on the borehole sensor.

Whale Song

Whales are a biological seismic source. Figure F91 shows a sample of a whale song as we arrived at Site 1224 on 26 December. This figure shows a time history of the vertical component of seafloor acceleration in 30-s segments for 2.5 min near 1550 UTC on 26 December. The largest-amplitude events are whale songs occurring in wave packets of four wavelets about once every 30 s. The four wavelets, separated by 3 to 7 s, correspond to the sound traveling directly from the whale to the seafloor plus multiple bounces (echoes) of the sound in the water column.

Figure F92 is formatted similarly to Figure F91 but covers a 25-min time interval. Water gun arrivals (see "Water Gun," p. 61) are observed in the first 10 min. The rest of the time series is punctuated with whale calls, except for the two bands of three traces each shown in red. A characteristic feature of the whale songs is that they stop every 15 to 20 min while the whale breathes. In this case, the whale sings for 15 min, takes a breath for 1.5 min, and then repeats the process.

Water Gun

Figure F92 shows the last 10 min of the water gun shooting that we conducted as we approached the site on 26 December. The gun was fired every 10 s. The intermediate-amplitude event ~6 s after the primary event is the water multiple. Note that the repetition rate, amplitude, and frequency content of the water gun and whale song are remarkably similar.

Earthquakes

The principal motivation behind drilling at the H2O is to provide a high-quality seismic station for the Global Seismic Network. Some small earthquakes did occur while we were on site. A quick and easy way to scan all of the data continuously is to display root-mean-square (RMS) energy levels in one-octave bands as a function of time. An example for the horizontal (x) component on 7 January is shown in Figure F93. In this example, most of the variability during the day is occurring in the octave centered at 8 Hz. The major event occurring between 10 and 15 hr is a drilling-related effect discussed below. The large peaks near 5 and 20 hr can be identified as earthquakes.

Time series and spectra for the event near 21 hr are shown in Figure F94 The event has a duration of ~20 s and has a broad frequency content. Note that the energy level of the microseism peak near 1 Hz does

F90. Ambient noise levels on the horizontal component of the H2O seafloor seismometer, p. 157.

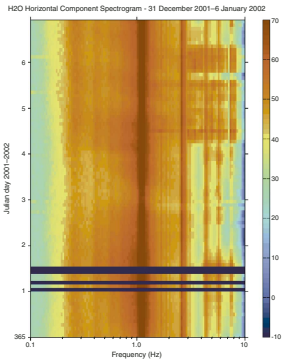

F91. Whale songs, p. 158.

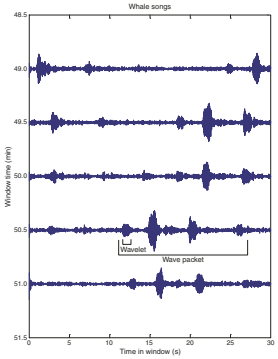

F92. Similarity between water guns and whale songs, p. 159.

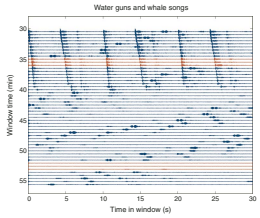

F93. RMS levels in octave bands on 7 January, p. 160.

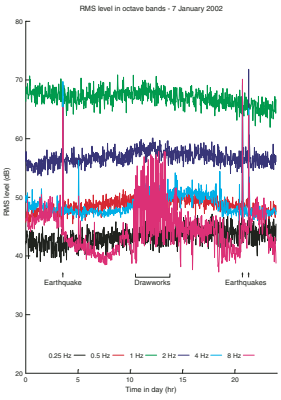

not increase with the arrival. The energy level of the sediment resonances near 2.8, 4.1, and 5.7 Hz, however, increases by up to 20 dB (a factor of 10 in amplitude).

A second earthquake example is shown in Figure F95. The arrival in this case is spread over a longer time interval, and there is no detectable energy below the microseism peak.

Passing Ships

Shipping is a major man-made source of noise in the ocean. Figure F96 shows an RMS summary of the horizontal (x) component for 25 December. The RMS level in the octave centered at 8 Hz increases by 40 dB from 5 to ~12 hr and decreases again at ~15 hr. This event can also be seen in Figure F89 halfway through 25 December (Julian day 359) near 8 Hz. This event is characteristic of a large ship approaching and then leaving the site. The energy is focused near 8 Hz, which is an indication of some type of machinery. This is a very large sound source. If the ship passed directly over the site traveling at ~20 kt, it was affecting noise levels at the station while it was 200 km away. (The large-amplitude peaks in the other frequency bands are an artifact of the processing.) The passage of a container ship bound for Honolulu on 25 December traveling at 17 kt was confirmed by the bridge (P. Mowat, pers. comm., 2001).

In contrast, the *JOIDES Resolution* is much quieter in this frequency band. While the *JOIDES Resolution* steamed directly over the site and we fired the water gun at 1500 UTC on 26 December, the RMS level in the 8-Hz octave increased <10 dB.

Drilling Effects

Without further processing, some drilling-related activities can be identified at the seismic station. In Figure F89, for example, the yellow blotches between 2 and 9 Hz on 26–28 December (Julian days 360 through 362) show some correspondence to drilling activity. The bright yellow band at almost exactly 6 Hz in the second half of 27 December (Julian day 361) corresponds to running pipe and is likely the noise of the drawworks. Drawworks noise is also seen between 1000 and 1500 hr on 7 January (Fig. F93). In Figure F90, the high-amplitude (red) regions from 1 to 9 Hz on 4 and 5 January correspond to drilling with the RCB bit.

On 11 January, drilling progress was slow, and we pulled the pipe to see what was wrong. The bit had fallen off in the hole during drilling. Figure F97 shows the noise record at the H2O seismometer (1.5 km away) during this critical period. From 0 to 4 hr the noise levels are typical for the 14¾-in bit. The dropout at 0400 hr occurred when drilling was stopped to circulate a pill. Excessive torque was observed at ~0500 hr, and the pipe was picked up (the weight on bit was zero) at 0620 hr. At 0800 hr there was a pressure drop, but the dramatic change in noise levels between the 4- and 8-Hz octaves occurred at ~0930 hr. We infer that 0930 hr is when the bit broke off the end of the pipe.

Future Work

Because of the cost of transmitting the data files to the ship, we only looked at a small subset of the available data. The primary data aboard ship were horizontal (x) component only. By comparing the samples in

F94. Time series and PSD diagrams for the last earthquake, p. 161.

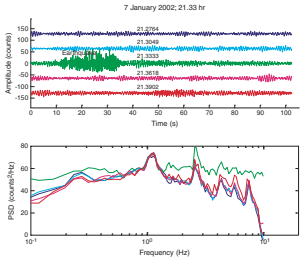

F95. Time series and PSD diagrams for the first earthquake, p. 162.

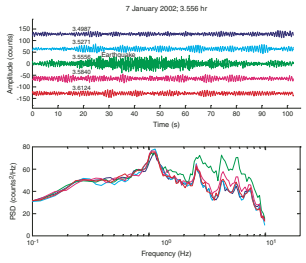

F96. RMS levels in octave bands on 25 December, p. 163.

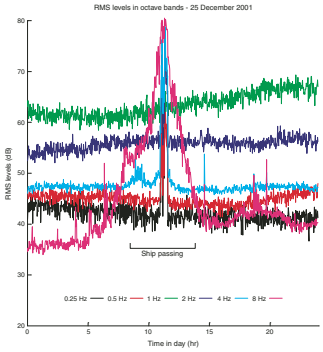

F97. RMS levels in octave bands during bit failure on 11 January, p. 164

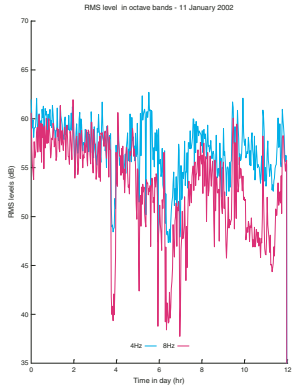

Figures F89 and F90 one can see that there are significant differences between horizontal and vertical components. For most intervals the "day files" had been decimated from 160 to 20 samples per second, so high-frequency (9–70 Hz) studies could only be conducted over very small time intervals such as that of the water gun shooting shown in Figure F92. Furthermore, we only used geophone data. By using data from the Guralp sensor, we can extend the analysis to frequencies below the microseism peak (down to 0.01 Hz).

REFERENCES

Acton, G.D., and Gordon, R.G., 1994. Paleomagnetic tests of Pacific plate reconstructions and implications for motion between hotspots. *Science,* 263:1246–1254.

Alt, J.C., Kinoshita, H., Stokking, L.B., et al., 1993. *Proc. ODP, Init. Repts.,* 148: College Station, TX (Ocean Drilling Program).

Atwater, T., 1989. Plate tectonic history of the northeast Pacific and western North America. *In* Winterer, E.L., Hussong, D.M., and Decker, R.W. (Eds.), *The Eastern Pacific Ocean and Hawaii*. Geol. Soc. Am., Geol. of North America Ser., N:21–72.

Atwater, T., and Severinghaus, J., 1989. Tectonic maps of the northeast Pacific. *In* Winterer, E.L., Hussong, D.M., and Decker, R.W. (Eds.), *The Eastern Pacific Ocean and Hawaii*. Geol. Soc. Am., Geol. of North America Ser., N:15–20.

Birch, F., 1960. The velocity of compressional waves in rocks to 10 kilobars, 1. *J. Geophys. Res.,* 65:1083–1102.

————, 1961. The velocity of compressional waves in rocks to 10 kilobars, 2. *J. Geophys. Res.,* 66:2199–2224.

Bralower, T.J., and Mutterlose, J., 1995. Calcareous nannofossil biostratigraphy of Site 865, Allison Guyot, Central Pacific Ocean: a tropical Paleogene reference section. *In* Winterer, E.L., Sager, W.W., Firth, J.V., and Sinton, J.M. (Eds.), *Proc. ODP, Sci. Results,* 143: College Station, TX (Ocean Drilling Program), 31–74.

Berggren, W.A., Kent, D.V., Aubry, M.-P., and Hardenbol, J., 1995. Geochronology, time scales and global stratigraphic correlation: unified temporal framework for an historical geology. *In* Berggren, W.A., Kent, D.V., Aubry, M.-P., and Hardenbol, J. (Eds.), *Geochronology, Time Scales and Global Stratigraphic Correlation*. Spec. Publ.—Soc. Econ. Paleontol. Mineral., 54:v–vi.

Bukry, D., and Bramlette, M.N., 1970. Coccolith age and determinations Leg 5, Deep Sea Drilling Project. *In* McManus, D.A., and Burns, R.E., et al., *Init. Repts. DSDP,* 5: Washington (U.S. Govt. Printing Office), 487–494.

Butler, R., 1995a. The Hawaii-2 Observatory: a deep-ocean geoscience facility reusing the Hawaii-2 telephone cable. *In* Purdy, G.M., and Orcutt, J.A. (Eds.), *Broadband Seismology in the Oceans—Towards a Five-Year Plan:* Washington, D.C. (Joint Oceanographic Institutions), 50–58.

————, 1995b. Proposed station locations and rationale for the OSN component of GSN. *In* Purdy, G.M., and Orcutt, J.A. (Eds.), *Broadband Seismology in the Oceans—Towards a Five-Year Plan:* Washington, D.C. (Joint Oceanographic Institutions), 20–25.

Cande, S.C., and Kent, D.V., 1992. A new geomagnetic polarity time scale for the Late Cretaceous and Cenozoic. *J. Geophys. Res.,* 97:13917–13951.

————, 1995. Revised calibration of the geomagnetic polarity timescale for the Late Cretaceous and Cenozoic. *J. Geophys. Res.,* 100:6093–6095.

Carson, B., Becker, K., Purdy, G.M., Wilkens, R., Gieskes, J., and Hildebrand, J., 1996. *BOREHOLE—A Plan to Advance Post-Drilling, Subseafloor Science:* Washington, D.C. (JOI/USSAC).

Chave, A.D., Butler, R., Pyle, T.E. (Eds.), 1990. *Workshop on Scientific Uses of Undersea Cables*. Washington, D.C. (Joint Oceanographic Institutions).

Chave, A.D., Green, A.W., Jr., Evans, R.L., Filloux, J.H., Law, L.K., Petitt, R.A. Jr., Rasson, J.L., Schultz, A., Spiess, F.N., Tarits, P., Tivey, M., and Webb, S.C., 1995. *Report of a Workshop on Technical Approaches to Construction of a Seafloor Geomagnetic Observatory:* Woods Hole, MA (Woods Hole Oceanographic Institution).

Collins, J.A., Vernon, F.L., Orcutt, J.A., Stephen, R.A., Peal, K.R., Wooding, F.B., Spiess, F.N., and Hildebrand, J.A., 2001. Broadband seismology in the oceans: lessons from the Ocean Seismic Network pilot experiment. *Geophys. Res. Lett.,* 28:49–52.

Cragg, B.A., Parkes, R.J., Fry, J.C., Weightman, A.J., Rochelle, P.A., and Maxwell, J.R., 1996. Bacterial populations and processes in sediments containing gas hydrates (ODP Leg 146: Cascadia Margin). *Earth Planet. Sci. Lett.,* 139:497–507.

Davis, E.E., Becker, K., Pettigrew, T., Carson, B., and MacDonald, R., 1992. CORK: a hydrologic seal and downhole observatory for deep-ocean boreholes. *In* Davis, E.E., Mottl, M.J., Fisher, A.T., et al., *Proc. ODP, Init. Repts.,* 139: College Station, TX (Ocean Drilling Program), 43–53.

Dick, H.J.B., and Mével, C., 1996. *The Oceanic Lithosphere and Scientific Drilling into the 21st Century:* Woods Hole, MA (ODP-InterRidge-IAVCEI).

Duennebier, F.K., Butler, R., Chave, A., Harris, D., Jolly, J., and Babinec, J., 2000. Broadband seismograms from the Hawaii-2 Observatory [paper presented at Am. Geophys. Union Mtg., San Francisco, Fall 2000.]

Duennebier, F.K., Harris, D.W., Jolly, J., Babinec, J., Copson, D., and Stiffel, K., 2002. The Hawaii-2 Observatory seismic system. *IEEE J. Oceanic Eng.,* 27:212–217.

Forsyth, D., Dziewonski, A., and Romanowicz, B., 1995. Scientific objectives and required instrumentation. *In* Purdy, G.M., and Orcutt, J.A. (Eds.), *Broadband Seismology in the Oceans—Towards a Five-Year Plan:* Washington, D.C. (Joint Oceanographic Institutions), 8–18.

Foucher, J.-P., Harmegnies, F., Floury, L., Lanteri, N., and Henry, P., 1995. Long-term observation and testing in boreholes: the ODP Leg 156 experiment. *In* Montagner J.-P., and Lancelot, Y. (Eds.), *Multidisciplinary Observatories on the Deep Seafloor:* Marseille (INSU/CNRS), 109–110.

Hamilton, E.L., 1976. Variations of density and porosity with depth in deep-sea sediments. *J. Sediment. Petrol.,* 46:280–300.

JOIDES Planning Committee, 1996. *Understanding our Dynamic Earth through Ocean Drilling: Ocean Drilling Program Long Range Plan into the 21st Century:* Washington, D.C. (JOI).

Kimball, C.V., and Marzetta, T.L., 1984. Semblance processing of borehole acoustic array data. *Geophysics,* 49:274–281.

Kulm, L.D., von Huene, R., et al., 1973. *Init. Repts. DSDP,* 18: Washington (U.S. Govt. Printing Office).

Laverne, C., Belarouchi, A., and Honnorez, J., 1996. Alteration mineralogy and chemistry of the upper oceanic crust from Hole 896A, Costa Rica Rift. *In* Alt, J.C., Kinoshita, H., Stokking, L.B., and Michael, P.J. (Eds.), *Proc. ODP, Sci. Results,* 148: College Station, TX (Ocean Drilling Program), 151–170.

Lay, T., and Wallace, T.C., 1995. *Modern Global Seismology:* New York (Academic).

Leinen, M., 1989. The pelagic clay province of the North Pacific Ocean. *In* Winterer, E.L., Hussong, D.M., and Decker, R.W. (Eds.), *The Geology of North America* (Vol. N): *The Eastern Pacific Ocean and Hawaii.* Geol. Soc. Am., 323–335.

Longuet-Higgins, M.S., 1950. A theory of the origin of microseisms. *Philos. Trans. R. Soc. London, Ser. A,* 243:1–35.

Malahoff, A., and Handschumacher, D.W., 1971. Magnetic anomalies south of the Murray Fracture Zone: new evidence for a secondary sea-floor spreading center and strike-slip movement. *J. Geophys. Res.,* 76:6265–6275.

Mammerickx, J., 1989. Large-scale undersea features of the northeast Pacific. *In* Winterer, E.L., Hussong, D.M., Decker, R.W. (Eds.), *The Eastern Pacific Ocean and Hawaii.* Geol. Soc. Am., Geol. of North Am. Ser., N:5–13.

Manz, W., Wagner, M., and Kalmbach, S., 2001. Assessment of metabolic potential of biofilm-associated bacteria. *In* Doyle, R.J. (Ed.), *Microbial Growth in Biofilms, Part A: Developmental and Molecular Biological Aspects.* Meth. Enzymol. Ser.: San Diego (Academic Press), 336:265–276.

McKinley, J.P., and Stevens, T.O., 2000. Microfossils and paleoenvironments in deep subsurface basalt samples. *Geomicrobiol. J.,* 17:43–54.

McManus, D.A., Burns, R.E., et al., 1970. *Init. Repts. DSDP,* 5: Washington (U.S. Govt. Printing Office).

Menard, H.W., 1964. *Marine Geology of the Pacific:* New York (McGraw-Hill).

Miyashiro, A., 1973. *Metamorphism and Metamorphic Belts:* London (George Allen and Unwin).

Montagner, J.-P., and Lancelot, Y. (Eds.), 1995. Multidisciplinary observatories on the deep seafloor. *INSU/CNRS, IFREMER, ODP-France, OSN/USSAC, ODP-Japan*.

Moore, J.C., 2000. Synthesis of results: logging while drilling, northern Barbados accretionary prism. *In* Moore, J.C., and Klaus, A. (Eds.), *Proc. ODP, Sci. Results,* 171A: College Station TX (Ocean Drilling Program), 1–25.

Moore, J.C., Klaus, A., et al., 1998. *Proc. ODP, Init. Repts.,* 171A: College Station, TX (Ocean Drilling Program).

Natland, J.H., and Dick, H.J.B., 1996. Formation of the lower ocean crust and the crystallization of gabbroic cumulates at a very slowly spreading ridge. *J. Volcanol. Geotherm. Res.,* 110:191–233.

Okada, H., and Bukry, D., 1980. Supplementary modification and introduction of code numbers to the low-latitude coccolith biostratigraphic zonation (Bukry, 1973; 1975). *Mar. Micropaleontol.,* 5:321–325.

Orcutt, J.A., and Stephen, R.A., 1993. OSN seismograph system is underway. *Seismic Waves,* 2:3–5.

Parkes, R.J., Cragg, B.A., and Wellsbury, P., 2000. Recent studies on bacterial populations and processes in marine sediments: a review. *Hydrogeol. Rev.,* 8:11–28.

Petronotis, K.E., Gordon, R.G., and Acton, G.D., 1994. A 57 Ma Pacific plate paleomagnetic pole determined from a skewness analysis of crossings of marine magnetic Anomaly 25r. *Geophys. J. Int.,* 118:529–554.

Pringle, M.S., Sager, W.W., Sliter, W.V., and Stein, S. (Eds.), 1993. *The Mesozoic Pacific: Geology, Tectonics, and Volcanism*. Geophys. Monogr., Am. Geophys. Union, 77.

Purdy, G.M., 1995. A five year plan. *In* Purdy, G.M., and Orcutt, J.A. (Eds.), *Broadband Seismology in the Oceans—Towards a Five-Year Plan:* Washington, D.C. (Joint Oceanographic Institutions), 68–75.

Raitt, R.W., 1963. The crustal rocks. *In* Hill, M.N. (Ed.), *The Sea—Ideas and Observations on Progress in the Study of the Seas* (Vol. 3): *The Earth Beneath the Sea:* New York (Wiley-Interscience), 85–102.

Shipboard Scientific Party, 1998. Site 395. *In* Becker, K., Malone, M.J., et al., *Proc. ODP, Init. Repts.,* 174B: College Station, TX (Ocean Drilling Program), 13–23.

Stephen, R.A., Swift, S.A., and Greaves, R.J,. 1997. *Bathymetry and Sediment Thickness Survey of the Hawaii-2 Cable:* Woods Hole, MA (Woods Hole Oceanographic Institution), WHOI-03-97.

Sutton, G.H., and Barstow, N., 1990. Ocean-bottom ultralow-frequency (ULF) seismoacoustic ambient noise: 0.002 to 0.4 Hz. *J. Acoustical Soc. Am.,* 87:2005–2012.

Sutton, G.H., McDonald, W.G., Prentiss, D.D., and Thanos, S.N., 1965. Ocean-bottom seismic observatories. *Proc. IEEE,* 53:1909–1921.

Tartarotti, P., Vanko, D.A., Harper, G.D., and Dilek, Y., 1996. Crack-seal veins in upper Layer 2 in Hole 896A. *In* Alt, J.C., Kinoshita, H., Stokking, L.B., and Michael, P.J. (Eds.), *Proc. ODP, Sci. Results,* 148: College Station, TX (Ocean Drilling Program), 281–288.

Vallier, T.L., 1970. Carbon carbonate results. *In* McManus, D.A., et al., *Init. Repts. DSDP,* 5: Washington (U.S. Govt. Printing Office), 431–440.

Webb, S.C., 1998. Broadband seismology and noise under the ocean. *Rev. Geophys.,* 36:105–142.

Whitman, W.B., Coleman, D.C., and Wiebe, W.J., 1998. Prokaryotes: the unseen majority. *Proc. Nat. Acad. Sci. U.S.A.,* 95:6578–6583.

Winterer, E.L., 1989. Sediment thickness map of the Northeast Pacific. *In* Winterer, E.L., Hussong, D.M., and Decker, R.W. (Eds.), *The Eastern Pacific Ocean and Hawaii*. Geol. Soc. Am., Geol. of North America Ser., N:307–310.

Wise, S.W. Jr., 1973. Calcareous nannofossils from cores recovered during Leg 18, Deep Sea Drilling Project: biostratigraphy and observations of diagenesis. *In* Kulm, L.D., von Huene, R., et al., *Init. Repts. DSDP,* 18: Washington (U.S. Govt. Printing Office), 569–615.

Zeldenrust, I., and Stephen, R.A., 2000. Shear wave resonances in sediments on the deep sea floor. *Eos Trans.,* 81 (suppl.): F819.

Figure F1. All Site 1224 drilling took place at proposed Site H2O-5, which is 1.48 km northeast of the junction box at the Hawaii-2 Observatory (H2O). Circles at 1, 2, and 3 km radius from the junction box are shown. The locations of the single-channel seismic lines acquired during the site survey cruise in 1997 are shown as dashed lines. The solid line between them is the approach line taken by the *JOIDES Resolution* on 26 December 2001. Echo sounder recordings (Fig. F2, p. 68) were made along this line. The symbols labeled H2O-1, H2O-2, H2O-3, and H2O-4 show alternate drilling sites that were discussed in the Leg 200 Scientific Prospectus.

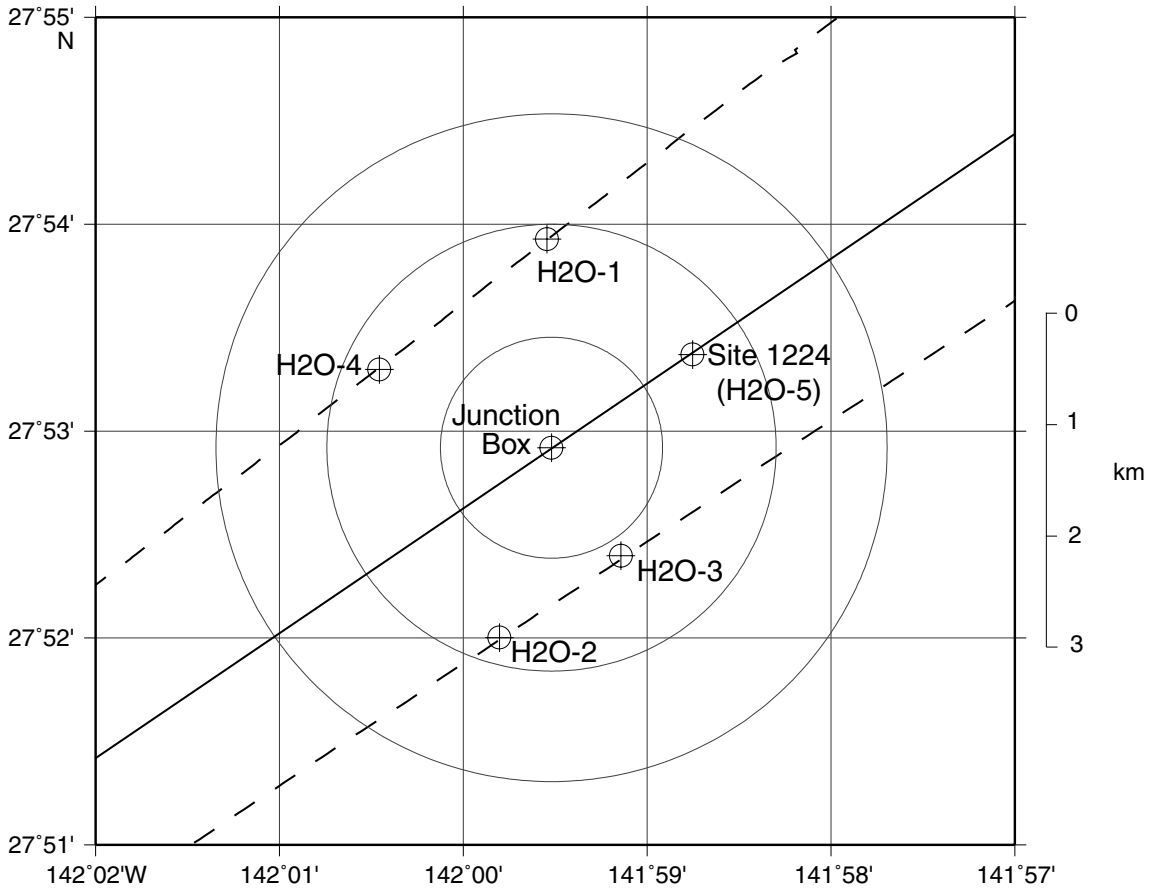

Figure F2. This 3.5-kHz echo sounder recording shows that the seafloor dips smoothly ~6 m from the junction box to the drill site (proposed Site H2O-5). One subbottom horizon at ~9 m is fairly uniform throughout the area. Based on drilling results, this is a mid-sediment reflector. A second reflector at ~30 m below the junction box can be associated with basaltic basement although it appears only occasionally in the record. PDR = precision depth recorder.

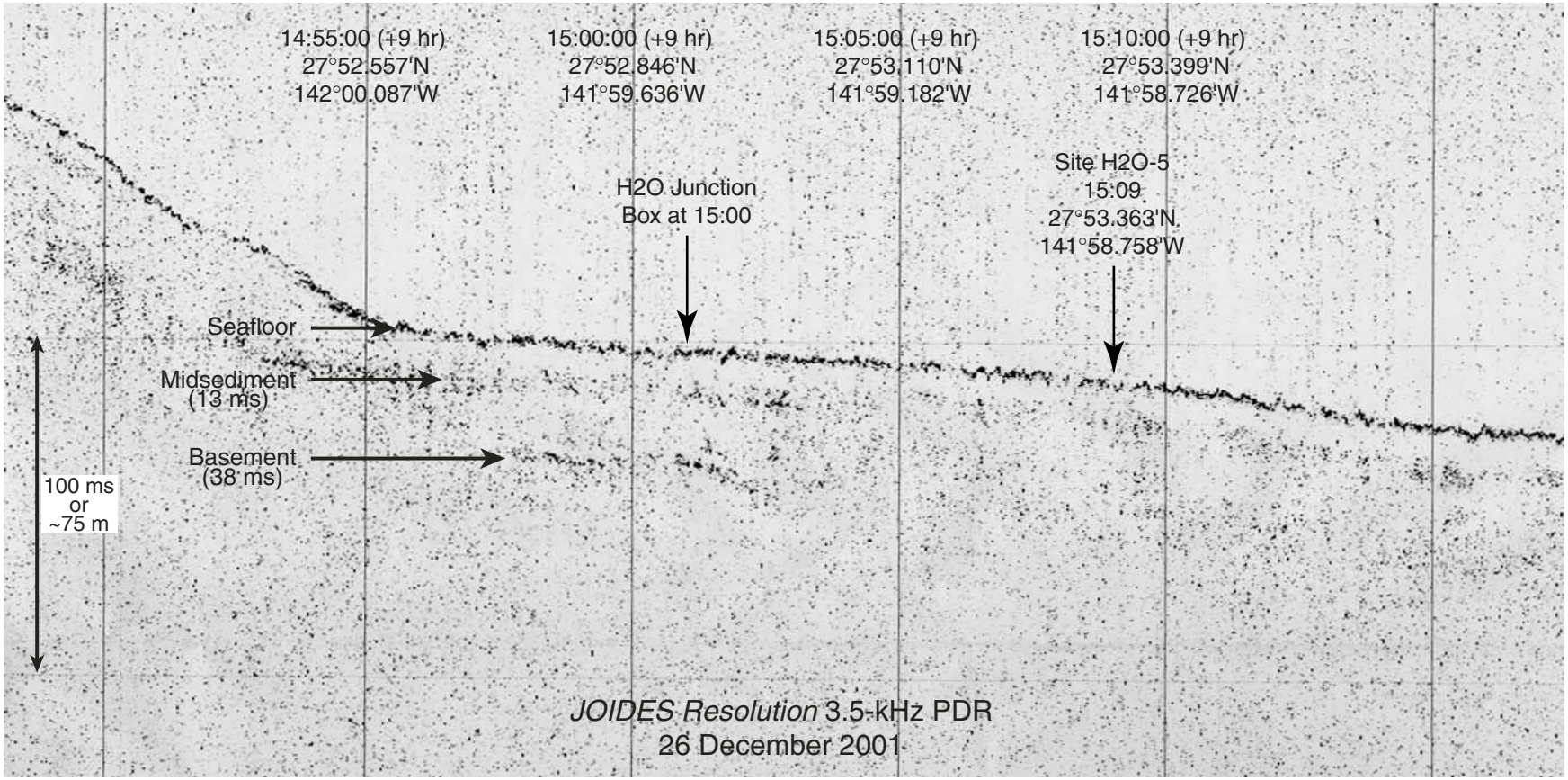

Figure F3. All of the drilling activity at the H2O occurred within a 20-m × 20-m area. The ship took up three positions by dynamic positioning (DP): the first jet-in test (JIT) and Holes 1224E and 1224F (DP-JIT1, E, and F), the first coring site (DP-A), and the site of the second jet-in test and Holes 1224B, 1224C, and 1224D (DP-JIT2, B, C, and D). Averages of the navigation fixes during each of these activities were computed in the underway geophysics laboratory and are denoted UG-A, UG-B, and so forth, for the various holes and jet-in tests. The circle shows the typical 2-σ bounds for the scatter in the navigation fixes.

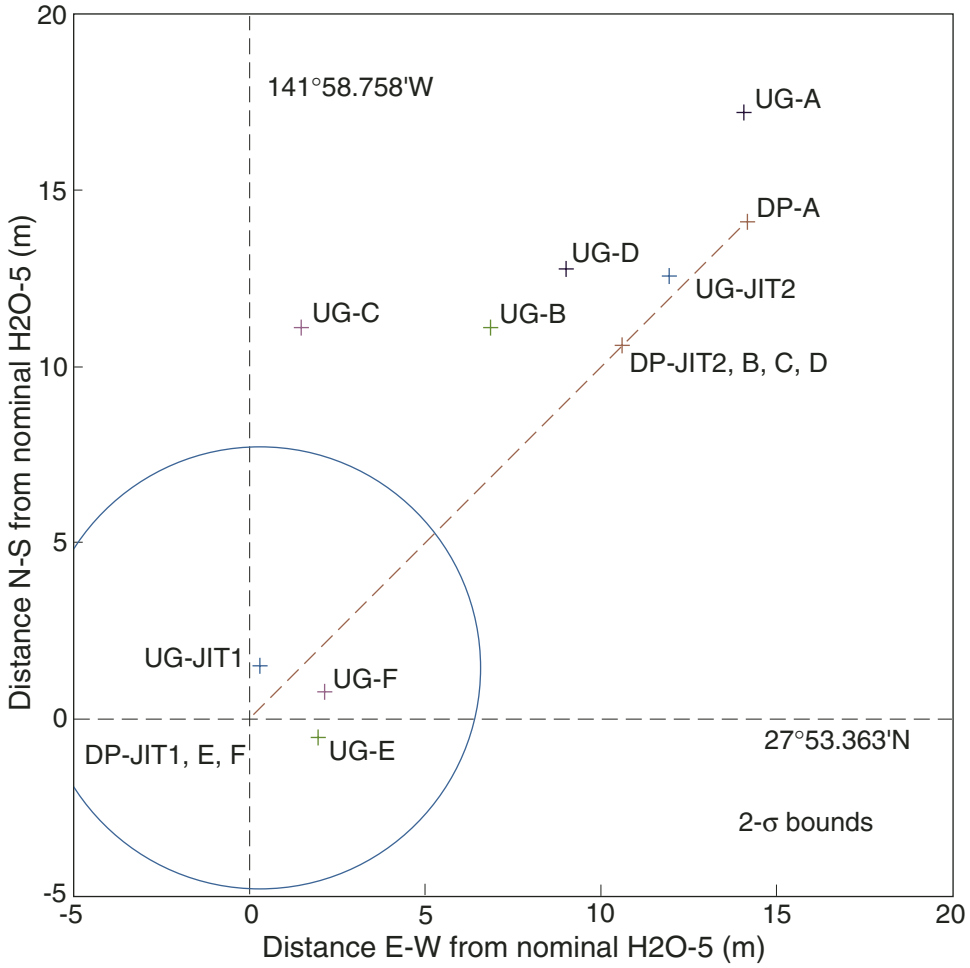

Figure F4. Summary of the critical dimensions of the reentry cone and casing deployed in Hole 1224D. On reentering the cone for the last time, it was observed that the reentry cone had settled 1.75 m below the mudline. The inside diameter (drift) of the 10¾-in casing is 9.9 in. CSG = casing, HGR = hanger, TD = total depth, ID = inner diameter. (Figure provided courtesy of Scott Pederson, Transocean Sedco Forex.)

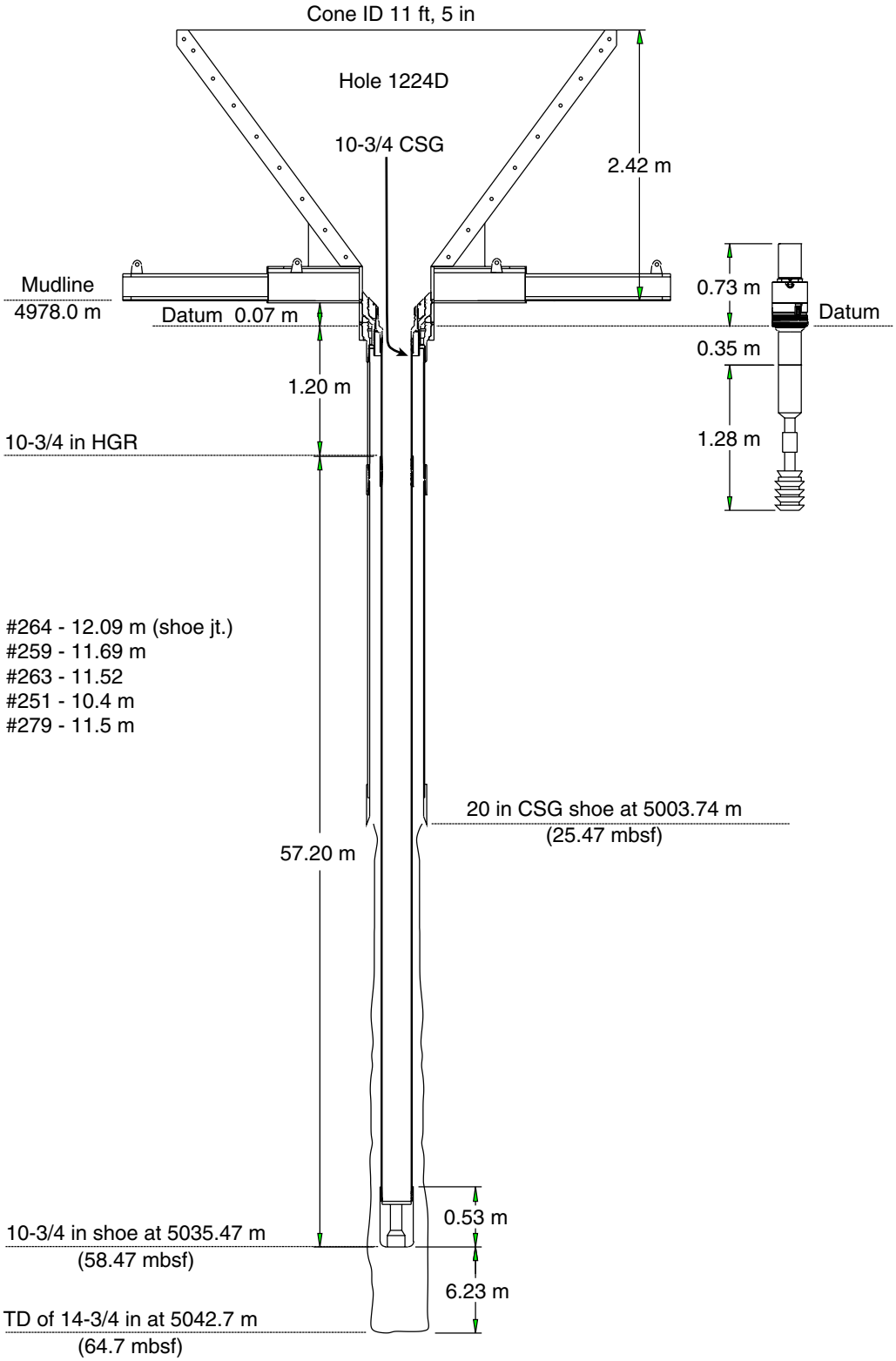

Figure F5. This photograph, taken from the video camera on the VIT sled, shows the reentry cone in Hole 1224D.

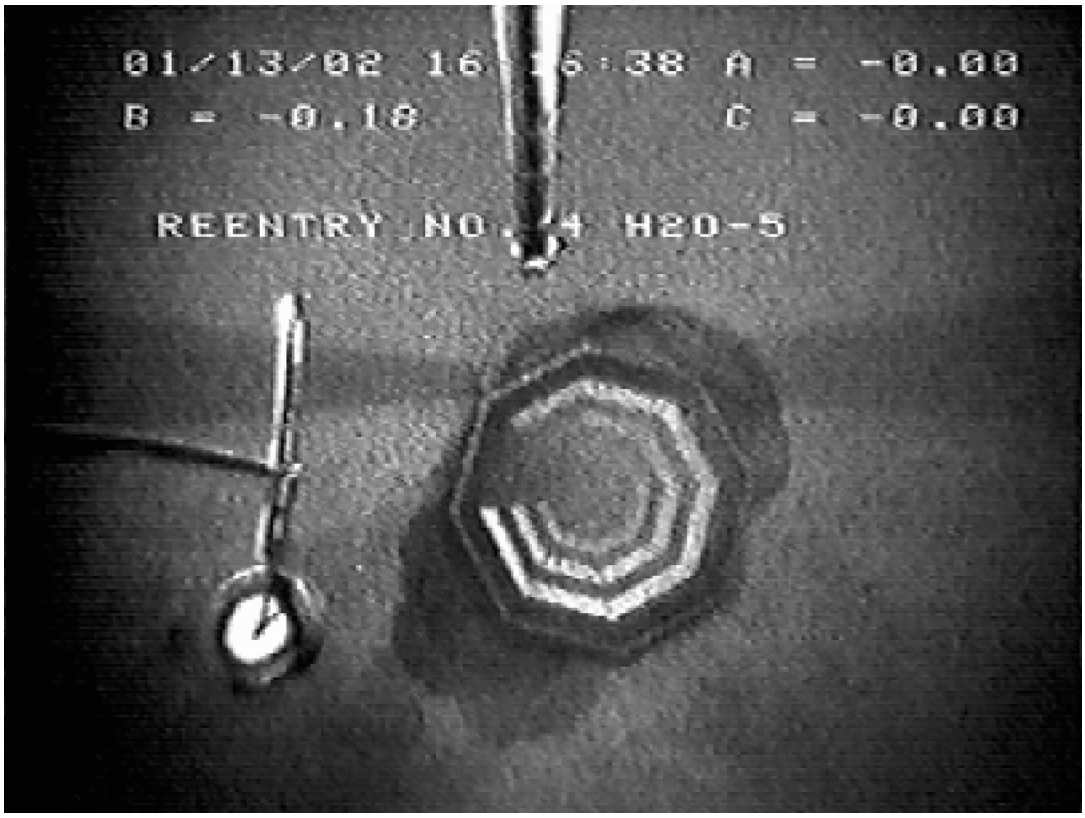

Figure F6. Summary of the critical dimensions of the free-fall funnel deployed in Hole 1224F. The throat inside diameter is 12.5 in. TD = total depth. (Figure provided courtesy of Scott Pederson, Transocean Sedco Forex.)

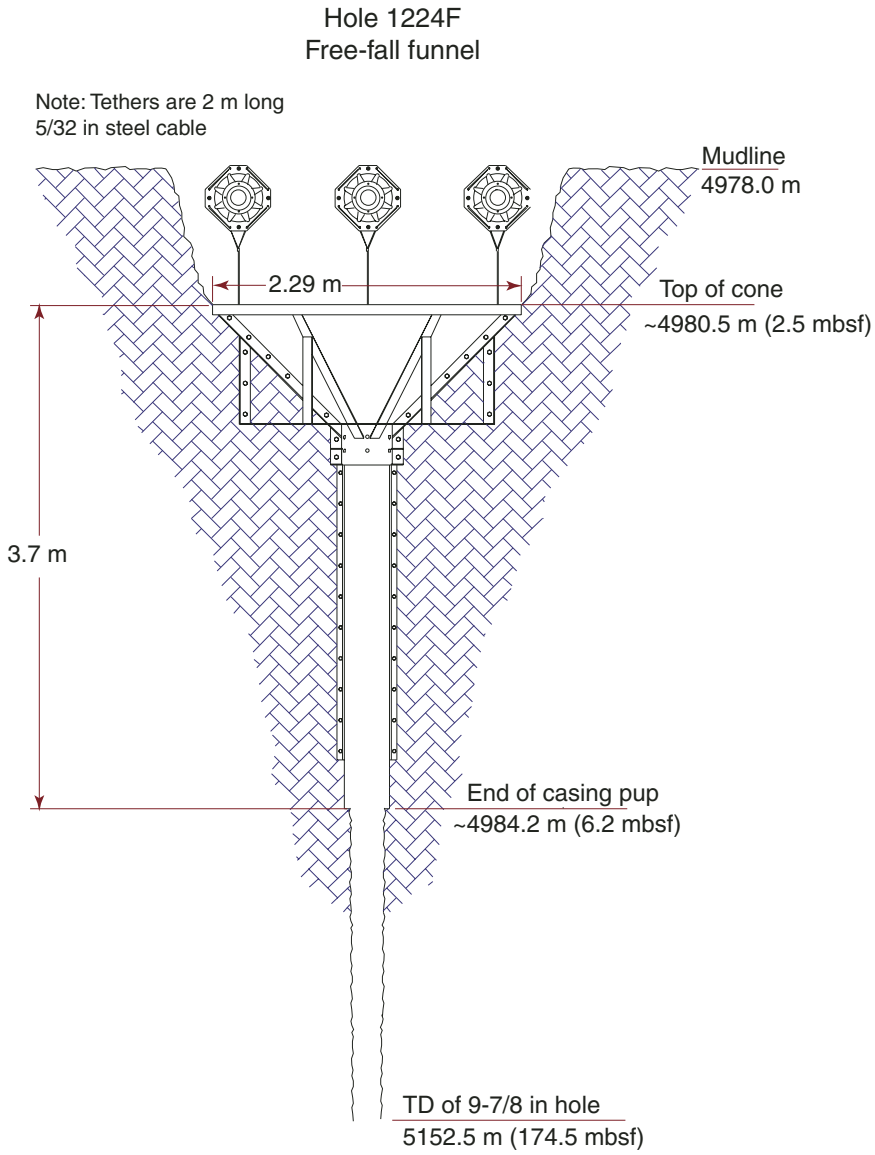

Figure F7. This photograph, taken from the video camera on the VIT sled, shows the free-fall funnel buried in the seafloor in Hole 1224F.

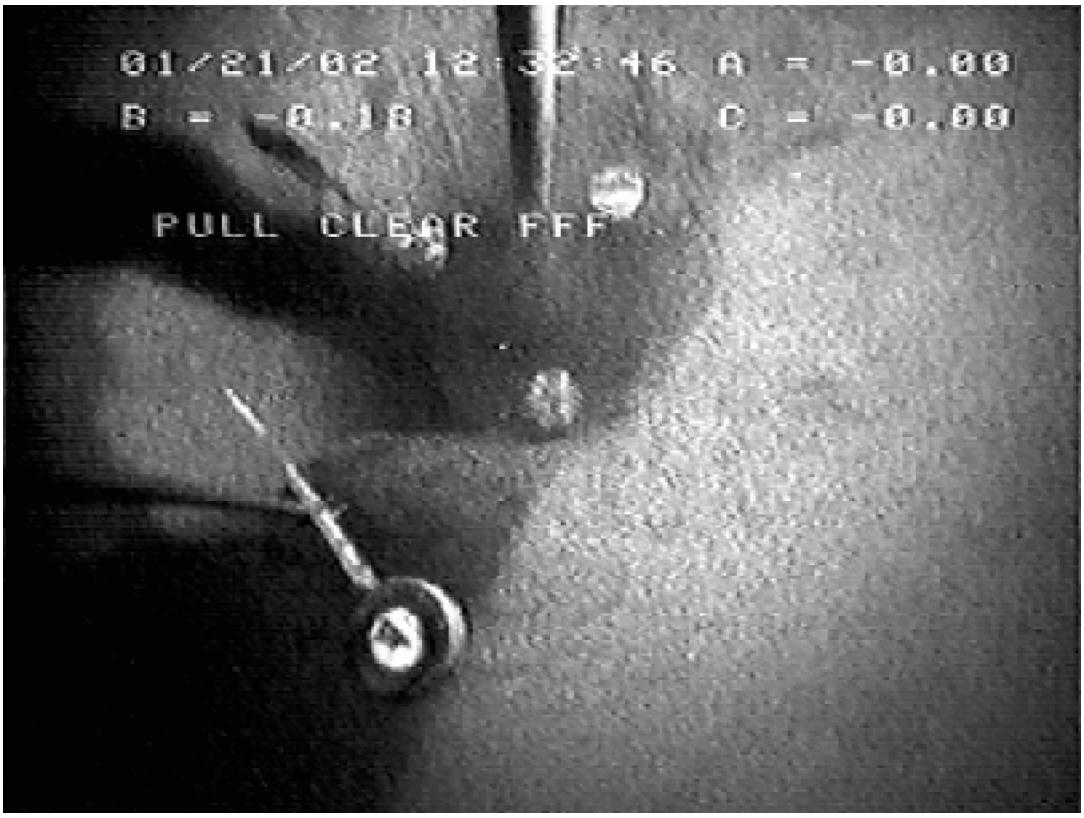

Figure F8. Locations are shown of Site 1224 and the Hawaii-2 Observatory (H2O) junction box (large star), Site 1223 (small star), repeater locations along the Hawaii-2 cable (crosses), major fracture zones (FZ), and previous drill sites (circles) from DSDP Legs 5 (Sites 38, 39, 40, and 41) and 18 (Site 172). Superimposed on the map is the satellite-derived bathymetry.

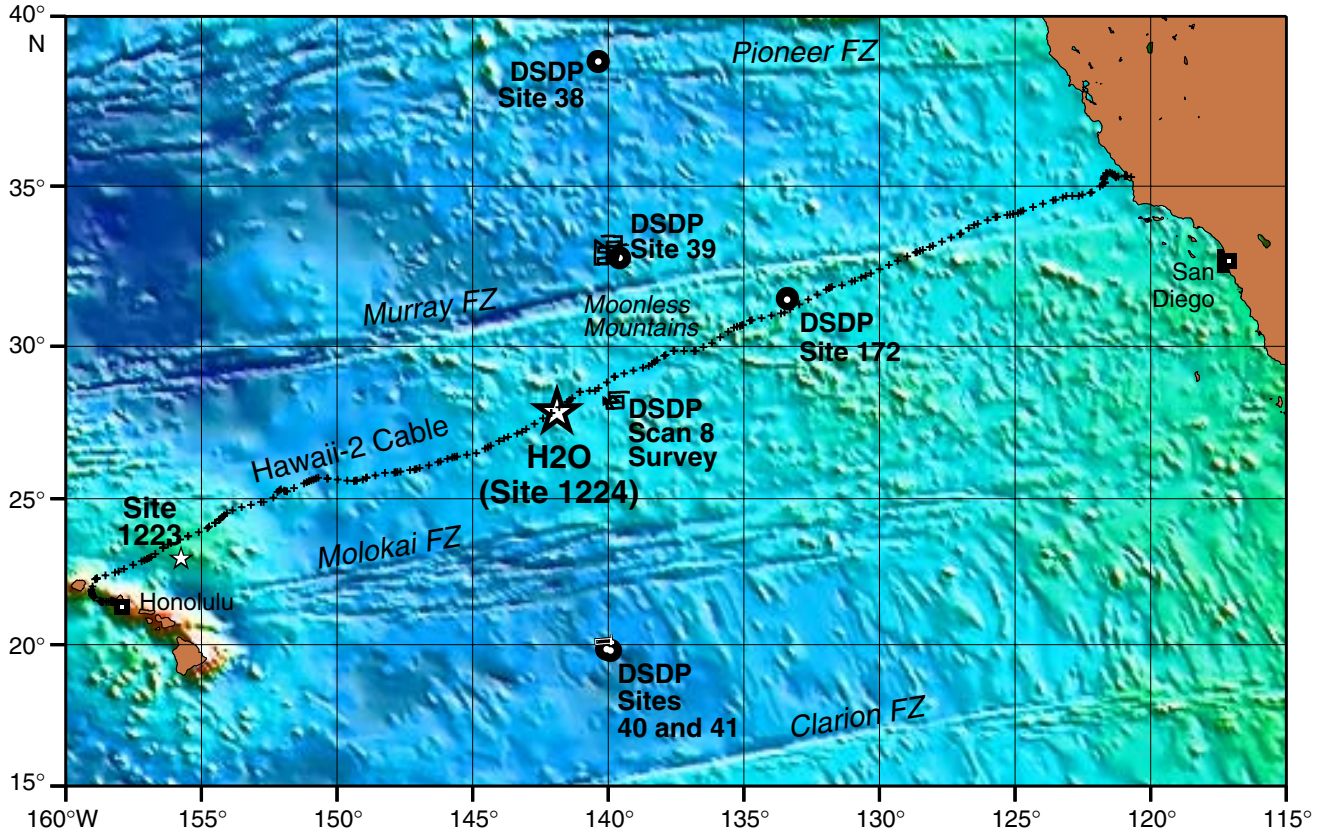

Figure F9. The Hydrosweep bathymetry around the H2O area acquired from the *Thompson* in September 1999. The site is on a relatively benign ribbon of "normal" oceanic crust. Total relief varies by ~40 m across the region within 2 km of the junction box.

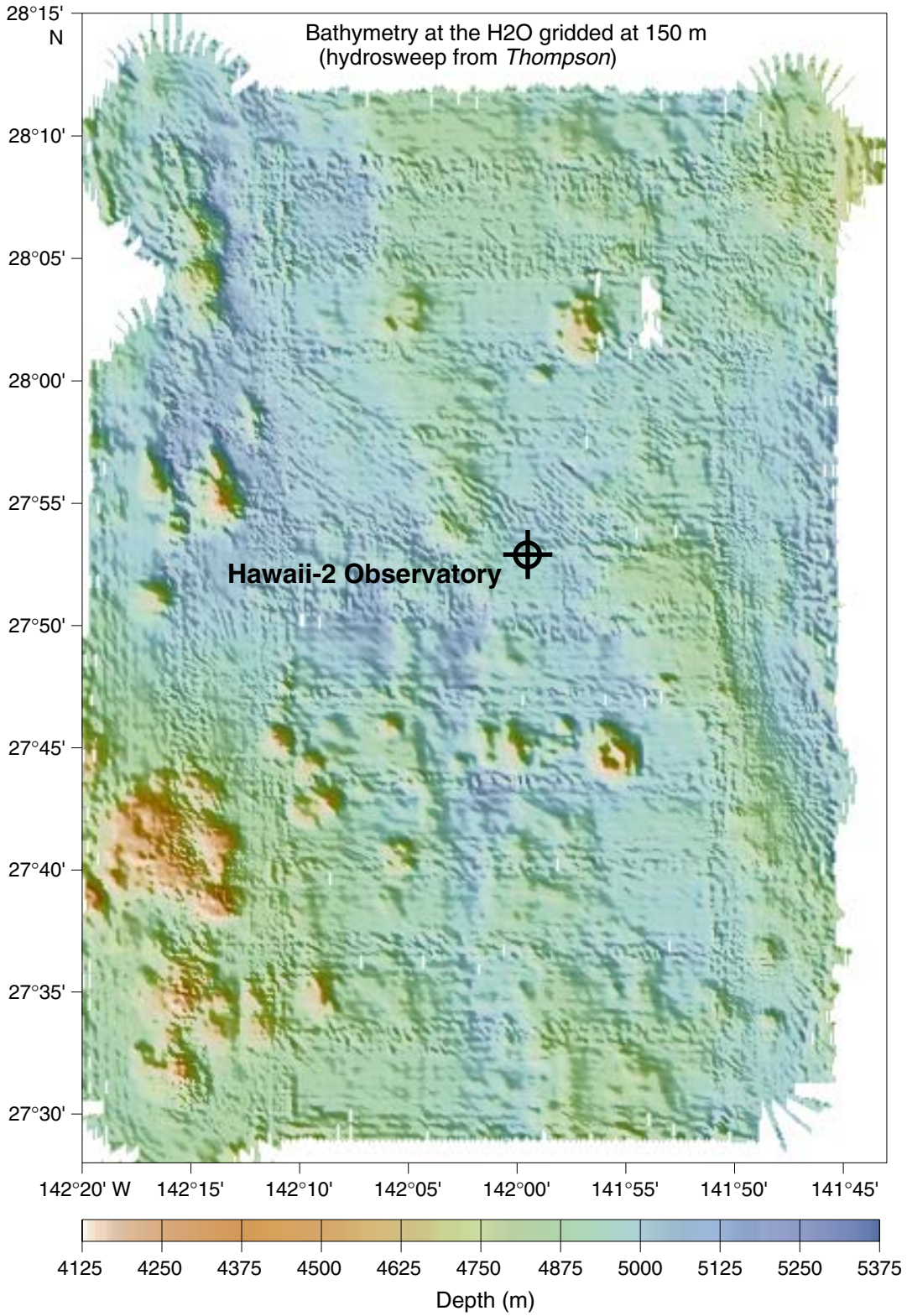

Figure F10. The location of the Hawaii-2 Observatory (H2O) junction box is shown on the SeaBeam bathymetry acquired during the site survey in August 1997 (Stephen et al., 1997). The locations of the repeaters (AT&T waypoints) on the cable are also shown (solid triangles).

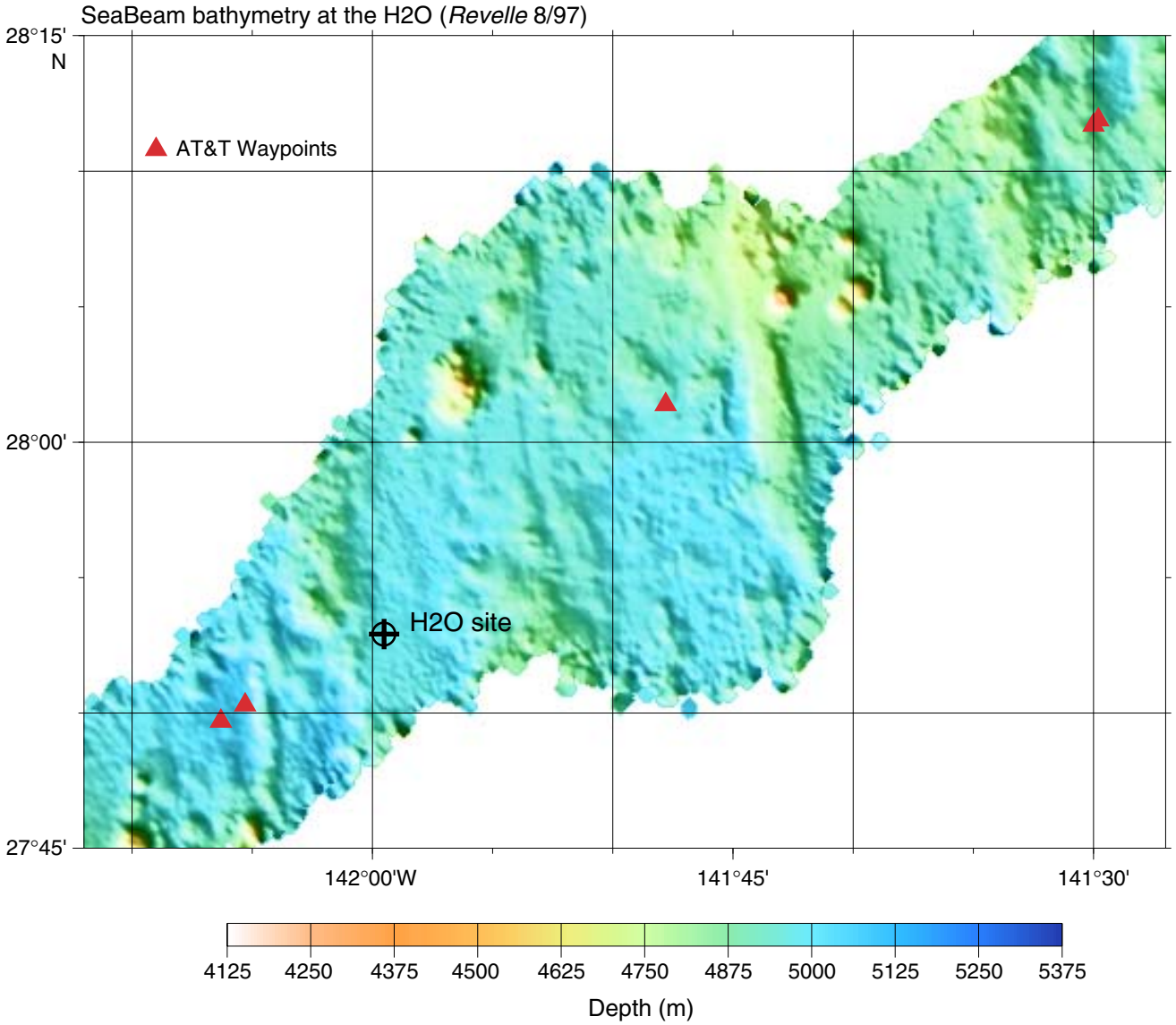

Figure F11. This artist's conception of the Hawaii-2 Observatory (H2O) summarizes some of the important components of the installation (© copyright Jayne Doucette, Woods Hole Oceanographic Institution [WHOI]. Reproduced with permission of WHOI).

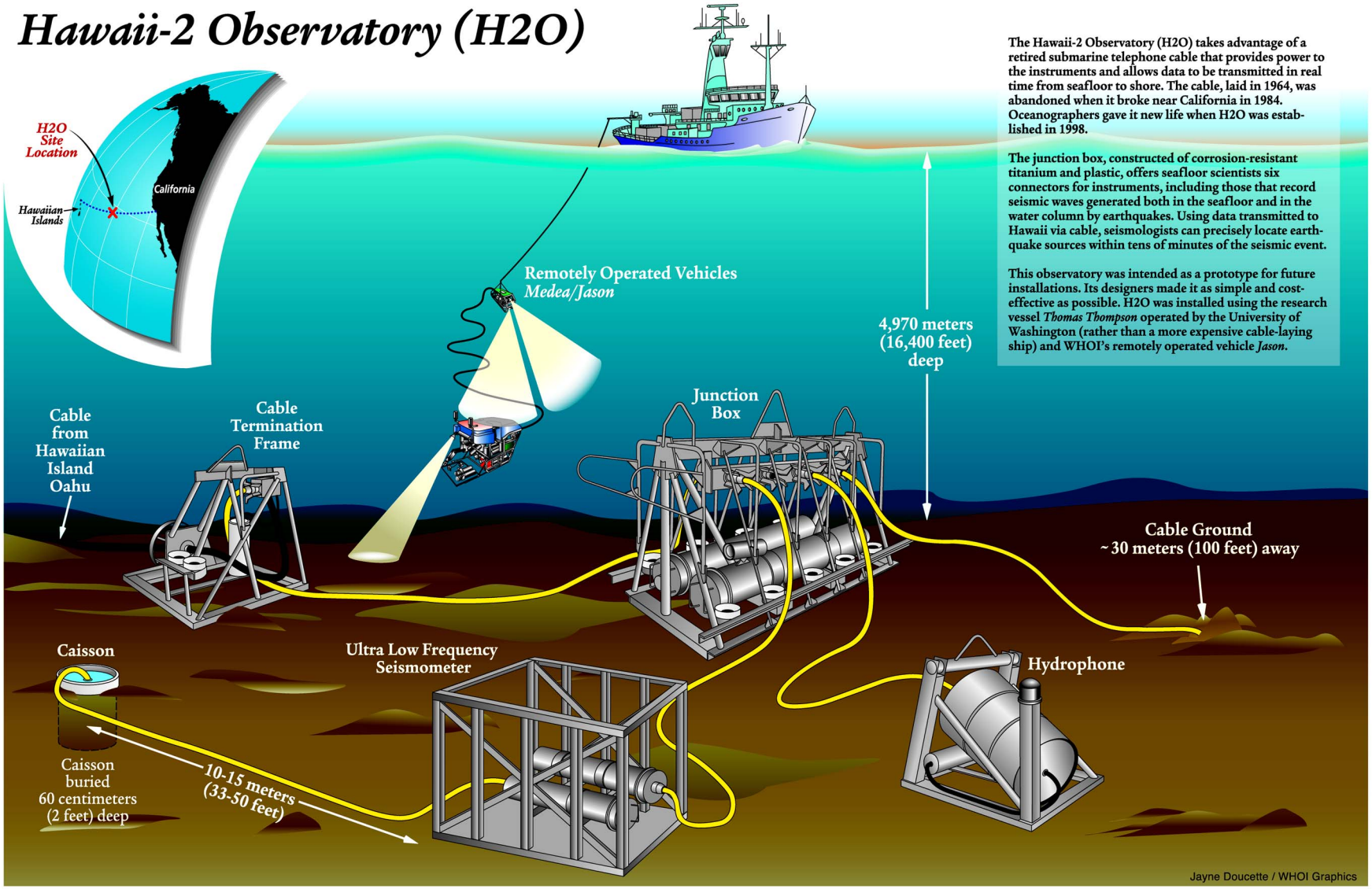

Figure F12. The Hawaii-2 Observatory (H2O) site lies on a normal band of oceanic crust with an estimated age of 46.3 Ma and a spreading half-rate of 71.0 mm/yr. On the magnetic lineation map of Malahoff and Handschumacher (1971) we drew a flow line perpendicular to the magnetic lineations in the ribbon of crust containing the Hawaii-2 cable track west of 140°W and between Anomalies 18 and 30. The geographic distances in kilometers along this line of the edges of the magnetic stripes relative to the start of Anomaly 18 are plotted as the ordinate of the graph in this figure. The ages of the magnetic stripes in units of million of years from Cande and Kent (1992, 1995) are plotted as the abscissa. The numbered bars above the abscissa indicate the normally magnetized chrons. The reversed chrons correspond to the gaps between the bars. Slopes on this graph give the spreading half-rate in kilometers per million years or millimeters per year. The average slope across all of the anomalies gives a spreading half-rate of 50 mm/yr, which agrees well with Malahoff and Handschumacher's value of 49 mm/yr. It is quite clear, however, that a better fit to the data is obtained by three straight lines for Anomalies 18–22, 22–25, and 25–30. The half-rates of these segments are 71, 49, and 35 mm/yr, respectively.

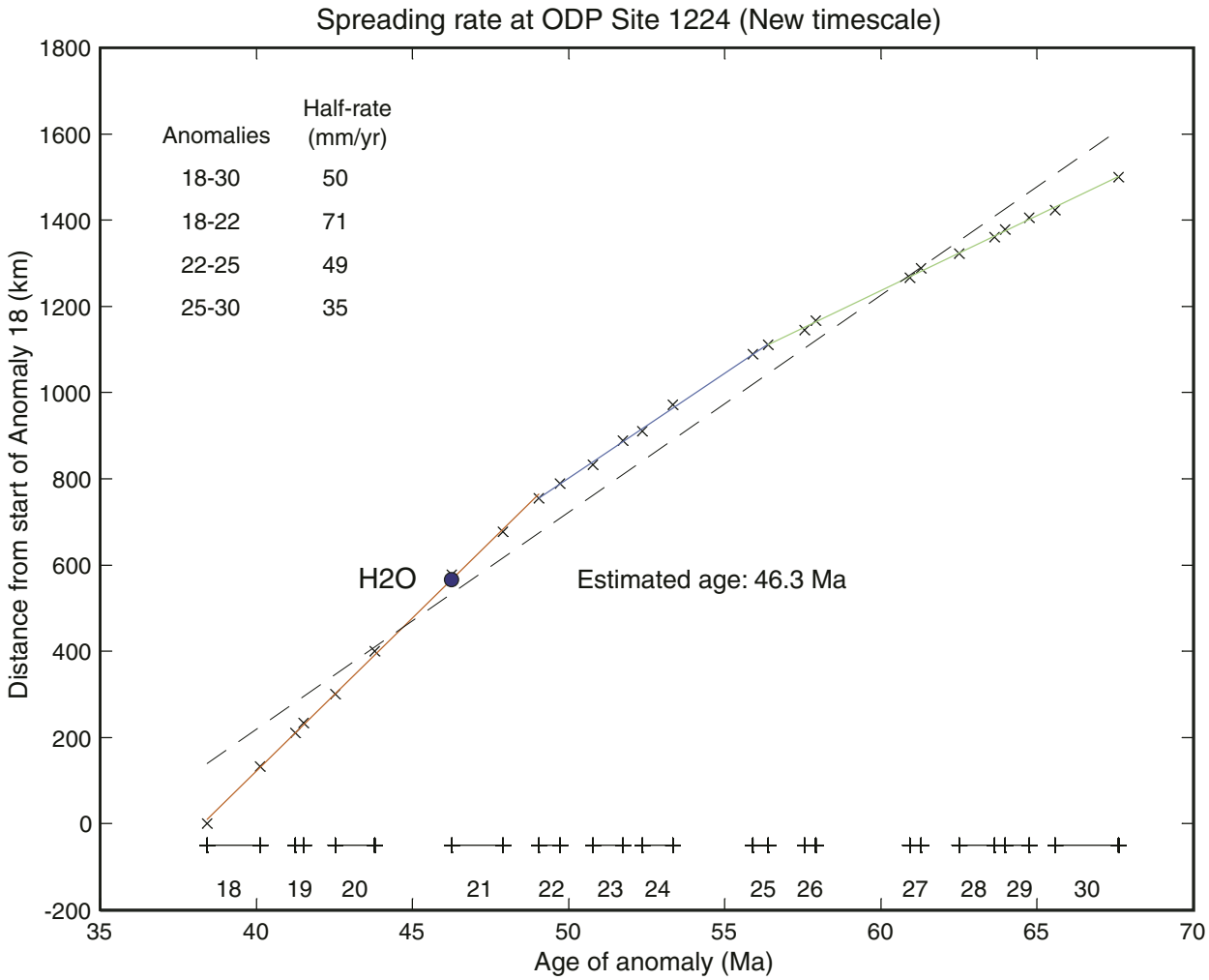

Figure F13. The track lines during the 1997 site survey cruise on *Revelle* (KIWI02) are shown with the location of the H2O junction box.

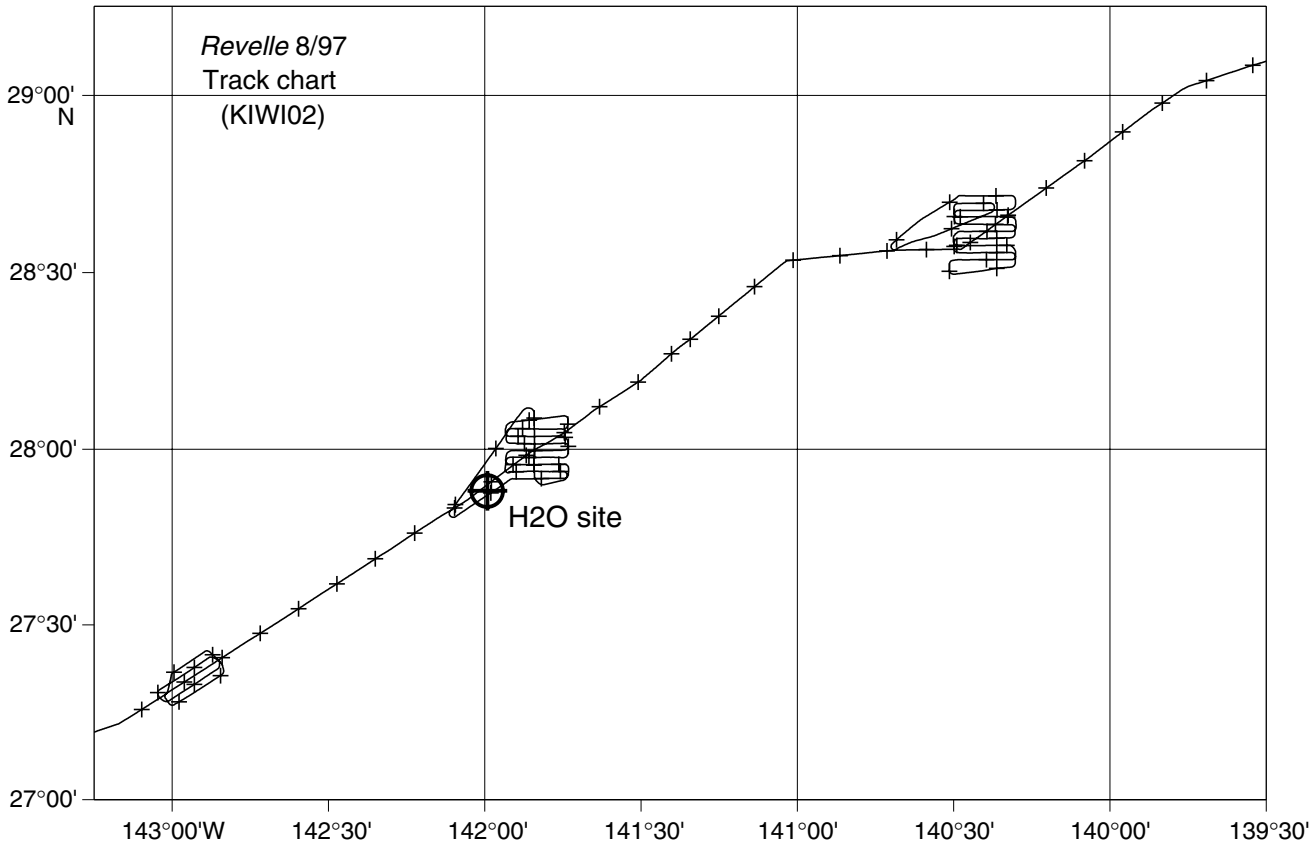

Figure F14. A detail of the track chart shows that the H2O junction box lies between two parallel track lines southwest of a well-surveyed area.

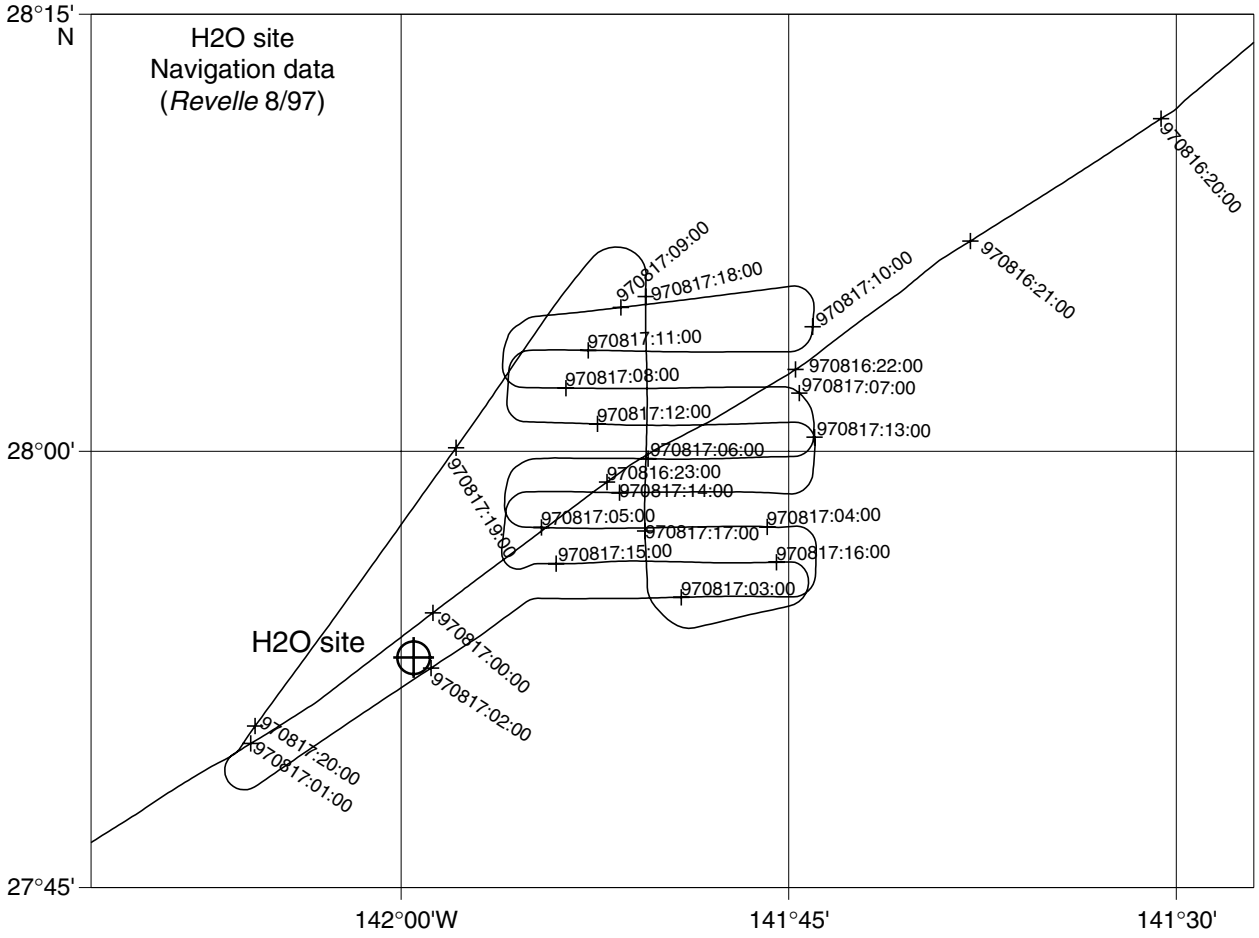

Figure F15. The locations of the four initially proposed drill sites (Sites H2O-1 through -4) are shown with the track lines of the 1997 survey. The track lines are annotated with single-channel seismic (SCS) shot numbers for comparison with the seismic data in Figures F19, p. 85, F20, p. 86, F21, p. 87, and F22, p. 88. Circles have been drawn at 1, 2, and 3 km radius from the junction box. Sites should be beyond a radius of 1 km to avoid conflicts with other experiments at the observatory. They should be within a radius of 2 km to minimize the effort in running cable to the junction box.

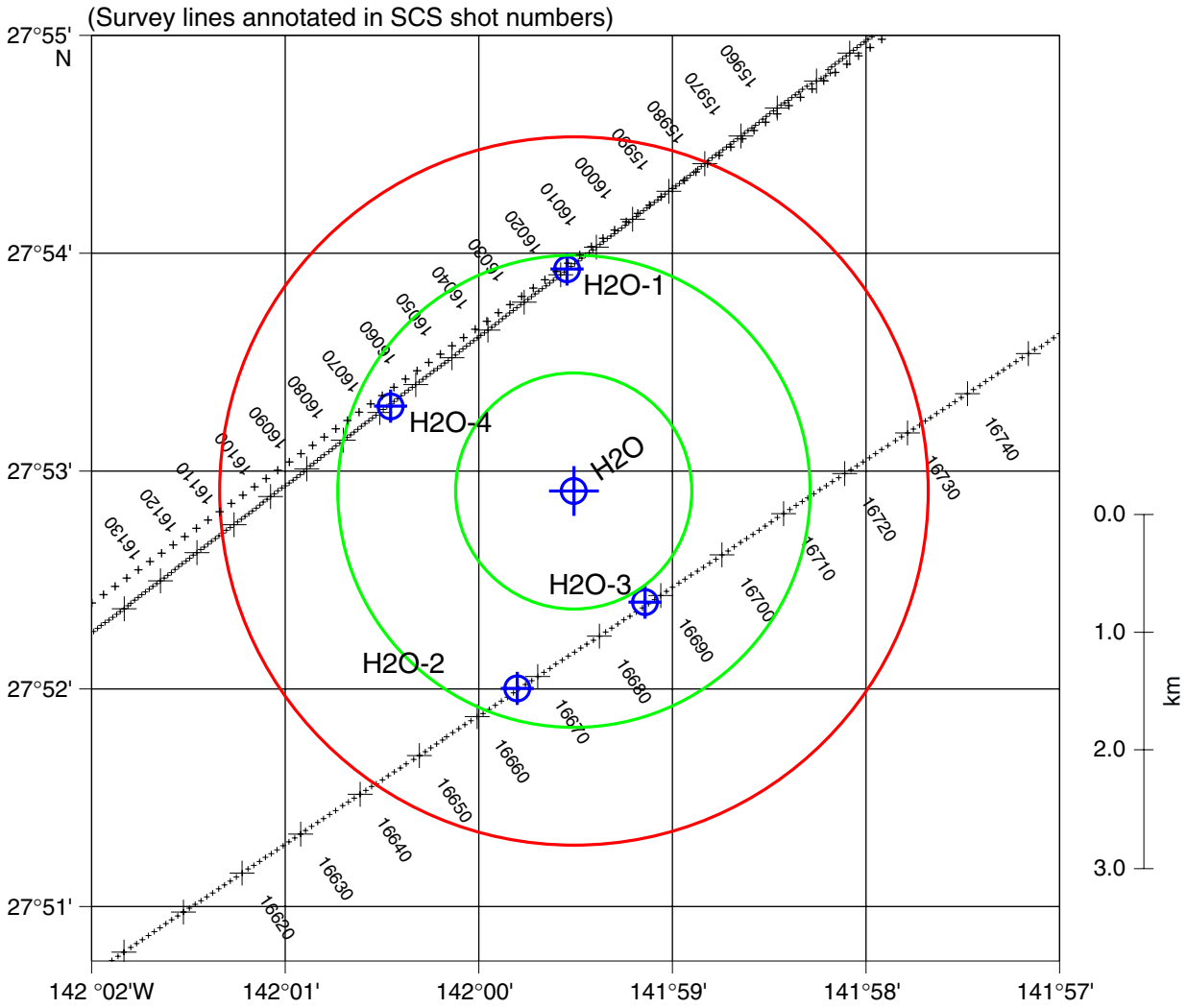

Figure F16. This figure is similar to Figure F15, p. 81, except the track lines are annotated with Julian day and time for comparison with the 3.5-kHz data in Figures F17, p. 83, and F18, p. 84.

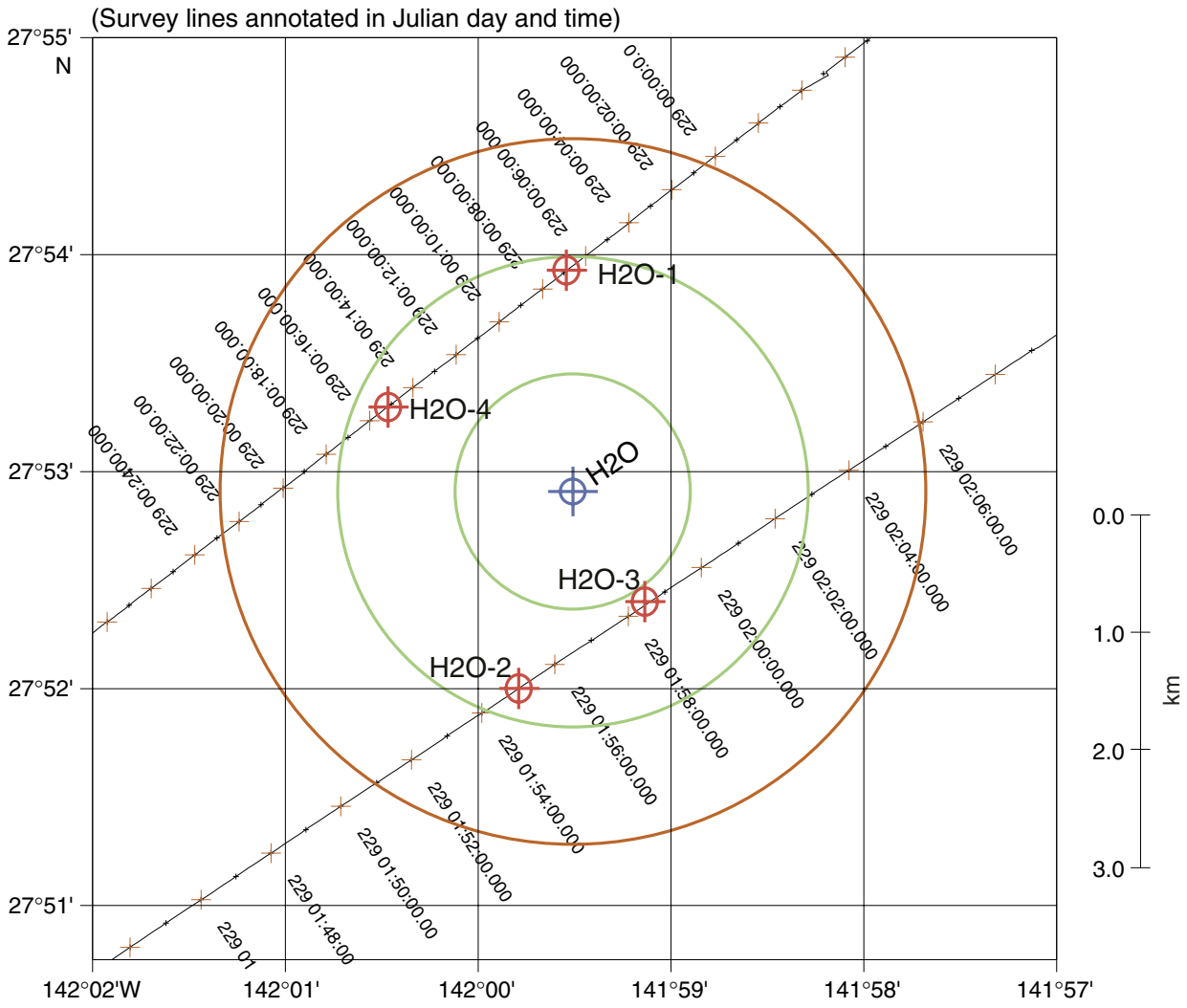

Figure F17. The 3.5-kHz data for the line north of Site 1224 show ~8–10 m of sediment above the first reflector, which we originally interpreted to be a chert layer. Drilling indicates that this is a mid-sediment reflector.

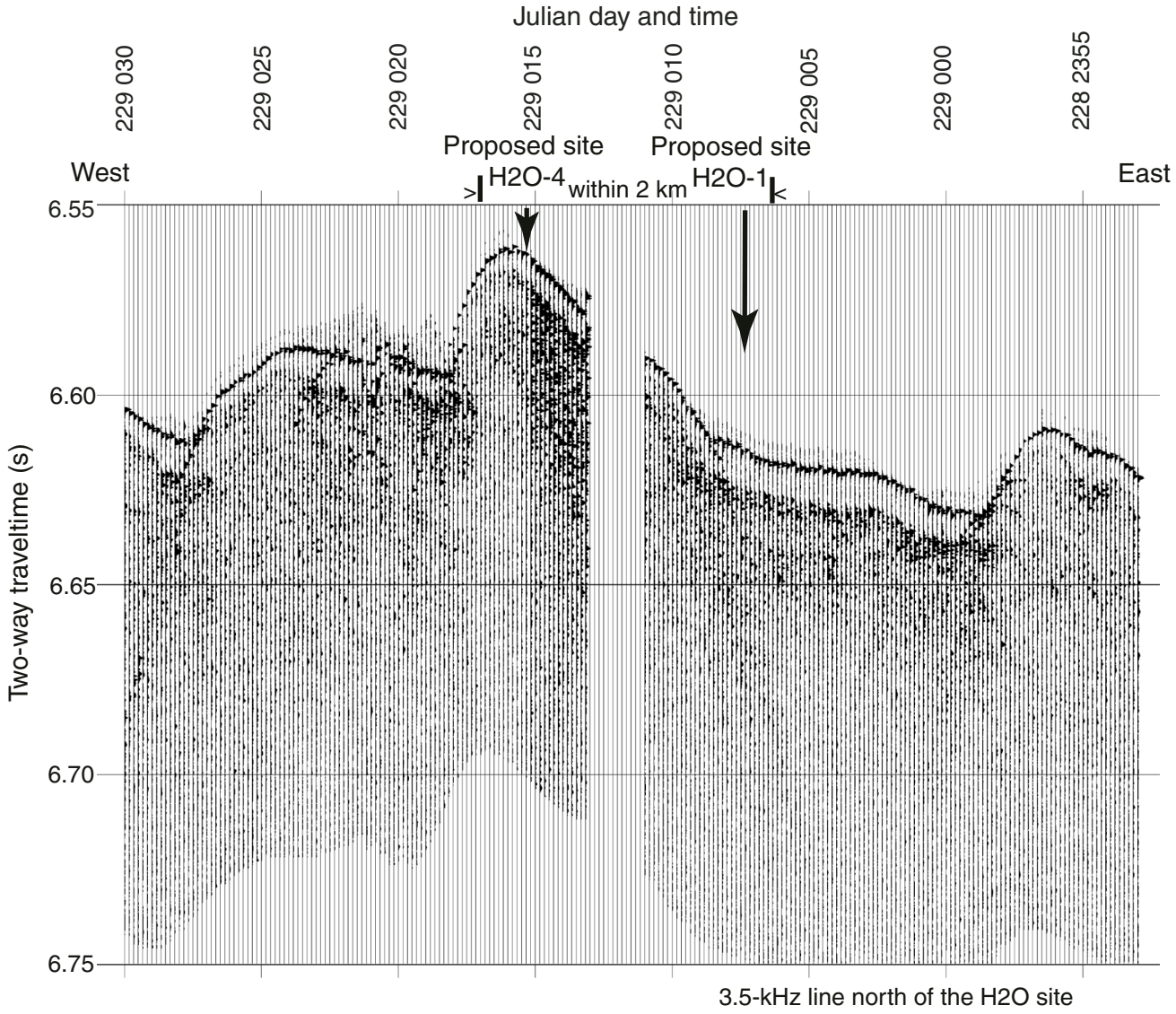

Figure F18. The 3.5-kHz data for the line south of Site 1224 show similar sediment thickness to the north line (Fig. F17, p. 83).

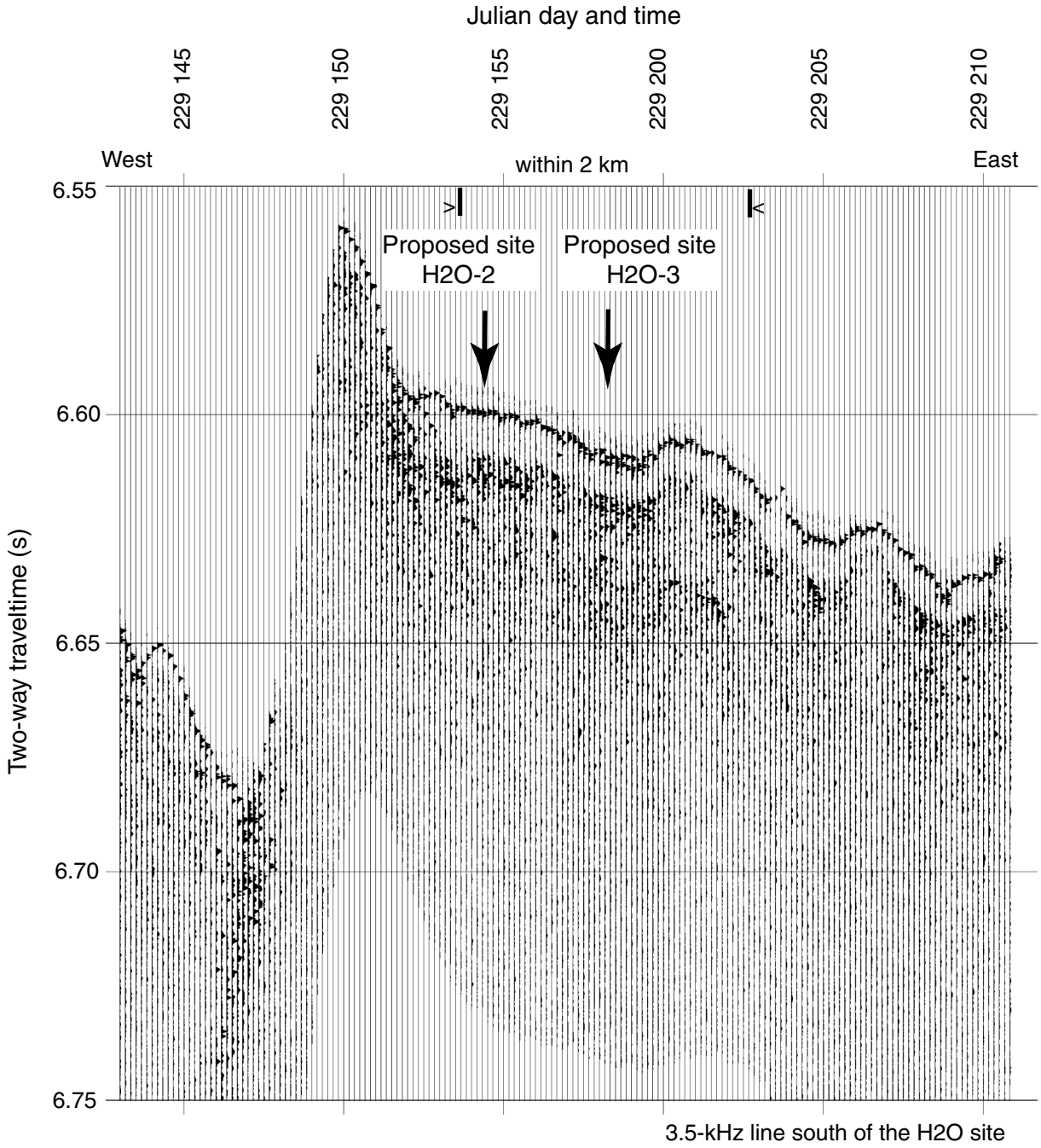

Figure F19. The unmigrated SCS line north of the site shows relief of ~40 m. Proposed Site H2O-1 is at the bottom of a fault block, and proposed Site H2O-4 is at the top of a fault block.

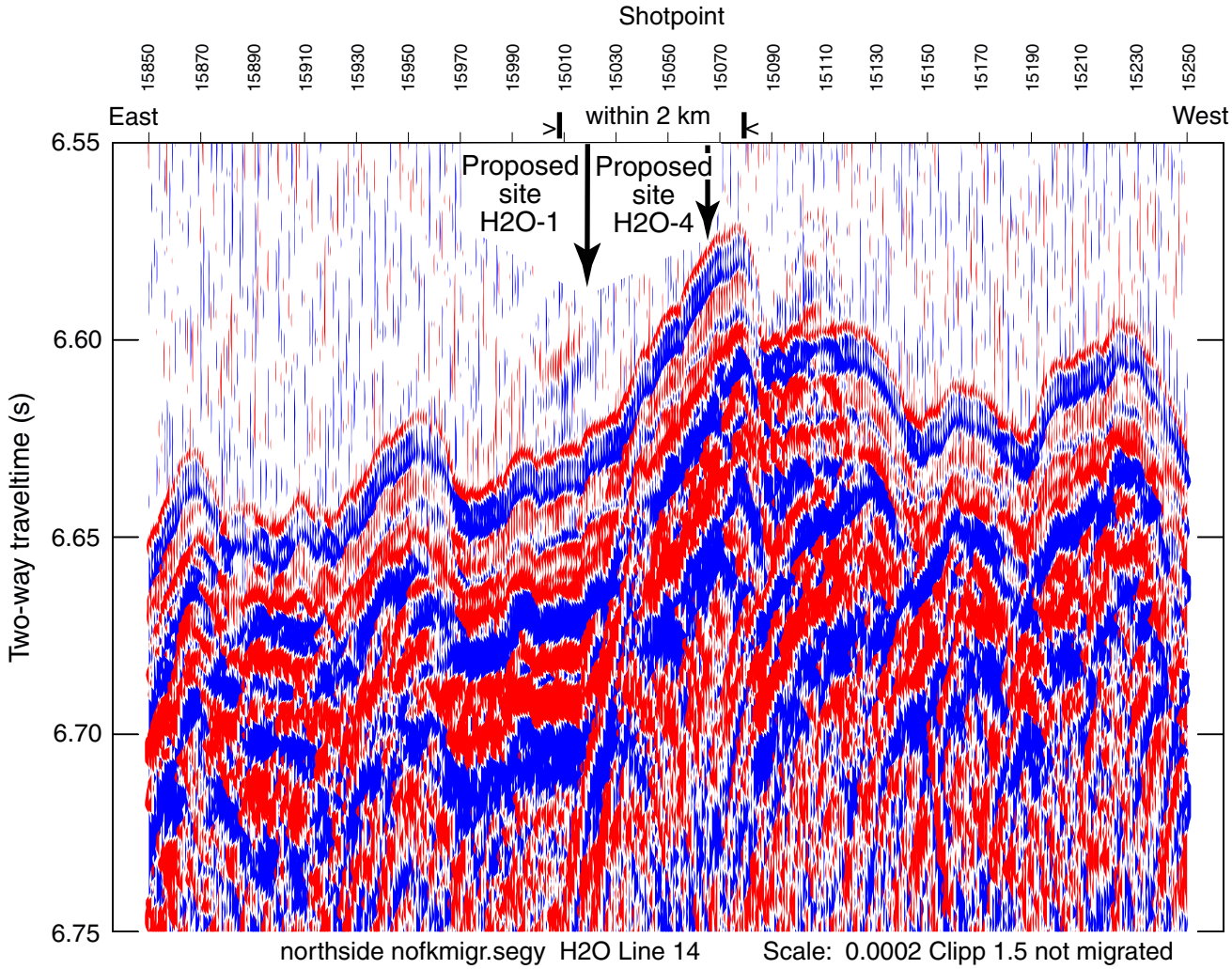

Figure F20. The migrated SCS line north of the site does not improve the resolution of sediment thickness.

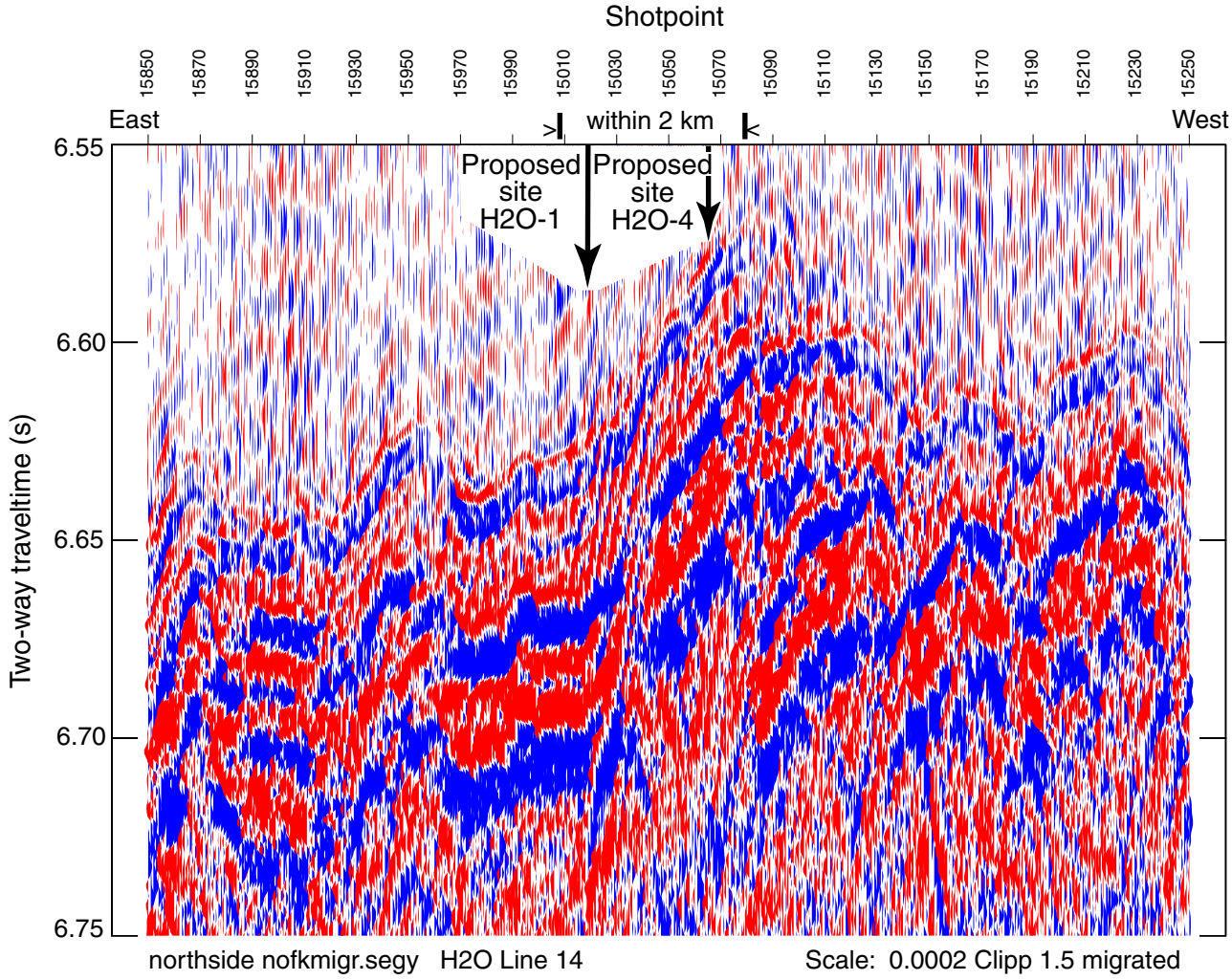

Figure F21. The unmigrated SCS line south of the site shows smooth relief within 2 km of the junction box. Proposed Site H2O-3 is at the bottom of a fault block, and proposed Site H2O-2 is in the middle of a block.

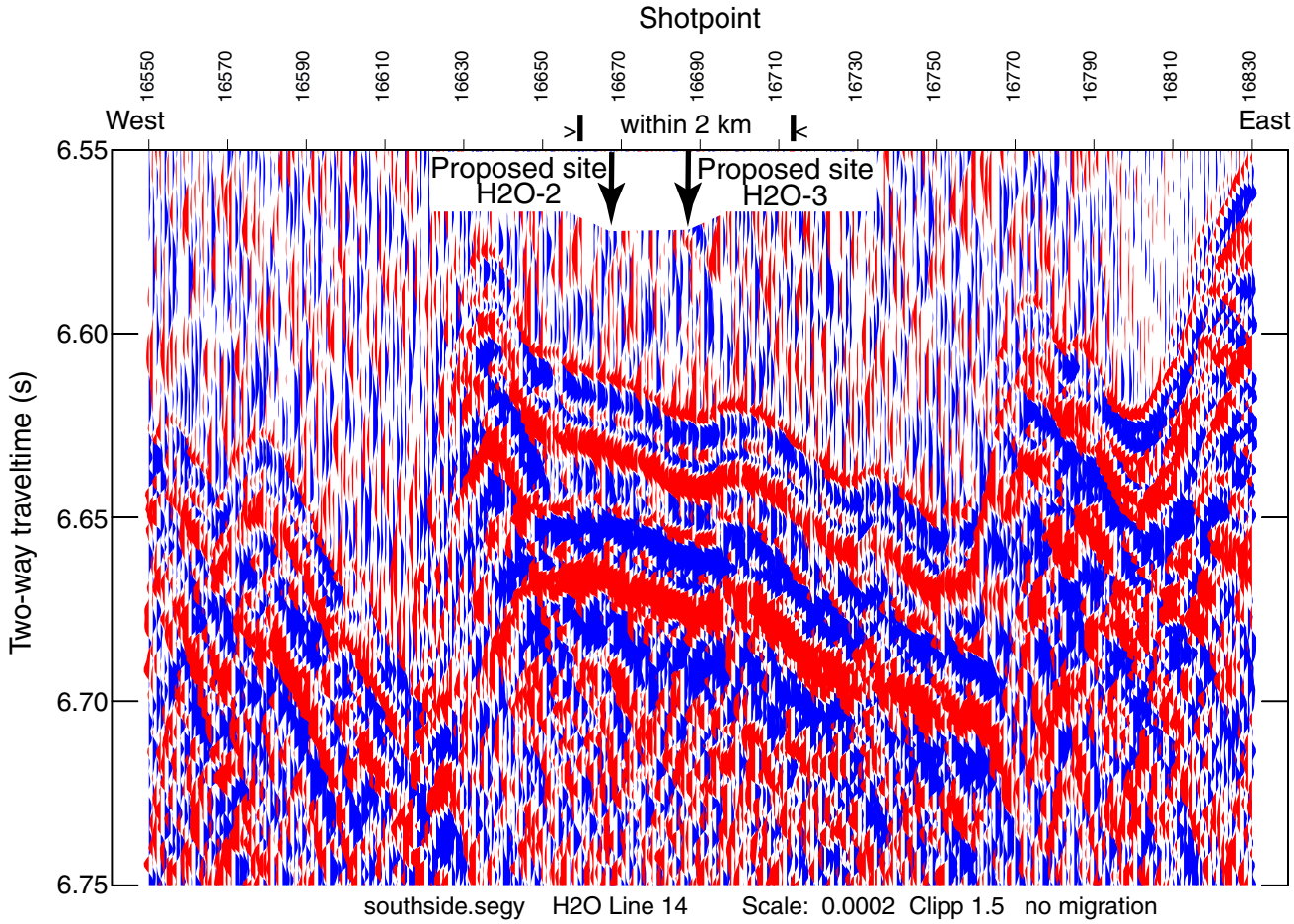

Figure F22. The migrated SCS line south of the site does not improve the resolution of sediment thickness.

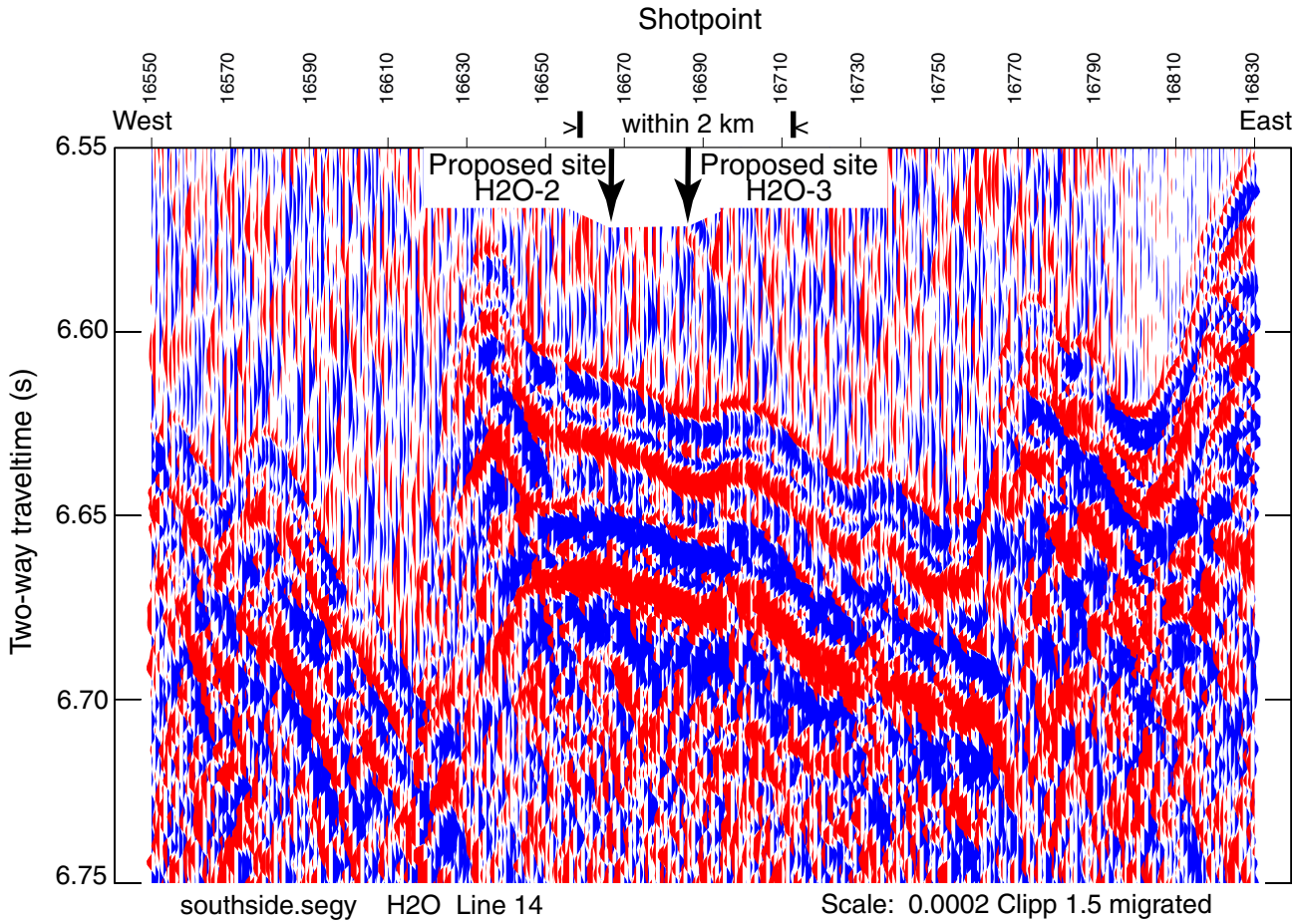

Figure F23. The Ocean Seismic Network site (OSN-1) is 225 km southwest of Oahu at a water depth of 4407 m. The Hawaii-2 Observatory (H2O) is halfway between Hawaii and California on the retired Hawaii-2 telecommunications cable and is at a water depth of 4970 m.

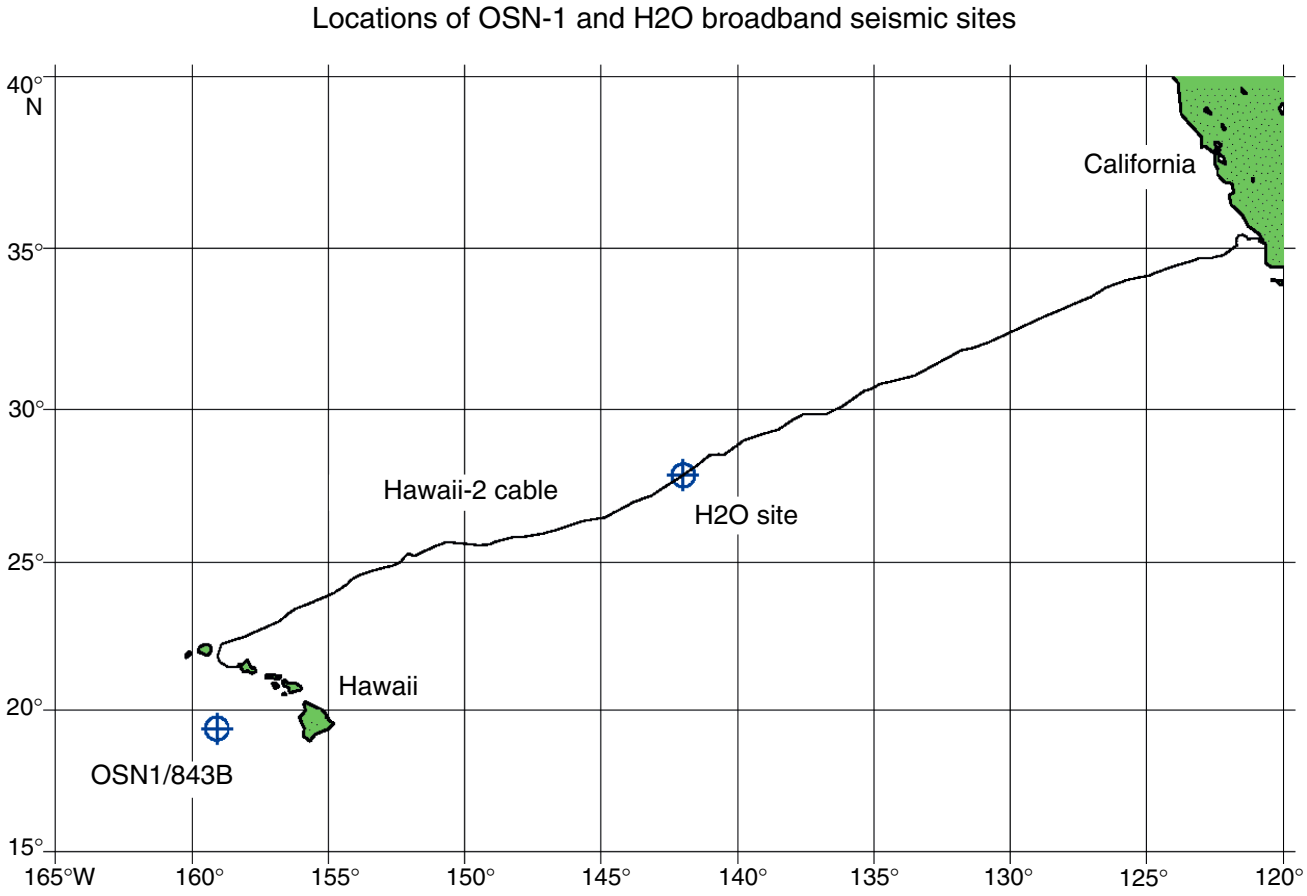

Figure F24. Vertical component spectra from the seafloor, buried, and borehole installations at the Ocean Seismic Network site (OSN-1) are compared with the spectra from the buried installation at the Hawaii-2 Observatory (H2O) and from the Kipapa, Hawaii (KIP), Global Seismograph Network station on Oahu. The H2O site has extremely low noise levels above 5 Hz and near the microseism peak from 0.1 to 0.3 Hz. The H2O site has high noise levels below 50 mHz. Otherwise, the H2O levels are comparable to the OSN borehole and KIP levels. The sediment resonances at the H2O near 1.1 and 2.3 Hz are very prominent. Power spectral density is given in decibels (dB) relative to 1 $(m/s^2)^2$/Hz.

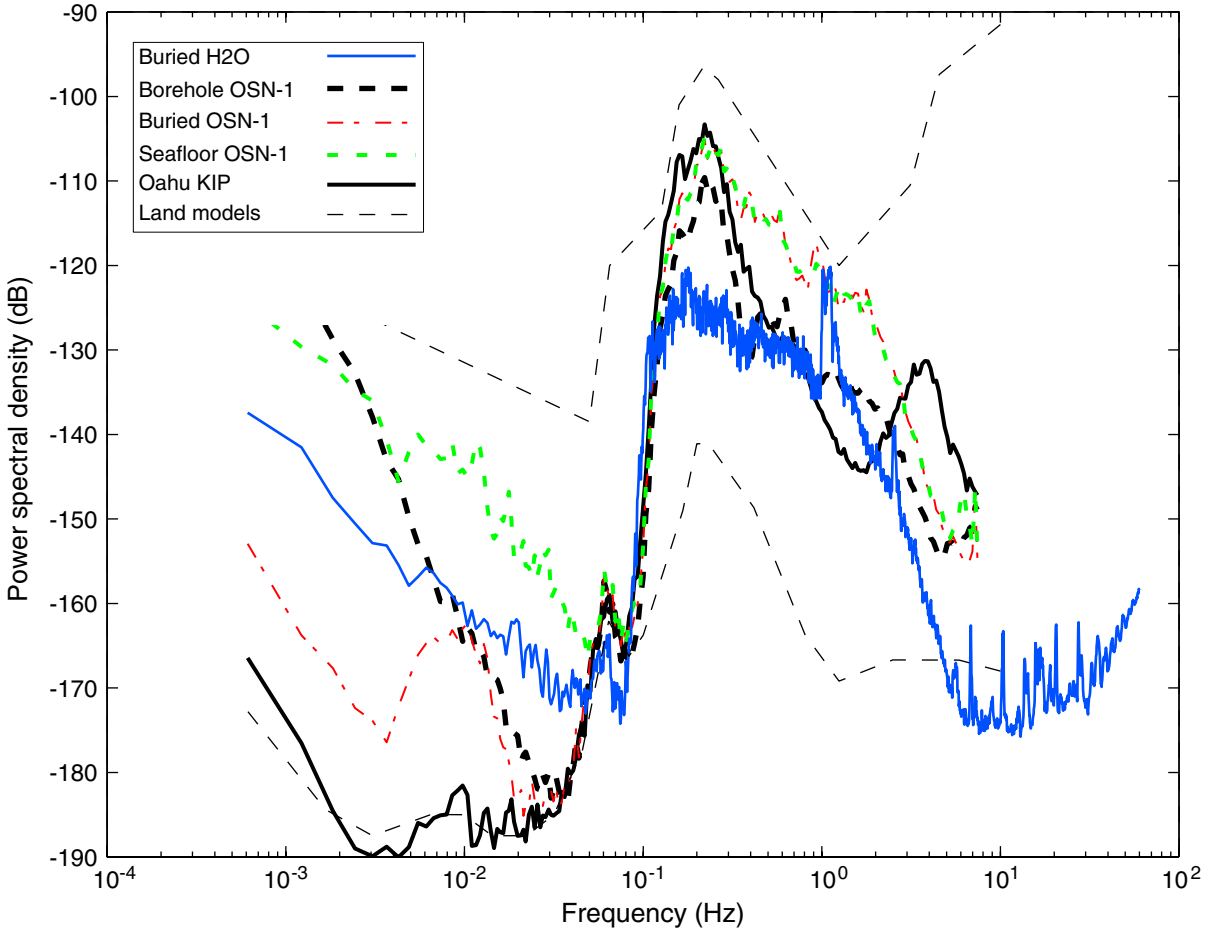

Figure F25. Horizontal component spectra from the seafloor, buried, and borehole installations at the Ocean Seismic Network site (OSN-1) are compared to the spectra from the buried installation at the Hawaii-2 Observatory (H2O) and from the Kipapa, Hawaii (KIP), Global Seismic Network station on Oahu. The sediment resonance peaks in the band 0.3 to 8 Hz are up to 35 dB louder than background levels and far exceed the microseism peak at 0.1 to 0.3 Hz. That the resonance peaks are considerably higher for horizontal components than for vertical components is consistent with the notion that these are related to shear wave resonances (or Scholte modes). Power spectral density is given in decibels (dB) relative to 1 $(m/s^2)^2$/Hz.

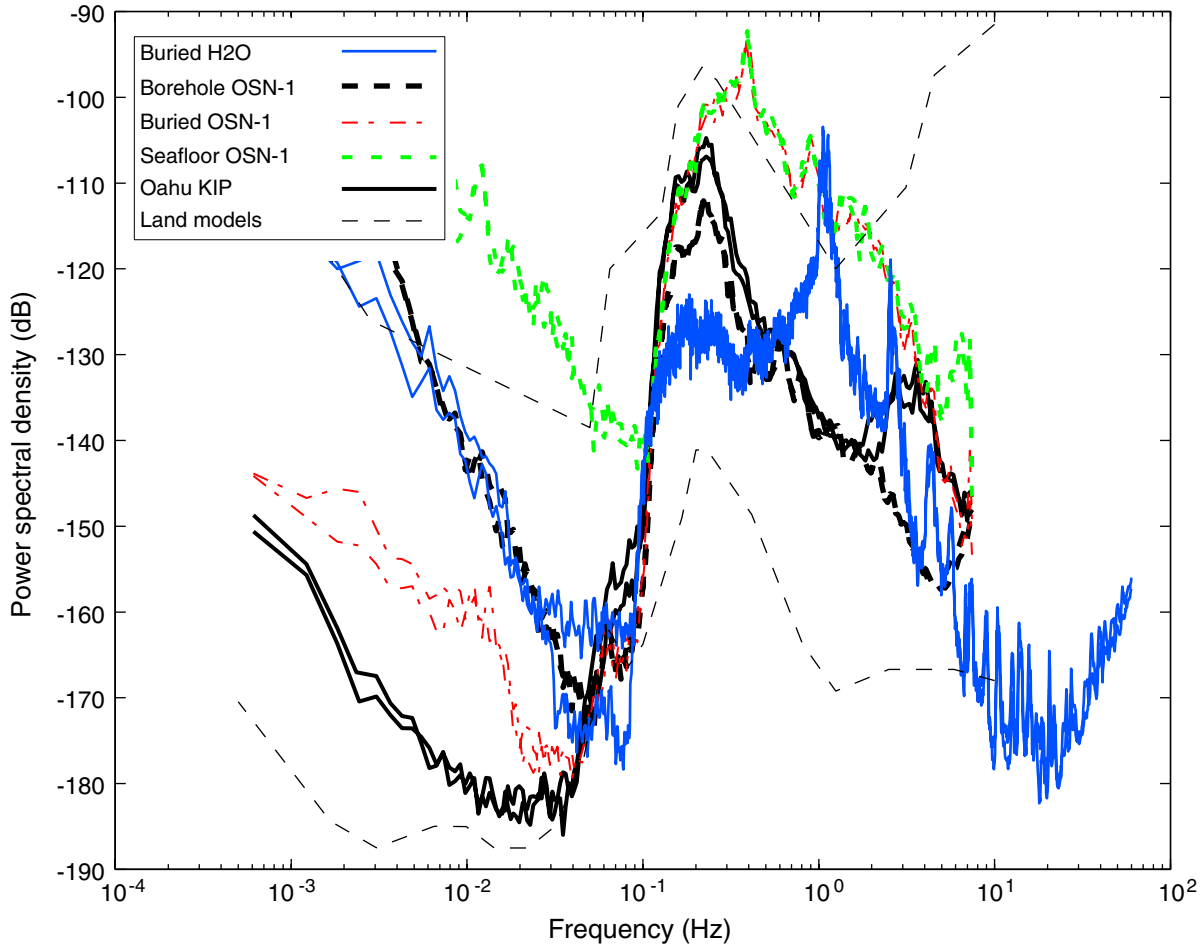

Figure F26. Photomicrograph of discoasters (Section 200-1224E-2R-7).

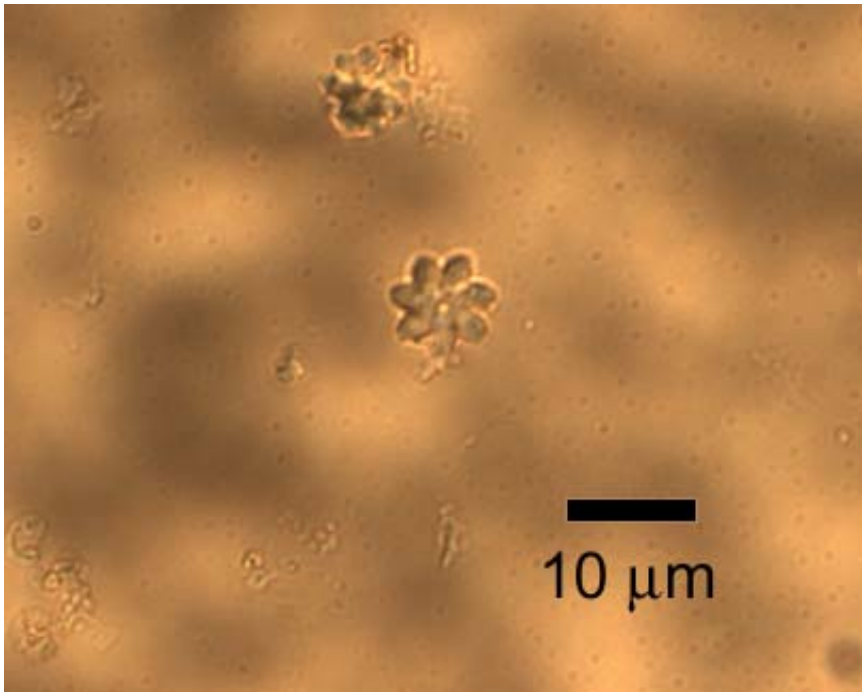

Figure F27. Photomicrograph of coccoliths (spherical) and discoasters (star shaped) (Section 200-1224E-2R-7).

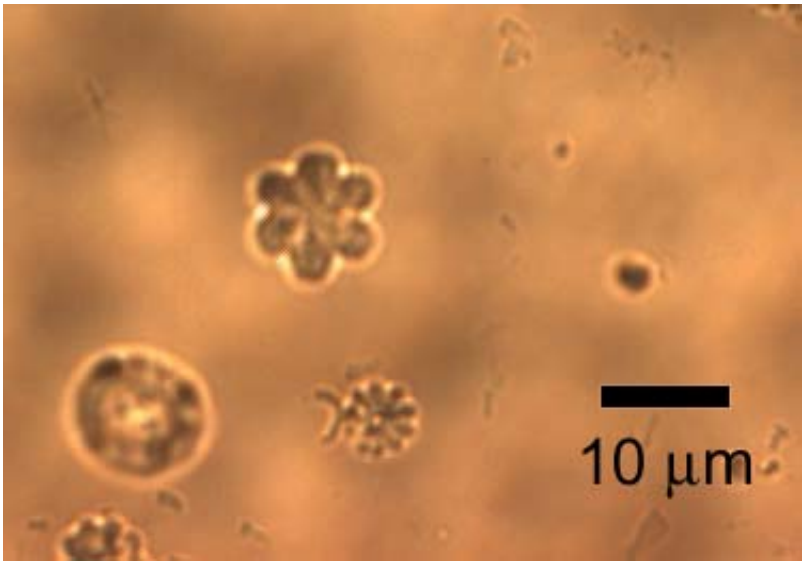

Figure F28. Lithologic summary of sediment and basalts cored at Site 1224. Recoveries of basalts in cores that crossed basement are placed below a presumed basement contact at 28 mbsf at all holes. Otherwise, recoveries are placed by convention at the top of each core. Locations of thin sections are shown by red dots. Sediments are shown down to the presumed basement contact at 28 mbsf but were not necessarily recovered above basalts in cores that crossed into basement.

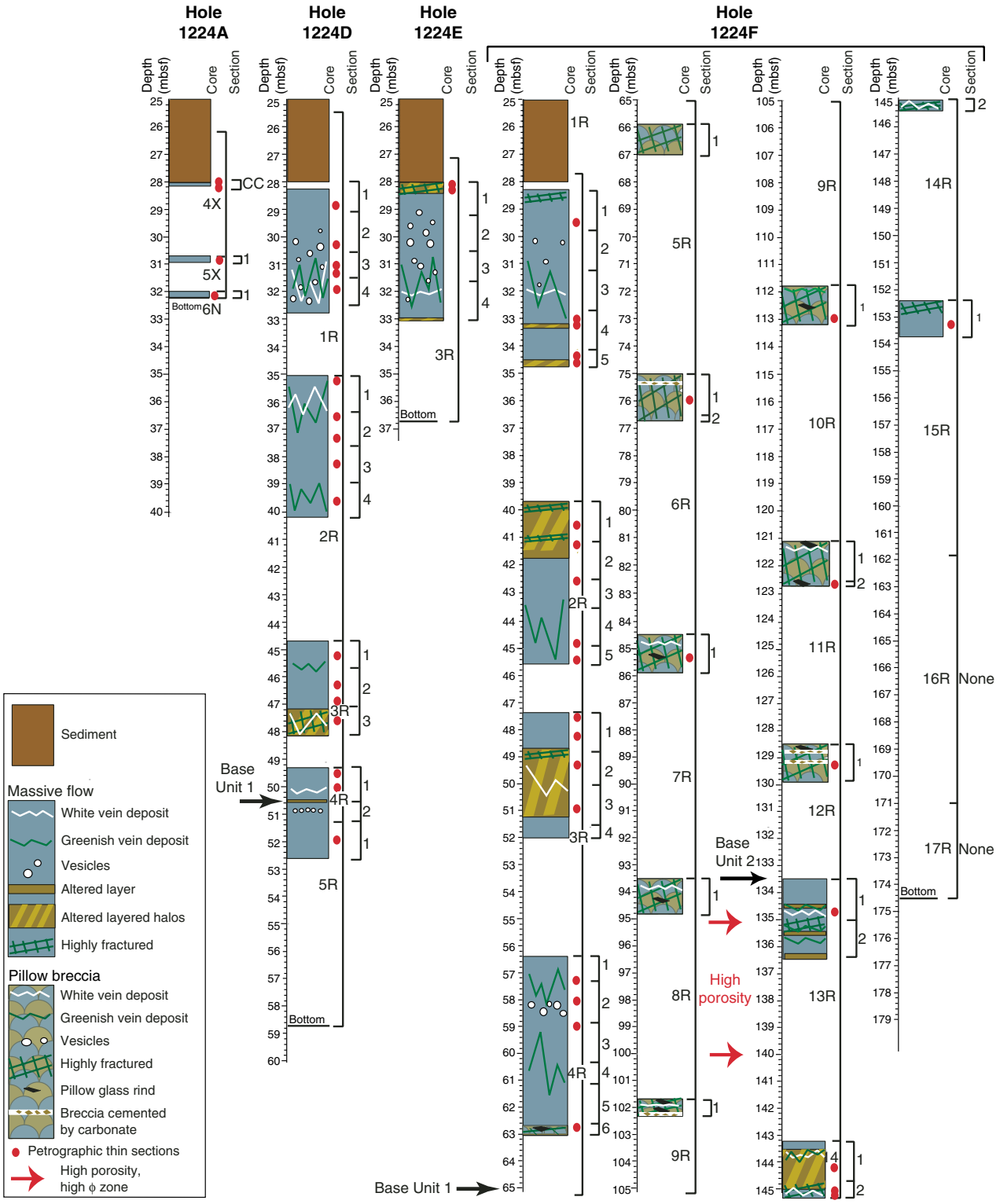

Figure F29. Close-up photograph of a portion of a Unit 1 basalt with clay-lined and calcite-filled vesicles (Sample 200-1224E-3R-2 [Piece 3, 67–70 cm]).

Figure F30. Gas pipe structure in Sample 200-1224D-4R-1 (Piece 3, 11.5–21.5 cm). **A**. Close-up photograph of the archive half, showing vertical pipes. **B**. Low-magnification photomicrograph of the large pipe at left in A (plane-polarized light), showing a large calcite-filled segregation vesicle within the pipe. Note the meniscus-like curvature at the base of the segregated basalt at the top of the vesicle. **C**. Low-magnification photomicrograph of two pipes at the right in A (plane-polarized light) **D**. Higher-magnification image of the texture of the igneous material in A (plane-polarized light). Oxide minerals (black) are prominent and include blocky titanomagnetite and finer trellislike ilmenite.

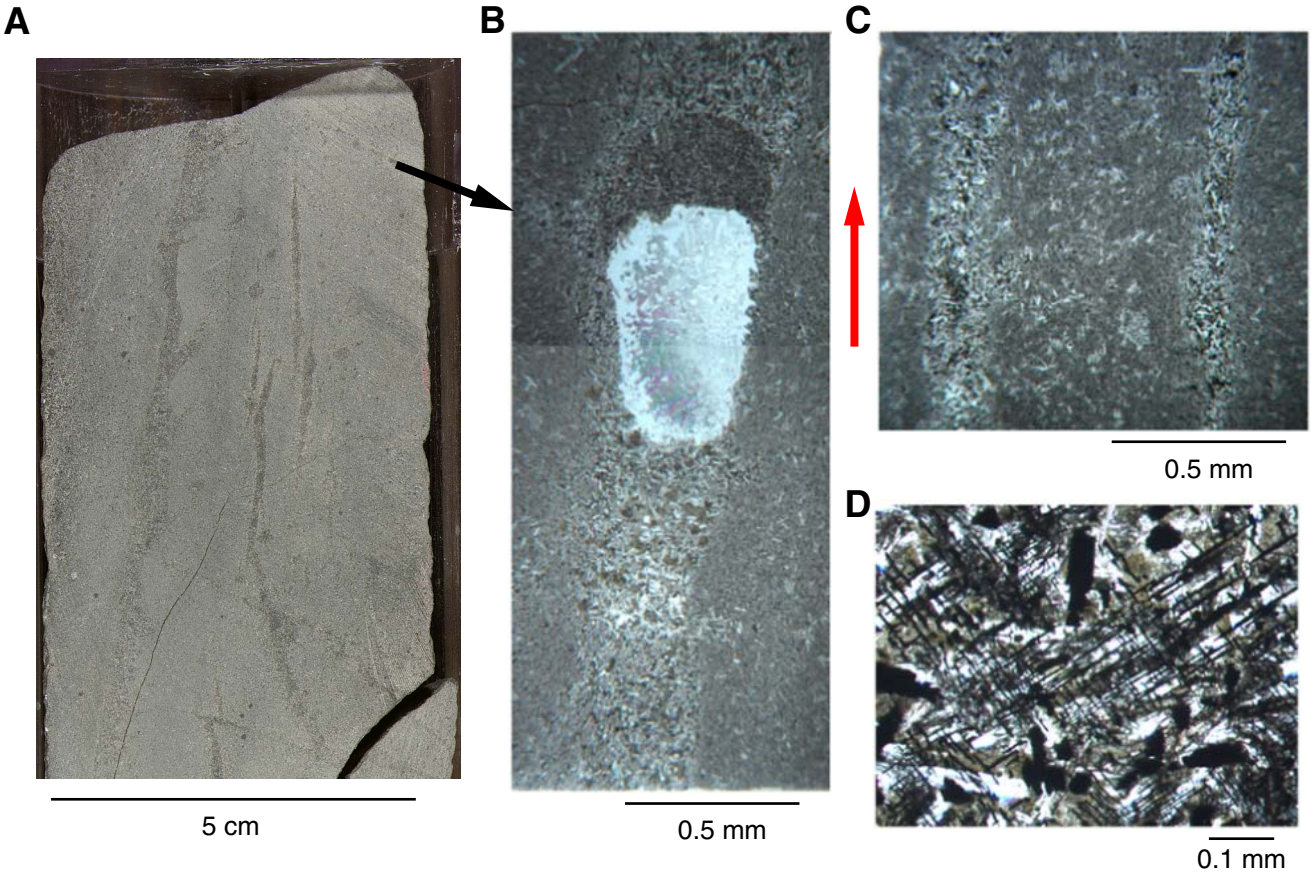

Figure F31. Close-up photograph of a wide oxidation halo at the bottom of Unit 1 (Sample 200-1224F-2R-2, [Piece 14, 81–95 cm]). The dark zone of most altered rock was formerly adjacent to a fracture lined with secondary minerals at the base of the rock that was beveled off during the coring process. The rock has three alteration zones: (1) dark orange-red next to the bottom of the piece; (2) dark gray above that, with small oblique extensions along microfractures; and (3) tannish gray, to the right of the vertical fracture at the top of the piece. The darker gray rock left of that fracture is the least altered in the specimen. The zone of most intense orange staining has possible dissolution cavities.

Figure F32. Close-up photograph of two nearly parallel subvertical fractures lined with iron oxyhydroxides and calcite from Unit 1 (Sample 200-1224F-3R-2, [Piece 8, 56.5–71.5 cm]). The fractures were first lined with iron oxyhydroxides then widened and filled with calcite. This surrounds small bits of iron oxyhydroxide that broke from the vein walls when the fracture widened. A later calcite-lined fracture diagonally crosses the larger fractures. Note the dark alteration stain next to the subvertical fracture on the right.

Figure F33. Close-up photograph of medium-grained basalt from Unit 1 with sharp alteration zones paralleling the top and bottom (Sample 200-1224F-2R-1 [Piece 9, 32–40.5 cm]). The sample is a piece of oriented whole-round core; thus, these alteration zones were originally horizontal. The specimen was cored near a vertical fracture inferred from the narrow alteration zone on the right. The swirling pattern appears to represent alteration staining along a series of concentric microfractures. The later horizontal alteration zones at the top and bottom overprint the swirls.

Figure F34. Close-up photograph of two consecutive small pieces of fine-grained basalt from Unit 2, both with nearly circumferential alteration halos (Sample 200-1224F-5R-1 [Pieces 16–17, 83.5–93.5 cm]). The dark specks are pinhole vesicles partially filled with clay minerals.

Figure F35. Scanned image of flow-top hyaloclastite from Unit 2 cemented by calcite (Sample 200-1224F-6R-1 [Piece 6, 29–33 cm]). Fresh glass is very dark gray; altered glass is gray; orange is palagonitized glass. Calcite is white to light gray.

Figure F36. Close-up photograph of an array of subparallel oblique fractures lined with iron oxyhydroxides and calcite (Sample 200-1224F-14R-1 [Pieces 7–8, 62.5–76.5 cm]; Unit 3). Most of the rock is at least partially stained uniformly with iron oxyhydroxides, which also line the three larger fractures in lower Piece 8. Calcite later lined the same fractures, as well as the fractures in Piece 7.

Figure F37. Close-up photograph of fine-grained basalt from Unit 3 cut by two generations of fractures (interval 200-1224F-13R-2 [Piece 11, 68.5–75.5 cm]). The older fractures are filled with iron oxyhydroxides and are bounded by alteration zones that form halos around fresher centers in each fracture-bound subdomain in the specimen. A second generation of calcite veins rims the left margin of the piece and forms an array of diagonal fractures extending into the center of the piece.

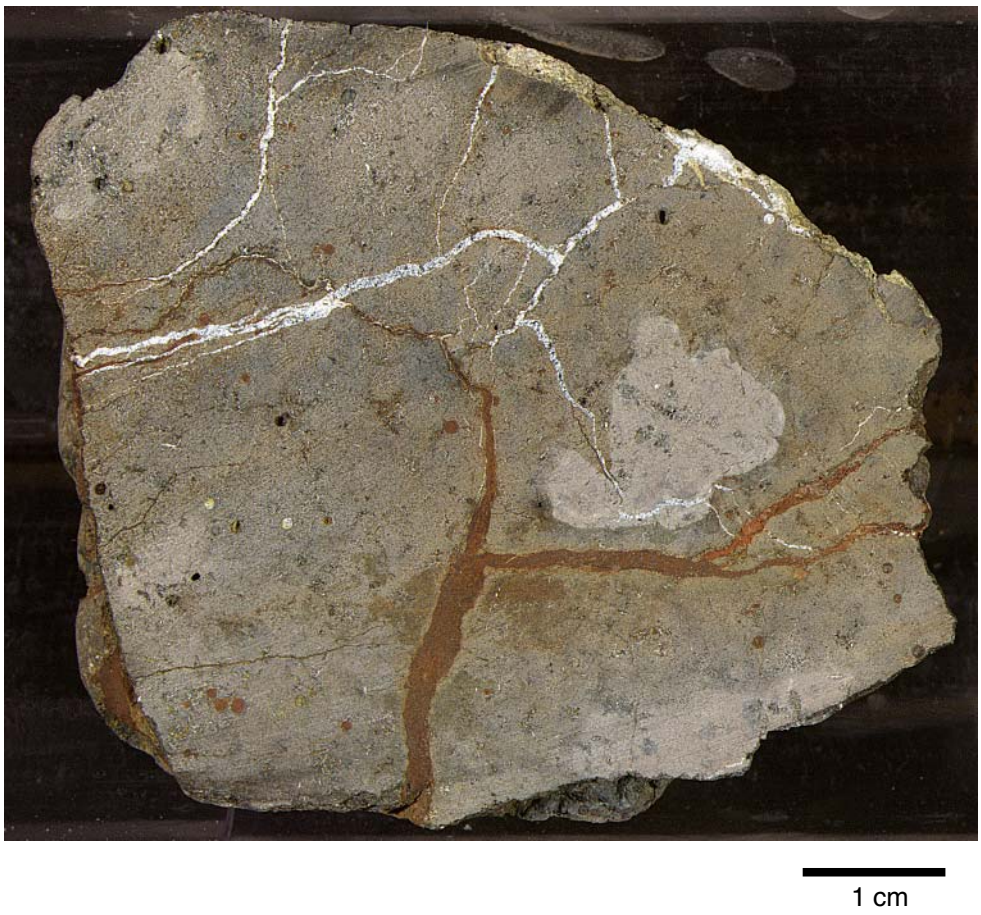

Figure F38. Petrographic features of basalt of Unit 1 from Holes 1224A and 1224D. **A.** A small glomerocryst of intergrown euhedral clinopyroxene (pale brown) and tabular plagioclase (white) set in a dark, fine-grained basaltic matrix (**Sample 200-1224A-4X-CC, 16–19 cm;** plane-polarized light). **B.** Upper massive lava flow of Unit 1 (**Sample 200-1224D-1R-2, 86–89 cm;** plane-polarized light). Note the presence of scattered dark fine-grained basaltic material in between the larger equigranular crystals of clinopyroxene (pale brown) and plagioclase (white). **C.** Detail of skeletal titanomagnetite (rhombic cross section) and ilmenite (vertical grid) seen using reflected light in one of the dark interstitial patches. The round, yellow objects are globular sulfide that segregated immiscibly from interstitial differentiated basaltic melt (**Sample 200-1224D-1R-2, 86–89 cm**). **D.** A segregation vesicle half filled with devitrified basaltic melt (right side) (**Sample 200-1224A-5X-1, 17–20 cm;** plane-polarized light). Note the curving meniscus. The remainder of the vesicle is filled with secondary nontronite (green) and a pyrite crystal (bottom center). **E.** Detail of another segregation vesicle showing coarser-grained host basalt on the left, and a fine-grained intergrowth of acicular to spherulitic plagioclase, clinopyroxene, and trellislike titanomagnetite and ilmenite in the vesicle itself (**Sample 200-1224D-1R-2, 86–89 cm;** plane-polarized light).

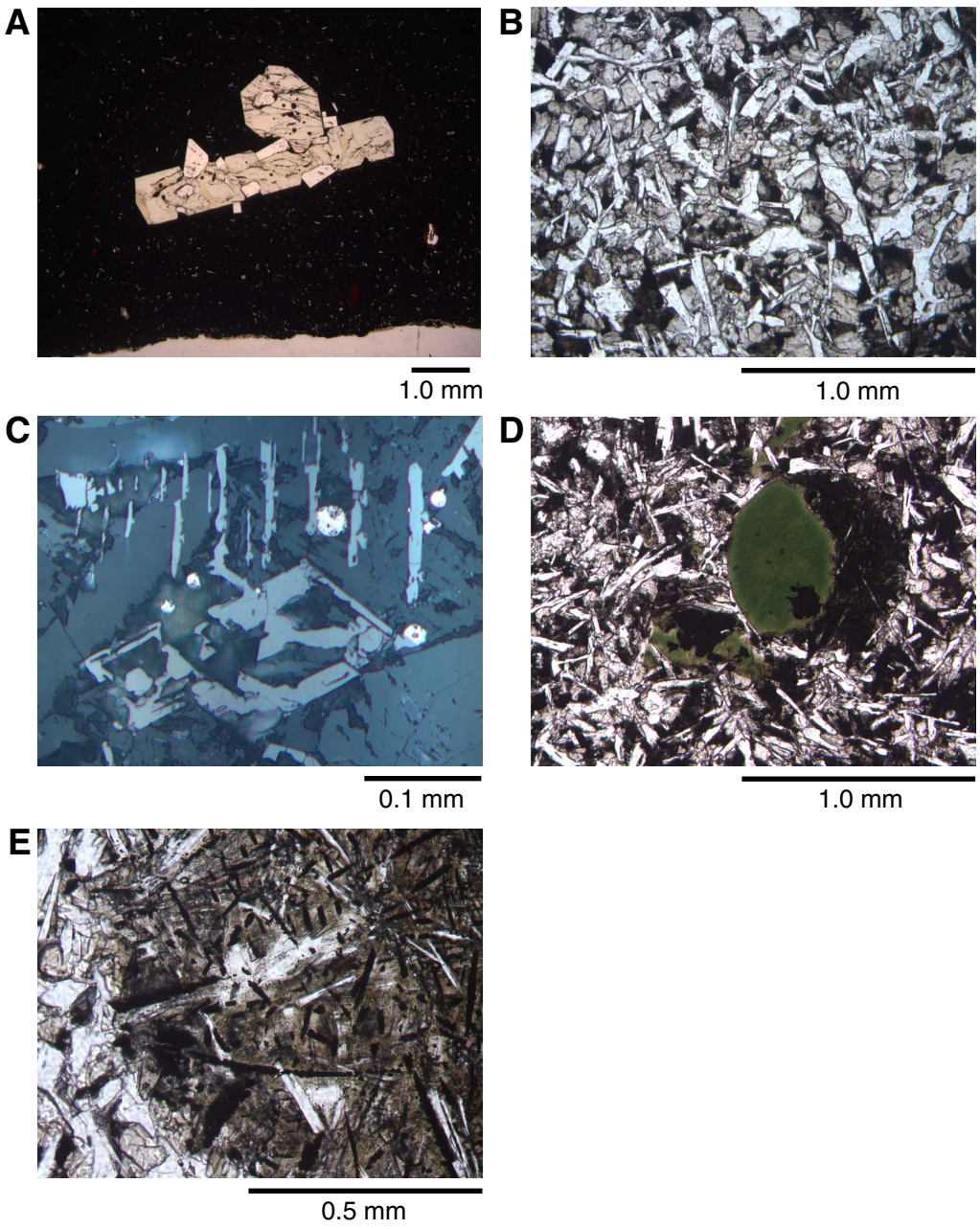

Figure F39. Textural and mineralogical features of the upper massive flow of Unit 1, Hole 1224D, all in plane-polarized light. **A.** Medium-grained basalt with minor interstitial patches of devitrified basaltic glass (**Sample 200-1224D-3R-1, 50–53 cm**). Tabular plagioclases and anhedral clinopyroxene are typical crystal morphologies in such basalts. **B.** Detail of central devitrified interstitial patch of A. **C.** Another portion of the same thin section as A with a higher proportion of devitrified interstitial material. Note the typical tabular plagioclases, the stellate plagioclase-clinopyroxene intergrowth at the lower right, and the dendritic projections on the plagioclase crystal at center right that extend into the interstitial patch. **D.** A euhedral pigeonite crystal projects from the rim of a larger plagioclase into a devitrified interstitial patch (**Sample 200-1224D-3R-2, 54–57 cm**). **E.** An interstitial patch is filled with plagioclase dendrites mantling larger crystals plus radiating needles of acicular plagioclase (**Sample 200-1224D-3R-1, 50–53 cm**). An equant crystal of euhedral titanomagnetite projects into the interstitial material at the top. The small round opaque object just below it is a globular sulfide. **F.** Same sample as E. A large, strikingly skeletal titanomagnetite has crystallized in another devitrified interstitial patch.

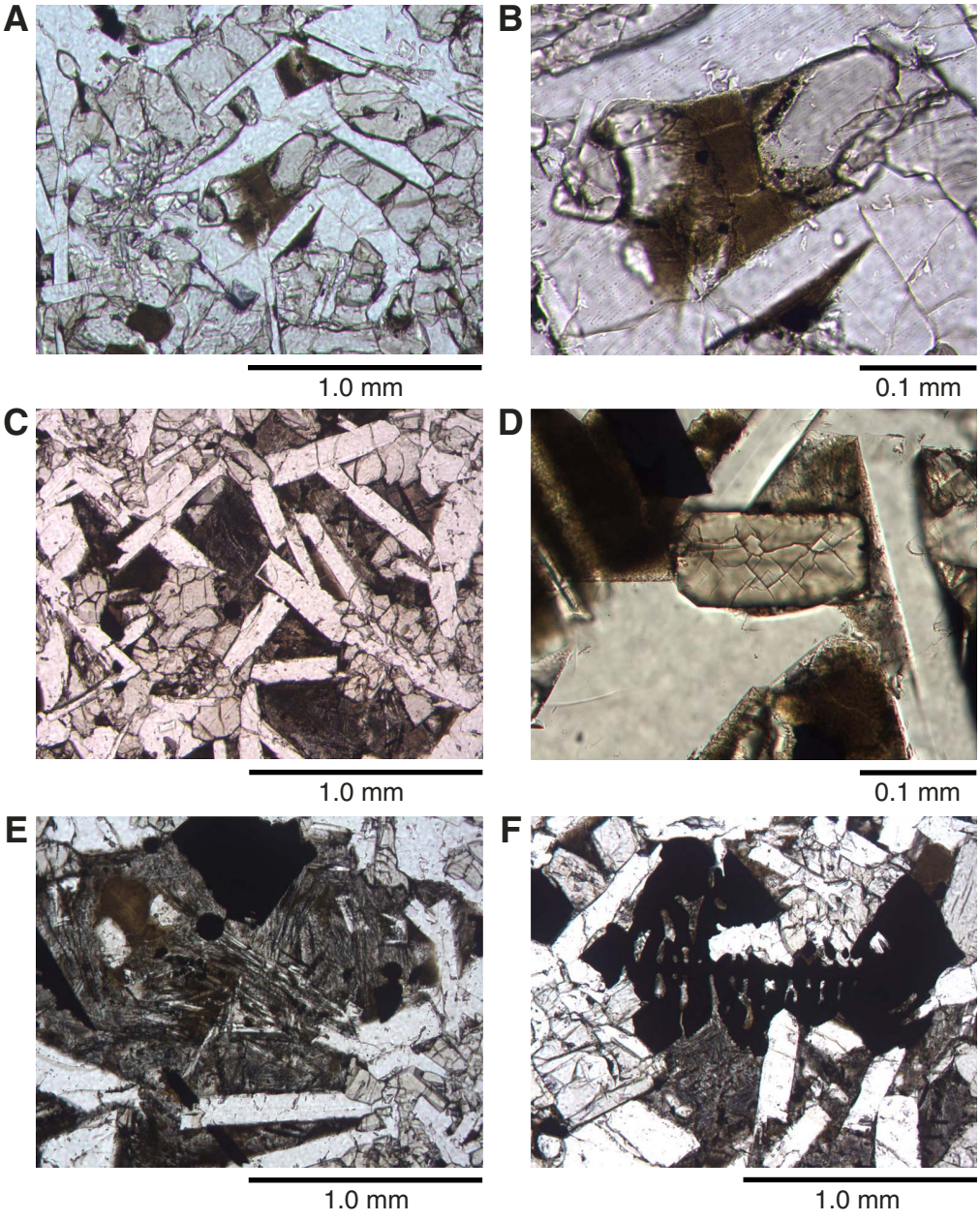

Figure F40. Features of hyaloclastite at the flow top of the upper massive flow (**Sample 200-1224E-3R-1, 6–10 cm;** all in plane-polarized light). Note the quasilayered aspect to the palagonite where it rims the glass. **A.** A palagonitic rim (yellow) embayed along cracks into fresh basalt glass (brown). **B.** Detail of palagonite rim (left) next to fresh glass. Note the layered aspect of the palagonite and the sharp boundary between it (left) and the glass (right). **C.** Detail of fresh quenched glass at the edge of a breccia shard showing small plagioclase euhedra and tiny acicular plagioclase crystals, some of them intergrown with clinopyroxene. A fracture lined with palagonite cuts vertically from the top of the photomicrograph nearly to its base. **D.** Individual tabular crystals of plagioclase and plagioclase-clinopyroxene intergrowths coated with dark-brown spherulitic material near the edge of a glass shard. **E.** Palagonite replacing glass with acicular needles of plagioclase and stellate plagioclase-clinopyroxene intergrowths. Most crystals are coated with a thin rim of brown spherulitic material. Note the fracture pattern in the altered glass. **F.** Detail of a palagonitized glass shard showing crystal intergrowths and an altered skeletal olivine replaced by orange secondary minerals.

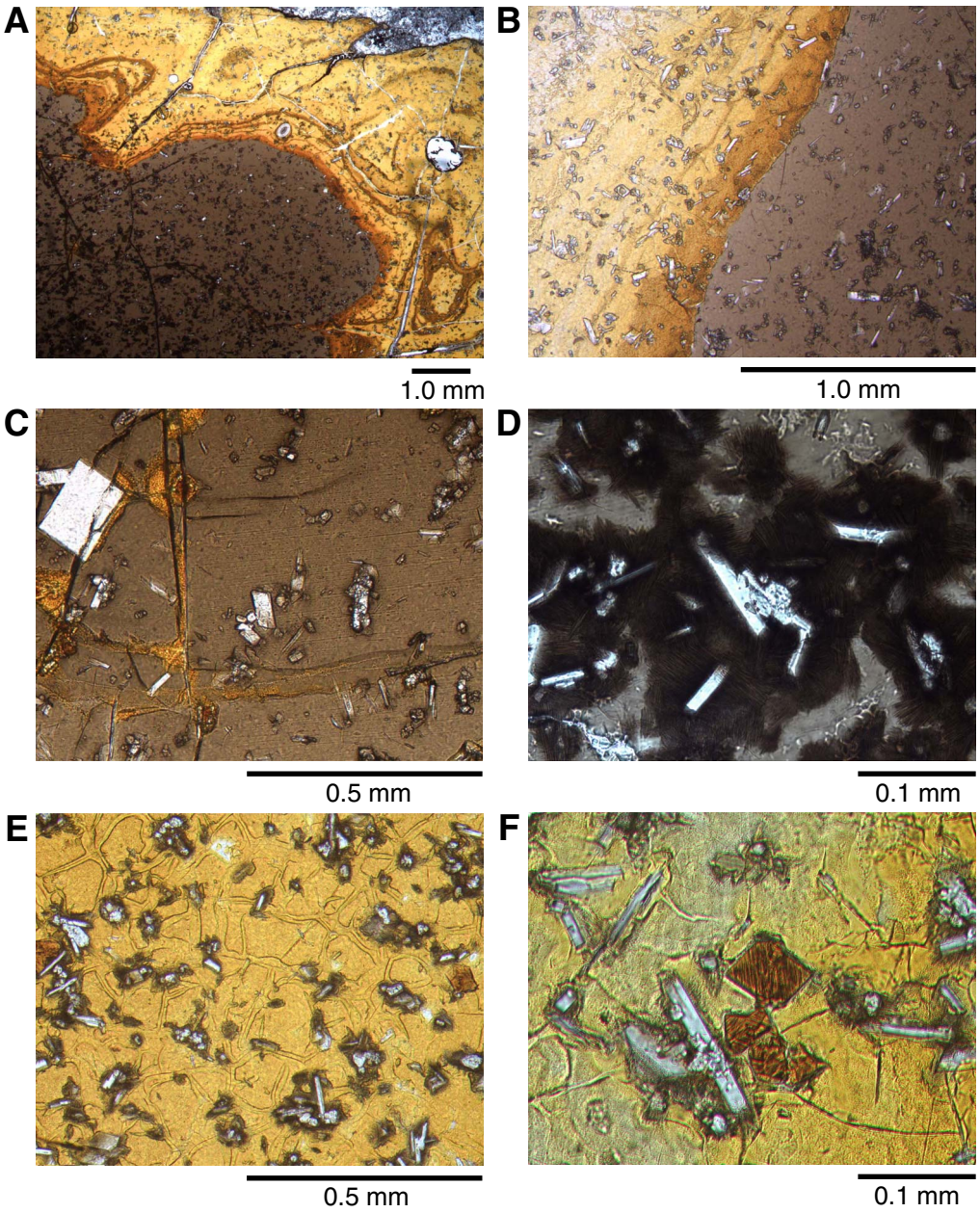

Figure F41. Quench textures and crystal morphologies of Unit 2 pillow rims from Hole 1224F. **A.** This full thin section scan, photographed in transmitted light, shows the progression downward from a glassy rim to completely coalesced dark-brown spherulites (**Sample 200-1224F-4R-6, 11–13 cm;** plane-polarized light). Near the rim, many of the dark-brown spherulites only mantle individual plagioclase crystals and stellate intergrowths. **B.** Another glassier pillow rim with abundant acicular plagioclase crystals and plagioclase-clinopyroxene intergrowth (**Sample 200-1224F-11R-2, 13–16 cm;** plane-polarized light). The crystals are mantled with thin dark spherulitic rims that coalesce toward the bottom of the photomicrograph. **C.** Euhedral olivine, partly altered at its rim, set in glass (**Sample 200-1224F-11R-2, 13–16 cm;** plane-polarized light). **D.** Euhedral and faintly zoned clinopyroxene microphenocryst set in glass (**Sample 200-1224F-11R-2, 13–16 cm;** plane-polarized light). **E.** A gabbro clot in fine-grained basalt (**Sample 200-1224F-3R-1, 90–92 cm;** plane-polarized light). Note the absence of titanomagnetite or other opaque minerals in the clot. **F.** **Sample 200-1224F-3R-1, 90–92 cm;** in cross-polarized light.

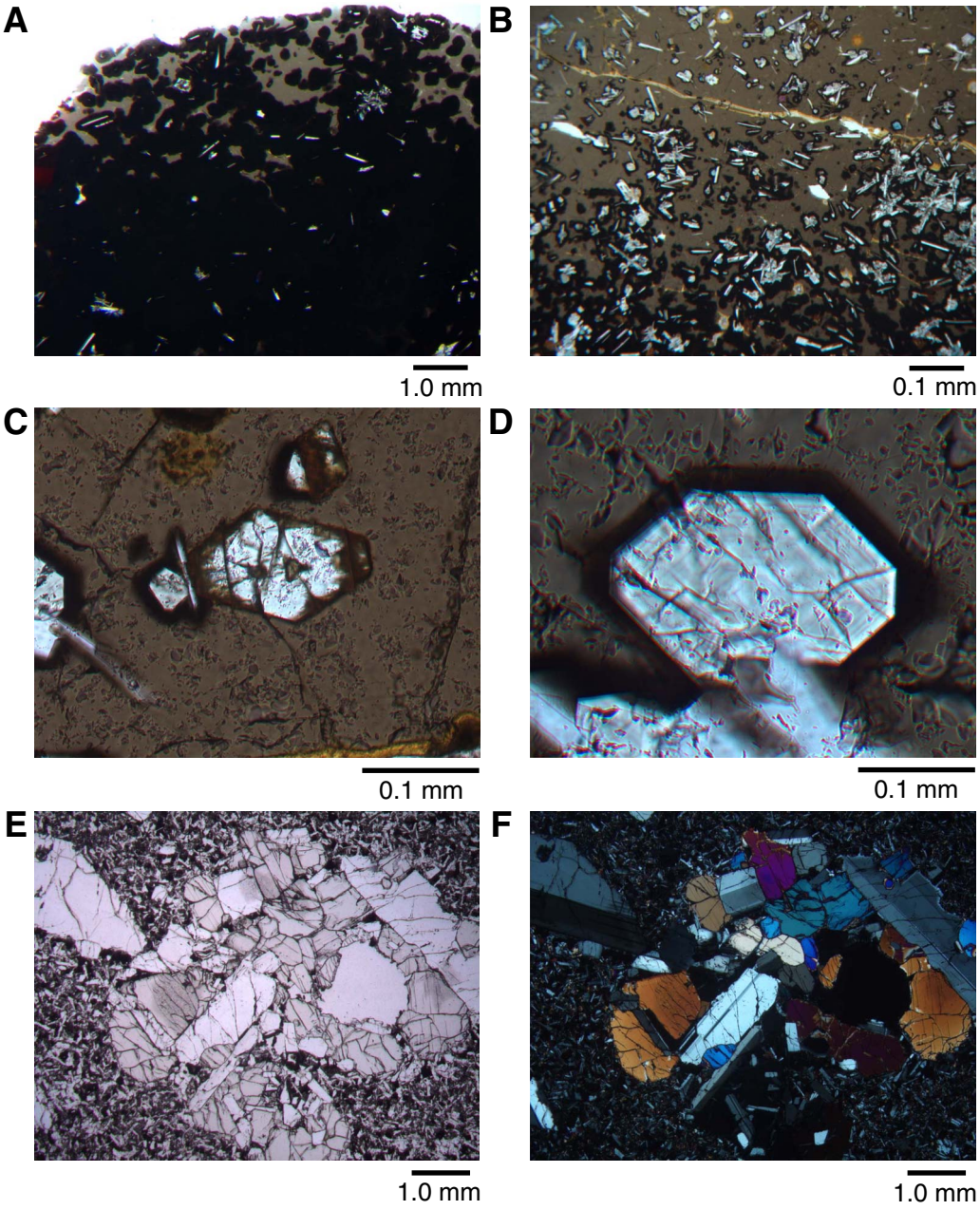

Figure F42. Textures of hyaloclastites and glass shards (**Sample 200-1224F-12R-1, 61–64 cm;** all in plane-polarized light). The sample is at the top of ferrobasalts of Unit 3. **A.** A low-magnification photomicrograph of palagonitized hyaloclastite. The altered glass shards are not vesicular. Note zoning of palagonitic alteration in several shards. **B.** Another portion of the same hyaloclastite showing palagonite rims surrounding relict fresh brown basaltic glass. The glass contains almost no crystallites. **C.** Detail of zoning of palagonite of one altered glass shard seen in A, center left. **D.** Tiny and numerous plagioclase and clinopyroxene crystallites in a glass shard in the hyaloclastite that experienced incipient crystallization. **E.** A slightly more crystalline glass shard similar to D but with a pale-brown spherulitic overgrowth on many of the crystallites.

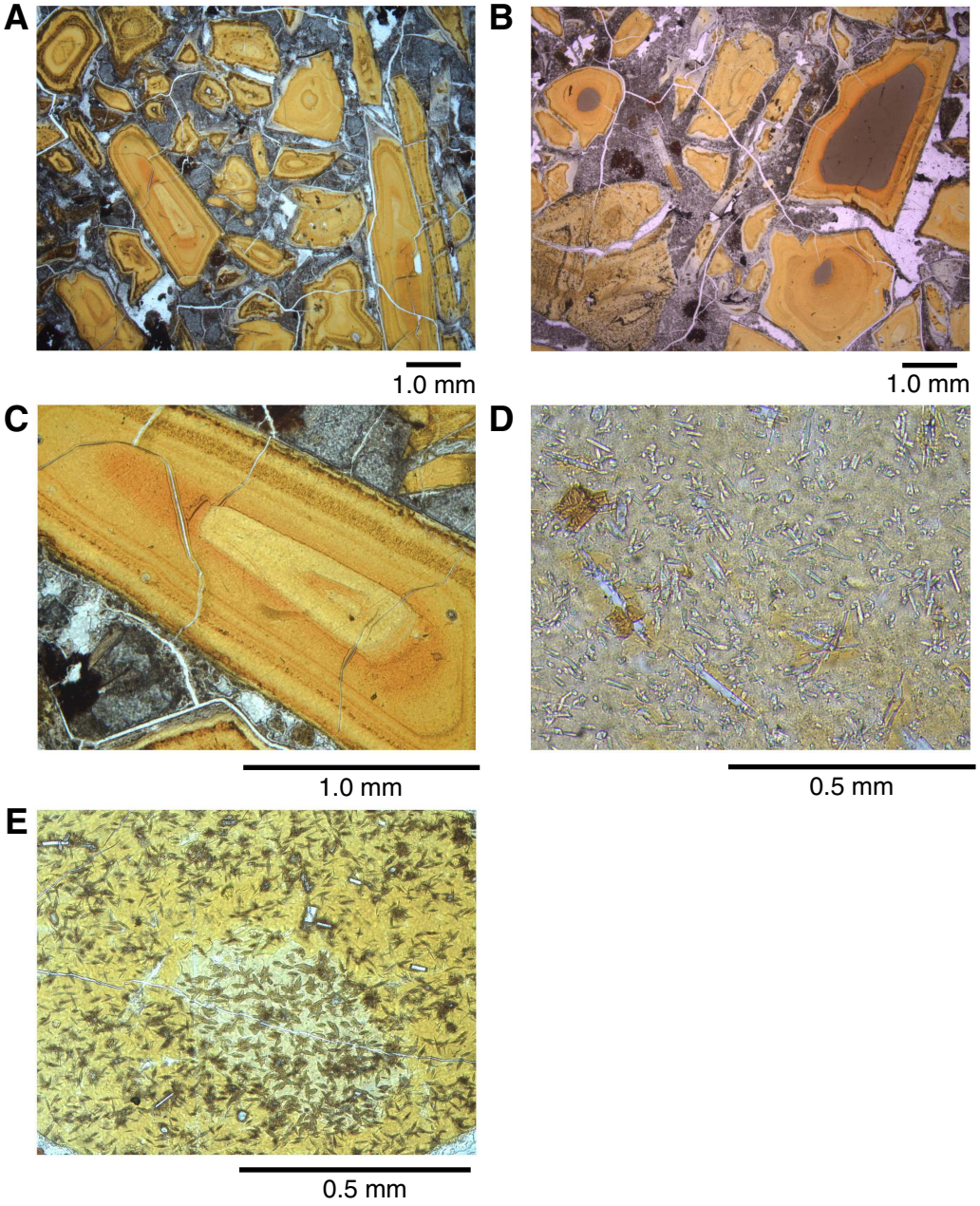

Figure F43. MgO vs. TiO_2 for basalts analyzed from Site 1224. Also plotted are compositions of normal mid-ocean-ridge basalt (N-MORB) glasses (small gray dots = basalts, half-filled magenta squares = andesites and rhyodacites) from the East Pacific Rise (compiled from the Lamont-Doherty Basalt Database; Y. Niu, J. Natland, and P. Castillo, unpubl. data). Blue dots = samples from the upper flow of lithologic Unit 1 at Site 1224, red dots = samples from the lower flow, green squares = pillow samples from lithologic Unit 2, dark-blue diamonds = pillow samples from lithologic Unit 3. Samples from the East Pacific Rise span the full range of enrichment in TiO_2 during differentiation to ferrobasalts. Samples from Site 1224 are at the low-MgO and high-TiO_2 end of the range, indicating that they are quite strongly differentiated.

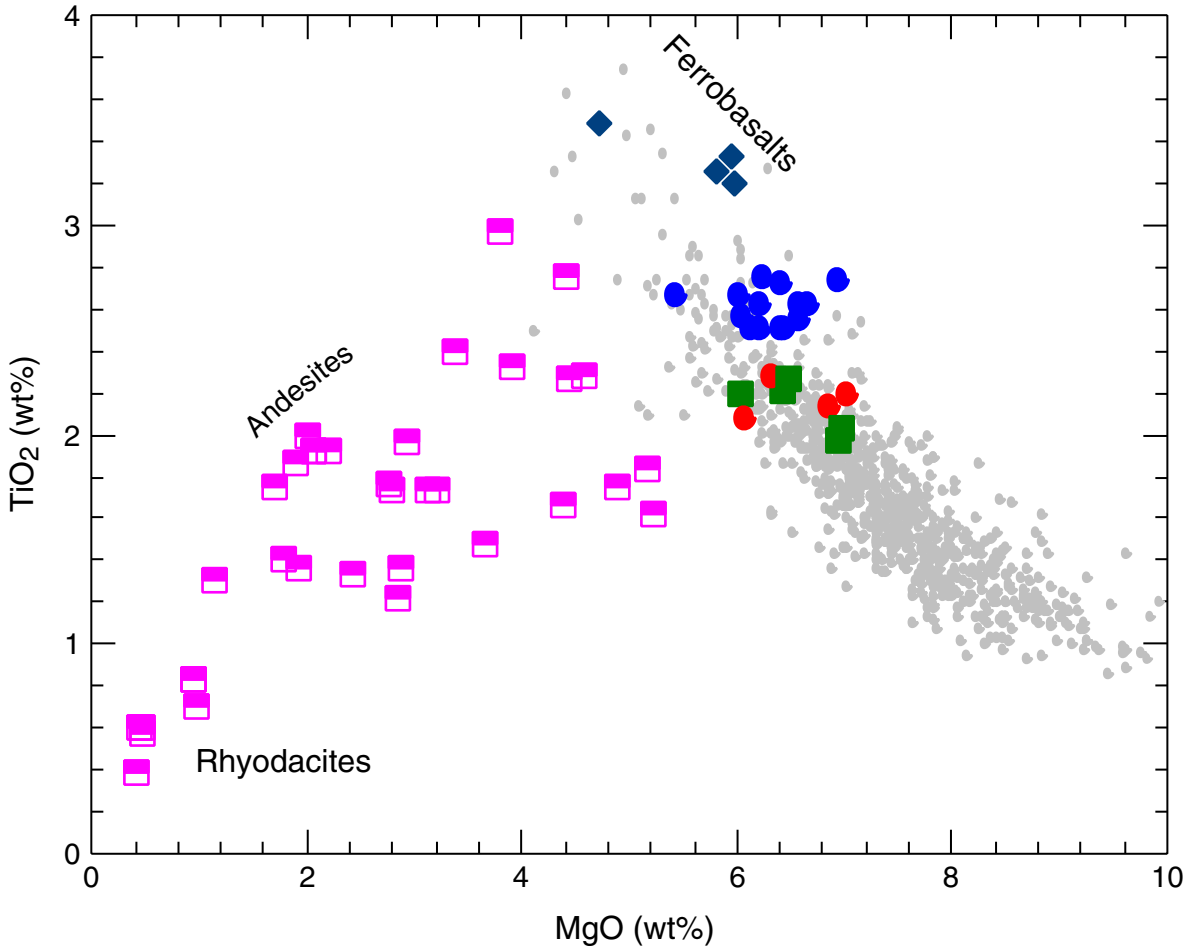

Figure F44. Chemical compositions vs. depth for basalts of Hole 1224D. **A.** TiO_2 vs. depth. **B.** Zr vs. depth. The vertical lines in A suggest the possible breakdown of the hole into three chemical types based on TiO_2. In B, an additional type may be represented by two samples at the top of the basalts based on Zr concentrations. Blue dots = samples from the upper flow of lithologic Unit 1 at Site 1224, red dots = samples from the lower flow, green squares = pillow samples from lithologic Unit 2, dark-blue diamonds = pillow samples from lithologic Unit 3.

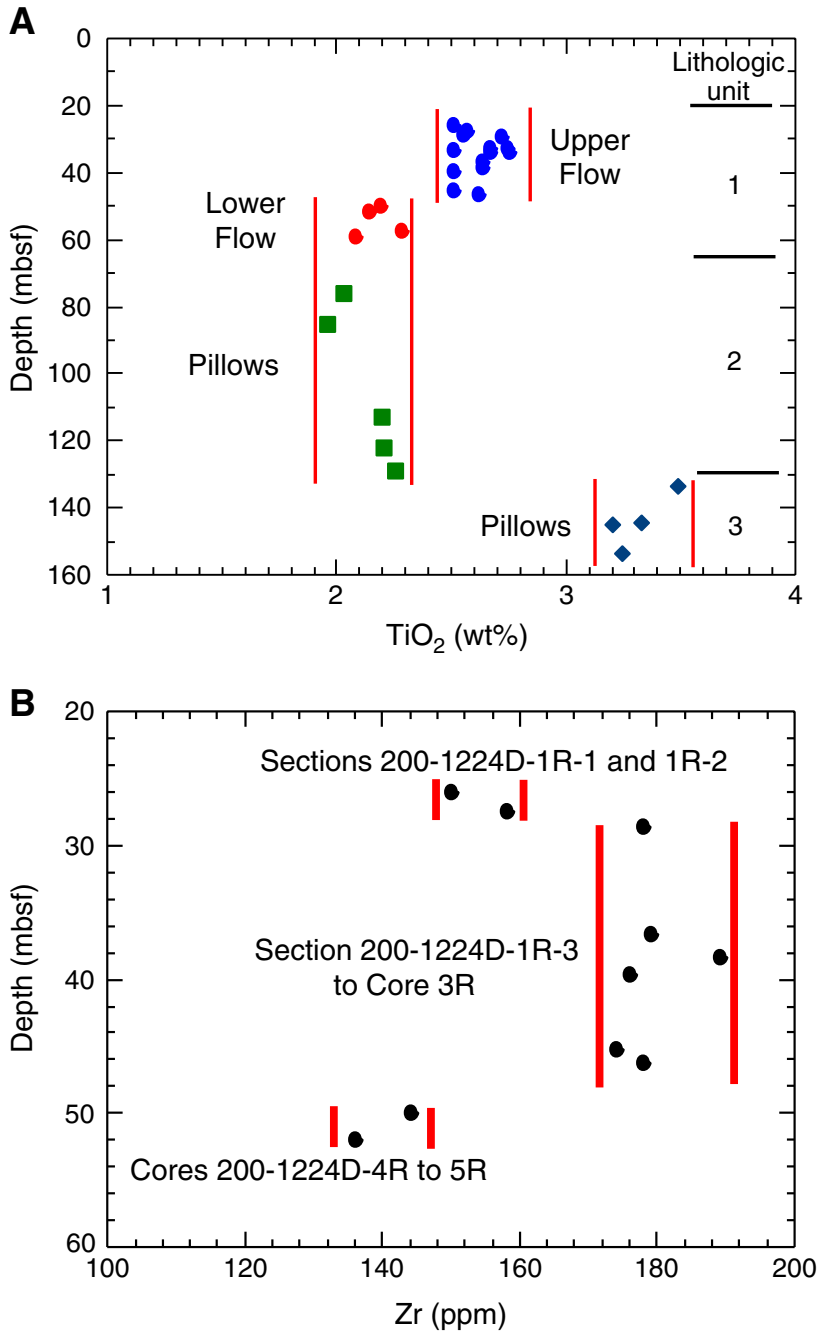

Figure F45. Loss on ignition (LOI) plotted vs. depth for (**A**) basalts from Hole 1224D and (**B**) vitric tuffs from Hole 1223A (red triangles = Units 5 and 11, gray triangles = siltstones). The basalts of Hole 1224D are significantly less altered.

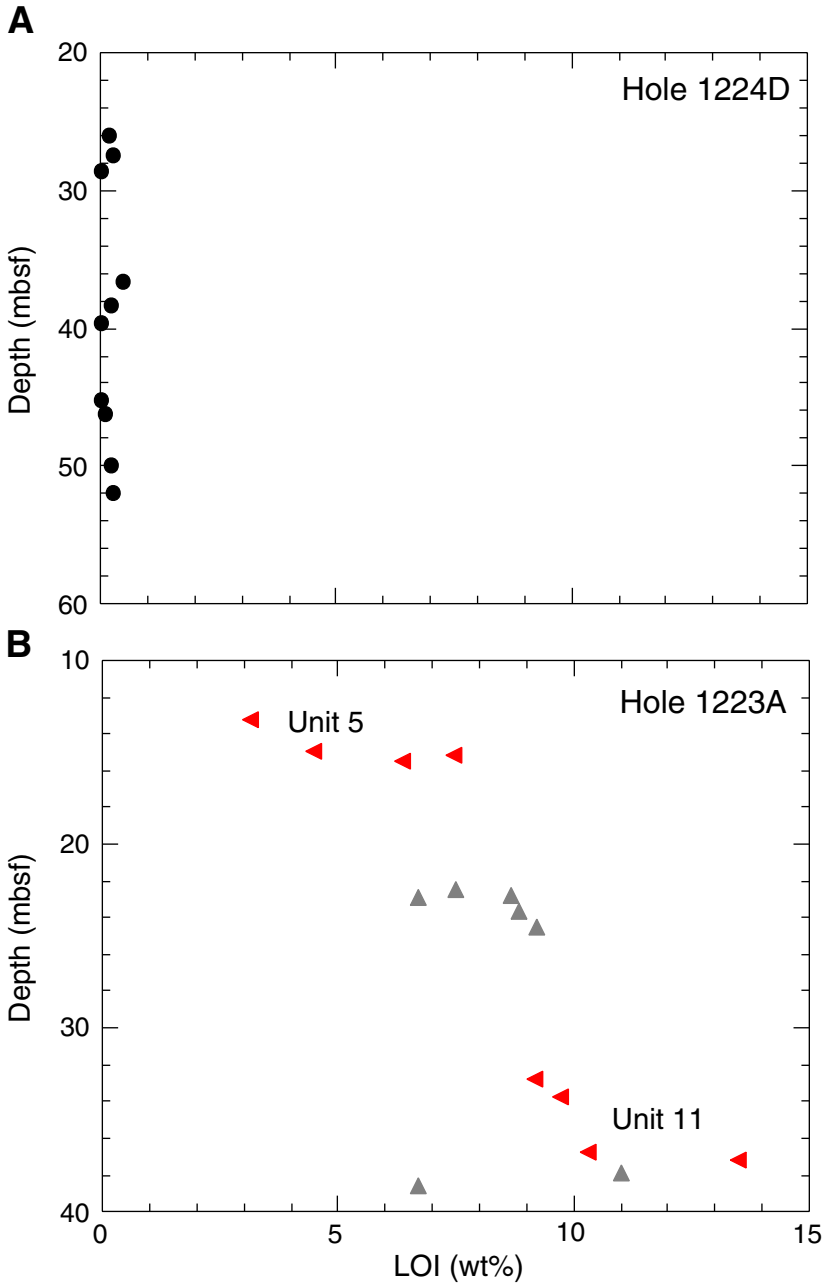

Figure F46. MgO vs. K_2O showing the small deviation from differentiated normal mid-ocean-ridge basalt (N-MORB) glass compositions of the fresh basalts of Hole 1224D (large black dots). Samples from Cores 200-1224D-1R to 3R are from the upper flow, and Cores 4R and 5R are from the lower flow. Also plotted are compositions of N-MORB glasses (small red dots) from the Pacific-Antarctic East Pacific Rise (Y. Niu, P. Castillo, and J. Natland, unpubl. data). These exemplify the range of differentiation from high to low MgO contents and low to high TiO_2 contents typical for basalts of the East Pacific Rise. Lines link three samples with slightly high K_2O to less altered samples.

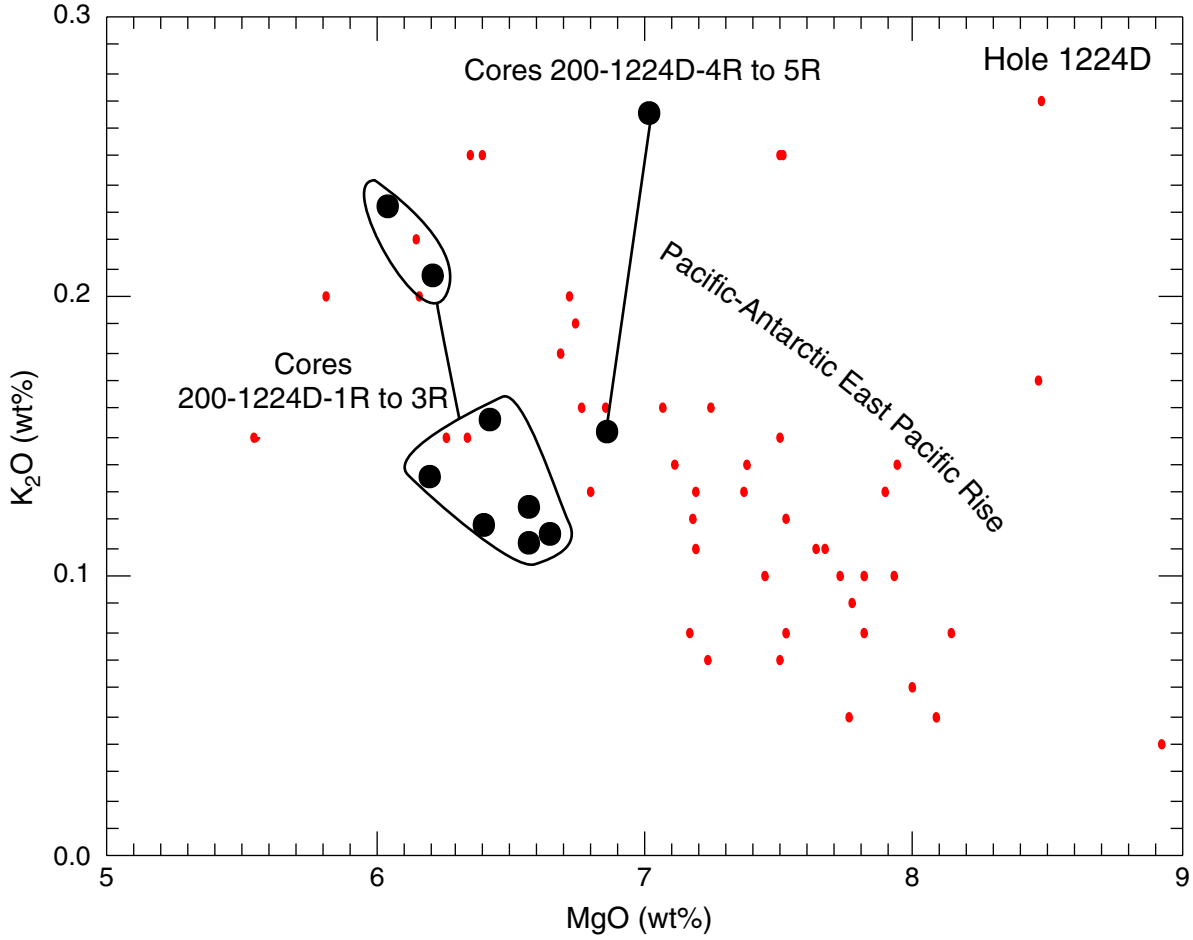

Figure F47. MgO vs. Ba for samples from Hole 1224D (large dots) compared with fresh glasses from the Pacific-Antarctic East Pacific Rise. Small dots = glass compositions, large dots = fresh basalts.

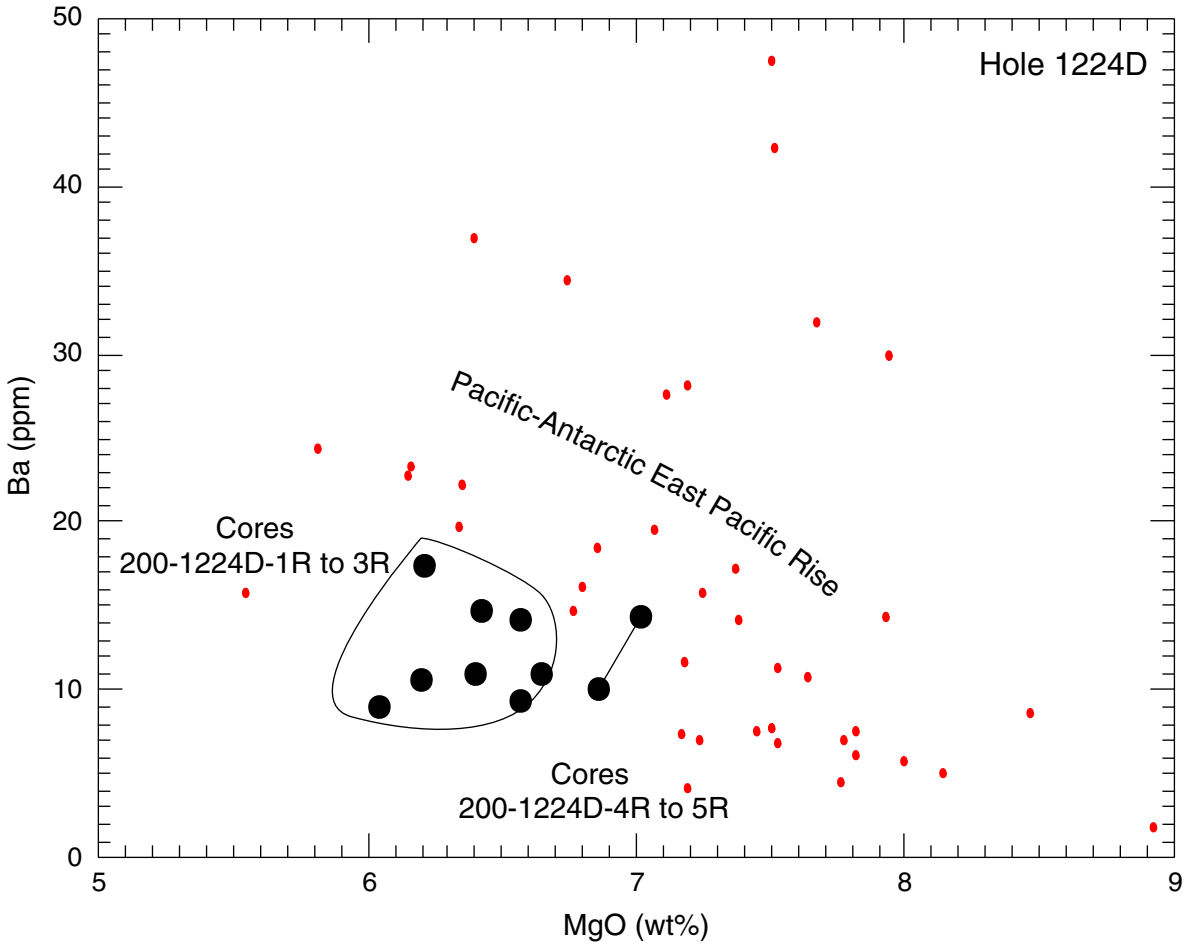

Figure F48. Sampling point and identification of the main secondary minerals in the basement section at Site 1224. Green = clay, blue = carbonate, gray = quartz, yellow = zeolite. Note that in order to minimize confusion with curated depths, the top basalt core in each hole on this figure has not been shifted to 28 mbsf as was done in Figure F28, p. 94. (Continued on next page.)

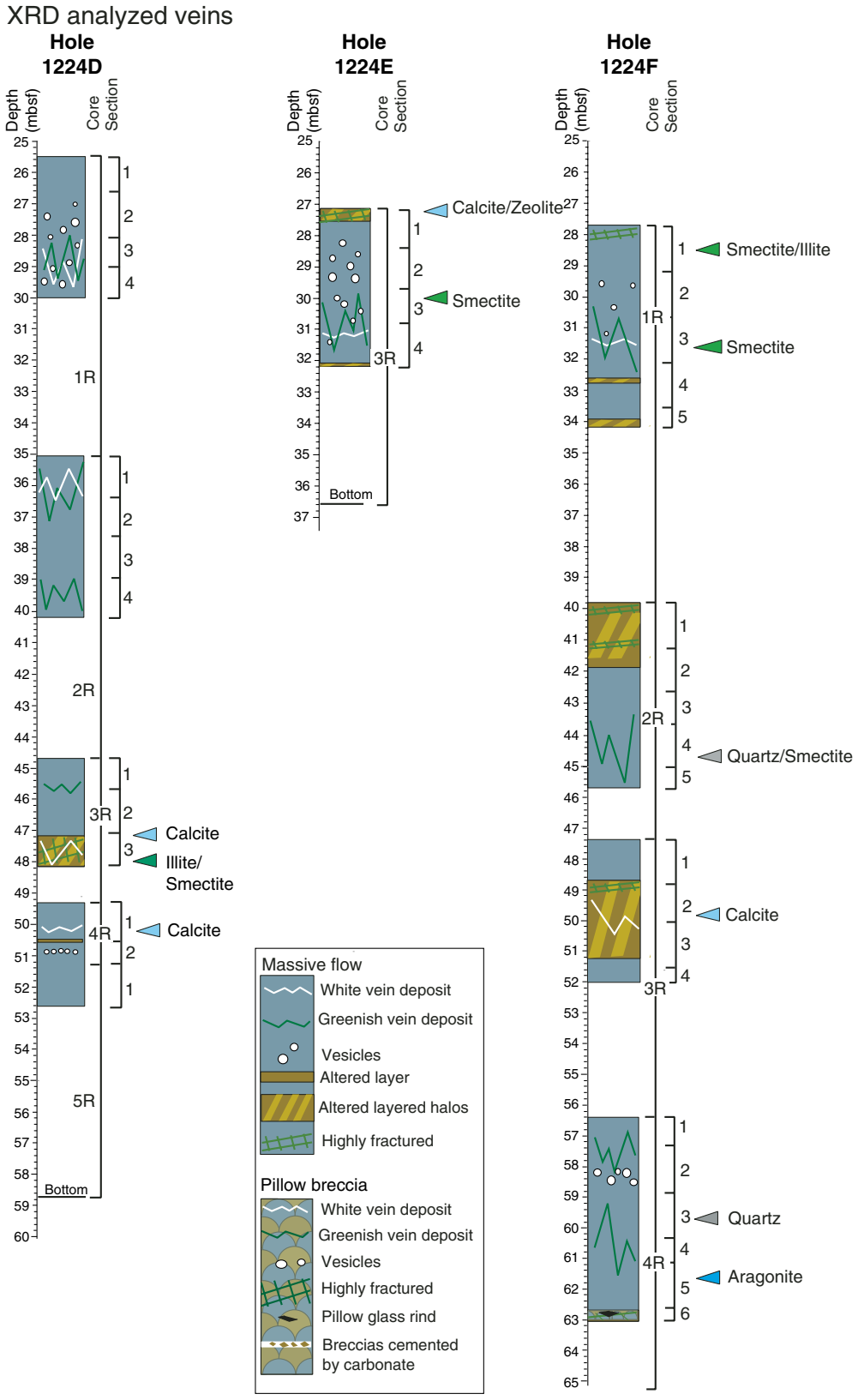

Figure F48 (continued).

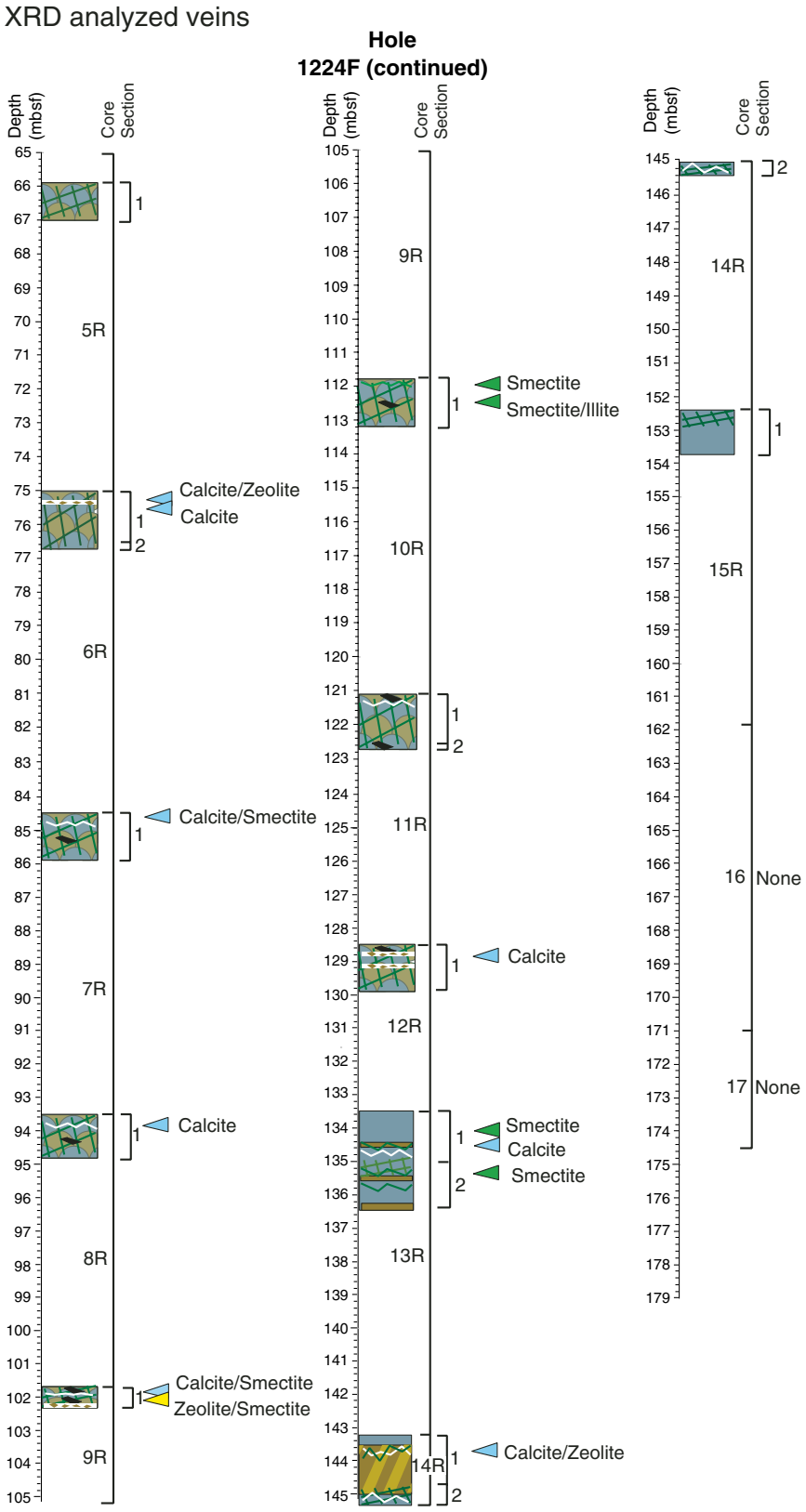

Figure F49. Typical XRD results for clay veins: (**A**) smectite (interval 200-1224E-3R-3, 46–50 cm) and (**B**) illite (interval 200-1223D-3R-3, 90–92 cm). Significant peaks are identified. Montmorillonite and saponite are in the smectite group. Laumonite is in the zeolite group. Green = montmorillonite, blue = saponite, red = illite, black = laumonite. Cps = counts per second.

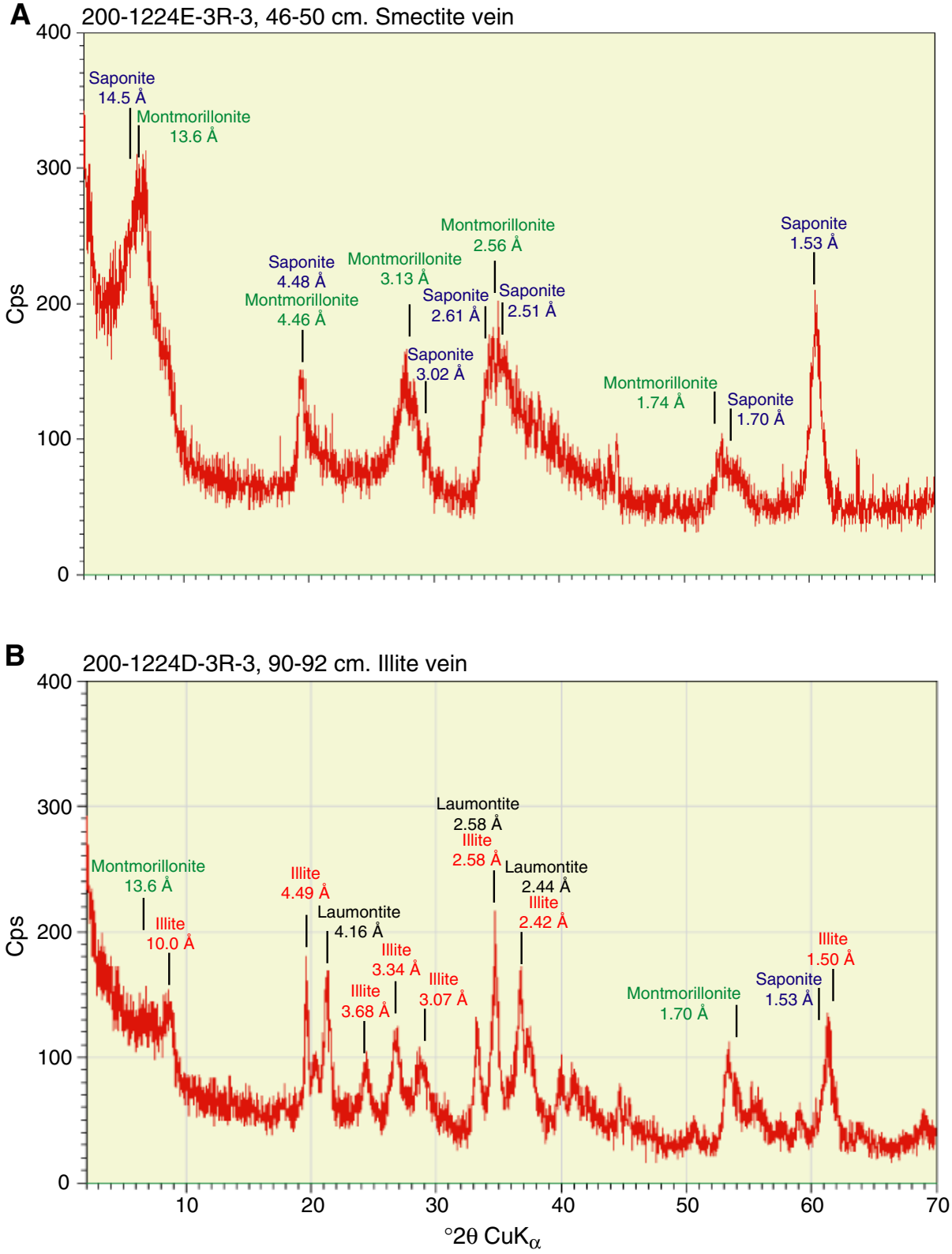

Figure F50. XRD results for carbonate veins: (**A**) calcite (interval 200-1224D-4R-1, 90–92 cm) and (**B**) aragonite (interval 200-1224F-4R-5, 43–47 cm), with principal peaks labeled. Cps = counts per second.

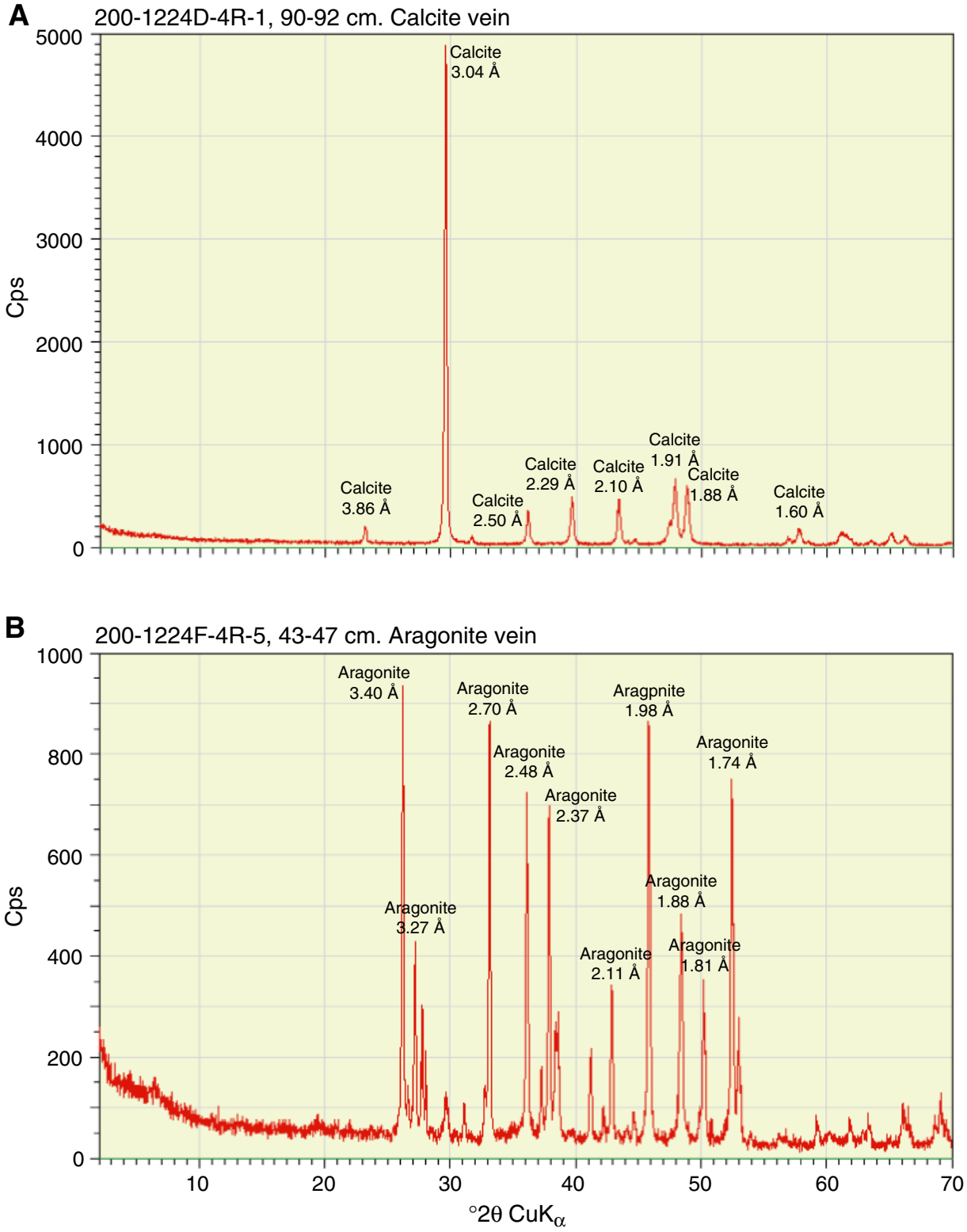

Figure F51. XRD result for a zeolite vein (interval 200-1224F-9R-1, 55–57 cm) with the main peaks of phillipsite and montmorillonite. Phillipsite is in the zeolite group. Montmorillonite is in the smectite group. Cps = counts per second.

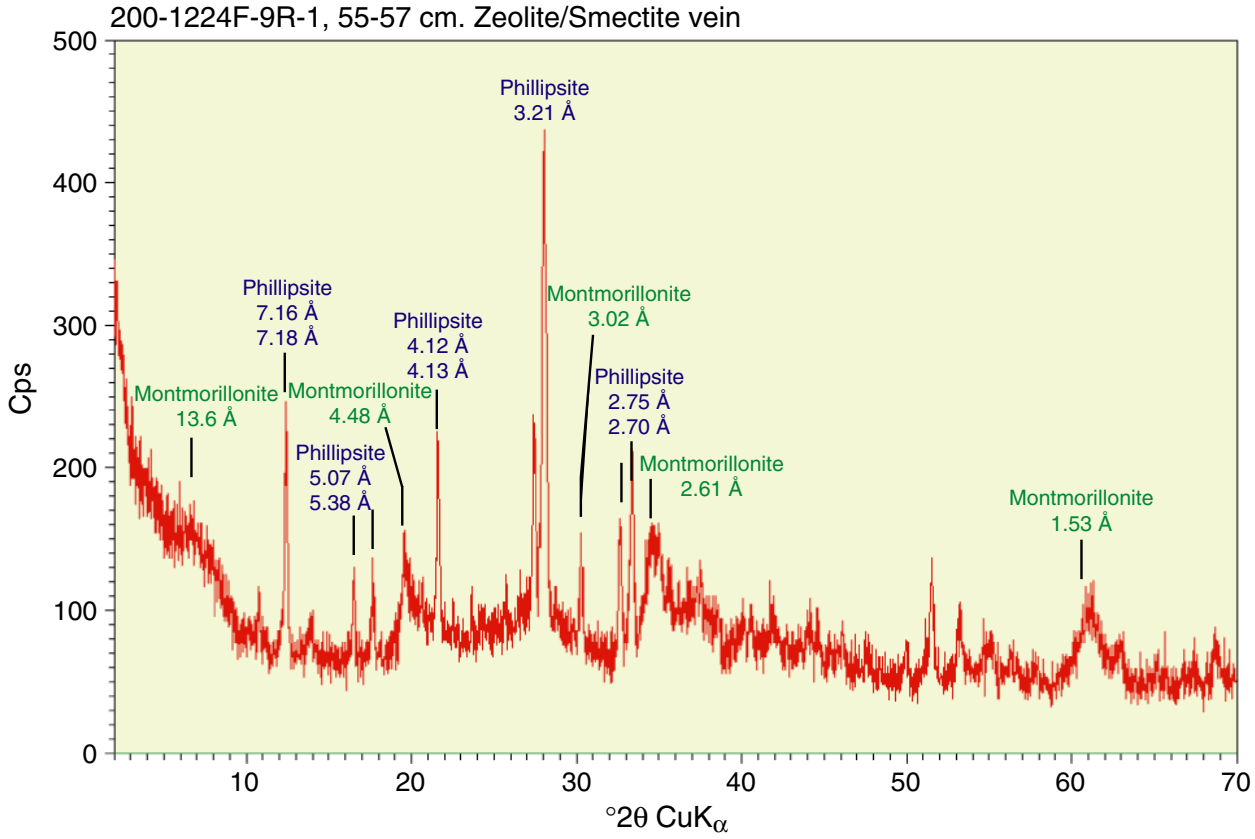

Figure F52. XRD result for a quartz vein (interval 200-1224F-2R-4, 120–123 cm) with the main quartz peaks labeled. Cps = counts per second.

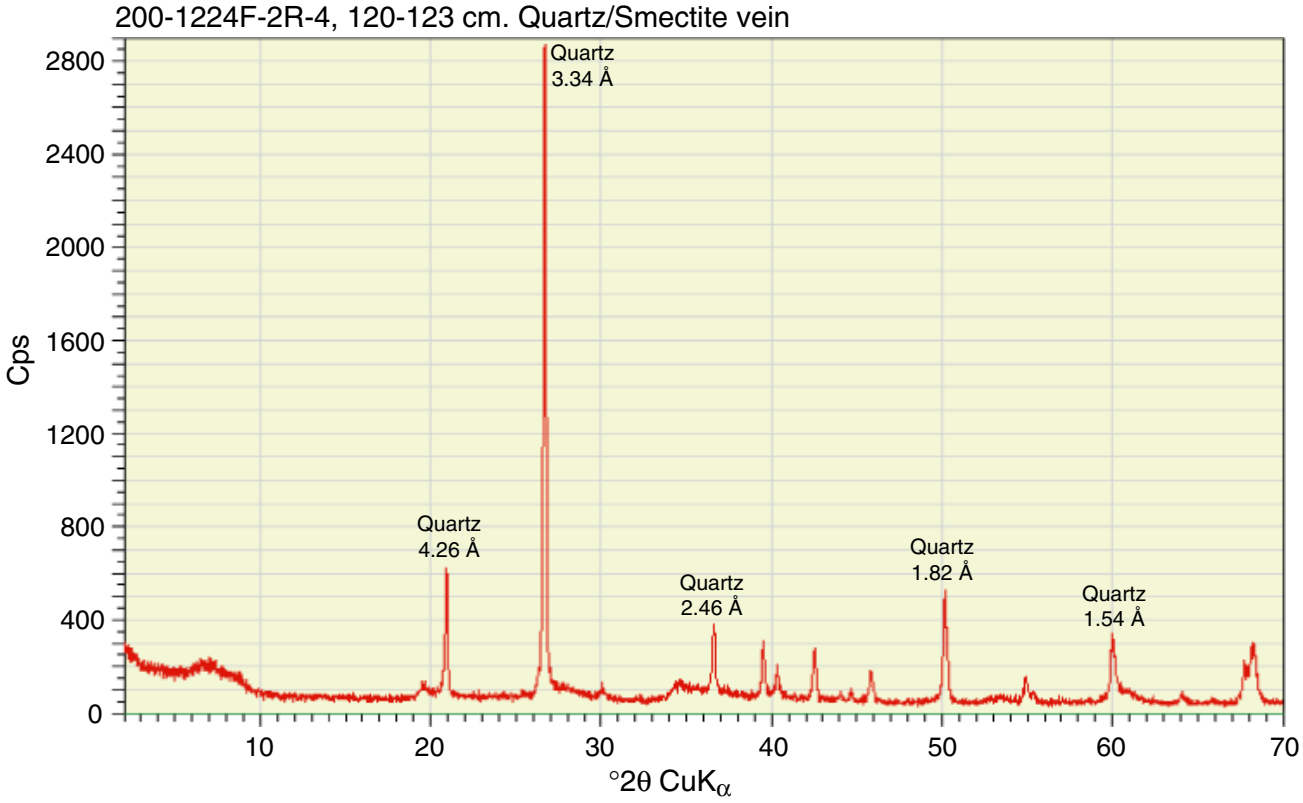

Figure F53. XRD result for a mixed calcite and smectite vein (interval 200-1224F-9R-1, 19–23 cm) with the main peaks identified. Montmorillonite and saponite are in the smectite group. Cps = counts per second.

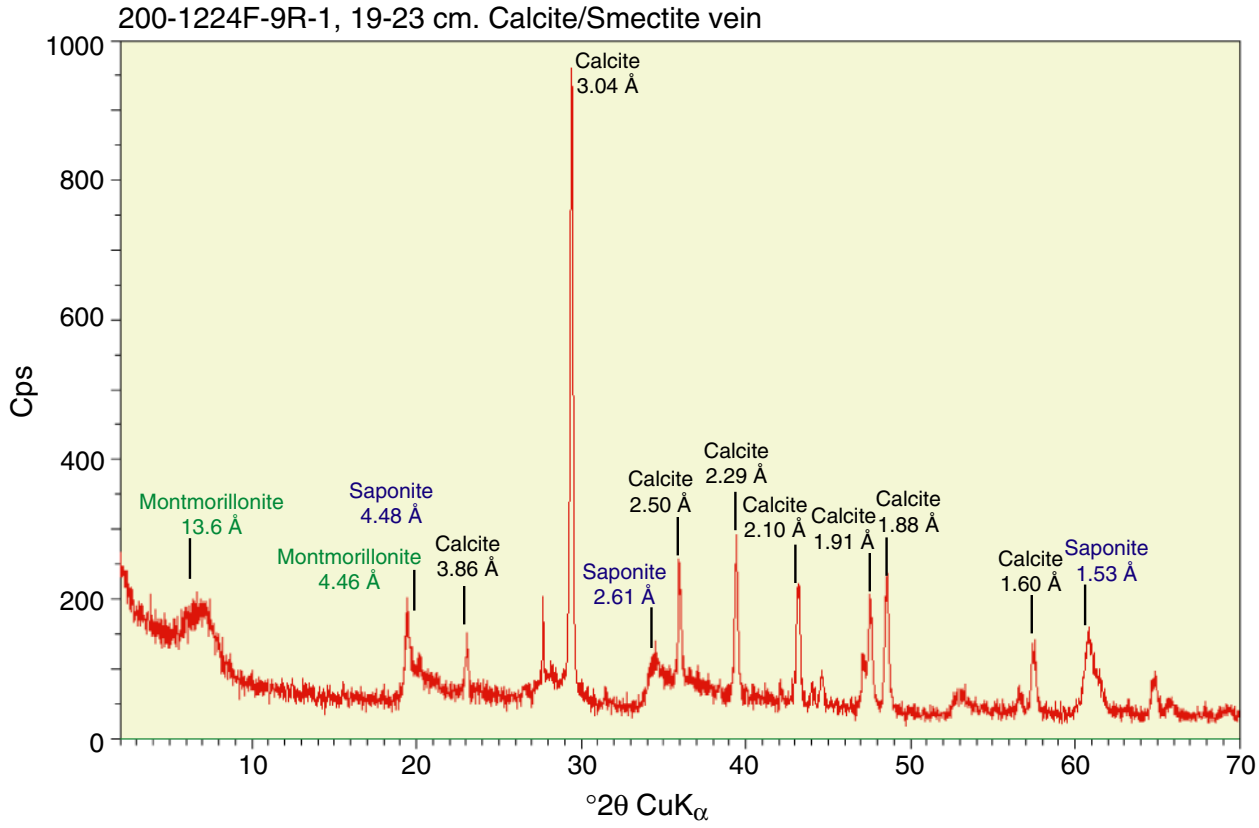

Figure F54. XRD result of zeolite pebbles in a sediment layer (Section 200-1224A-2X-CC) with the main peaks of phillipsite identified. Phillipsite is a zeolite-group mineral. Cps = counts per second.

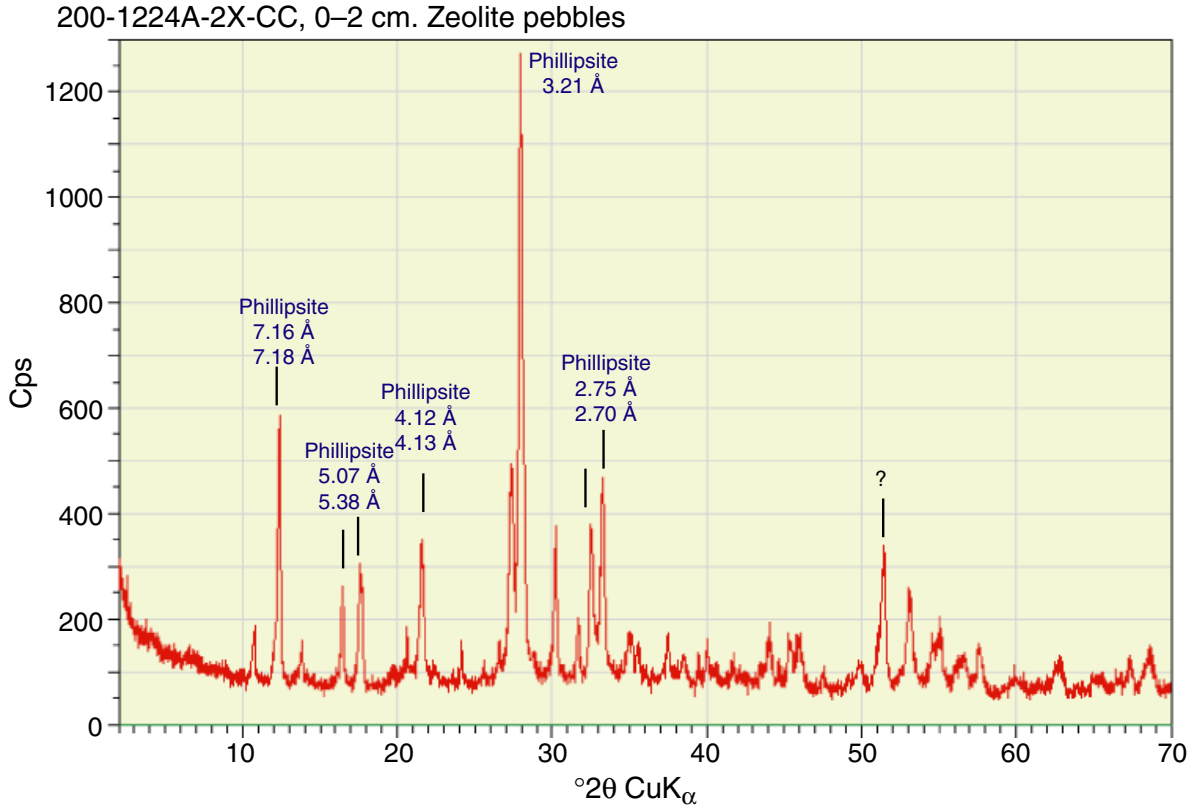

Figure F55. Summary of sediments cored at Site 1224. SS = the smear slides that were analyzed for calcareous nannofossils.

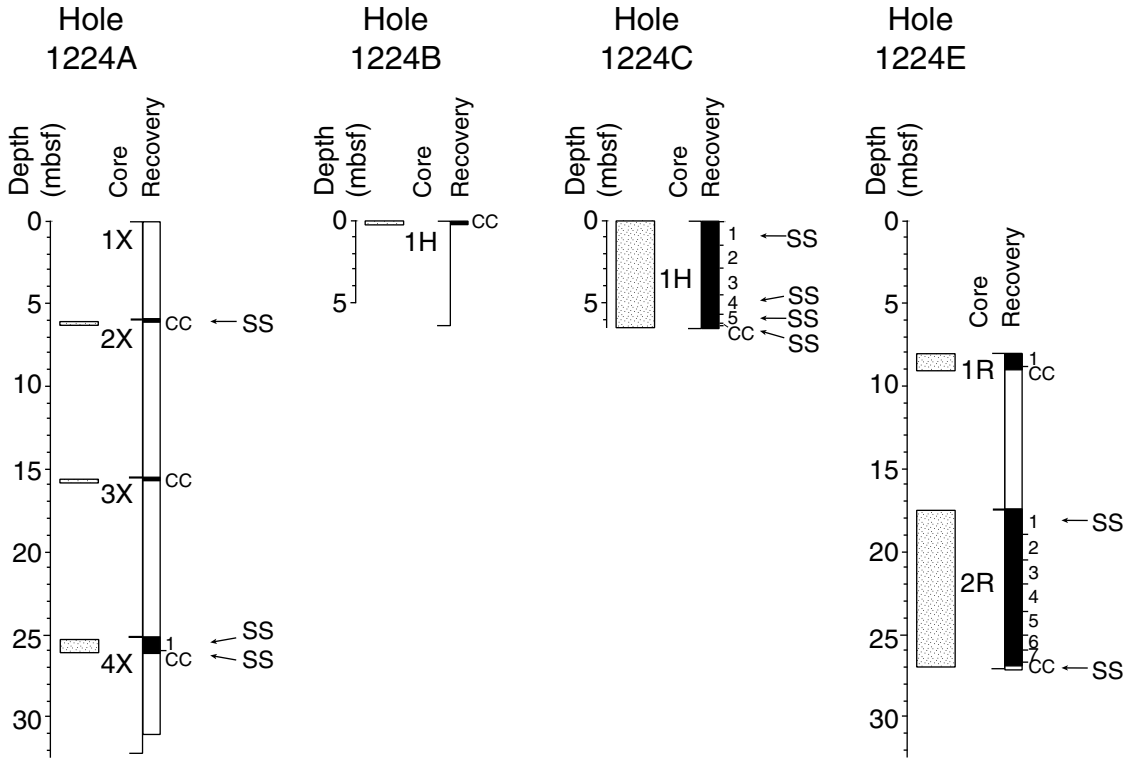

Figure F56. Inclination, declination, and intensity from archive-half split-core sections prior to AF demagnetization are plotted vs. depth downhole for Holes 1224A, 1224C, 1224D, 1224E, and 1224F. Also shown are the whole-core susceptibility results (in raw meter SI units).

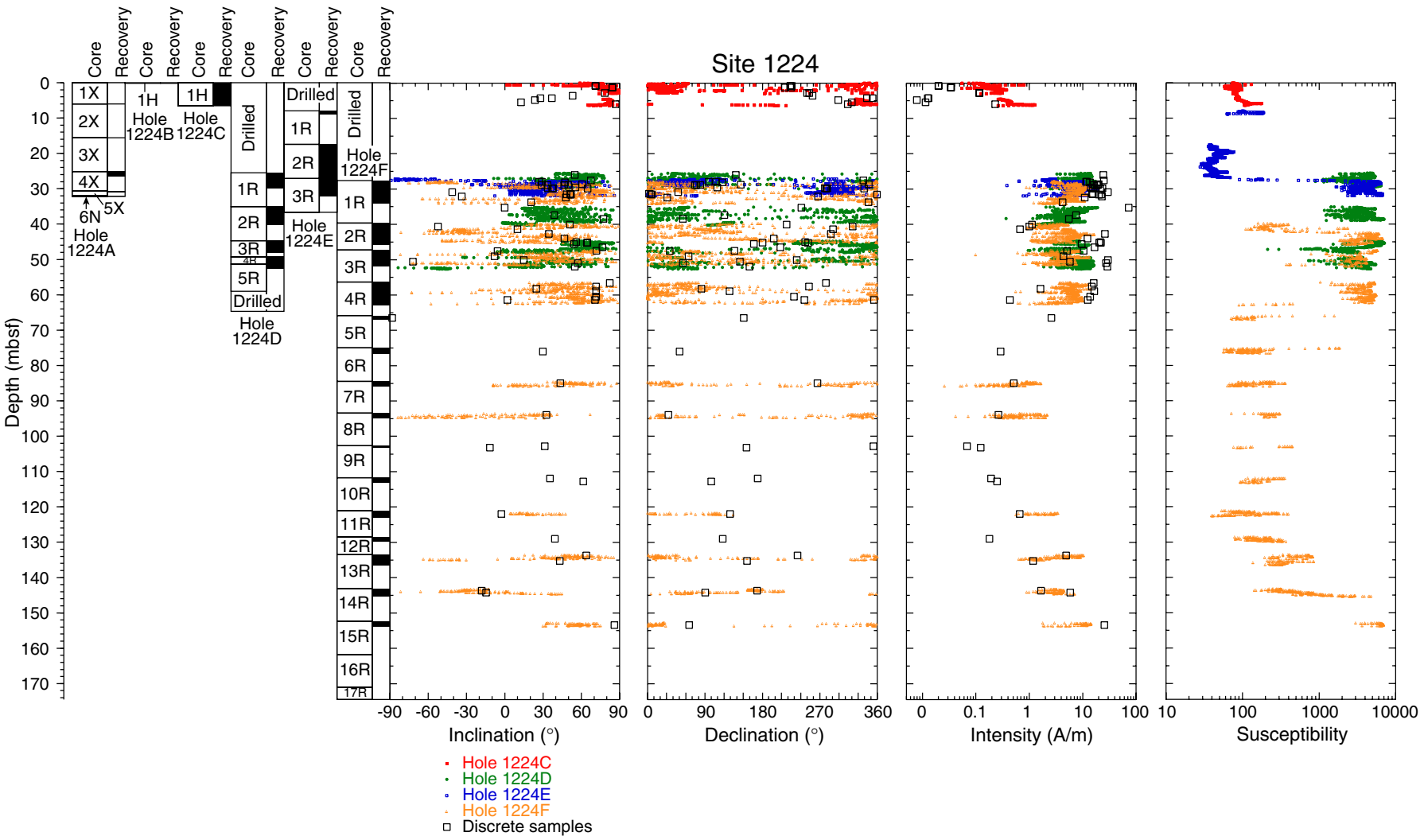

Figure F57. Inclination and intensity from archive halves, one working half, one whole round, and several discrete samples from Hole 1224C. All samples were demagnetized to 30 mT.

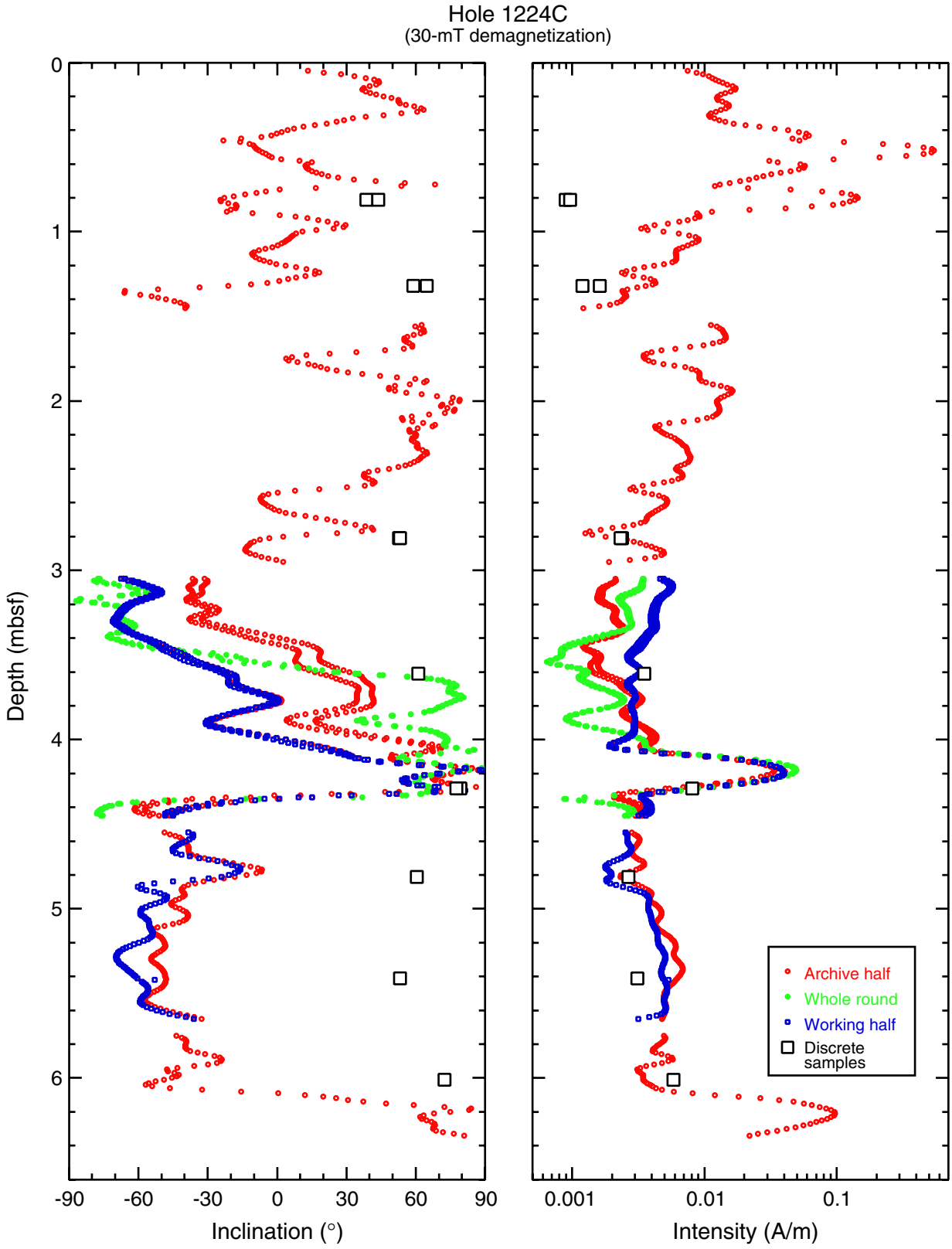

Figure F58. AF demagnetization results from a basalt sample (Sample 200-1224A-5X-1, 17 cm; 30.87 mbsf). The top left diagram shows the intensity variation with progressive demagnetization; the top right diagram shows vector endpoints on a vector demagnetization diagram (orthogonal projections, where open squares are inclination and solid squares are declination); the bottom right diagram is an enlargement of the region near the origin of the above diagram; and the bottom left diagram shows the magnetization directions on an equal-area projection (open squares = directions with negative inclinations).

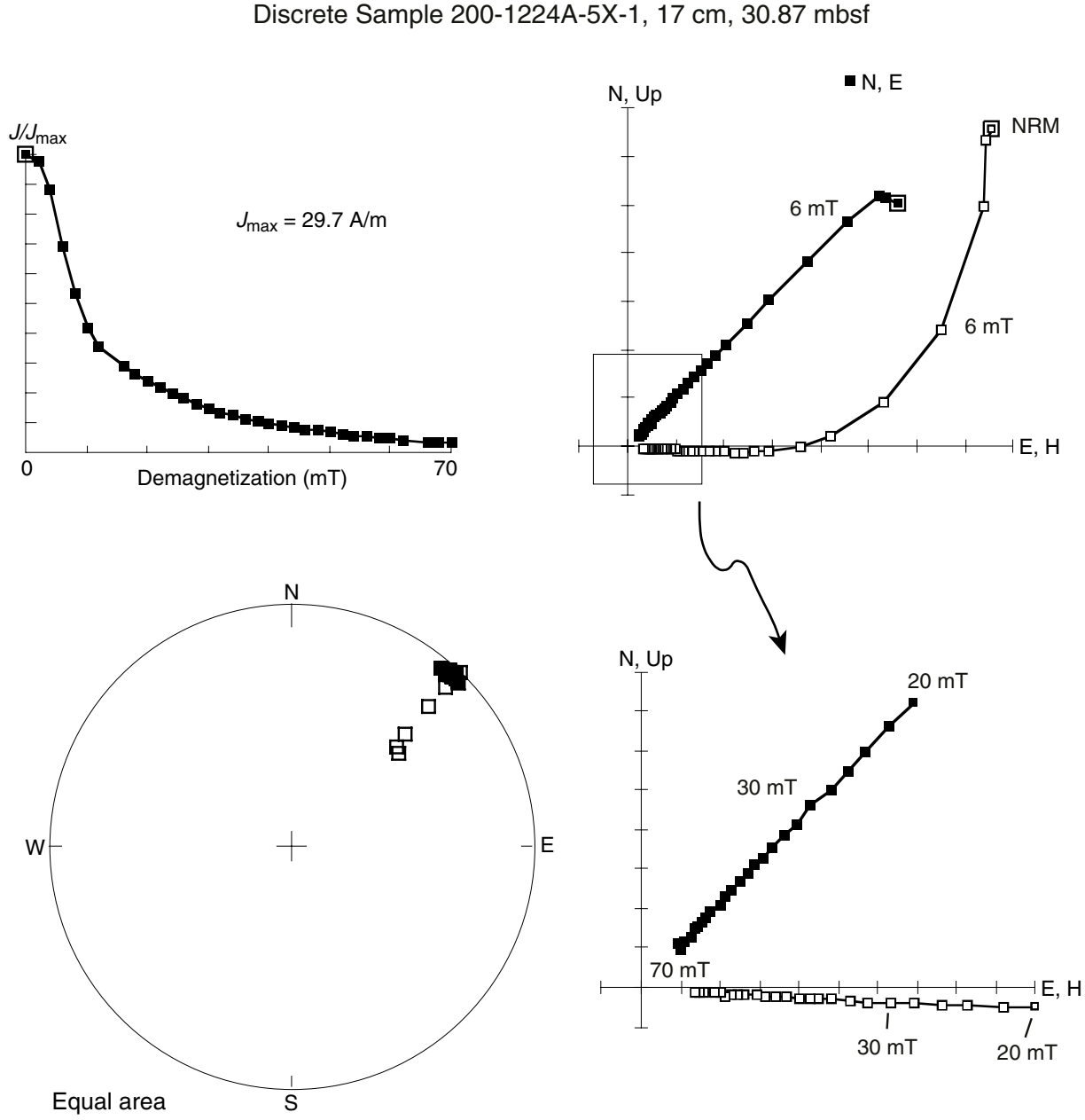

Figure F59. AF demagnetization results from a basalt sample (Sample 200-1224F-2R-1, 91 cm; 40.61 mbsf). The top left diagram shows the intensity variation with progressive demagnetization; the top right diagram shows vector endpoints on a vector demagnetization diagram (orthogonal projections, where open squares are inclination and solid squares are declination); the middle right diagram is an enlargement of the region near the origin of the above diagram; the bottom left table shows the data; and the bottom right diagram shows the magnetization directions on an equal-area projection (open squares = directions with negative inclinations).

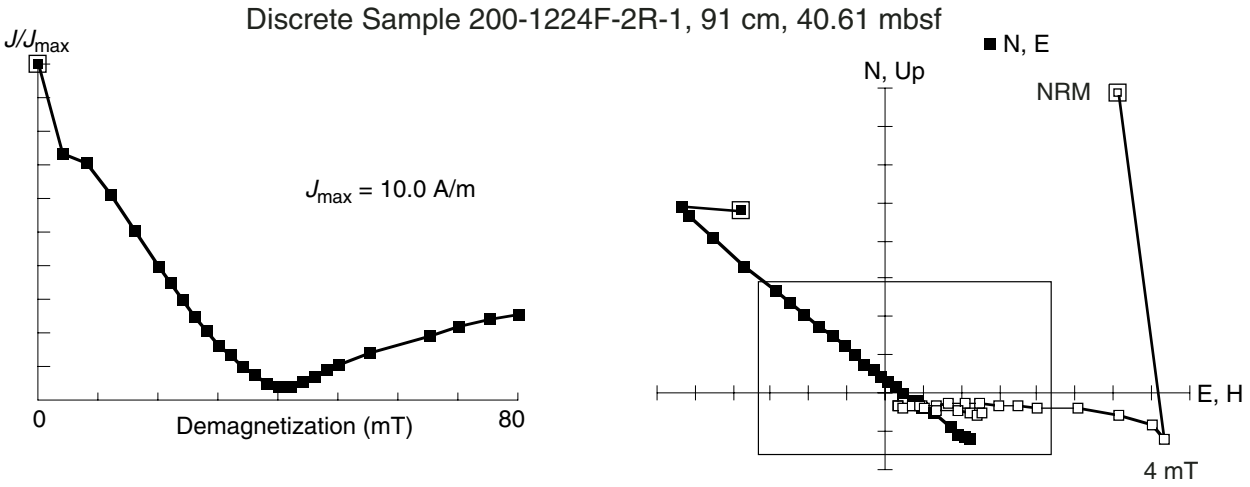

Demag (mT)	Dec (°)	Inc (°)	Intensity
0.0	321.5	-52.2	1.00E+0
4.0	312.3	9.6	7.39E-01
8.0	312.1	6.5	7.04E-01
12.0	311.9	5.1	6.15E-01
16.0	312.1	4.6	5.04E-01
20.0	313.0	5.1	4.01E-01
22.0	313.5	5.6	3.48E-01
24.0	314.0	6.3	2.98E-01
26.0	315.1	6.4	2.50E-01
28.0	317.2	7.6	2.10E-01
30.0	318.8	9.2	1.67E-01
32.0	321.4	12.8	1.33E-01
34.0	324.8	17.8	9.98E-02
36.0	330.5	22.3	7.53E-02
38.0	345.9	30.7	4.92E-02
40.0	13.9	45.4	4.24E-02
42.0	60.0	43.5	4.38E-02
44.0	92.7	40.5	5.79E-02
46.0	105.4	25.3	7.34E-02
48.0	104.6	22.1	9.23E-02
50.0	111.4	20.8	1.09E-01
55.0	113.0	17.8	1.42E-01
65.0	117.0	13.1	1.95E-01
70.0	118.7	12.4	2.23E-01
75.0	118.9	13.2	2.44E-01
80.0	118.7	11.6	2.58E-01

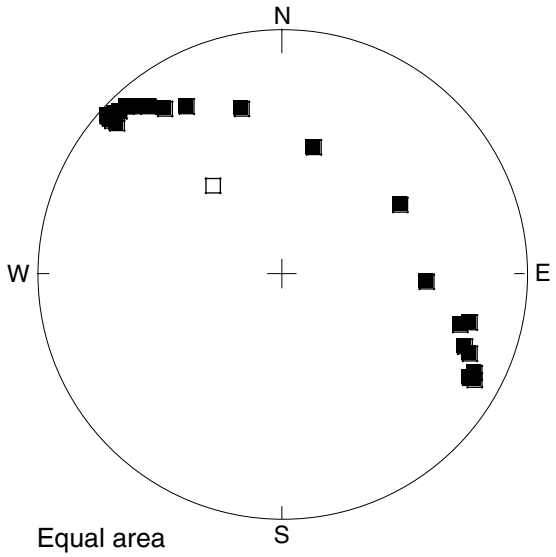

Figure F60. Photomicrograph showing bacterial cells from an upper sediment layer from a depth of 1.45 mbsf (Sample 200-1224C-1H-4, 145–150 cm) after (**A**) staining with the DNA-binding fluorochrome SYBR Green I and (**B**) and hybridization with the Bacteria-specific, CY3-labeled probe EUB338. Note the numerous bacteria responding to the specific hybridization, indicating the high amount of metabolically active bacteria within the sediment.

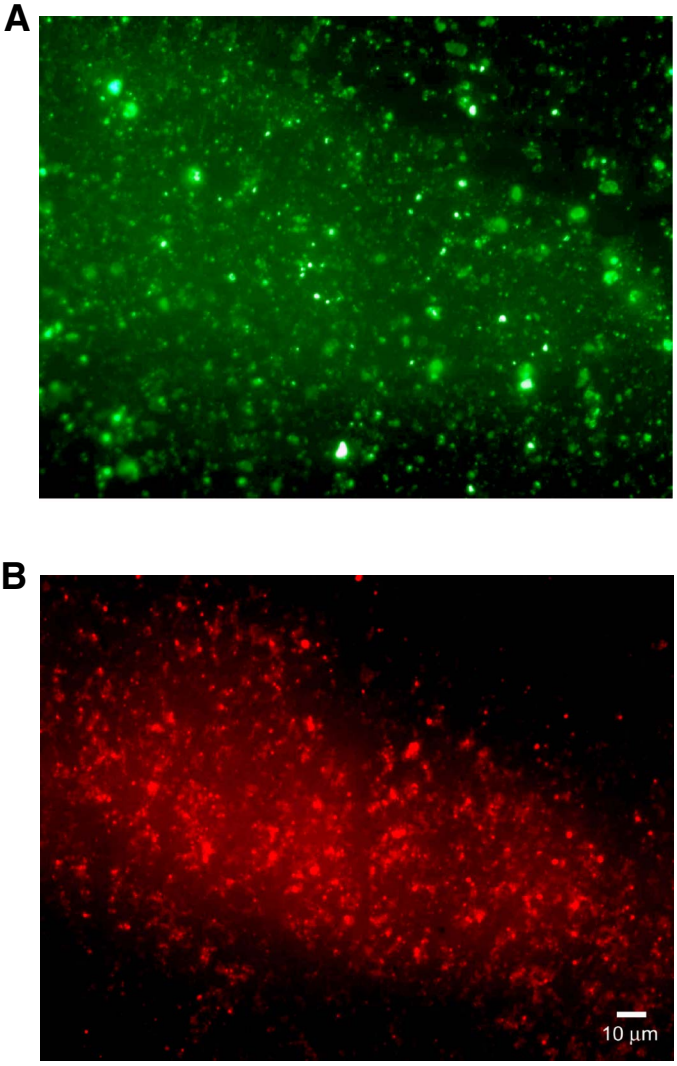

Figure F61. Macroscopic image of Fe^{2+}-oxidizing bacterial colony obtained from ground rock material taken at a depth of 27 mbsf (Sample 200-1224D-1R-2, 10–15 cm) and aerobically grown on an artificial seawater agar plate.

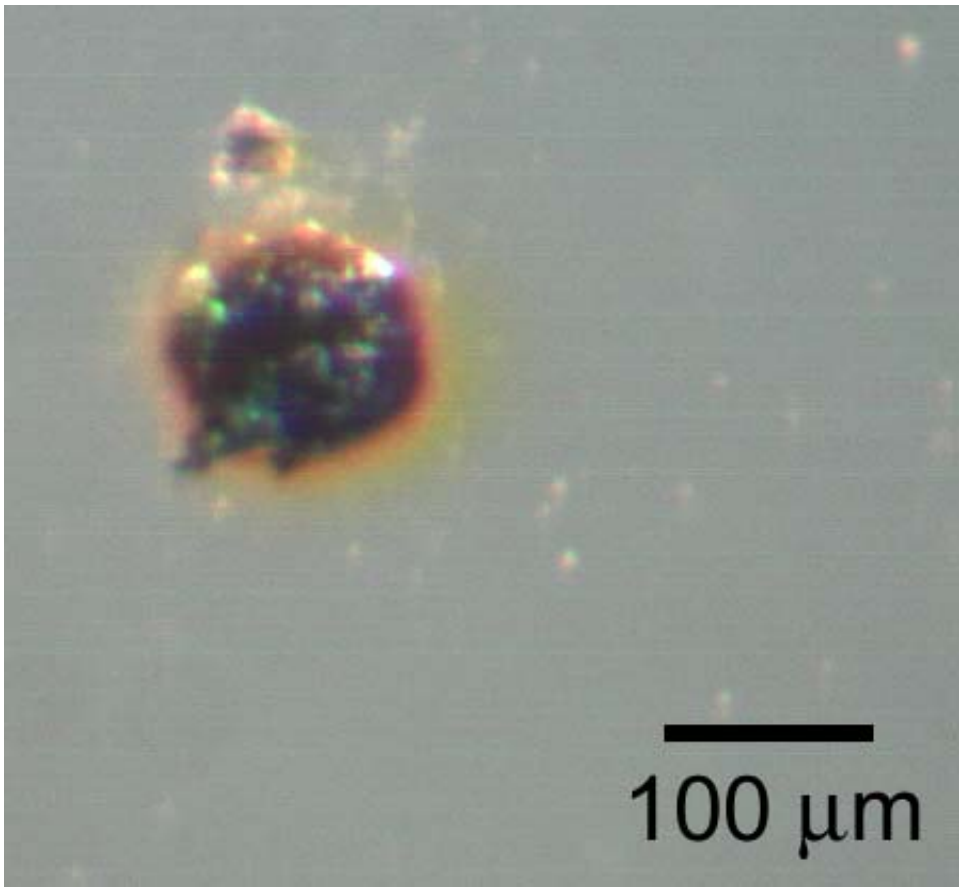

Figure F62. Fungal hyphae divided into distinctive cells by septae (arrow).

Figure F63. Fungal hyphae grown in a $CaCO_3$-filled cavity within a massive tholeiitic lava flow unit.

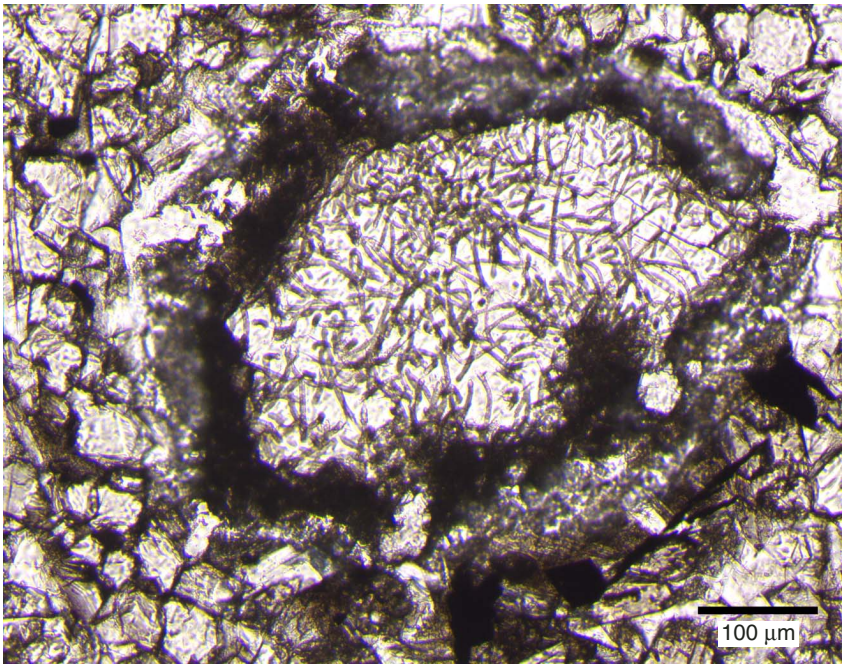

Figure F64. Fe-oxide encrusted fungal hyphae in a carbonate-filled vein within a massive tholeiitic lava flow unit.

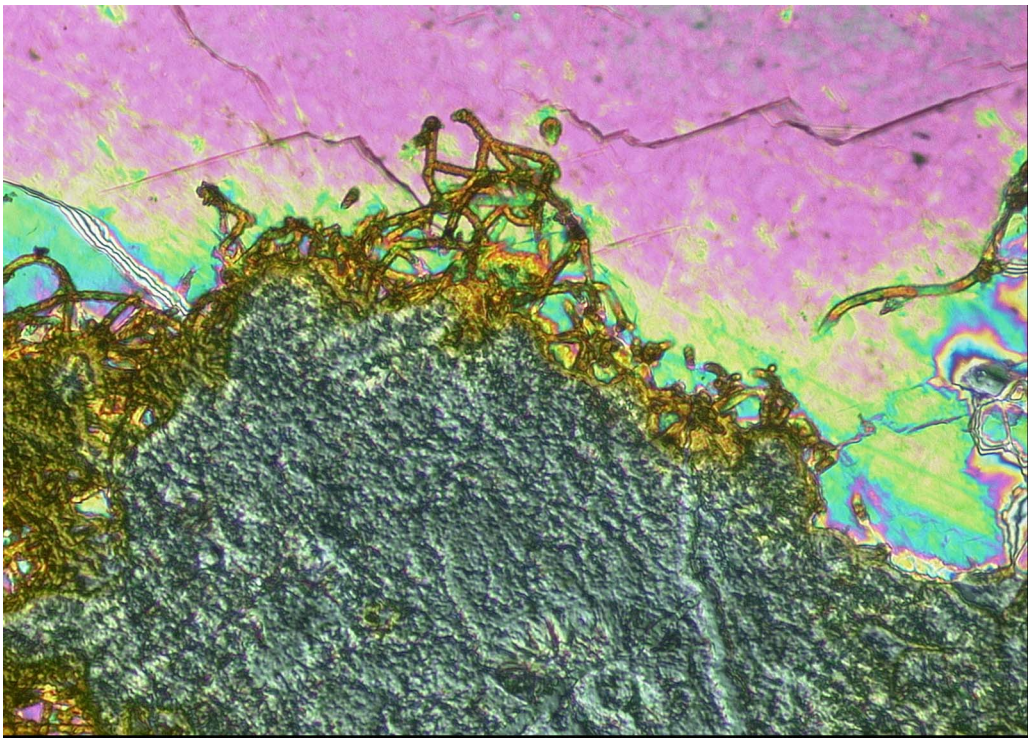

Figure F65. MST measurements of (**A**) GRA bulk density, (**B**) magnetic susceptibility, and (**C**) natural gamma radiation as functions of depth in the soft sediments cored in Hole 1224C. Three units are identified at 0–2 mbsf, 2–4.5 mbsf, and below 4.5 mbsf. cps = counts per second.

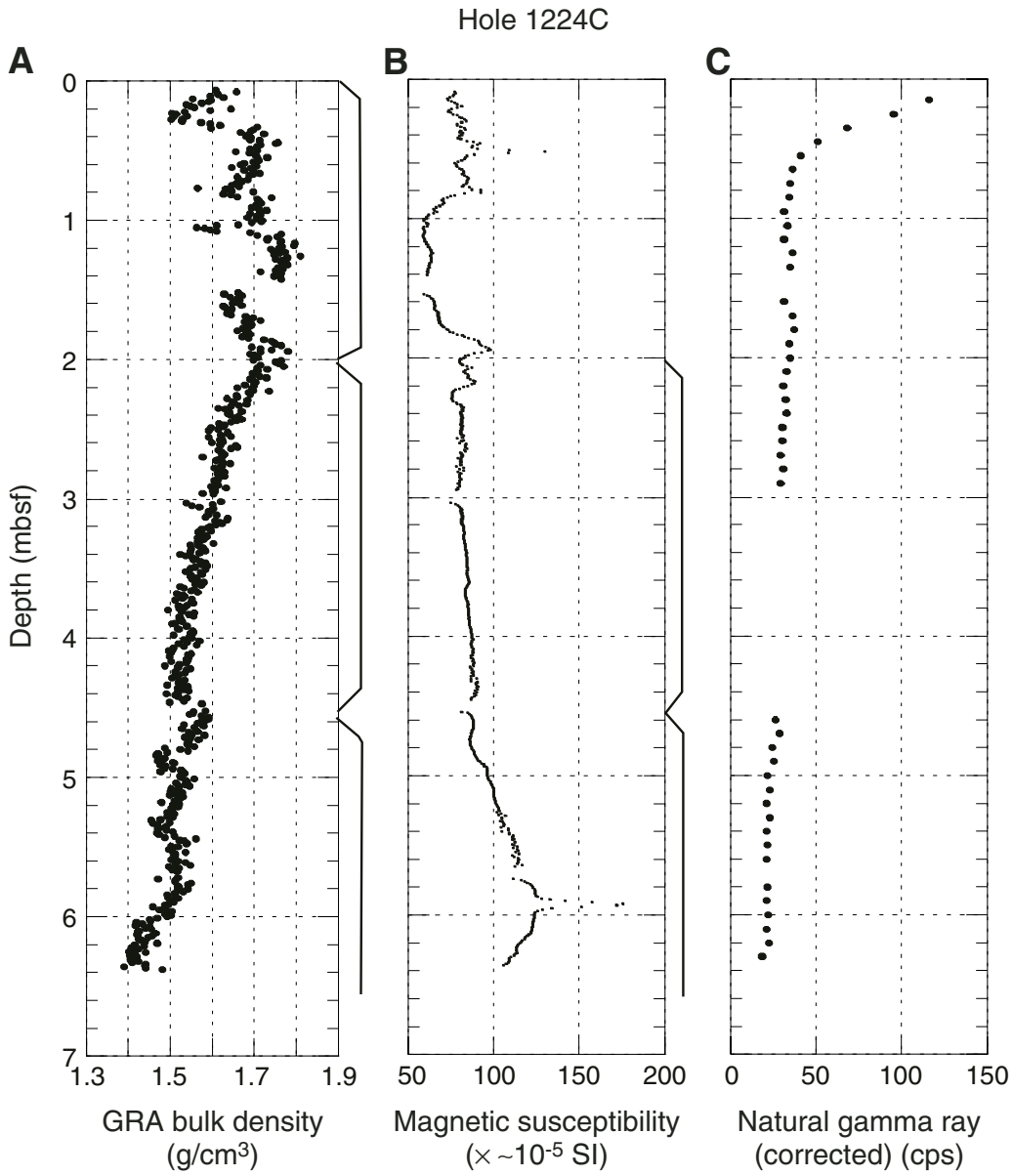

Figure F66. Summary of moisture and density measurements in Hole 1224C.

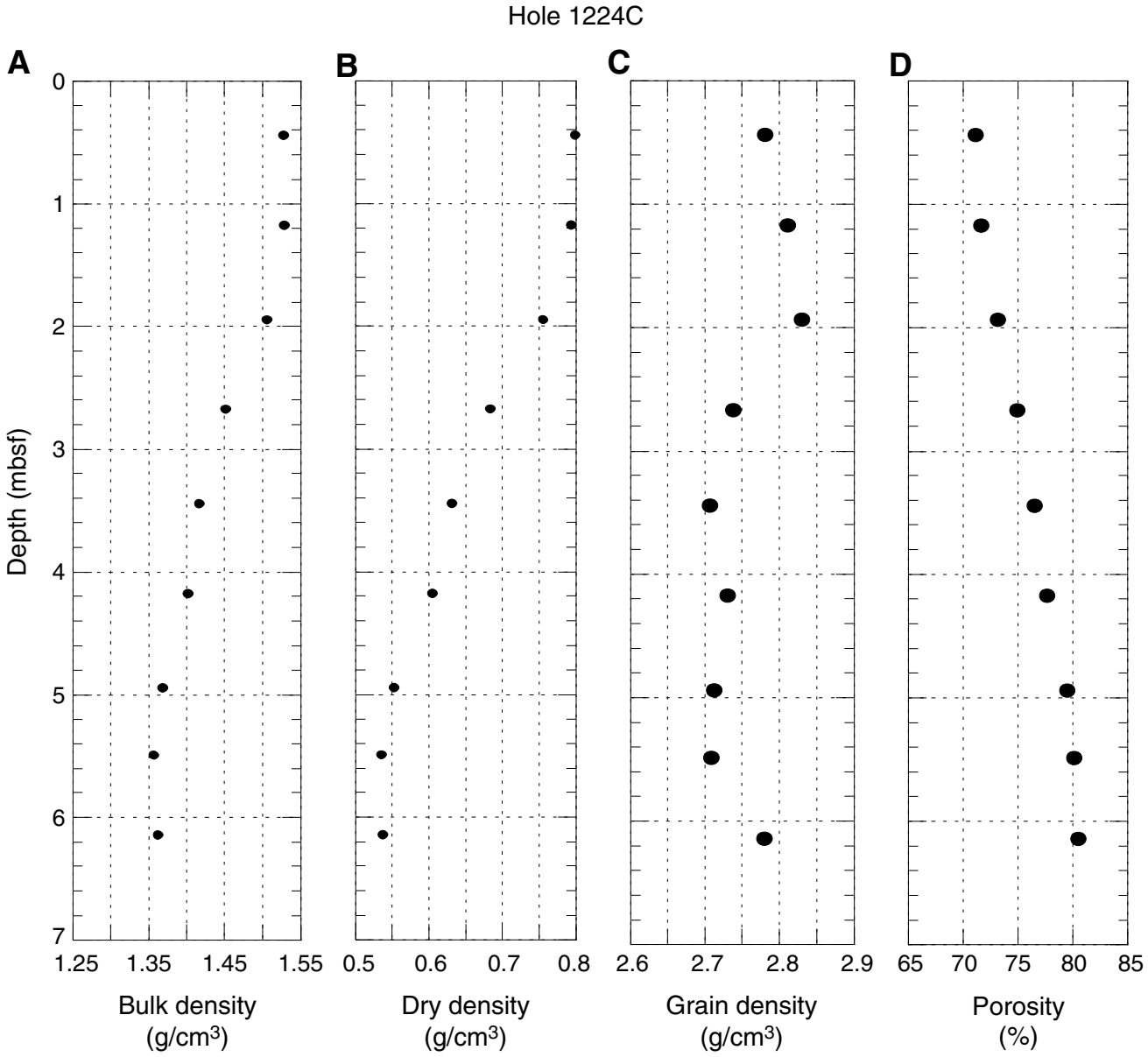

Figure F67. (**A**) Thermal conductivity, (**B**) PWL and PWS compressional wave velocities, and (**C**) GRA density and bulk density as a function of depth in Hole 1224C.

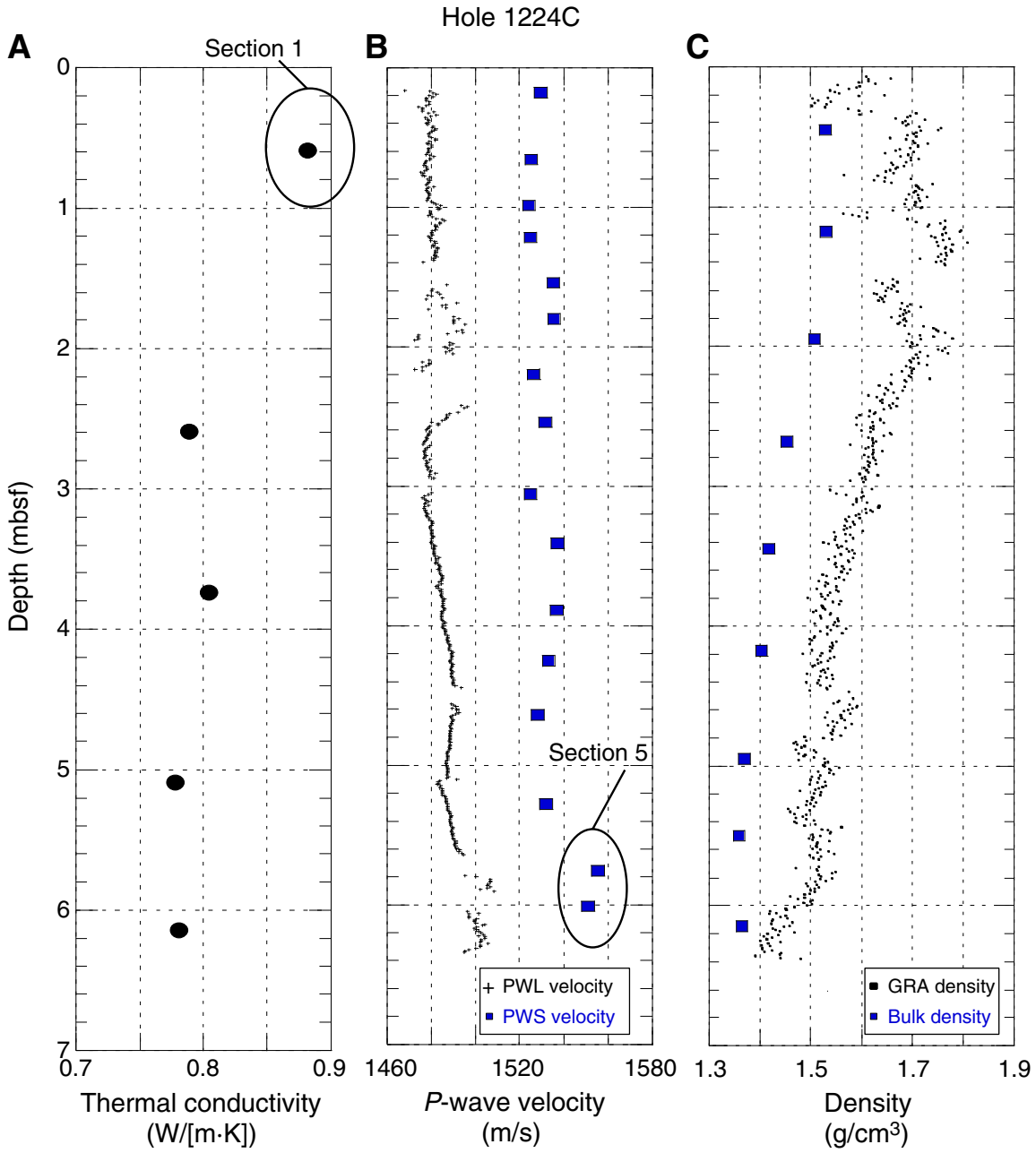

Figure F68. PWL velocity vs. GRA density in Hole 1224C.

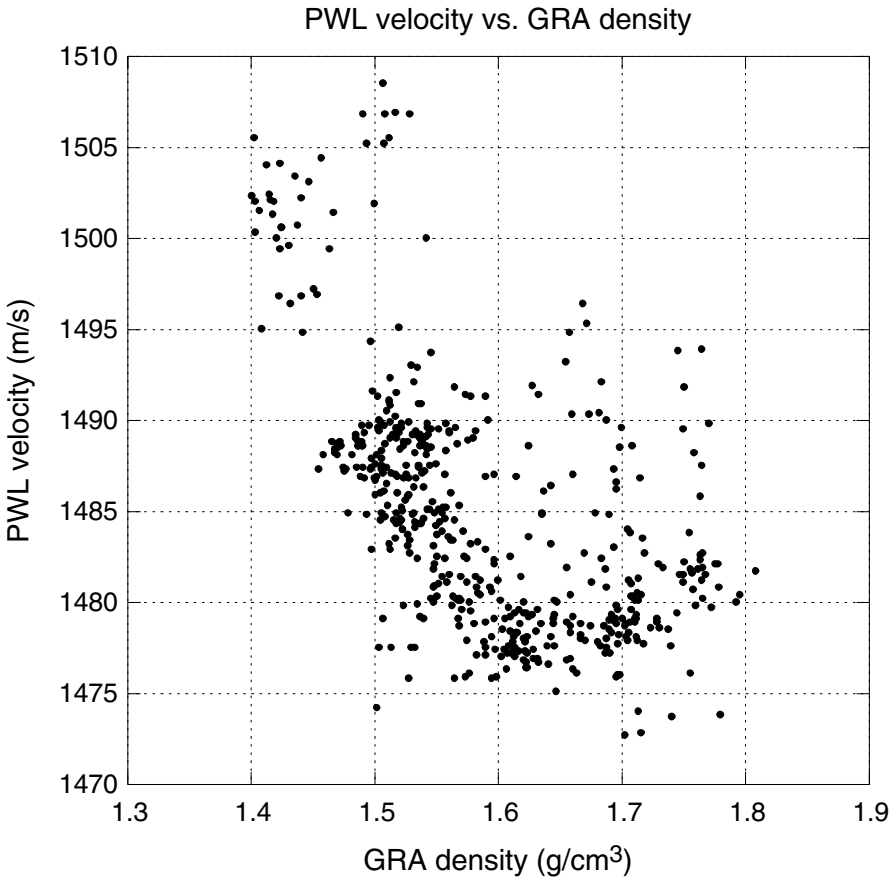

Figure F69. MST measurements of (**A**) GRA bulk density, (**B**) magnetic susceptibility, and (**C**) natural gamma ray with depth in Hole 1224D. cps = counts per second.

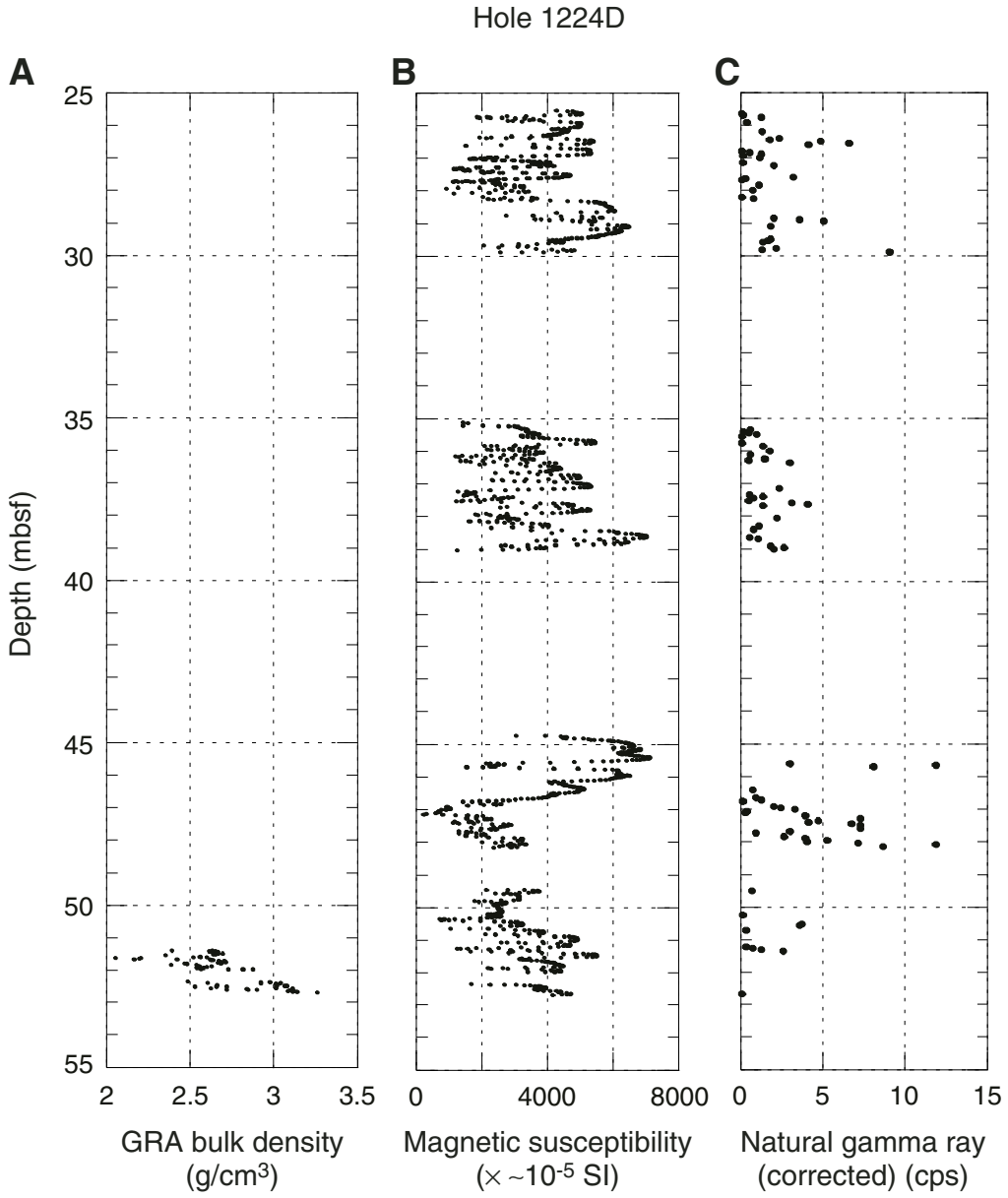

Figure F70. Summary of moisture and density measurements and thermal conductivity measurements with depth in Hole 1224D.

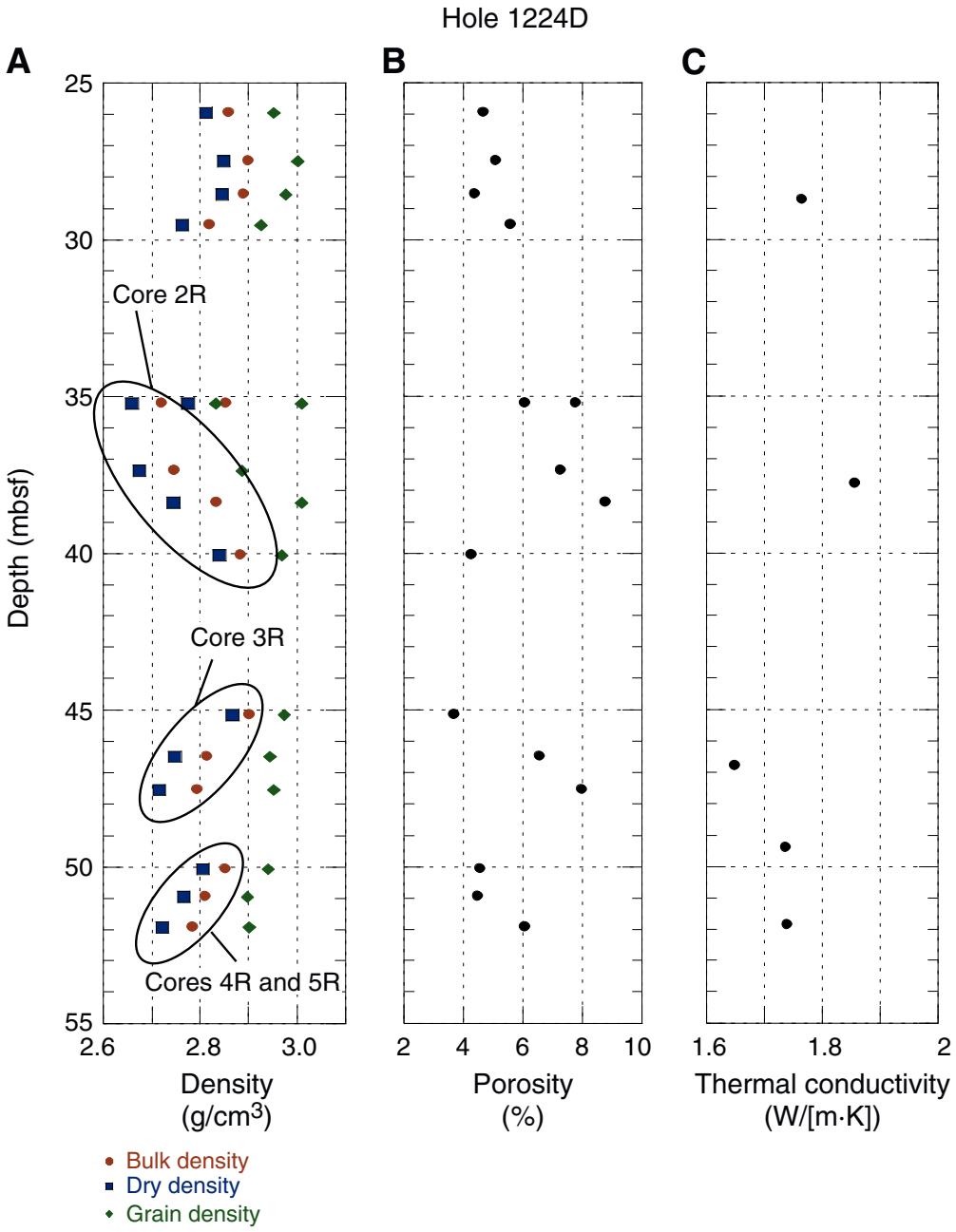

Figure F71. Compressional wave velocity vs. depth in (**A**) Holes 1224D, (**B**) 1124E, and (**C**, **D**) 1224F. Seven depth zones are introduced as shown on the far right. Compressional wave velocities for the three holes have similar depth dependence between 27 and 53 mbsf.

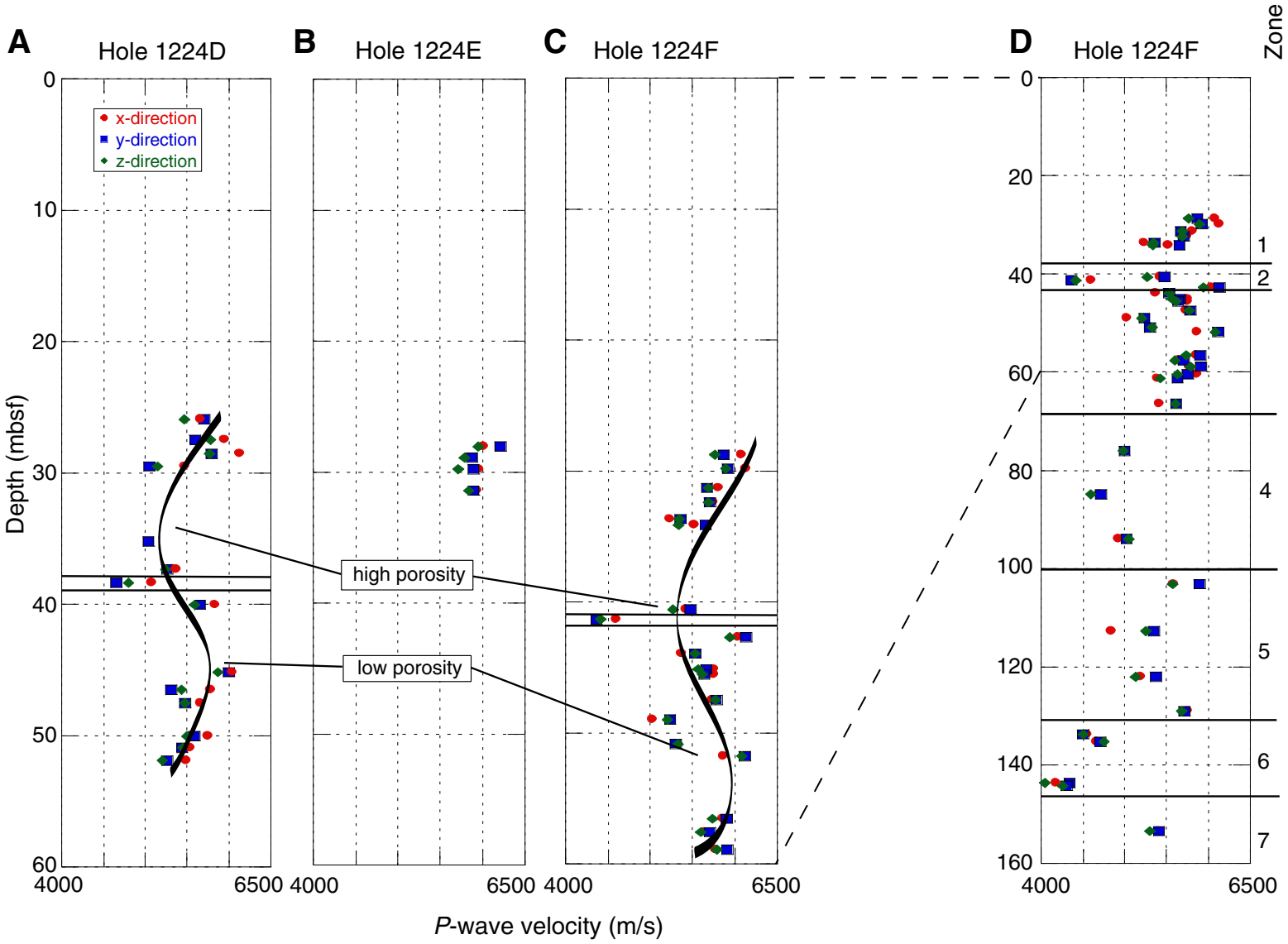

Figure F72. (**A**) Compressional wave velocity vs. bulk density and (**B**) compressional wave velocity vs. porosity in Hole 1224D. Samples A and B in both figures have exceptional characteristics and large anisotropies.

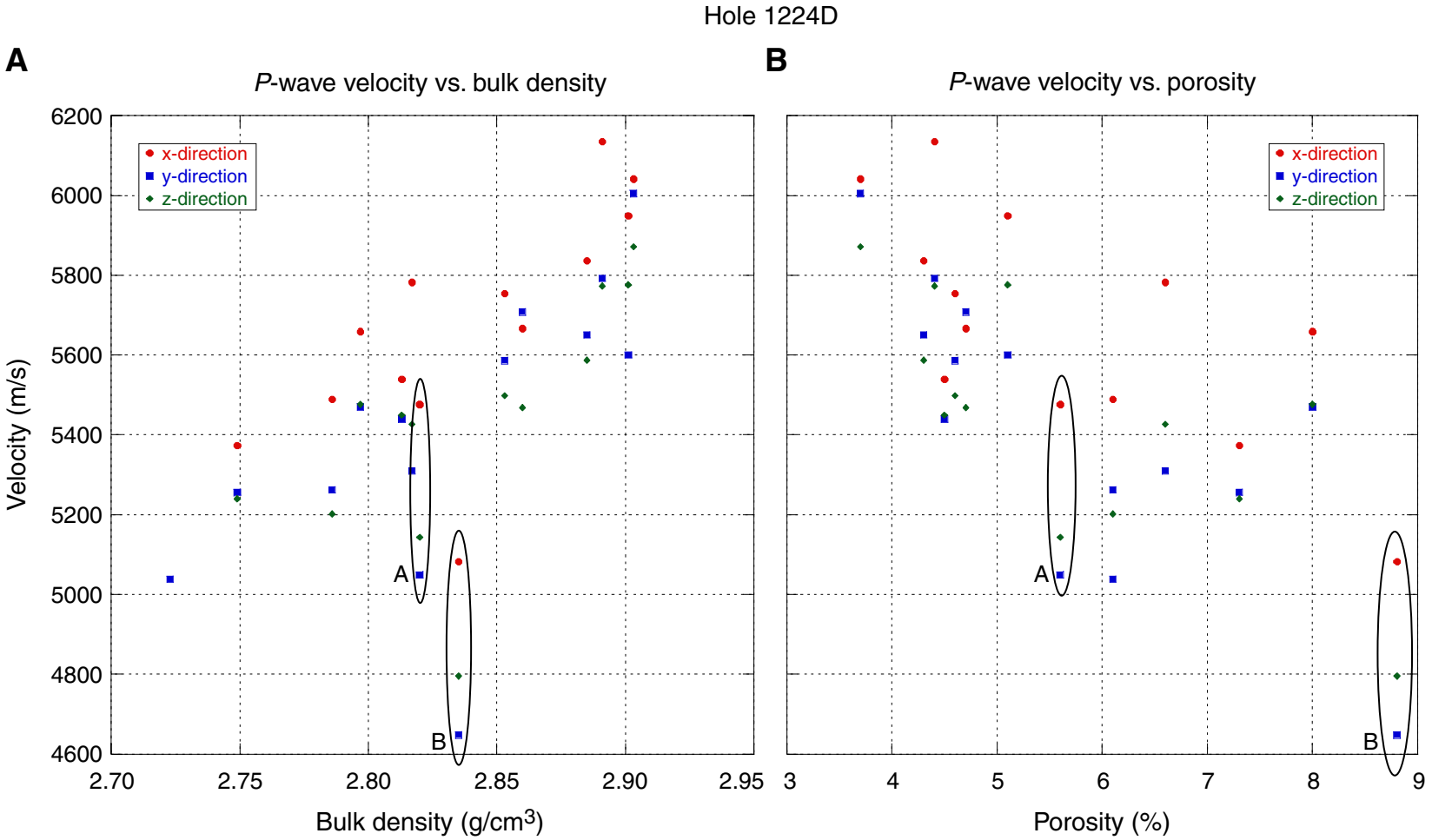

Figure F73. MST measurements of (**A**) GRA bulk density, (**B**) magnetic susceptibility, and (**C**) natural gamma ray with depth in Hole 1224E. cps = counts per second.

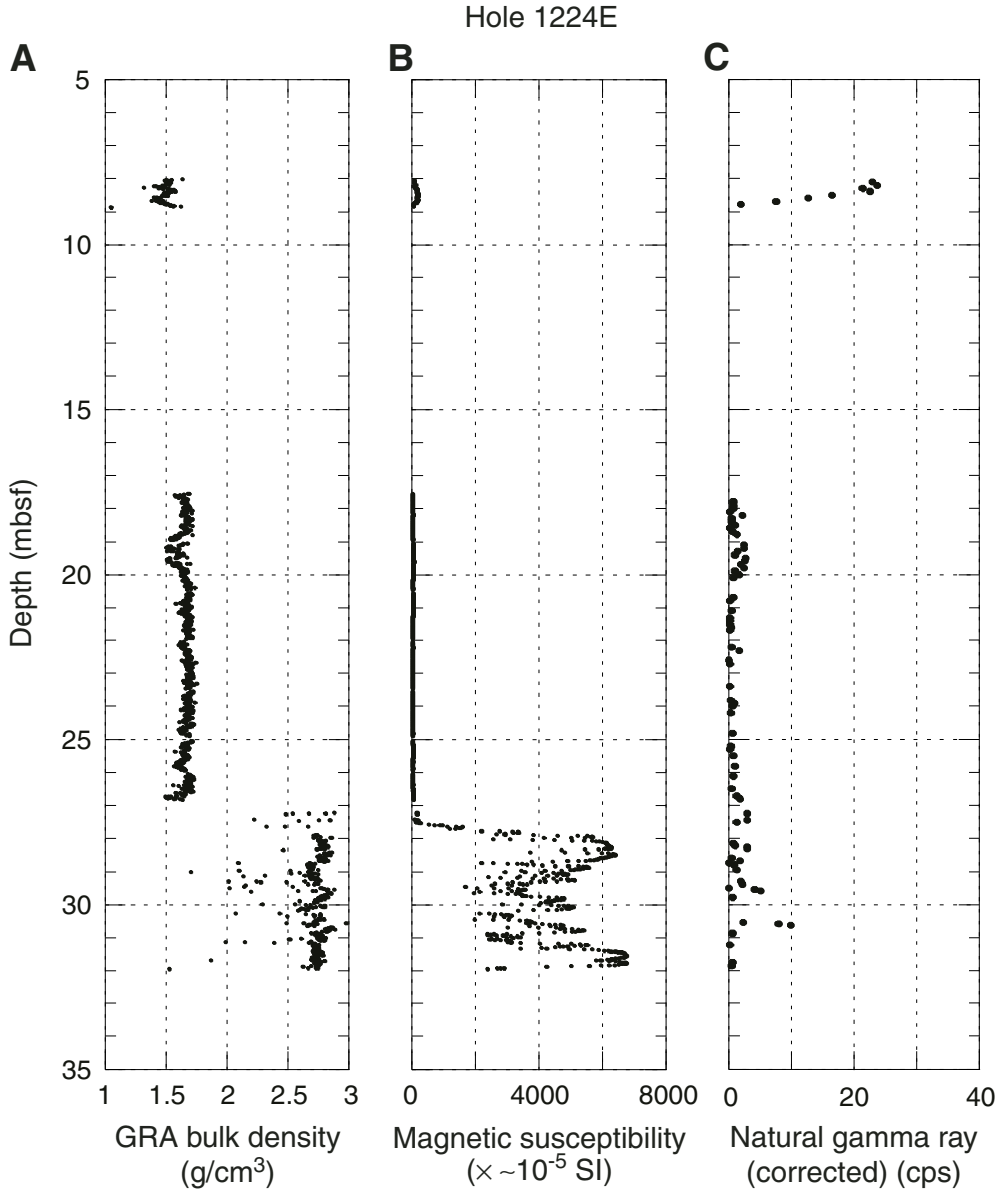

Figure F74. MST measurement of (**A**) GRA bulk density, (**B**) magnetic susceptibility, and (**C**) natural gamma ray with depth in Hole 1224F. Most of the measurements have large ambiguities in measured values because of diameter changes, but maximum values are close to true values. cps = counts per second.

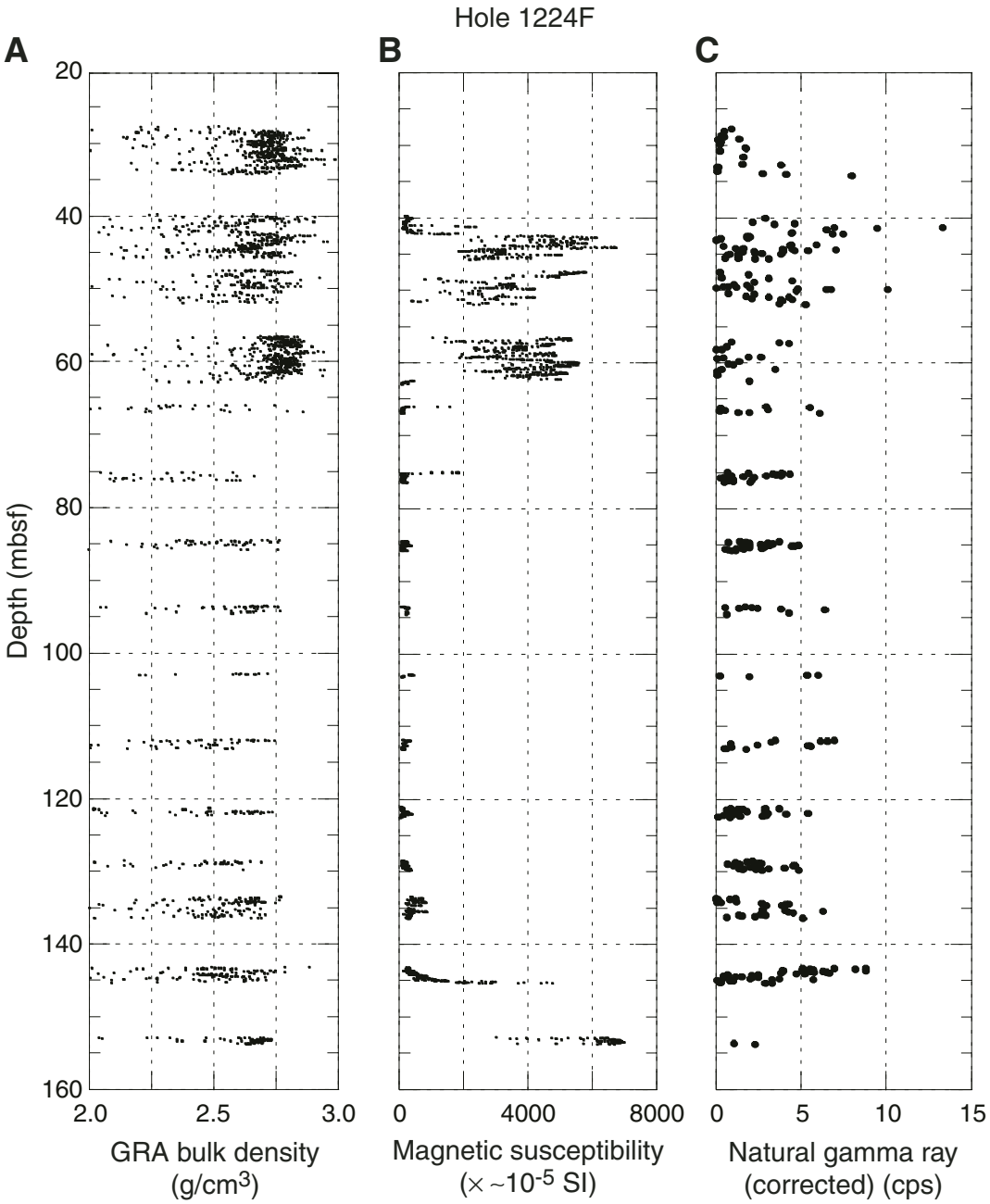

Figure F75. Moisture and density measurements with depth in Hole 1224E.

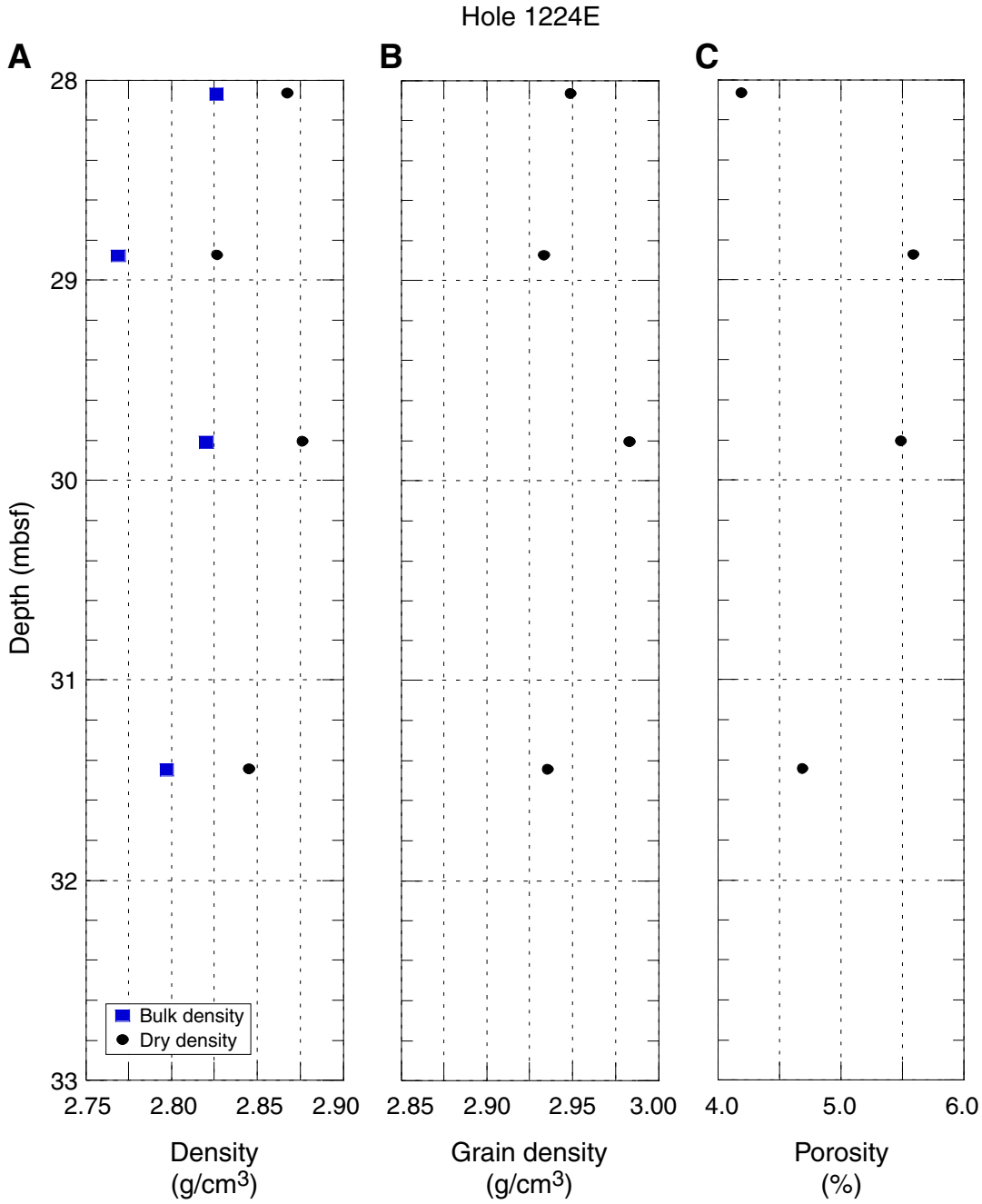

Figure F76. Moisture and density measurements and thermal conductivity with depth in Hole 1224F. **A.** bulk density. **B.** Grain density. **C.** Porosity. **D.** Thermal conductivity. The seven depth zones are shown in A (the bulk and dry densities) and C (porosity).

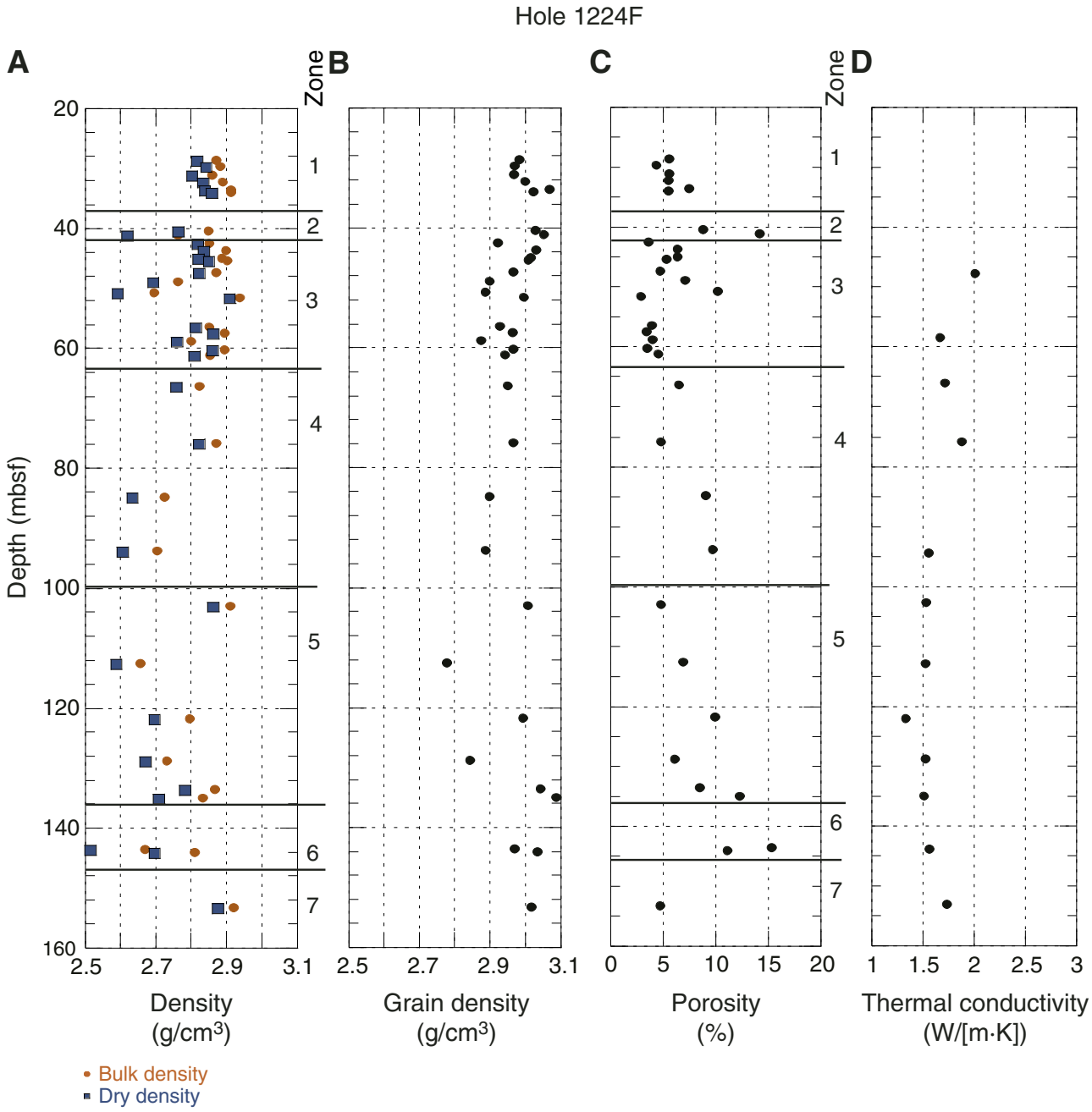

Figure F77. (**A**) Compressional wave velocity vs. bulk density and (**B**) compressional wave velocity vs. porosity in Hole 1224E.

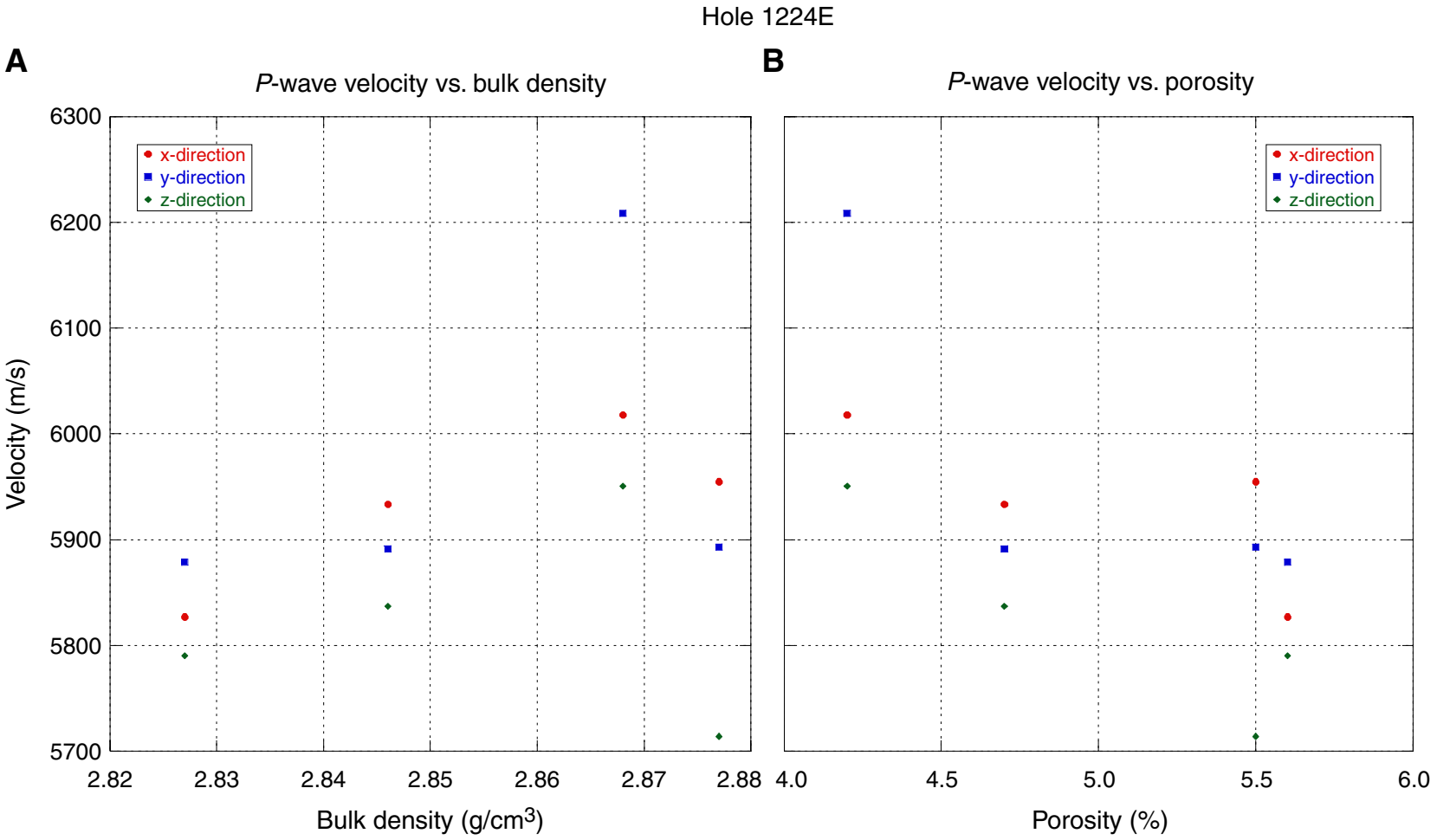

Figure F78. (**A**) Compressional wave velocity vs. bulk density and (**B**) compressional wave velocity vs. porosity in Hole 1224F. Note that bulk densities are poorly correlated with velocities, although porosities are well correlated to velocities.

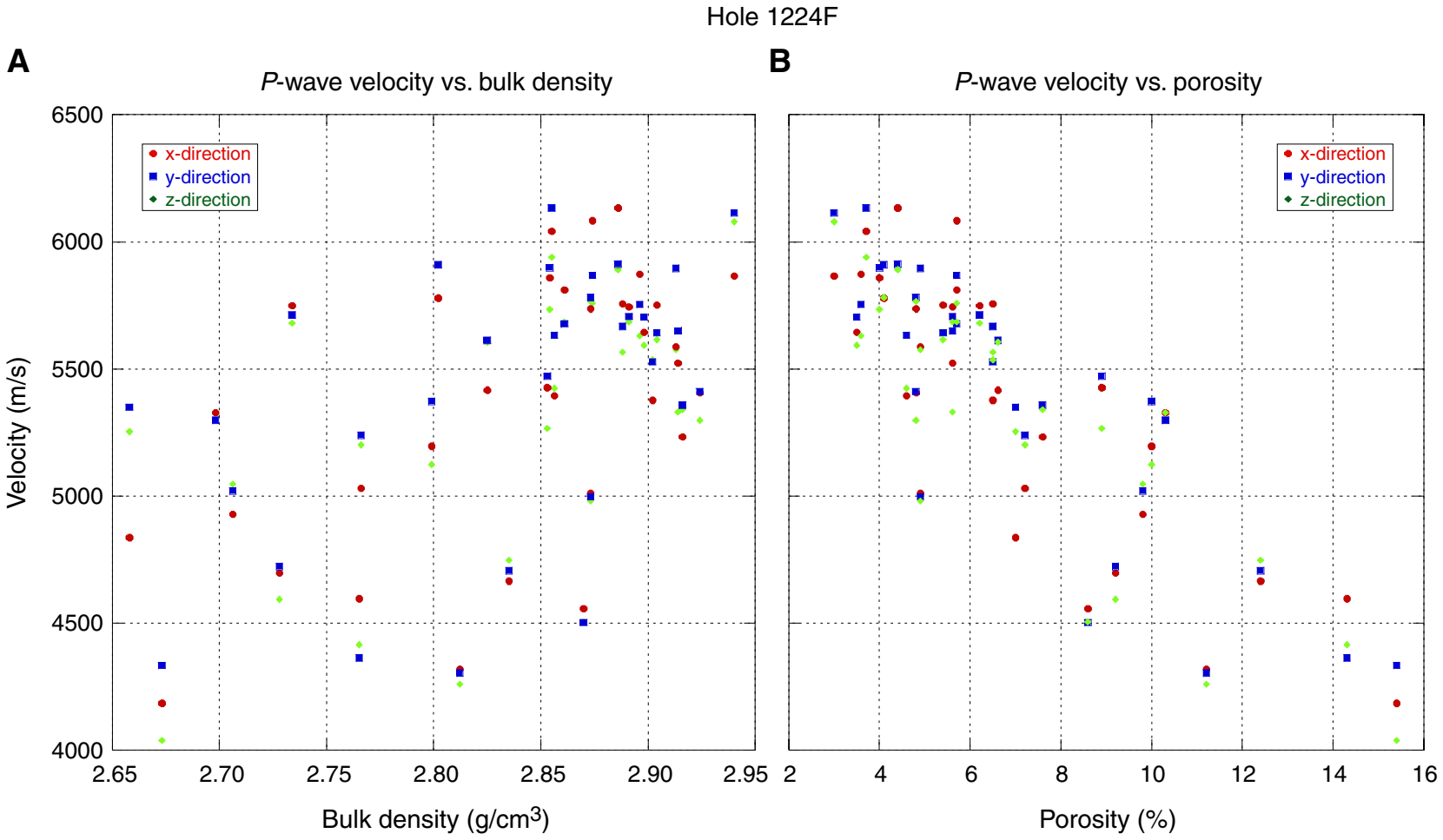

Figure F79. Composite log of hole parameters and magnetic field logs recorded in Hole 1224F. Track 1: calipers C1 (black) and C2 (red) from the FMS tool and the caliper log (blue) from the triple combo tool string. Track 2: hole deviation log (DEVI) from the FMS tool. Track 3: Pad 1 azimuth of the FMS tool (P1AZ; black) and hole azimuth (HAZI; red). Track 4: computed magnetic intensity (FNOR, A/m; black) and magnetic inclination (FINC, degree; red) logs.

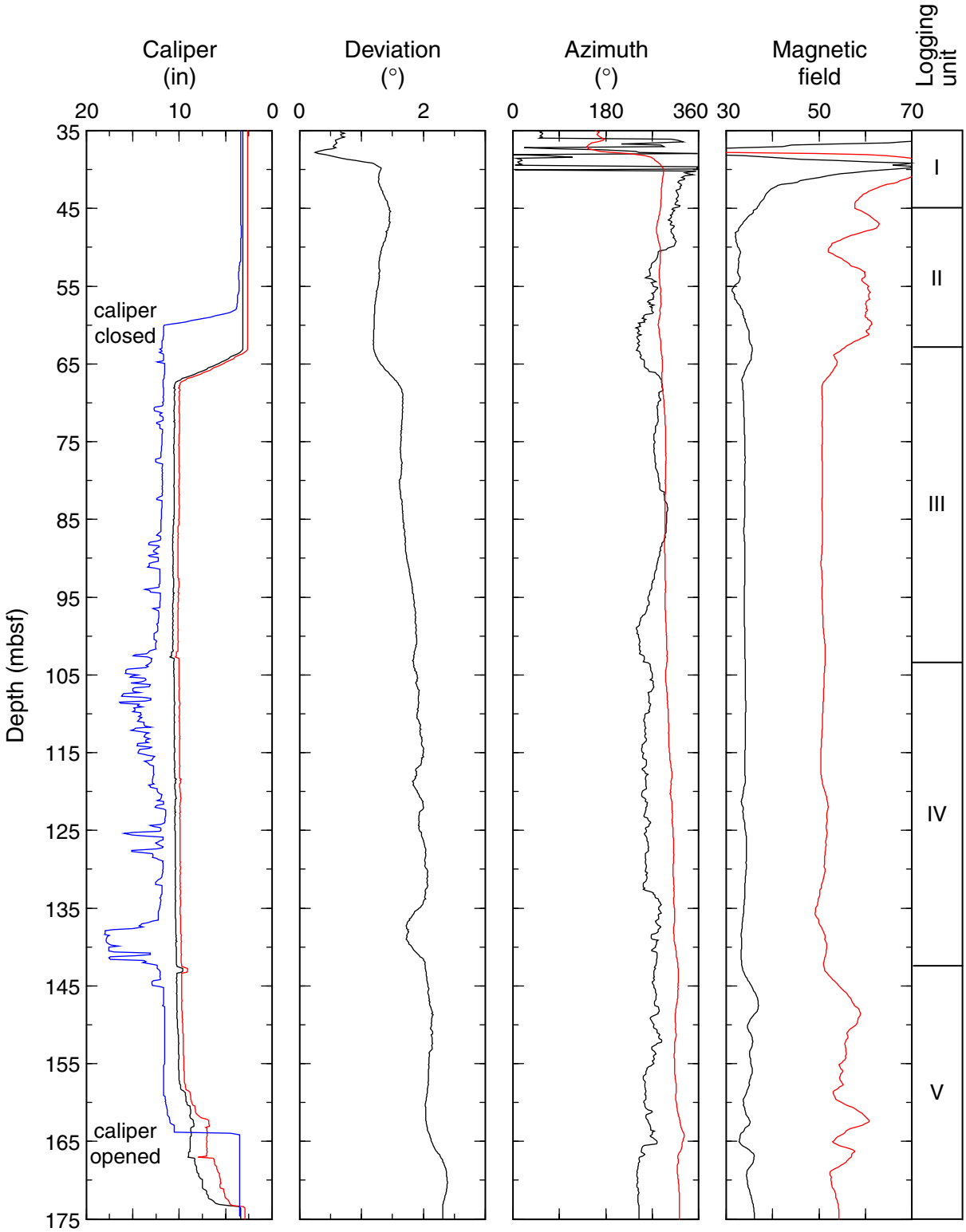

Figure F80. Composite log of the temperature, spontaneous potential (SP), and electrical resistivity logs recorded in Hole 1224F. Track 1: temperature. Track 2: SP. Track 3: deep induction resistivity (ILD). Track 4: spherically focused resistivity log (SFLU).

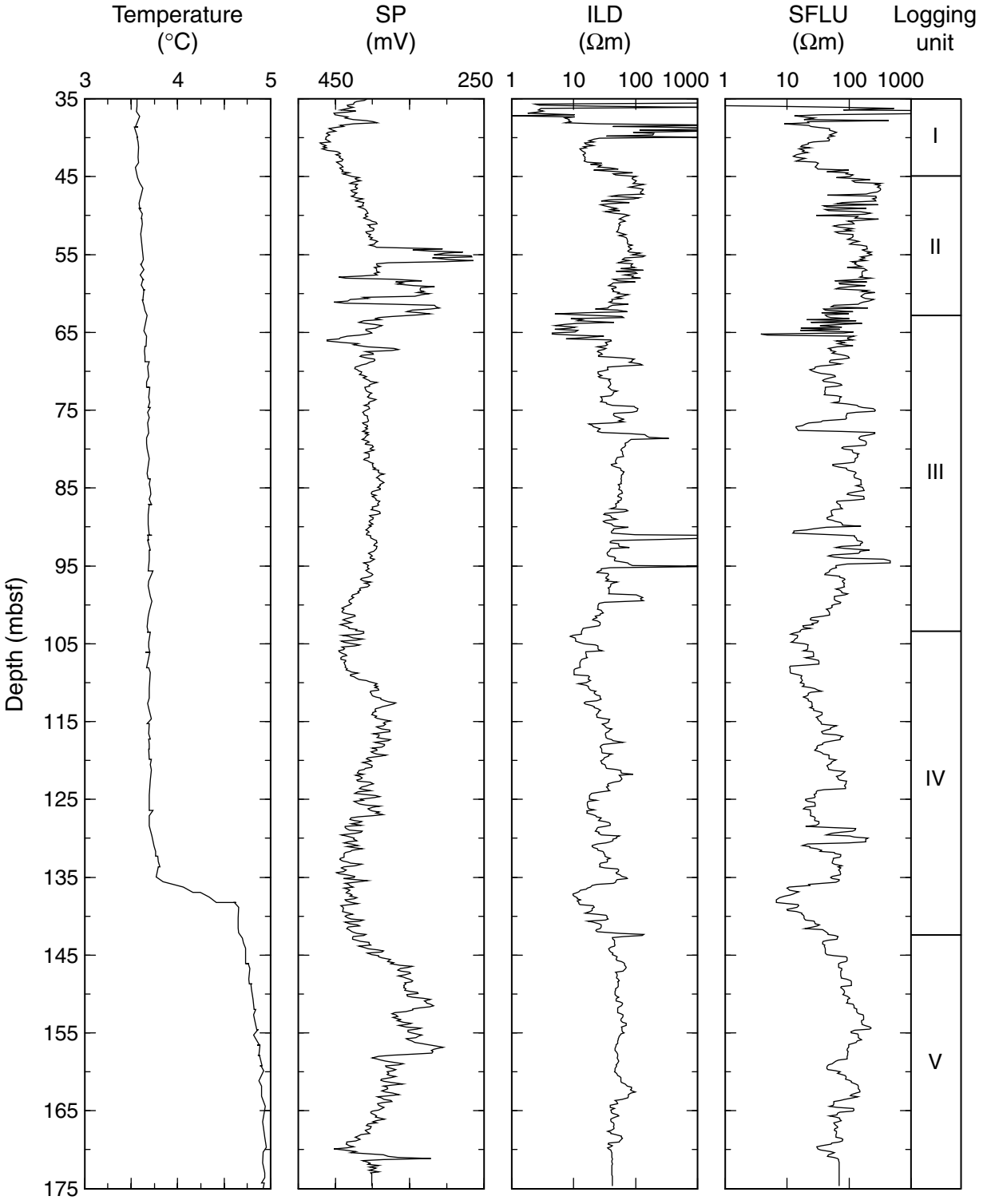

Figure F81. FMS images produced from the microresistivity recorded in Hole 1224F. The FMS images show considerably greater resolution centimeter scale of the relative conductivity changes over this interval and reflect formation characteristics that are not apparent at the broad scale of the other logs.

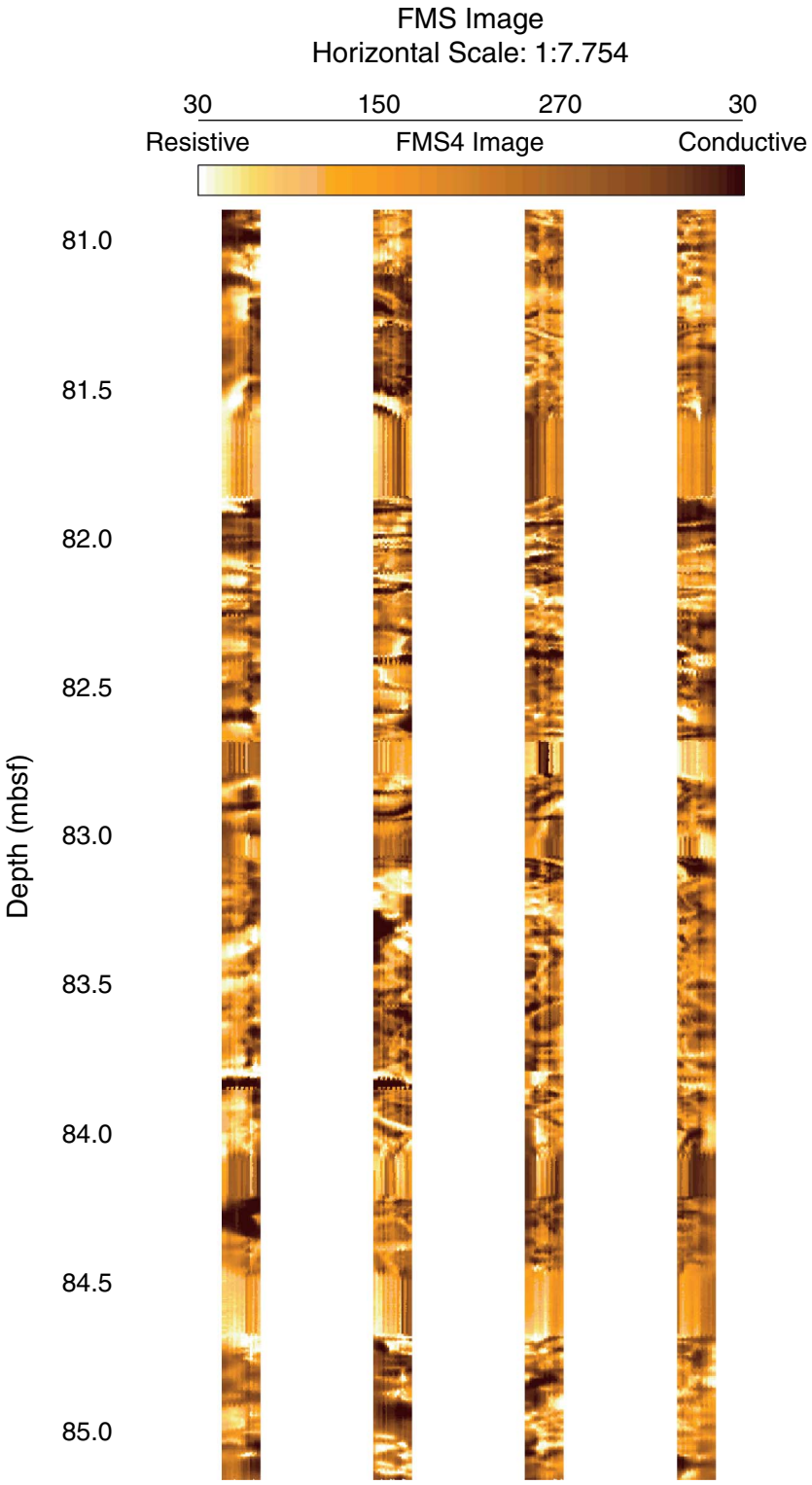

Figure F82. Composite log of the density, neutron porosity, and sonic logs recorded in Hole 1224F. Track 1: bulk density (RHOB). Track 2: neutron porosity (NPHI). Track 3: compressional wave velocity from the monopole source (VPMP). Track 4: shear wave velocity (V_S) log from the monopole source (black) and the shear wave velocity log from the lower dipole (red).

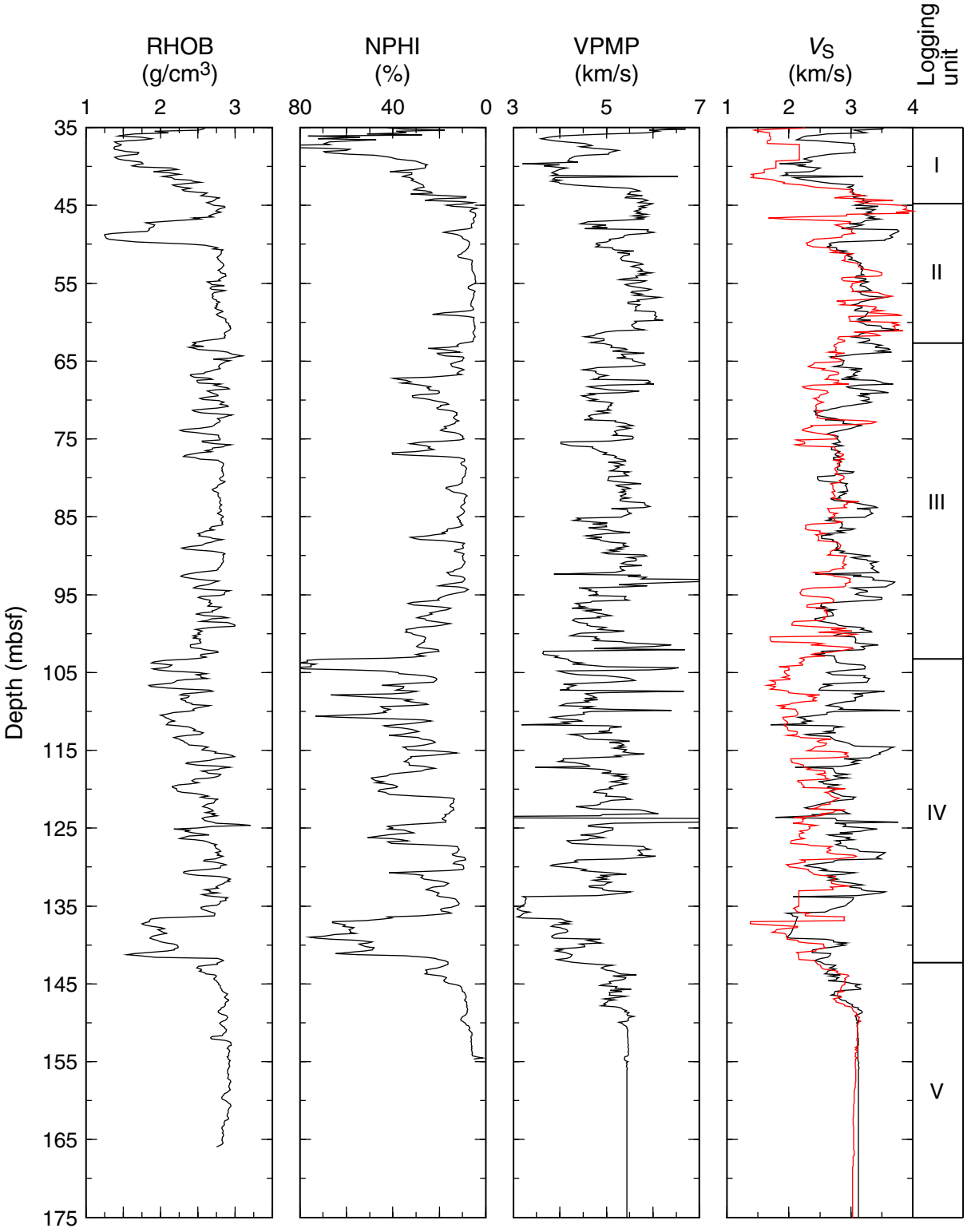

Figure F83. Composite log of the spectral gamma ray logs recorded in Hole 1224F during ODP Leg 200. Track 1: total spectral gamma ray (HSGR, black) and computed gamma ray (HCGR, red). Track 2: contents of potassium (POTA). Track 3: contents of thorium (THOR). Track 4: contents of uranium (URAN).

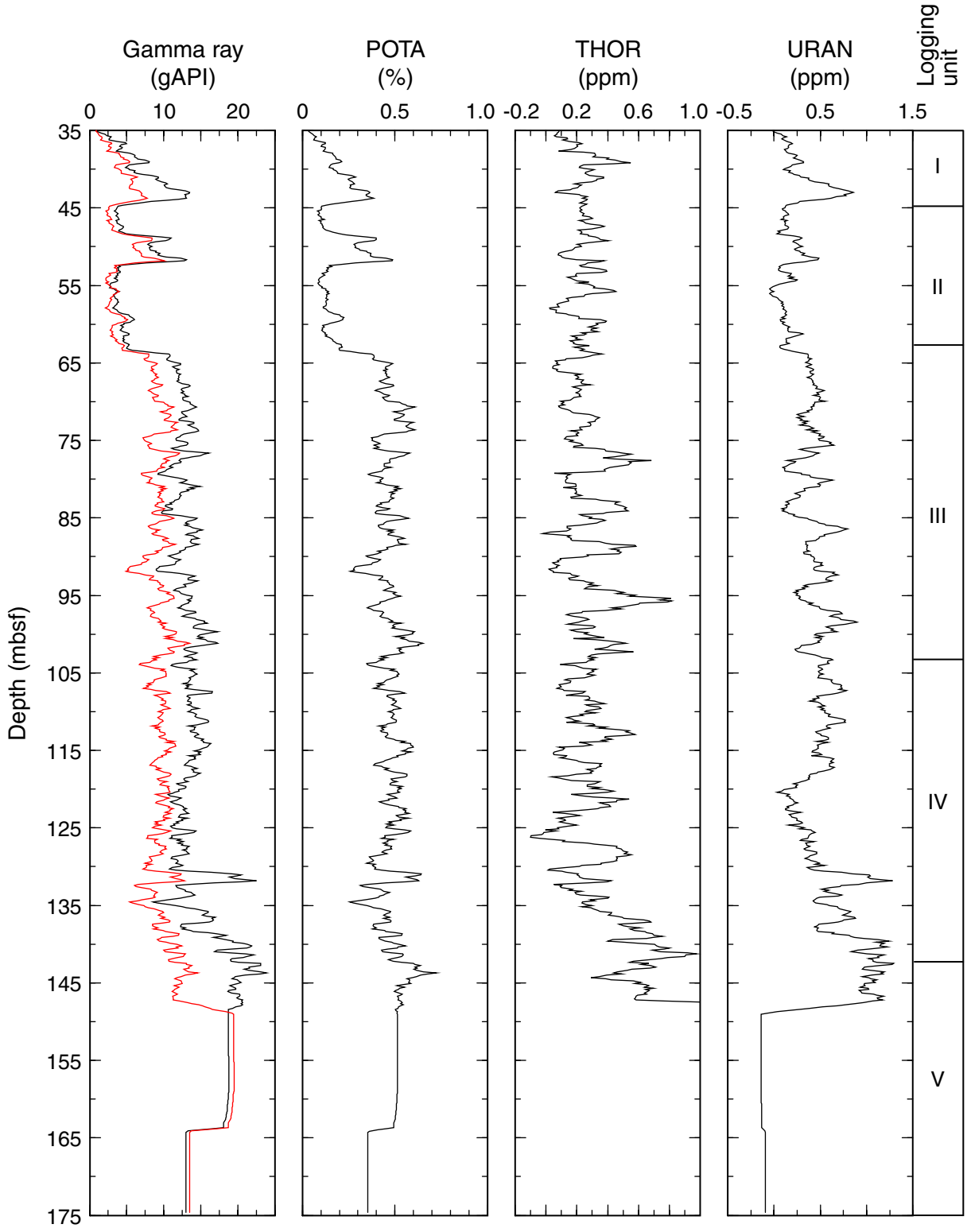

Figure F84. Installation of the reentry cone and steel casing in Hole 1224D as observed on deep-source records. This figure is shown in five sections. It is extracted from the EPC graphic recording for the period 2118 to 2220 hr on 2 January. The traveltime interval shown is ~410 ms; the light horizontal traces are spaced at 100 ms. The heavier vertical traces are 5-min marks. The 14-s fluctuation with an amplitude of up to 4 ms in the traveltime of the direct water wave is primarily due to the heave of the ship pulling and slackening the vibration isolated television (VIT) cable. The 1- to 2-ms fluctuations in the traveltime for the reentry cone is a measure of the VIT heave plus the uncompensated heave of the drill string because the cone is rigidly linked to the ship's heave compensator by the drill string. CHRT = casing hanger running tool.

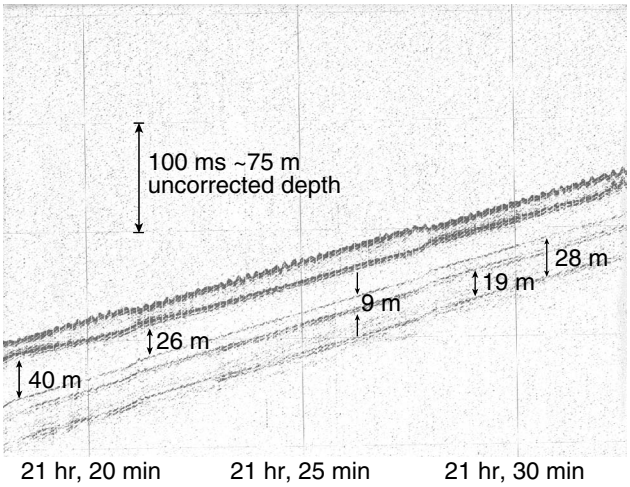

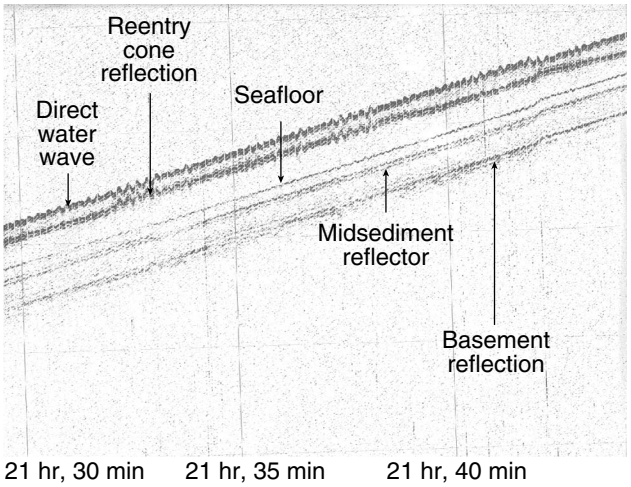

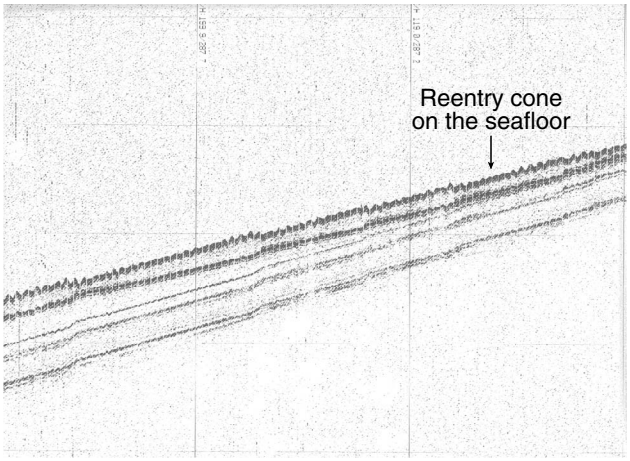

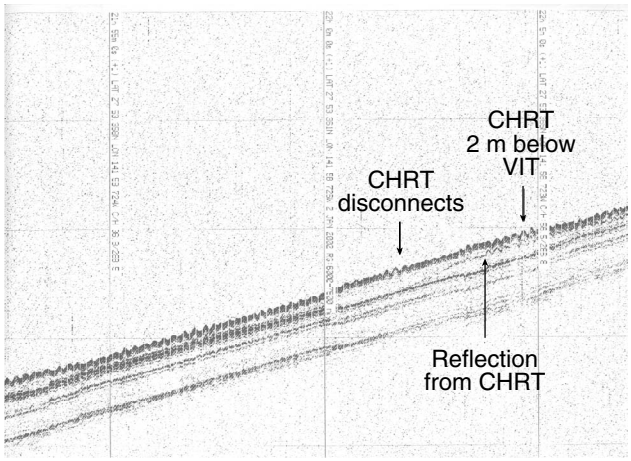

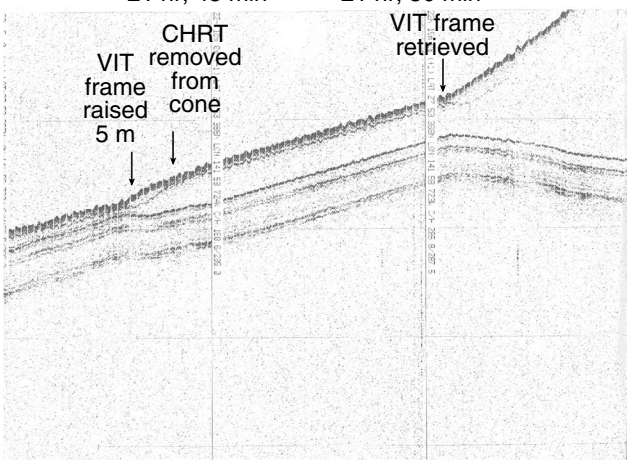

Figure F85. Radiolarians in Hole 1224C. Note that radiolarians are abundant below 4 mbsf.

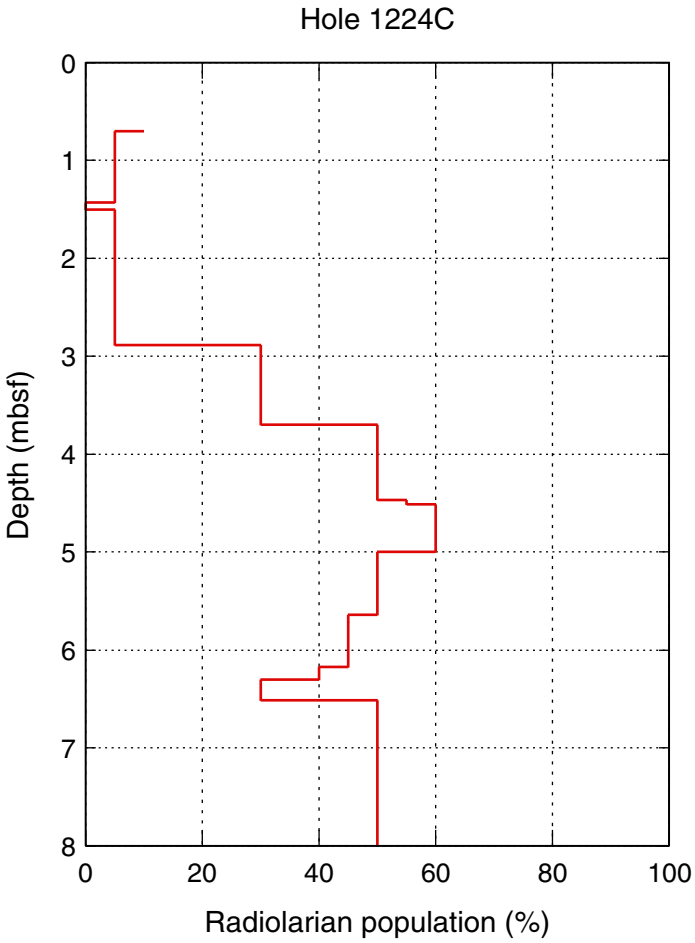

Figure F86. Logging data from Hole 1224F. NPHI = neutron porosity. RHOB = gamma ray bulk density.

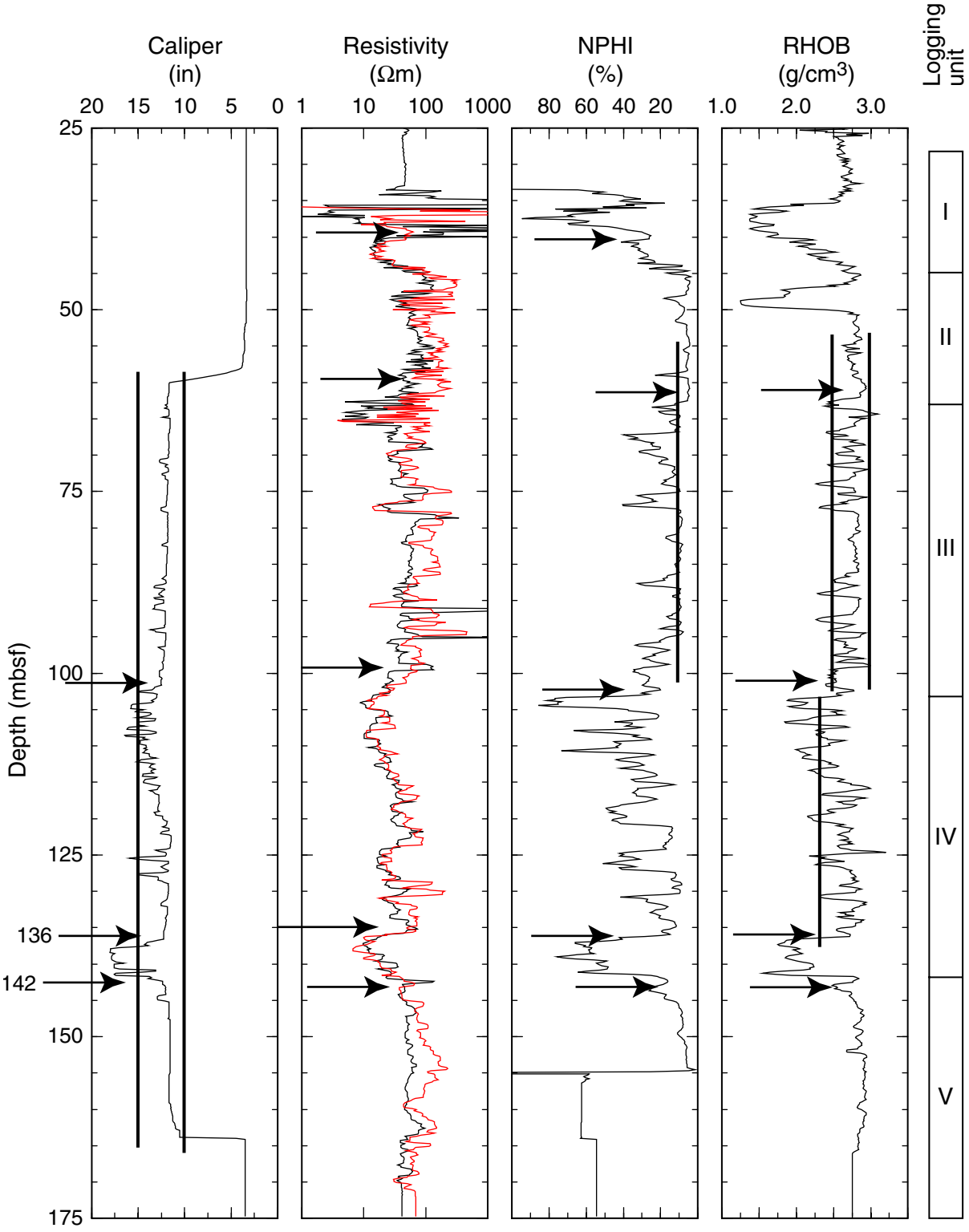

Figure F87. PWS compressional wave velocity (V_P) measurements from Hole 1224F. Seven zones are shown on the right based on PWS, porosity measurements, and logging data.

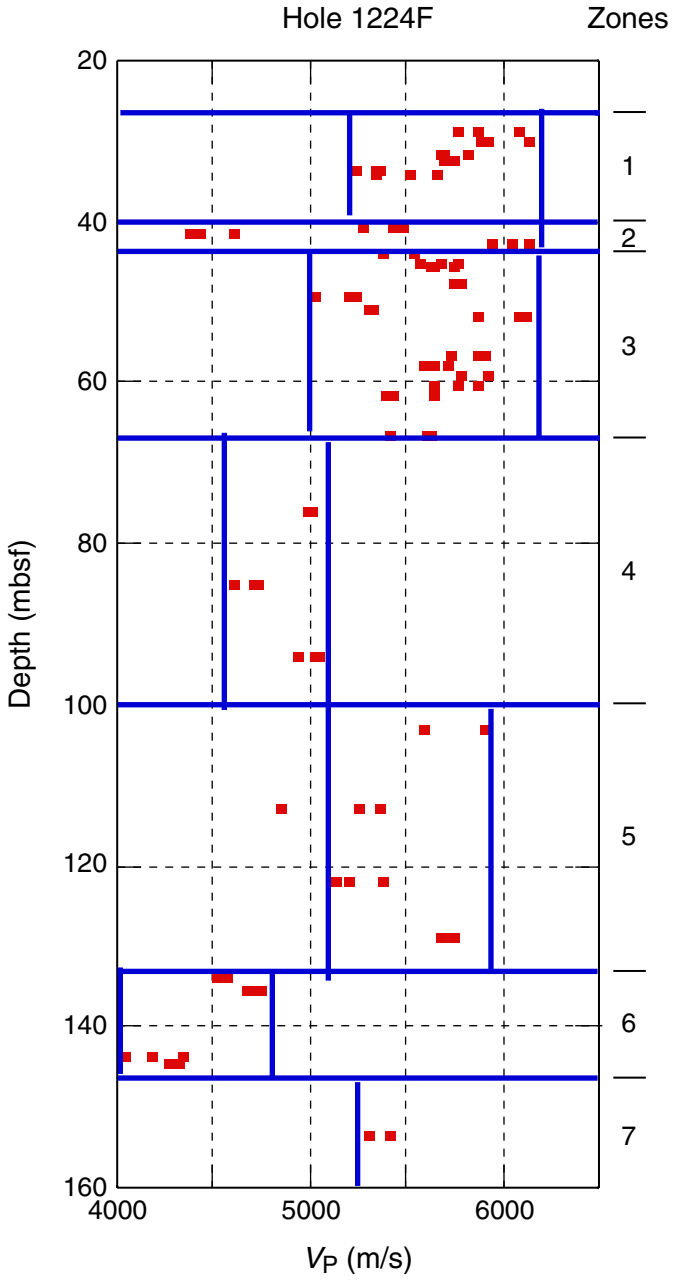

Figure F88. Compressional wave velocity (V_P) model based on PWS velocity measurements.

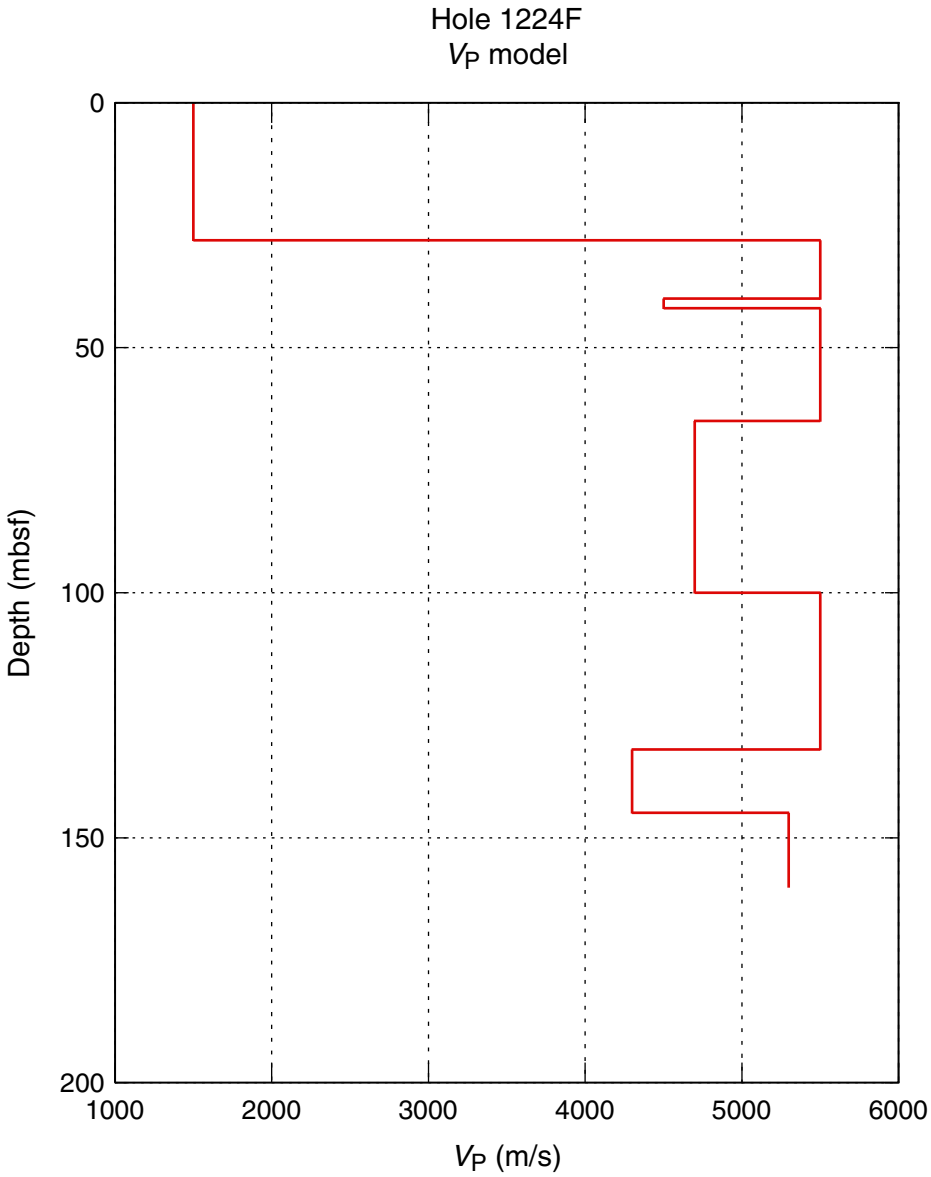

Figure F89. Spectrogram summary of ambient noise levels on the vertical component of the Hawaii-2 Observatory (H2O) seafloor seismometer for the 1-week interval from 22 to 28 December. Color, as defined in the bar on the right, indicates the relative energy content in decibels relative to counts squared per hertz (from –10 to 70 dB) as a function of frequency from 0.1 to 10 Hz. The broad red band at ~0.2–0.3 Hz throughout the week is the microseism peak generated by wave-wave interaction of ocean gravity waves. The thinner red bands at 1.1 and 2.0 Hz are resonances in the thin sediment cover at this site. This spectrogram also shows two and a half storm cycles. These are the broad red bands that slope upward to the left from ~1 to 0.2 Hz over 1.5 to 2 days for each storm cycle. The high-energy peak at 8 Hz, on 25 December (Julian day 359), is a passing ship (see Fig. **F96,** p. 163). The *JOIDES Resolution* arrived on site at 1500 hr on 26 December (Julian day 360). The patches of yellow from 4 to 9 Hz on 26–29 December (Julian days 360 to 363) can be associated with *JOIDES Resolution* activities (also see Figs. **F90,** p. 157, **F92,** p. 159, **F93,** p. 160, **F96,** p. 163, **F97,** p. 164).

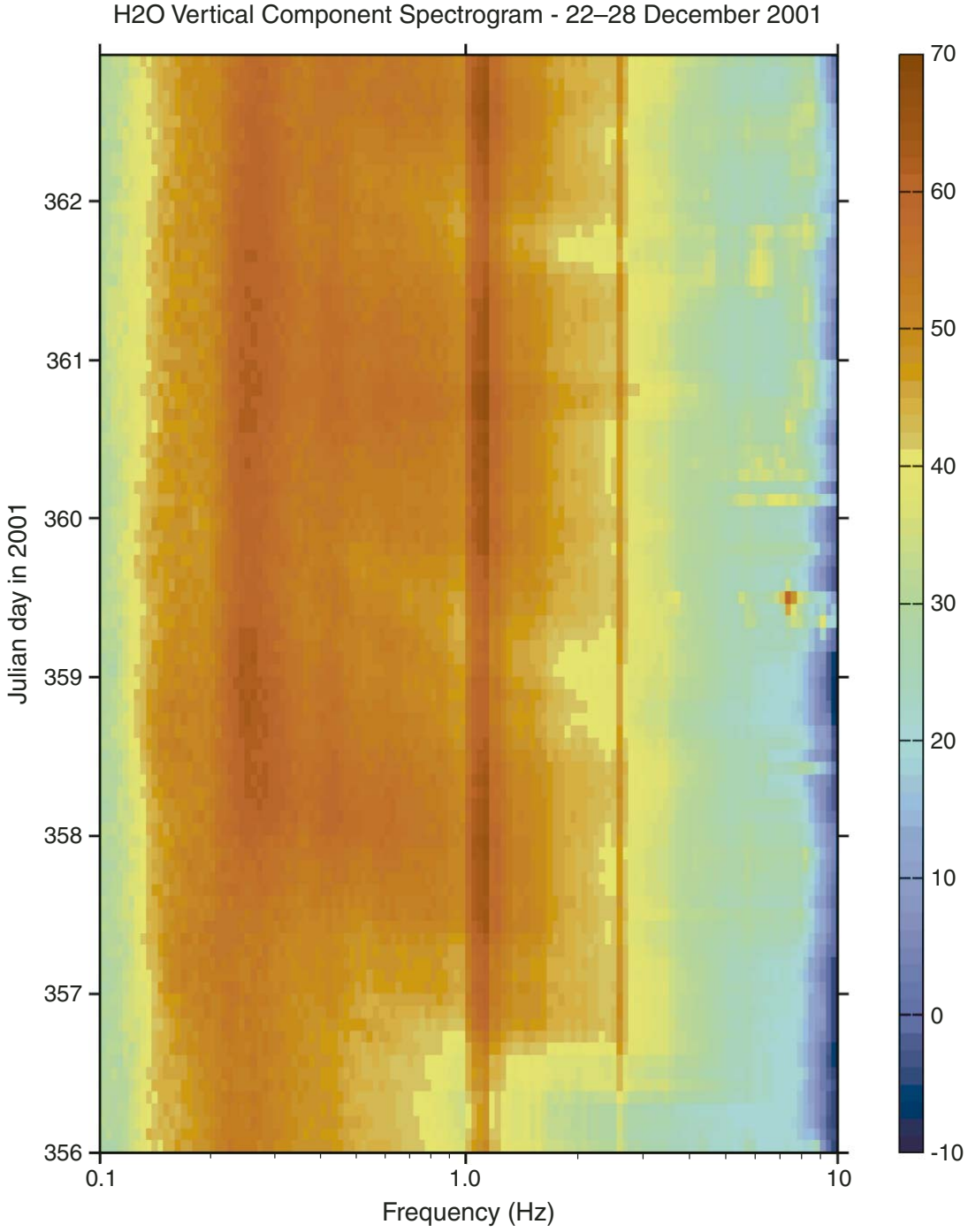

Figure F90. Spectrogram summary of ambient noise levels on the horizontal component of the Hawaii-2 Observatory (H2O) seafloor seismometer for the 1-week interval from 31 December 2001 to 6 January 2002. Color, as defined in the bar on the right, indicates the relative energy content in decibels relative to counts squared per hertz as a function of frequency from 0.1 to 10 Hz. By comparing this horizontal component with the vertical component in Figure F89, p. 156, one can see many more constant frequency bands. The main sediment resonances at 1.1 and 2 Hz dominate even the microseism peak near 0.2 to 0.3 Hz. The red blotches from 4.2 to 6.2 days at frequencies from 2 to 9 Hz correspond to drilling with the RCB bit. The horizontal dark-blue bands on 1 January are data dropouts.

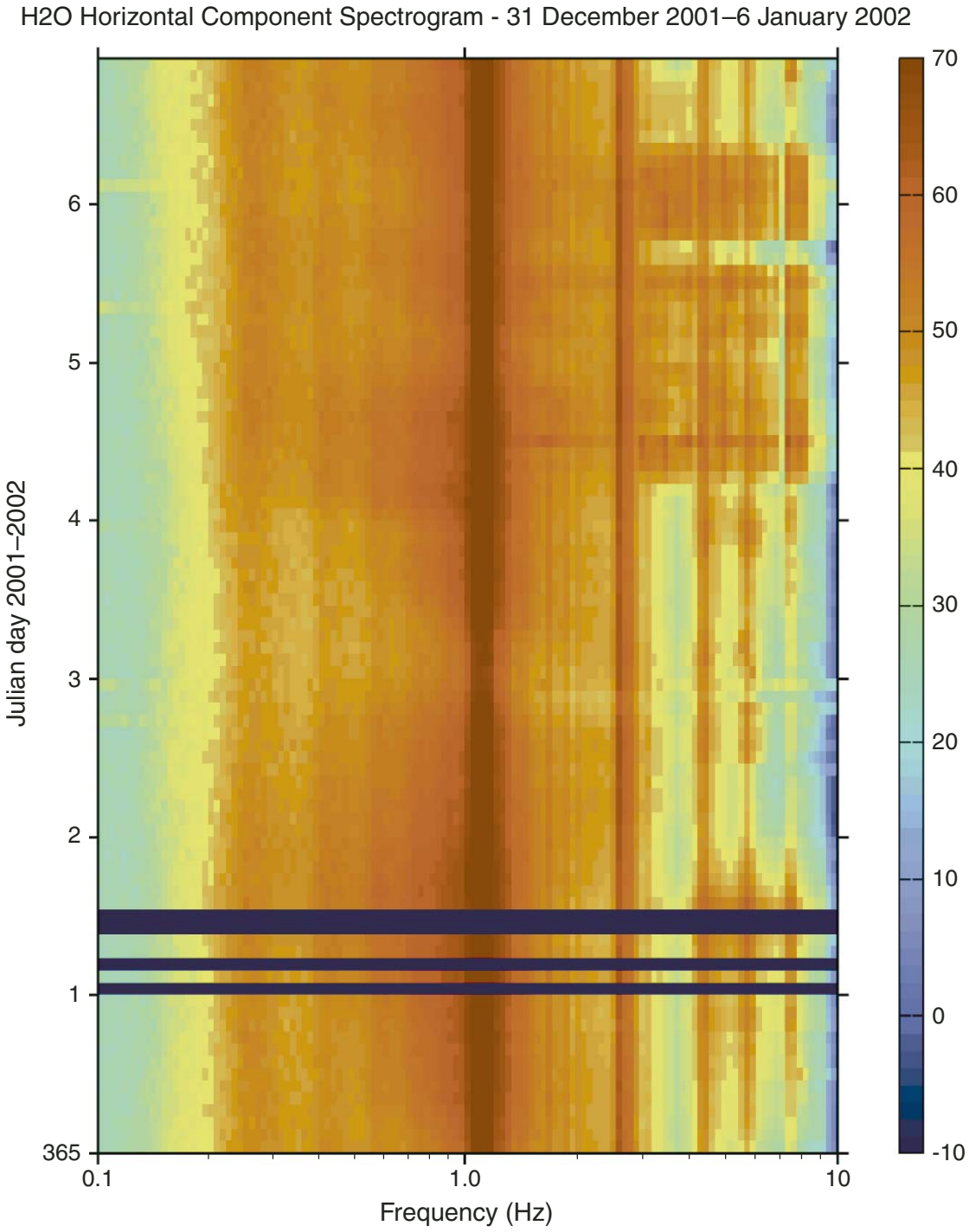

Figure F91. Although no whales were seen around the ship while on site, whale songs were frequently observed on the seafloor seismometer. The largest-amplitude wavelets occur in wave packets of four, which repeat about every 30 s. It takes this long for the water multiples to die down to an acceptable level before the whale sings the next song.

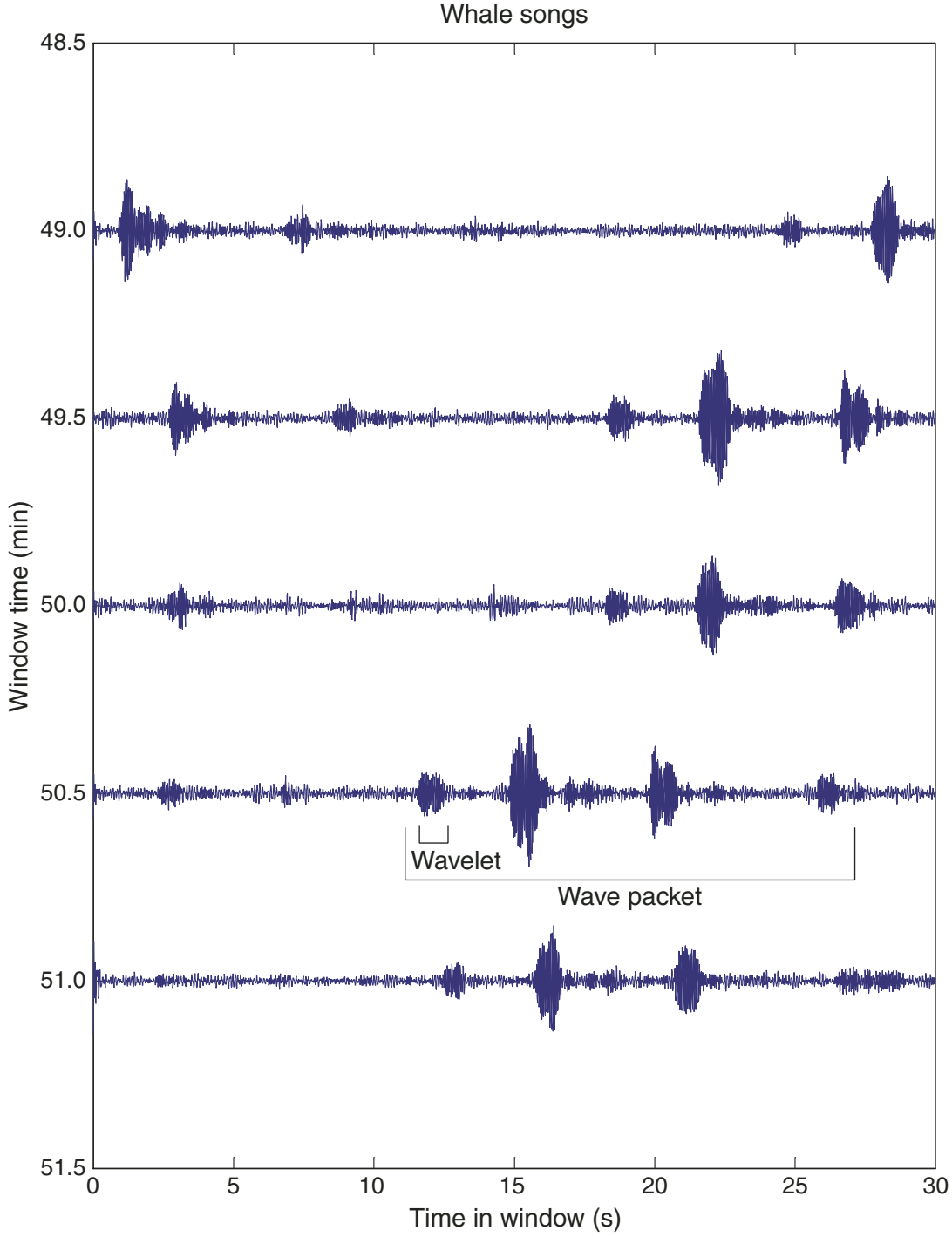

Figure F92. There is a similarity between water guns and whale songs. The water guns are fired every 10 s in the top 10 min of this figure (30–40 s window time). The amplitude, frequency content, and event interval are similar for the two sources. Note that no whale songs are observed in the red traces ~15 min apart. In these intervals the whale stops to breathe.

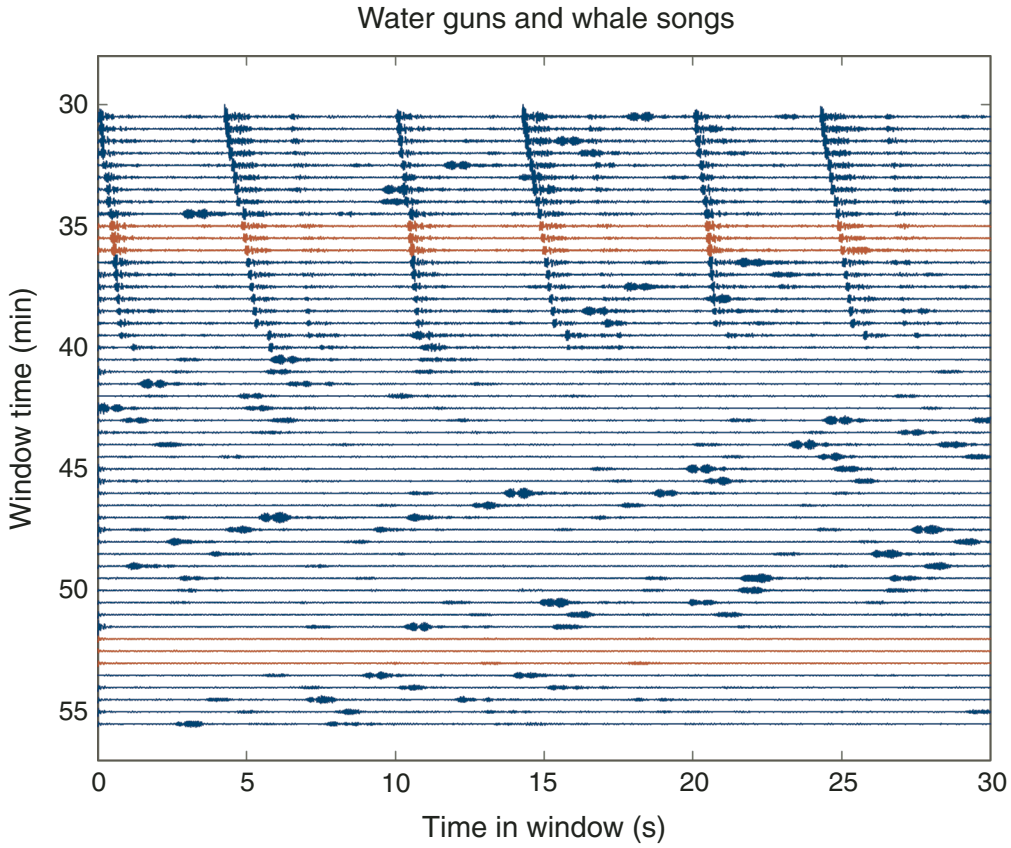

Figure F93. Tracking root-mean-square (RMS) levels in one-octave bands is a convenient way to observe time-dependent effects in the data. The spikes around 5 and 20 hr in this figure correspond to earthquake events. The intense activity between 10 and 15 hr can be associated with the drawworks. RMS levels are given in decibels relative to a count.

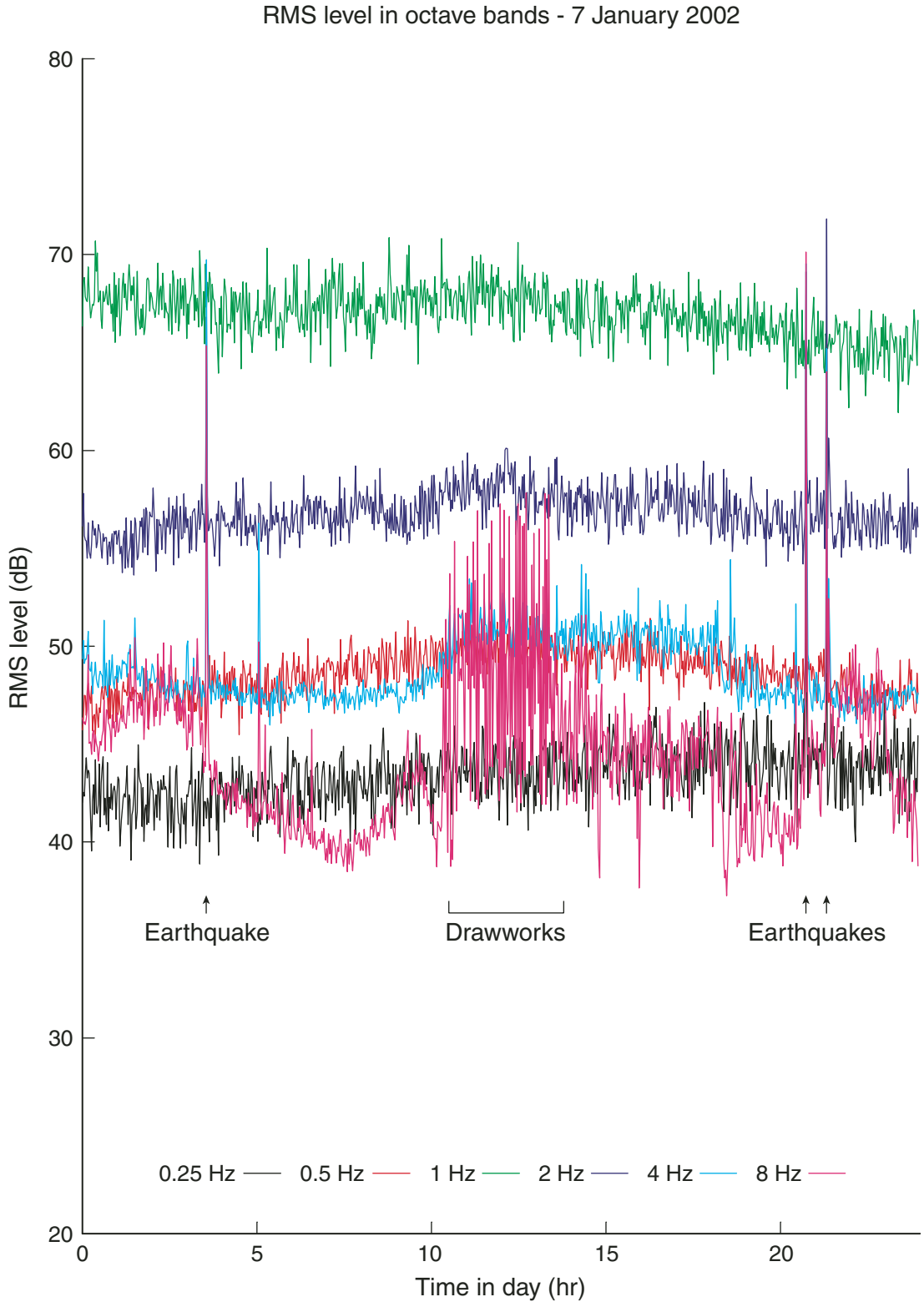

Figure F94. The top panel shows time series near the earthquake at 21.3333 hr in Figure F93, p. 160. The earthquake occurs between 10 and 35 s on the middle trace. The bottom panel shows the corresponding color-coded power spectral density (PSD) in counts squared per hertz. The microseism peak level is unchanged, but levels above the microseism peak increase by up to 20 dB.

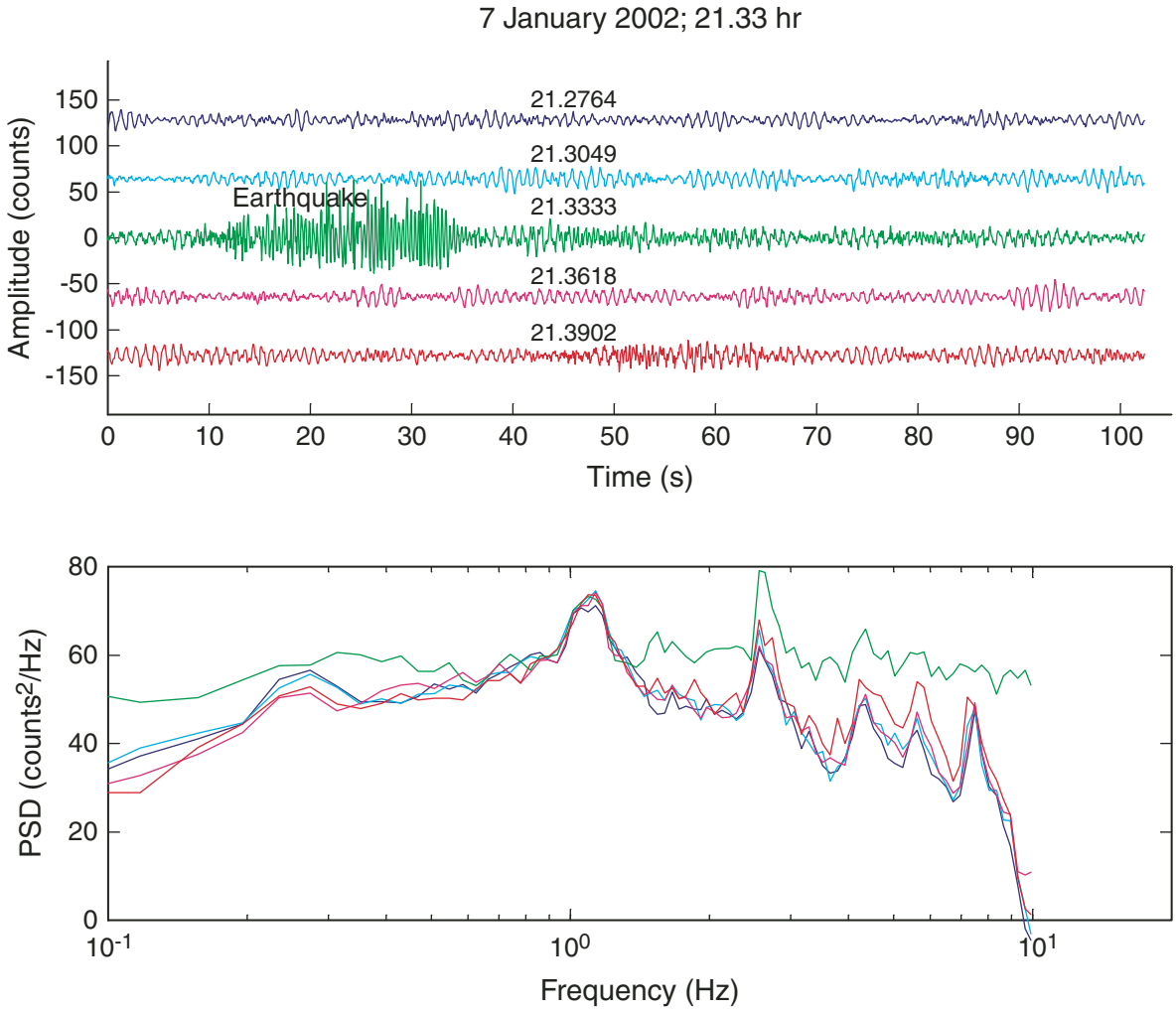

Figure F95. The earthquake at 3.556 hr has a longer duration and higher frequency content than the event in Figure F93, p. 160. PSD = power spectral density.

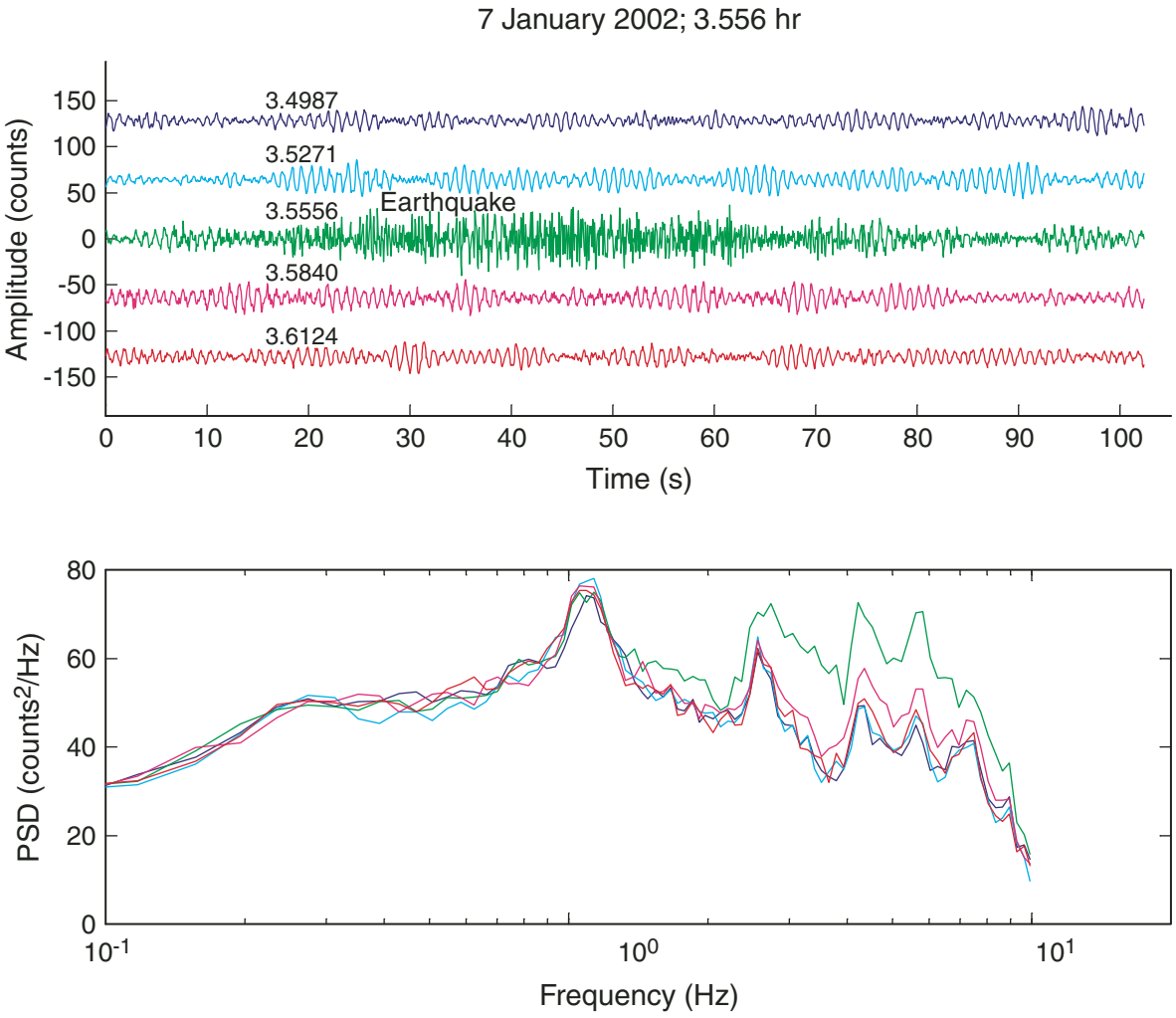

Figure F96. A container ship, with considerable energy near 8 Hz, dominated the noise field near the sensor on 25 December. The ship starts raising noise levels at the site 6 hr before its closest approach to the *JOIDES Resolution,* although it is ~180 km away (traveling at 17 kt). Root-mean-square (RMS) levels are given in decibels relative to a count.

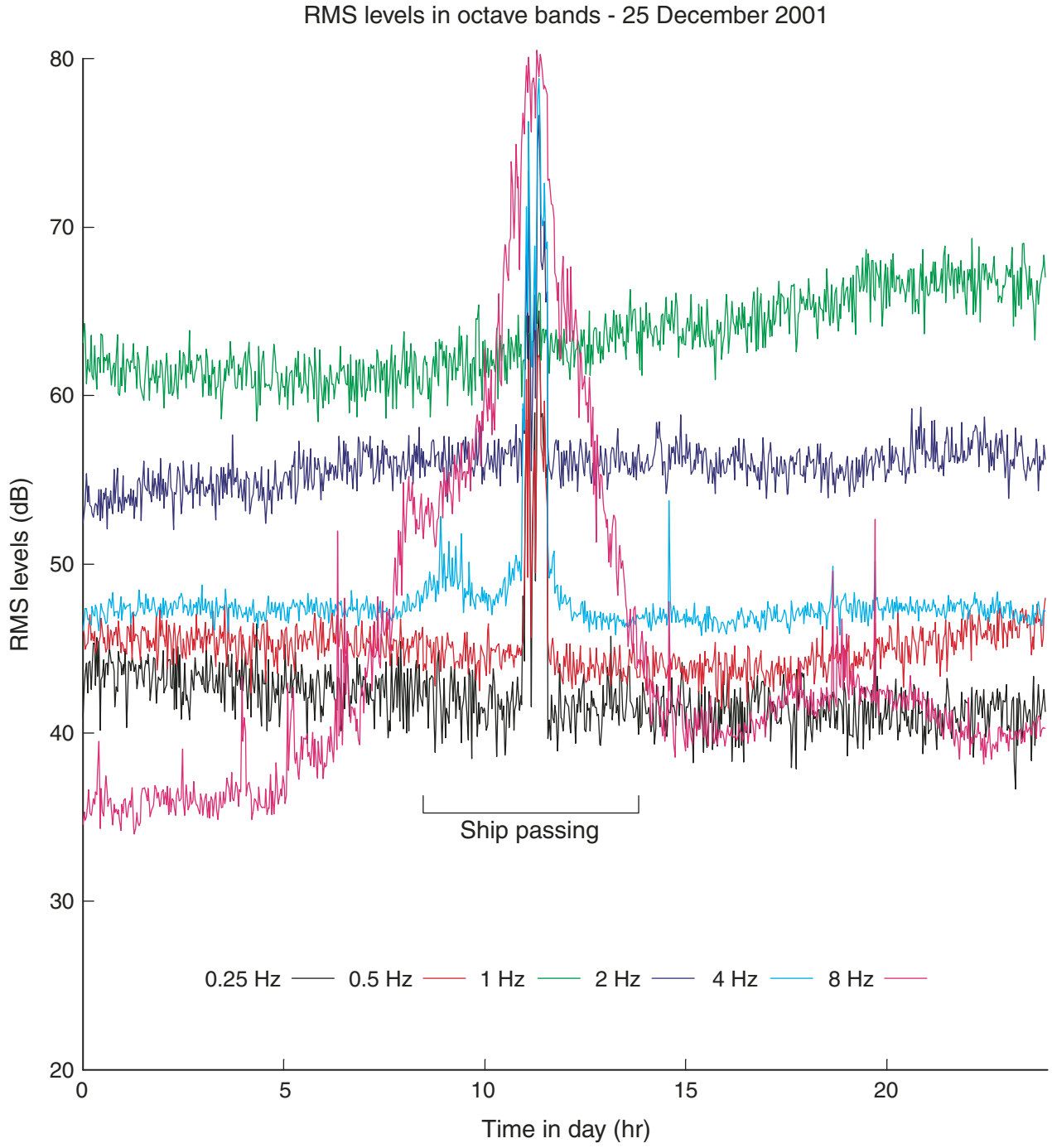

Figure F97. Root-mean-square (RMS) energy levels in octaves at ~4 and 8 Hz (in decibels relative to counts) changed as the 14.75-in bit failed at 0930 hr on 11 January

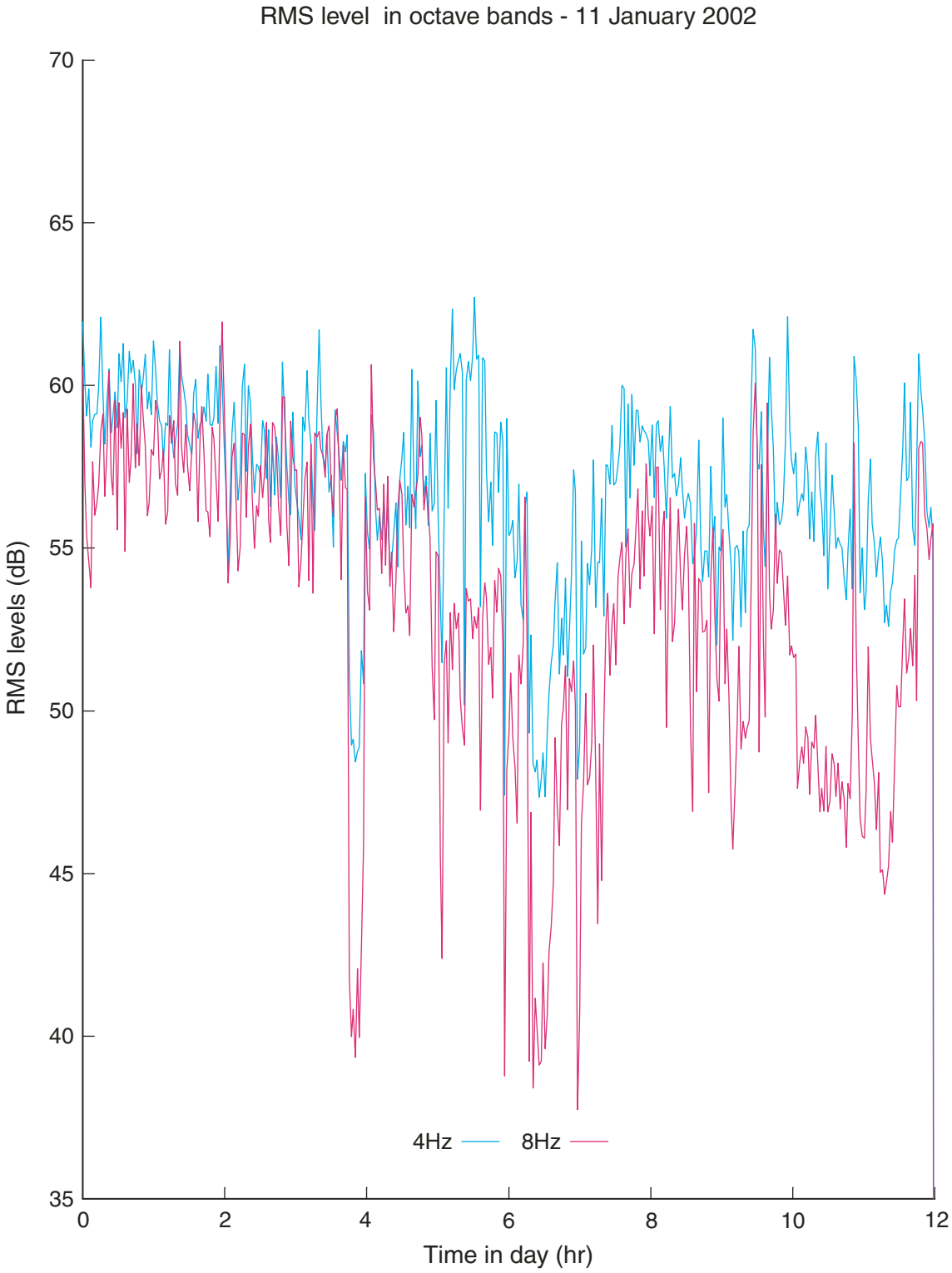

Table T1. Summary of holes drilled in normal crust on the Pacific plate with an age <100 Ma and penetration into basement >10 m.

Leg	Hole	Age (Ma)	Latitude	Longitude	Basement penetration (m)	Sediment thickness (m)
DSDP:						
16	163	72.0	11°N	150°W	18	176
54	420	3.4	09°N	106°W	29	118
54	421	3.4	09°N	106°W	29	85
54	429	4.6	09°N	107°W	21	31
63	469*	17.0	33°N	121°W	58	391
63	470A	15.0	29°N	118°W	48	167
63	471	12.0	23°N	112°W	82	741
63	472	15.0	23°N	114°W	25	112
65	483B	1.7	23°N	109°W	157	110
92	597B	29.0	19°S	130°W	25	48
92	597C†	29.0	19°S	130°W	91	53
ODP:						
136	843B‡	95.0	19°N	159°W	71	243
200	1224D	46.3	28°N	142°W	36	29
200	1224F	46.3	28°N	142°W	145	29

Notes: * = at the foot of Patton Escarpment. † = a reentry cone was emplaced at this site. ‡ = this is the location of Hole OSN-1.

Table T2. Coring summary, Site 1224. (Continued on next two pages.)

Hole 1224A
Latitude: 27°53.3723′N
Longitude: 141°58.7494′W
Time on site (hr): 592.17 (0845 hr, 28 December 2001–2355 hr, 21 January 2002)
Time on hole (hr): 14.58 (1455 hr, 28 December–0530 hr, 29 December 2001)
Seafloor (drill pipe measurement from rig floor, mbrf): 4977.0
Distance between rig floor and sea level (m): 10.9
Water depth (drill pipe measurement from sea level, m): 4966.1
Total depth (drill pipe measurement from rig floor, mbrf): 5009.2
Total penetration (meters below seafloor, mbsf): 32.2
Total length of cored section (m): 32.2
Total core recovered (m): 1.67
Core recovery (%): 5.19
Total number of cores: 6

Hole 1224B
Latitude: 27°53.3690′N
Longitude: 141°58.7538′W
Time on hole (hr): 2.25 (0530 hr, 29 December–0745 hr, 29 December 2001)
Seafloor (drill pipe measurement from rig floor, mbrf): 4981.3
Distance between rig floor and sea level (m): 10.9
Water depth (drill pipe measurement from sea level, m): 4970.4
Total depth (drill pipe measurement from rig floor, mbrf): 4981.5
Total penetration (meters below seafloor, mbsf): 0.2
Total length of cored section (m): 0.2
Total core recovered (m): 0.20
Core recovery (%): 100.0
Total number of cores: 1

Hole 1224C
Latitude: 27°53.369′N
Longitude: 141°58.7571′W
Time on hole (hr): 30.75 (0745 hr, 29 December–1430 hr, 30 December 2001)
Seafloor (drill pipe measurement from rig floor, mbrf): 4978.0
Distance between rig floor and sea level (m): 10.9
Water depth (drill pipe measurement from sea level, m): 4967.1
Total depth (drill pipe measurement from rig floor, mbrf): 4984.5
Total penetration (meters below seafloor, mbsf): 6.5
Total length of cored section (m): 6.5
Total core recovered (m): 6.53
Core recovery (%): 100.46
Total number of cores: 1

Hole 1224D
Latitude: 27°53.3699′N
Longitude: 141°58.7525′W
Time on hole (hr): 268.9 (1220 hr, 2 January–1815 hr, 13 January 2002)
Seafloor (drill pipe measurement from rig floor, mbrf): 4978.0
Distance between rig floor and sea level (m): 10.9
Water depth (drill pipe measurement from sea level, m): 4967.1
Total depth (drill pipe measurement from rig floor, mbrf): 5042.7
Total penetration (meters below seafloor, mbsf): 64.7
Total length of cored section (m): 33.5
Total length of drilled intervals (m): 31.2
Total core recovered (m): 15.65
Core recovery (%): 46.72
Total number of cores: 5
Total number of drilled intervals: 2

Hole 1224E
Latitude: 27°53.3627′N
Longitude: 141°58.7568′W
Time on hole (hr): 20 (1900 hr, 13 January–1500 hr, 14 January 2002)
Seafloor (drill pipe measurement from rig floor, mbrf): 4978.0
Distance between rig floor and sea level (m): 10.9
Water depth (drill pipe measurement from sea level, m): 4967.1
Total depth (drill pipe measurement from rig floor, mbrf): 5014.7
Total penetration (meters below seafloor, mbsf): 36.7
Total length of cored section (m): 28.7
Total length of drilled intervals (m): 8.0
Total core recovered (m): 14.91
Core recovery (%): 51.95
Total number of cores: 3
Total number of drilled intervals: 1

Table T2 (continued).

Hole 1224F
Latitude: 27°53.3634′N
Longitude: 141°58.7567′W
Time on hole (hr): 176.9 (1500 hr, 14 January–2355 hr, 21 January 2002)
Seafloor (drill pipe measurement from rig floor, mbrf): 4978.0
Distance between rig floor and sea level (m): 10.9
Water depth (drill pipe measurement from sea level, m): 4967.1
Total depth (drill pipe measurement from rig floor, mbrf): 5152.5
Total penetration (meters below seafloor, mbsf): 174.5
Total length of cored section (m): 146.8
Total core recovered (m): 37.7
Core recovery (%): 25.68
Total number of cores: 17

Core	Date	Local time (hr)	Depth (mbsf) Top	Depth (mbsf) Bottom	Length (m) Cored	Length (m) Recovered	Recovered (%)
200-1224A-							
1X	28 Dec 2001	1610	0.0	6.0	6.0	0.00	0.00
2X	28 Dec 2001	1720	6.0	15.6	9.6	0.02	0.21
3X	28 Dec 2001	1835	15.6	25.2	9.6	0.01	0.10
4X	28 Dec 2001	2210	25.2	30.7	5.5	1.24	22.55
5X	29 Dec 2001	0105	30.7	32.0	1.3	0.18	13.85
6N	29 Dec 2001	0430	32.0	32.2	0.2	0.22	110.00
			Cored totals:		32.2	1.67	5.19
200-1224B-							
1H	29 Dec 2001	0725	0.0	0.2	0.2	0.20	100.00
			Cored total:		0.2	0.20	100.00
200-1224C-							
1H	29 Dec 2001	0850	0.0	6.5	6.5	6.53	100.46
			Cored total:		6.5	6.53	100.46
200-1224D-							
			*****Drilled from 0.0 to 25.5 mbsf*****				
1R	4 Jan 2002	0530	25.5	35.1	9.6	4.15	43.23
2R	4 Jan 2002	1710	35.1	44.7	9.6	4.81	50.10
3R	5 Jan 2002	0025	44.7	49.3	4.6	3.30	71.74
4R	5 Jan 2002	0555	49.3	51.3	2.0	1.99	99.50
5R	6 Jan 2002	0100	51.3	59.0	7.7	1.40	18.18
			*****Drilled from 59.0 to 64.7 mbsf*****				
			Cored totals:		33.5	15.65	46.72
			Drilled totals:		31.2		
			Total:		64.7		
200-1224E-							
			*****Drilled from 0.0 to 8.0 mbsf*****				
1R	13 Jan 2002	2005	8.0	17.5	9.5	1.03	10.84
2R	13 Jan 2002	2110	17.5	27.1	9.6	9.49	98.85
3R	14 Jan 2002	1505	27.1	36.7	9.6	4.39	45.73
			Cored totals:		28.7	14.91	51.95
			Drilled total:		8.0		
			Total:		36.7		
200-1224F-							
1R	15 Jan 2002	0455	27.7	39.7	12.0	6.13	51.08
2R	15 Jan 2002	0930	39.7	47.3	7.6	5.32	70.00
3R	15 Jan 2002	2125	47.3	56.4	9.1	4.13	45.38
4R	16 Jan 2002	0650	56.4	65.9	9.5	6.20	65.26
5R	16 Jan 2002	1225	65.9	75.0	9.1	0.95	10.44
6R	16 Jan 2002	2035	75.0	84.5	9.5	1.50	15.79
7R	17 Jan 2002	0240	84.5	93.5	9.0	1.20	13.33
8R	17 Jan 2002	0750	93.5	102.7	9.2	1.31	14.24
9R	17 Jan 2002	1225	102.7	111.8	9.1	0.60	6.59
10R	17 Jan 2002	1645	111.8	121.1	9.3	1.40	15.05
11R	17 Jan 2002	2315	121.1	128.5	7.4	1.71	23.11
12R	18 Jan 2002	1130	128.5	133.5	5.0	1.20	24.00
13R	18 Jan 2002	1505	133.5	143.2	9.7	2.73	28.14

Table T2 (continued).

Core	Date	Local time (hr)	Depth (mbsf) Top	Depth (mbsf) Bottom	Length (m) Cored	Length (m) Recovered	Recovered (%)
14R	19 Jan 2002	0300	143.2	152.4	9.2	2.02	21.96
15R	19 Jan 2002	1045	152.4	161.8	9.4	1.30	13.83
16R	19 Jan 2002	1700	161.8	171.0	9.2	0.00	0.00
17R	19 Jan 2002	2250	171.0	174.5	3.5	0.00	0.00
			Cored totals:		146.8	37.70	25.68

Table T3. Expanded coring summary, Site 1224.

Hole 1224A
Position: 27°53.3723′N, 141°58.7494′W
Water depth from sea surface = 4966.1 m

Hole 1224B
Position: 27°53.3690′N, 141°58.7538′W
Water depth from sea surface = 4970.4 m

Hole 1224C
Position: 27°53.369′N, 141°58.7571′W
Water depth from sea surface = 4967.1 m

Hole 1224D
Position: 27°53.3699′N, 141°58.7525′W
Water depth from sea surface = 4967.1 m

Hole 1224E
Position: 27°53.3627′N, 141°58.7568′W
Water depth from sea surface = 4967.1 m

Hole 1224F
Position: 27°53.3634′N, 141°58.7567′W
Water depth from sea surface = 4967.1 m

Leg	Site	Hole	Core	Type	Date (2001–2002)	Local time (hr)	Depth (mbsf) Top	Depth (mbsf) Bottom	Length (m) Cored	Length (m) Recovered	Recovery (%)	Section	Length (m) Liner	Length (m) Curated	Section depth (mbsf) Top	Section depth (mbsf) Bottom	Catwalk samples	Comment
200	1224	A	1	X	28 Dec	1610	0.0	6.0	6.0	0.00	0.0							One wire line run for jet-in test on 27 Dec
												1	0.00	0.00				
												Total:	0.00	0.00				
200	1224	A	2	X	28 Dec	1720	6.0	15.6	9.6	0.02	0.2							
												CC(w/CC)	0.02	0.02	6.00	6.02		
												Total:	0.02	0.02				
200	1224	A	3	X	28 Dec	1835	15.6	25.2	9.6	0.01	0.1							Shattered liner
												CC(w/CC)	0.01	0.01	15.60	15.61		
												Total:	0.01	0.01				
200	1224	A	4	X	28 Dec	2210	25.2	30.7	5.5	1.24	22.5							Oil saver unseated
												1	1.02	1.02	25.20	26.22		
												CC(w/CC)	0.22	0.22	26.22	26.44		
												Totals:	1.24	1.24				
200	1224	A	5	X	29 Dec	0105	30.7	32.0	1.3	0.18	13.8							
												1	0.18	0.23	30.70	30.93		
												Total:	0.18	0.23				
200	1224	A	6	N	29 Dec	0430	32.0	32.2	0.2	0.22	110.0							MDCB cored min for 30 min
												1	0.22	0.23	32.00	32.23		
												Total:	0.22	0.23				
								Totals:	32.2	1.67	5.2							

Notes: NA = not applicable. CC = core catcher (number in parenthesis indicates which section the core catcher is stored with). MDCB = motor-driven core barrel, AHC = advanced hydraulic corer. Only a portion of this table appears here. The complete table is available in **ASCII.**

Table T4. Operation synopsis, Leg 200. (See table note. Continued on next two pages.)

Site/Hole	Activity	Local time (hr)	Date	Time on hole (hr)		Time on site (hr)	Comments
Port call Honolulu	First line ashore	0752	16 Dec 2001				
Leg 200	Last line aboard	1404	20 Dec 2001	102.20		102.20	
					Total:	102.20	
Honolulu	Depart	1404	20 Dec 2001				
	End of sea voyage Nuuanu	0730	21 Dec 2001	17.43		17.43	Traveled 175 nmi at 10.0 kt
					Total:	17.43	
1223A	Position on GPS	0730	21 Dec 2001				Spud at 2030 hr
	Spud Hole 1223A	2030	21 Dec 2001	13.00		13.00	Run in hole
	Clear seafloor Hole 1223A	1725	22 Dec 2001	20.92		20.92	Science objective obtained
	Clear rotary	0130	23 Dec 2001	8.08		8.08	Pull out of hole
	Depart site	0130	23 Dec 2001	0.00		0.00	
					Total:	42.00	
Nuuanu	Depart site	0130	23 Dec 2001				
	Arrive at H2O	0000	26 Dec 2001	70.50		70.50	Traveled 766 nmi at 10.9 kt
	Seismic survey	0745	26 Dec 2001	7.75		7.75	Mechanical breakdown 43 nmi at 5.5 kt
					Total:	78.25	
	ODP mechanical downtime					7.75	
1224A	Arrive on location	0745	26 Dec 2001				
	Position on GPS	0845	26 Dec 2001	1.00		1.00	On location in DP mode
	Waiting on weather	2200	26 Dec 2001	13.25		13.25	
	Run in hole	1230	27 Dec 2001	14.50		14.50	
	Box survey	1430	27 Dec 2001	2.00		2.00	Tag seafloor for jet-in 1525 hr
	Jet-in test	1715	27 Dec 2001	2.75		2.75	Finish jet-in 1715 hr
	Pull out of hole	1745	27 Dec 2001	0.50		0.50	Clear seafloor at 1740 hr
	Retrieve VIT	0000	28 Dec 2001	6.25		6.25	
	Hang off drill string	0030	28 Dec 2001	0.50		0.50	
	Waiting on weather	1345	28 Dec 2001	13.25		13.25	
	Drop core barrel	1455	28 Dec 2001	1.17		1.17	
	Spud Hole 1224A	1455	28 Dec 2001			0.00	
	Clear seafloor	0530	29 Dec 2001	14.58		14.58	
					Total:	69.75	
	Hole 1224A waiting on weather					33.25	
1224B	Offset	0530	29 Dec 2001				
	Spud Hole 1224B	0650	29 Dec 2001	1.33		1.33	APC for mudline
	Clear seafloor	0745	29 Dec 2001	0.92		0.92	Mechanical shear
					Total:	2.25	
1224C	Run in hole with core barrel	0745	29 Dec 2001			0.00	APC for mudline
	Spud Hole 1224C	0820	29 Dec 2001	0.58		0.58	
	Clear seafloor	0915	29 Dec 2001	0.92		0.92	
	Hang off drill string	1000	29 Dec 2001	0.75		0.75	
	Waiting on weather	0115	30 Dec 2001	15.25		15.25	
	Jet-in test spud 0118 hr	0230	30 Dec 2001	1.25		1.25	Cleared seafloor at 0230 hr
	Cleared rotary	1430	30 Dec 2001	12.00		12.00	Pull out of hole
					Total:	30.75	
	Hole 1224C waiting on weather					16.00	
1224D	Pick up casing tools and position reentry cone	1830	30 Dec 2001	4.00		4.00	Arrive hole
	Waiting on weather	1715	1 Jan 2002	46.75		46.75	
	Launch reentry assembly	2335	1 Jan 2002	6.33		6.33	Make up casing and BHA
	Spud Hole 1224D	1220	2 Jan 2002	12.75		12.75	Run in hole and space out to jet-in
	Release running tool	1300	2 Jan 2002	0.67		0.67	Jet-in 20-in casing 20-in casing at 25.47 mbsf
	Cleared seafloor	1315	2 Jan 2002				
	Cleared rotary	0200	3 Jan 2002	13.00		13.00	Pull out of hole for RCB BHA
	Install upper guide horn	0300	3 Jan 2002	1.00		1.00	
	Detorque CHRT	0315	3 Jan 2002	0.25		0.25	
	Slip and cut drilling line	0445	3 Jan 2002	1.50		1.50	
					Total:	86.25	
	Make up RCB BHA and run in hole	1800	3 Jan 2002	13.25		13.25	
	Search and reenter	1845	3 Jan 2002	0.75		0.75	Reenter Hole 1224D 1837 hr
	Run in hole to 20-in shoe 25.5 m	1915	3 Jan 2002	0.50		0.50	
	Recover VIT	2130	3 Jan 2002	2.25		2.25	
	RCB 25.5–51.3 m	0430	5 Jan 2002	31.00		31.00	Tag hard at 29.5 m (0.8 m/hr)
	Pull out of hole into casing	0500	5 Jan 2002	0.50		0.50	Increasing heave and roll
	Retrieve Core 4R	0600	5 Jan 2002	1.00		1.00	

Table T4 (continued).

Site/Hole	Activity	Local time (hr)	Date	Time on hole (hr)		Time on site (hr)	Comments
	Waiting on weather	0945	5 Jan 2002	3.75		3.75	
	Run in hole	1015	5 Jan 2002	0.50		0.50	
	RCB 51.3–59.0 mbsf	2245	5 Jan 2002	12.50		12.50	Cored Hole 1224D TD
	Pull out of hole into casing	2345	5 Jan 2002	1.00		1.00	
	Retrieve Core 5R	0100	6 Jan 2002	1.25		1.25	
	Waiting on weather	0045	7 Jan 2002	23.75		23.75	Pull out of hole into casing and pull out of hole to 4907 mbrf
	Clear seafloor	1000	6 Jan 2002				Reentry required to core ahead
		0045	7 Jan 2002				Pull out of hole preparation good weather
	Pull out of hole for 14 3/4-in bit	1100	7 Jan 2002	10.25		10.25	Clear rotary at 1100 hr
	Prepare cement manifold	1200	7 Jan 2002	1.00		1.00	
	Make up running tool	1400	7 Jan 2002	2.00		2.00	
	Make up 14 3/4 BHA	1715	7 Jan 2002	3.25		3.25	Strip upper guide horn
	Run in hole to 4790 m	2345	7 Jan 2002	6.50		6.50	
	Hang off DP on rotary	0000	8 Jan 2002	0.25		0.25	
	Waiting on weather	1200	8 Jan 2002	12.00		12.00	
	Launch VIT	1330	8 Jan 2002	1.50		1.50	
	Run in hole, space out for reentry	1500	8 Jan 2002	1.50		1.50	
	Reentry Hole 1224D	1515	8 Jan 2002	0.25		0.25	Reenter Hole 1224D at 1515 hr
	Run in hole to 23.84 mbsf	1530	8 Jan 2002	0.25		0.25	
	Pull out of hole with VIT	1845	8 Jan 2002	3.25		3.25	
	Open hole to 14 3/4 in	1515	9 Jan 2002	20.50		20.50	AHC shut down at 1515 hr
	Open hole to 14 3/4 in	1500	10 Jan 2002	23.75		23.75	To RCB TD of 59 mbsf
	Drill hole for 14 3/4 in	0730	11 Jan 2002	16.50		16.50	Excess torque from 62.7 mbsf
							TD Hole 1224D at 64.7 mbsf
	Short trip to casing shoe	0830	11 Jan 2002	1.00		1.00	Condition hole
	Run in hole and tag bottom	0915	11 Jan 2002	0.75		0.75	Tag 64.7 with 0.5 m soft fill
	Displace hole to mud	1000	11 Jan 2002	0.75		0.75	Circulate hole for casing
	Pull out of hole	2030	11 Jan 2002	10.50		10.50	Clear seafloor at 1100 hr
							Clear rotary at 2025 hr
	Rig up to run 10 3/4 -in casing	0000	12 Jan 2002	3.50		3.50	Deploy casing at 2355 hr
	Run in hole with casing	1300	12 Jan 2002	13.00		13.00	TD 10¾ -in casing at 58.47 mbsf
	Reentry Hole 1224D	1330	12 Jan 2002	0.50		0.50	Reenter Hole 1224D at 1336 hr
	Run in hole, space out to land casing	1515	12 Jan 2002	1.75		1.75	Land 10¾ casing at 1515 hr
	Cement with 18.8 bbl of 15.5 ppg	1645	12 Jan 2002	1.50		1.50	Release dart at 1635 hr
							Bump plug with 900 psi; no flowback
	Release running tool from casing	1715	12 Jan 2002	0.50		0.50	Release on second attempt at 1715 hr
	Recover VIT	2000	12 Jan 2002	2.75		2.75	
	Slip and cut drill line	2115	12 Jan 2002	1.25		1.25	Clear seafloor at 1715 hr
	Pull out of hole	0600	13 Jan 2002	8.75		8.75	Clear rotary at 0530 hr
	Make up BHA and run in hole	1600	13 Jan 2002	10.00		10.00	Clean out Hole 1224D inside casing
	Reenter Hole 1224D	1630	13 Jan 2002	0.50		0.50	Reenter Hole 1224D at 1630 hr
							Reentry cone sank 1.75 m
	Wash out soft cement	1715	13 Jan 2002	0.75		0.75	54.6–58.1 mbsf
	Circulate casing clean	1745	13 Jan 2002	0.50		0.50	Science objective obtained
	Pull out of hole	1815	13 Jan 2002	0.50		0.50	Clear seafloor at 1817 hr
					Total:	253.50	
	Hole 1224D waiting on weather					97.50	
1224E	Offset 15 m southwest	1845	13 Jan 2002	0.50		0.50	
	Tag seafloor at 4978 mbrf	1900	13 Jan 2002	0.25		0.25	Tag seafloor at 1840 hr
	Wash, punch Cores 1R and 2R	2215	13 Jan 2002	3.25		3.25	0–8 mbsf; 8–27.1 mbsf
	3R, 27.1–36.7 mbsf	1500	14 Jan 2002	16.75		16.75	Tag hard at 27.7 mbsf
	Cleared seafloor	1500	14 Jan 2002	0.00		0.00	Pulled out of basement
					Total:	20.75	
1224F	Looking for Hole 1224E	1630	14 Jan 2002	1.50		1.50	Pulled out of basement as pulled out of hole
	Spud hole	1630	14 Jan 2002				
	Core 1R, 27.7–39.70 mbsf	0455	15 Jan 2002	12.42		12.42	New hole with bare rock spud
	Cores 2R–4R, 39.70–65.90 mbsf	0650	16 Jan 2002	25.92		25.92	Flow basalt and high recovery
							Drilling break 62.7 mbsf, Hole 1224D
	Cores 5R–11R, 65.9–128.50 mbsf	2315	17 Jan 2002	40.42		40.42	Altered basalt poor recovery
	Short trip for knobbies	0115	18 Jan 2002	2.00		2.00	Pull out of hole above basement contact
	Search for and reenter Hole F	0200	18 Jan 2002	0.75		0.75	
	Run in hole from 25.69–93.16 mbsf	0330	18 Jan 2002	1.50		1.50	
	TSF mechanical breakdown	0700	18 Jan 2002	3.50		3.50	Repack swivel on top drive

Table T4 (continued).

Site/Hole	Activity	Local time (hr)	Date	Time on hole (hr)		Time on site (hr)	Comments
	Run in hole from 93.16–128.5 mbsf	0830	18 Jan 2002	1.50		1.50	12-m soft fill circulated out
	Cores 12R–14R, 128.5–143 mbsf	1700	18 Jan 2002	8.50		8.50	3-m fill on Core 14R
	Work pipe to clean hole	1745	18 Jan 2002	0.75		0.75	400 amp and 4-m fill
	Cores 14R–16R, 143–171 mbsf	1700	19 Jan 2002	23.25		23.25	Zero recovery Core 16R
	Run bit deplugger	2015	19 Jan 2002	3.25		3.25	Did not appear to seat in bit
	Core 17R, 171–174.5 mbsf	2245	19 Jan 2002	2.50		2.50	Zero recovery Core 17R
	Run in hole with rotary shifter tool	0000	20 Jan 2002	1.25		1.25	Drop bit at 2320 hr
	Displace hole for logging	0045	20 Jan 2002	0.75		0.75	
	Pull out of hole for logging	0230	20 Jan 2002	1.75		1.75	EOP 49.94 mbsf
	Drop FFF	0515	20 Jan 2002	2.75		2.75	
	Rig up and run log 1	1615	20 Jan 2002	11.00		11.00	DITE/HLDT/APS/HNGS In at 0745 hr, depth 5152 m; out at 1520 hr
	Rig up and run log 2	1945	20 Jan 2002	3.50		3.50	FMS/NGT/DSI Misrun replace telemetry tool
	Log 2 in	1945	20 Jan 2002	0.00		0.00	Depth 5152 m (174 mbsf)
	Log 2 out	0530	21 Jan 2002	9.75		9.75	Out at 0525 hr
	Rig up and run log 3	0945	21 Jan 2002	4.25		4.25	WST in; 0745 hr misrun Depth 1057 m, out at 0945 hr
	Rig down logging	1030	21 Jan 2002	0.75		0.75	
	Pull upper guide horn and launch VIT	1100	21 Jan 2002	0.50		0.50	
	Run in hole with VIT to observe FFF	1230	21 Jan 2002	1.50		1.50	Observe FFF at 1225 hr
	Clear seafloor	1238	21 Jan 2002	0.13		0.13	
	Pull out of hole with DP and VIT	1415	21 Jan 2002	1.62		1.62	
	Recover VIT	1500	21 Jan 2002	0.75		0.75	
	1st beacon on deck	1612	21 Jan 2002				
	2nd beacon on deck	1800	21 Jan 2002				
	Pull out of hole with DP to 112.92 mbrf	2115	21 Jan 2002	6.25		6.25	
	MBR clear rotary	2355	21 Jan 2002				
	Lay out DC to catwalk	0000	22 Jan 2002	2.75		2.75	
	Secure ship for sea voyage	0030	22 Jan 2002	0.50		0.50	Depart site at 0030 hr
	Seismic survey over H2O-5 (Site 1224)	0145	22 Jan 2002	1.25		1.25	Functional test
					Total:	178.75	
	Hole 1224F						
	TSF mechanical downtime					3.50	
	LDEO logging downtime					7.75	
	ODP mechanical downtime					0.00	
H2O-5 (Site 1224)	Depart site	0145	22 Jan 2002				
San Diego	End of sea voyage (pilot aboard)	0700	27 Jan 2002	125.25		125.25	Traveled 1320 nmi at 10.49 kt
	First line ashore	0820	27 Jan 2002			1.33	
					Total:	126.58	
		Total hours:				779.68	
		Total days:				32.49	

Note: GPS = global positioning system, DP = drill pipe, VIT = vibration isolated television, APC = advanced piston corer, BHA = bottom-hole assembly, CHRT = casing hanger running tool, RCB = rotary core barrel, TD = total depth, AHC = active heave compensator, EOP = end of pipe, FFF = free-fall funnel, DITE = Digital Dual Induction Tool model E, HLDT = Hostile Environment Litho-Density Tool, APS = accelerator porosity sonde, HNGS = Hostile Environment Natural Gamma Ray Sonde, FMS = Formation MicroScanner, NGT = Natural Gamma Spectrometry Tool, DSI = Dipole Sonic Imager, WST = Well Seismic Tool, DC = drill collar, MBR = mechanical bit release, TSF = Transocean Sedco Forex.

Table T5. Summary of cooling units and alteration, Site 1224. (Continued on next page.)

Core, section	Length (m)	Curated length (m)	Section (mbsf) Top	Section (mbsf) Bottom	Bottom of cooling unit (cm)	Bottom of cooling unit (m)	Cooling unit	Contact characteristics	Alteration interval (cm)	Altered piece	Alteration type	Comment
200-1224A-												
4X-CC	0.22	0.22	26.22	26.44			1	Glass in Piece 1			Slight	Top of unit?
5X-1	0.18	0.23	30.70	30.93			1				Slight	
6N-1	0.22	0.23	32.00	32.23			1				Slight	
200-1224D-												
1R-1	1.43	1.14	25.50	26.64			1				Slight	
1R-2	1.50	1.46	26.64	28.10			1				Slight	
1R-3	1.22	0.89	28.10	28.99			1				Slight	
1R-4	0.00	1.01	28.99	30.00			1				Slight	
2R-1	0.80	1.29	35.10	36.39	2	35.12		Glass in Piece 2	5–10	2	Moderate: clays, increase in carbonate, Fe oxyhydroxides, and pyrite, no halos	Glass fell down hole
2R-2	1.42	1.32	36.39	37.71			1				Slight	
2R-3	1.13	1.32	37.71	39.03			1				Slight	
2R-4	1.46	1.22	39.03	40.25			1				Slight	
3R-1	0.86	1.00	44.70	45.70			1				Slight	
3R-2	0.96	1.44	45.70	47.14			1		118–132	3	Moderate: clays, Fe oxyhydroxides, and pyrite, halos	
3R-3	1.48	1.04	47.14	48.18	70	47.84	1	Coarsest grained, with spherulitic textures	40–104	5–12	Moderate to high: carbonate and Fe oxyhydroxides, halos	
4R-1	0.88	1.32	49.30	50.62			2				Slight	
4R-2	1.11	0.76	50.62	51.38			2				Slight	
5R-1	1.40	1.40	51.30	52.70			2				Slight	
200-1224E-												
3R-1	0.00	1.29	27.1	28.39	0	27.10		Hyaloclastite	10–43	3–9	Moderate: Fe oxyhydroxides, clays, halos	
3R-2	1.44	1.24	28.39	29.63			1				Slight	
3R-3	1.50	1.03	29.63	30.66			1				Slight	
3R-4	1.45	1.37	30.66	32.03			1				Slight	
200-1224F-												
1R-1	1.50	1.44	27.70	29.14			1		0–62	1–13	Moderate: Fe oxyhydroxides, clays, halos	
1R-2	1.40	1.44	29.14	30.58			1				Slight	
1R-3	1.40	1.51	30.58	32.09			1				Slight	
1R-4	1.50	1.43	32.09	33.52			1		52–75	3–6	Moderate: clays, Fe oxyhydroxides, bleached, halos	
1R-5	0.33	0.66	33.52	34.18			1		40–65	4–7	Moderate: clays, Fe oxyhydroxides, carbonate, halos	
2R-1	1.46	1.50	39.70	41.20			1		0–150	1–24	Moderate: clays, Fe oxyhydroxides, bleached, bright orange-red material, halos	
2R-2	1.50	1.42	41.20	42.62			1		0–142	1–18	Moderate: clays, Fe oxyhydroxides, bleached, bright orange-red material, halos; high: Pieces 14–15	
2R-3	1.40	1.14	42.62	43.76			1				Slight	
2R-4	0.96	1.45	43.76	45.21			1				Slight	
2R-5	0.00	0.69	45.21	45.90			1				Slight	
3R-1	0.00	1.50	47.30	48.80			1		108–150	10–19	Moderate: clays, Fe oxyhydroxides, slight bleaching, halos	
3R-2	1.42	1.23	48.80	50.03			1		0–124	1–12	Moderate: clays, Fe oxyhydroxides, carbonate, halos	
3R-3	1.03	1.50	50.03	51.53			1				Slight	
3R-4	0.79	0.40	51.53	51.93			1				Slight	
3R-5	0.89	0.00					1				Slight	
4R-1	1.29	0.90	56.40	57.30			1				Uppermost appearance of yellow-green smectite?	
4R-2	1.50	1.50	57.30	58.80			1				Slight	

Table T5 (continued).

Core, section	Length (m)	Curated length (m)	Section (mbsf) Top	Section (mbsf) Bottom	Bottom of cooling unit (cm)	Bottom of cooling unit (m)	Cooling unit	Contact characteristics	Alteration interval (cm)	Altered piece	Alteration type	Comment
200-1224F-												
4R-3	1.50	1.43	58.80	60.23			1				Slight	
4R-4	1.50	0.78	60.23	61.01			1				Slight	
4R-5	0.41	1.47	61.01	62.48			1				Slight	
4R-6	0.00	0.42	62.48	62.90	10	62.58	2	Glass in Piece 2				
5R-1	0.95	1.07	65.90	66.97			2				Slight	
6R-1	1.50	1.50	75.00	76.50	8	75.08	3	Glass in Pieces 2 and 3	0–150	1–23	Moderate: clays, carbonate, and Fe oxyhydroxides, halos	
6R-2	0.00	0.20	76.50	76.70			3				Slight	
7R-1	1.20	1.33	84.50	85.83	94	85.44	4	Glass in Piece 10	0–132	1–14	Moderate: clays, carbonate, and Fe oxyhydroxides, halos	
8R-1	1.31	1.33	93.50	94.83	68	94.18	5	Glass in Piece 7	0–134	1–14	Moderate: clays, carbonate, and Fe oxyhydroxides, halos	
9R-1	0.60	0.61	102.70	103.31	0	102.70	6	Glass in Piece 1	0–62	1–7	Moderate: clays, carbonate, and Fe oxyhydroxides, halos, epidote	
					52	0.52	7	Glass in Piece 7				
10R-1	1.40	1.45	111.80	113.25	38	112.18	8	Glass in Piece 4				
					98	0.98	9	Glass in Piece 14				
11R-1	0.41	1.50	121.10	122.60	14	121.24	10	Glass in Piece 4	0–150	1–22	Moderate: clays, carbonate, and Fe oxyhydroxides, halos	
11R-2	1.30	0.37	122.60	122.97	12	122.72	11	Glass in Pieces 3 and 4	0–36	1–6	Moderate: clays, carbonate, and Fe oxyhydroxides, halos	
					30	123.02	12	Glass in Piece 6				
12R-1	1.20	1.33	128.50	129.83	60	129.10	13	Hyaloclastite with glass and carbonate matrix	0–135	1–16	Moderate: clays, carbonate, and Fe oxyhydroxides, halos, epidote	
13R-1	1.46	1.48	133.50	134.98			13		48–76	5–6	High: clays, carbonate, high amount of Fe oxyhydroxides, epidote, halos, moderate alteration elsewhere in section	
13R-2	1.27	1.50	134.98	136.48			13		0–150	1–22	Moderate: clays, carbonate, and Fe oxyhydroxides, halos, epidote	
14R-1	0.77	1.42	143.20	144.62			13		35–90	3–9	High: clays, carbonate, high amount of Fe oxyhydroxides, halos, moderate alteration elsewhere in section	This section is coarser than above sections
14R-2	1.25	0.79	144.62	145.41			13					This section is coarser than above sections
					78		14	Coarse grained in bottom of Section 14R-2; fine grained in top of Section 15R-1			Bottom of cooling unit?	
15R-1	1.30	1.34	152.40	153.74			14		0–40	1–9	Moderate: clays, carbonate, and Fe oxyhydroxides, halos	Top is aphanitic, bottom 50–135 cm is fine grained
16R-1	0.00	0.00					14				Slight	

Table T6. XRD analysis samples and identified minerals.

Core, section, interval (cm)	Depth (mbsf)	Piece	Comments	Main minerals	Accessory minerals
200-1224A-					
2X-CC, 0–2	6.00		White grain in sediment	Phillipsite‡	
200-1224D-					
3R-3, 15–17	47.29		Crystallized white vein	Calcite†	
3R-3, 90–92	48.04		Thin greenish vein	Illite*	Montmorillonite,* saponite,* laumontite‡
4R-1, 90–92	50.20		Crystallized white vein	Calcite†	
200-1224E-					
3R-1, 1–4	27.11	1	Translucent crystals in hyaloclastite	Calcite†	Phillipsite‡
3R-3, 46–50	30.09	2	Thin greenish vein	Montmorillonite,* saponite*	
200-1224F-					
1R-1, 70–72	28.40	15a	Thin greenish vein	Montmorillonite,* saponite*	Illite,* laumontite‡
1R-3, 86–89	31.44	4b	Thin greenish vein	Montmorillonite, saponite*	
2R-4, 120–123	44.96	3	Thin consolidated greenish vein	Quartz	Montmorillonite,* illite*
3R-2, 81–83	49.61	10	Crystallized white vein	Calcite†	
4R-3, 74–78	59.54	4a	Thin consolidated greenish vein	Quartz	
4R-5, 43–47	61.41	1c	Colorless fibrous crystallized deposit	Aragonite†	
6R-1, 29–34	75.29	6	Crystallized carbonate deposit	Calcite†	Phillipsite‡
6R-1, 44–47	75.94	8	Thin crystallized carbonate and brownish clay	Calcite†	
7R-1, 10–13	84.60	1b	Light-green clay and crystallized carbonate	Calcite†	Montmorillonite,* talc*
8R-1, 34–37	93.84	2a	Thin crystallized white vein	Calcite†	
9R-1, 19–23	102.89	2	Fibrous light-green clay and crystallized carbonate	Calcite,† montmorillonite,* saponite*	
9R-1, 55–57	103.25	7	Crystallized white vein with altered fragment	Phillipsite‡	Montmorillonite,* saponite*
10R-1, 31–36	112.11	3	Thin light-brown clay	Montmorillonite,* saponite*	
10R-1, 87–88	112.67	12	Thin reddish brown clay	Montmorillonite,* saponite*	Illite,* laumontite‡
12R-1, 57–58	129.07	6	Soft white deposit	Calcite†	
13R-1, 77–78	134.27	6b	Fibrous light-green clay	Montmorillonite,* saponite*	
13R-1, 114–115	134.64	10	Crystallized white deposit	Calcite†	
13R-2, 52–54	135.50	19	Fibrous light-green clay	Montmorillonite,* saponite*	
14R-1, 27–36	143.47	2	Thin reddish brown clay	Calcite†	Phillipsite,‡ illite,* montmorillonite*
?	?	4c	Layered white-greenish vein	Calcite†	Montmorillonite,* talc,* phillipsite‡

Notes: * = clay, † = carbonate, ‡ = zeolite. ? = unknown.

Table T7. Moisture and density, Site 1224.

Leg	Site	Hole	Core	Type	Section	Interval (cm) Top	Interval (cm) Bottom	Depth (mbsf)	Water content (%) Bulk	Water content (%) Dry	Density (g/cm³) Bulk	Density (g/cm³) Dry	Density (g/cm³) Grain	Porosity (%)
200	1224	A	5	X	1	16	18	30.86	1.5	1.5	2.850	2.809	2.928	4.1
200	1224	A	6	N	1	10	12	32.10	1.6	1.6	2.870	2.824	2.958	4.5
200	1224	C	1	H	1	45	47	0.45	47.7	91.2*	1.529	0.800	2.782	71.3
200	1224	C	1	H	1	118	120	1.18	48.0	92.4*	1.530	0.795	2.813	71.7
200	1224	C	1	H	2	45	47	1.95	49.8	99.0*	1.507	0.757	2.831	73.2
200	1224	C	1	H	2	118	120	2.68	52.9	112.2*	1.453	0.685	2.739	75.0
200	1224	C	1	H	3	45	47	3.45	55.3	123.9*	1.418	0.633	2.708	76.6
200	1224	C	1	H	3	118	120	4.18	56.8	131.4*	1.403	0.606	2.731	77.8
200	1224	C	1	H	4	45	47	4.95	59.5	147.1*	1.369	0.554	2.714	79.6
200	1224	C	1	H	4	100	102	5.50	60.5	152.9*	1.358	0.537	2.710	80.2
200	1224	C	1	H	5	45	47	6.15	60.5	153.3*	1.364	0.539	2.781	80.6
200	1224	D	1	R	1	45	47	25.95	1.7	1.7	2.860	2.812	2.952	4.7
200	1224	D	1	R	2	86	88	27.50	1.8	1.8	2.901	2.849	3.002	5.1
200	1224	D	1	R	3	47	49	28.57	1.6	1.6	2.891	2.845	2.977	4.4
200	1224	D	1	R	4	56	58	29.55	2.0	2.1	2.820	2.763	2.927	5.6
200	1224	D	2	R	1	13	15	35.23	2.3	2.3	2.723	2.660	2.833	6.1
200	1224	D	2	R	1	14	16	35.24	2.8	2.9	2.855	2.775	3.010	7.8
200	1224	D	2	R	2	98	100	37.37	2.7	2.8	2.749	2.674	2.886	7.3
200	1224	D	2	R	3	68	70	38.39	3.2	3.3	2.835	2.745	3.010	8.8
200	1224	D	2	R	4	104	106	40.07	1.5	1.6	2.885	2.841	2.969	4.3
200	1224	D	3	R	1	47	49	45.17	1.3	1.3	2.903	2.866	2.975	3.7
200	1224	D	3	R	2	80	82	46.50	2.4	2.5	2.817	2.749	2.944	6.6
200	1224	D	3	R	3	42	44	47.56	2.9	3.0	2.797	2.715	2.952	8.0
200	1224	D	4	R	1	78	80	50.08	1.7	1.7	2.853	2.806	2.942	4.6
200	1224	D	4	R	2	34	36	50.96	1.6	1.7	2.813	2.767	2.897	4.5
200	1224	D	5	R	1	63	65	51.93	2.3	2.3	2.786	2.723	2.902	6.1
200	1224	E	3	R	1	97	99	28.07	1.5	1.5	2.868	2.826	2.949	4.2
200	1224	E	3	R	2	49	51	28.88	2.0	2.1	2.827	2.769	2.934	5.6
200	1224	E	3	R	3	18	20	29.81	2.0	2.0	2.877	2.820	2.984	5.5
200	1224	E	3	R	4	79	81	31.45	1.7	1.7	2.846	2.797	2.936	4.7
200	1224	F	1	R	1	107	109	28.77	2.0	2.1	2.874	2.816	2.985	5.7
200	1224	F	1	R	2	68	70	29.82	1.6	1.6	2.886	2.841	2.972	4.4
200	1224	F	1	R	3	73	75	31.31	2.0	2.1	2.861	2.803	2.971	5.7
200	1224	F	1	R	4	32	34	32.41	2.0	2.0	2.891	2.833	3.002	5.6
200	1224	F	1	R	5	18	20	33.70	2.7	2.7	2.916	2.839	3.071	7.6
200	1224	F	1	R	5	61	63	34.13	2.0	2.0	2.914	2.857	3.026	5.6
200	1224	F	2	R	1	90	92	40.60	3.2	3.3	2.853	2.763	3.031	8.9
200	1224	F	2	R	2	13	15	41.33	5.3	5.6	2.765	2.619	3.056	14.3
200	1224	F	2	R	3	8	10	42.70	1.3	1.3	2.855	2.817	2.925	3.7
200	1224	F	2	R	4	19	21	43.95	2.3	2.4	2.902	2.835	3.033	6.5
200	1224	F	2	R	4	139	141	45.15	2.3	2.4	2.888	2.821	3.018	6.5
200	1224	F	2	R	5	32	34	45.53	1.9	1.9	2.904	2.849	3.011	5.4
200	1224	F	3	R	1	17	19	47.47	1.7	1.8	2.873	2.823	2.967	4.8
200	1224	F	3	R	2	21	23	49.01	2.7	2.7	2.766	2.692	2.901	7.2
200	1224	F	3	R	3	84	86	50.87	3.9	4.1	2.698	2.592	2.890	10.3
200	1224	F	3	R	4	26	28	51.79	1.0	1.0	2.940	2.910	2.998	3.0
200	1224	F	4	R	1	15	17	56.55	1.4	1.5	2.854	2.813	2.931	4.0
200	1224	F	4	R	2	29	31	57.59	1.2	1.3	2.898	2.862	2.966	3.5
200	1224	F	4	R	3	9	11	58.89	1.5	1.5	2.802	2.759	2.878	4.1
200	1224	F	4	R	4	21	23	60.44	1.3	1.3	2.896	2.859	2.967	3.6
200	1224	F	4	R	5	33	35	61.34	1.6	1.7	2.856	2.809	2.944	4.6
200	1224	F	5	R	1	57	59	66.47	2.4	2.4	2.825	2.758	2.952	6.6
200	1224	F	6	R	1	101	103	76.01	1.7	1.8	2.873	2.823	2.969	4.9
200	1224	F	7	R	1	42	44	84.92	3.5	3.6	2.728	2.634	2.902	9.2
200	1224	F	8	R	1	46	48	93.96	3.7	3.9	2.706	2.606	2.889	9.8
200	1224	F	9	R	1	44	46	103.14	1.7	1.7	2.913	2.863	3.009	4.9
200	1224	F	10	R	1	92	94	112.72	2.7	2.8	2.658	2.587	2.780	7.0
200	1224	F	11	R	1	88	90	121.98	3.7	3.8	2.799	2.696	2.997	10.0
200	1224	F	12	R	1	50	52	129.00	2.3	2.4	2.734	2.671	2.847	6.2
200	1224	F	13	R	1	24	26	133.74	3.1	3.2	2.870	2.782	3.045	8.6
200	1224	F	13	R	2	24	26	135.22	4.5	4.7	2.835	2.708	3.092	12.4
200	1224	F	14	R	1	47	49	143.67	5.9	6.3	2.673	2.515	2.973	15.4
200	1224	F	14	R	1	106	108	144.26	4.1	4.2	2.812	2.697	3.037	11.2
200	1224	F	15	R	1	100	102	153.40	1.7	1.7	2.924	2.876	3.020	4.8

Notes: * = erroneous numbers are a result of less sensitivity. This table is also available in **ASCII**.

Table T8. Thermal conductivity measurements, Site 1224.

Leg	Site	Hole	Core	Type	Section	Interval (cm) Top	Interval (cm) Bottom	Depth (mbsf)	Type	Thermal conductivity (W/[m·K])
200	1224	C	1	H	1	60	60	0.60	Full	0.883
200	1224	C	1	H	2	110	110	2.60	Full	0.790
200	1224	C	1	H	3	75	75	3.75	Full	0.805
200	1224	C	1	H	4	60	60	5.10	Full	0.779
200	1224	C	1	H	5	45	45	6.15	Full	0.782
200	1224	D	1	R	3	65	76	28.75	Half	1.766
200	1224	D	2	R	3	8	17	37.79	Half	1.858
200	1224	D	3	R	2	109	118	46.79	Half	1.651
200	1224	D	4	R	1	12	25	49.42	Half	1.739
200	1224	D	5	R	1	57	70	51.87	Half	1.741
200	1224	F	3	R	1	64	73	47.94	Half	2.025
200	1224	F	4	R	2	137	149	58.67	Half	1.680
200	1224	F	5	R	1	32	39	66.22	Half	1.725
200	1224	F	6	R	1	96	106	75.96	Half	1.890
200	1224	F	8	R	1	105	115	94.55	Half	1.567
200	1224	F	9	R	1	14	28	102.84	Half	1.539
200	1224	F	10	R	1	118	127	112.98	Half	1.533
200	1224	F	11	R	1	120	125	122.30	Half	1.343
200	1224	F	12	R	1	43	51	128.93	Half	1.535
200	1224	F	13	R	2	20	30	135.18	Half	1.526
200	1224	F	14	R	1	77	86	143.97	Half	1.577
200	1224	F	15	R	1	80	90	153.20	Half	1.746

Note: This table is also available in **ASCII**.

Table T9. *P*-wave sensor (PWS) measurements, Site 1224.

Leg	Site	Hole	Core	Type	Section	Interval (cm) Top	Interval (cm) Bottom	Depth (mbsf)	Direction	Velocity (m/s)
200	1224	A	5	X	1	16.0	18.0	30.86	x	5931.0
200	1224	A	5	X	1	16.0	18.0	30.86	y	5905.2
200	1224	A	5	X	1	16.0	18.0	30.86	z	5814.3
200	1224	A	6	N	1	10.0	12.0	32.10	x	5849.7
200	1224	A	6	N	1	10.0	12.0	32.10	y	5763.8
200	1224	A	6	N	1	10.0	12.0	32.10	z	5898.9
200	1224	C	1	H	1	18.1	18.1	0.18	x	1529.8
200	1224	C	1	H	1	66.4	66.4	0.66	x	1525.2
200	1224	C	1	H	1	98.5	98.5	0.99	x	1524.1
200	1224	C	1	H	1	122.3	122.3	1.22	x	1525.1
200	1224	C	1	H	2	4.3	4.3	1.54	x	1535.2
200	1224	C	1	H	2	30.3	30.3	1.80	x	1535.7
200	1224	C	1	H	2	70.3	70.3	2.20	x	1526.5
200	1224	C	1	H	2	103.9	103.9	2.54	x	1531.7
200	1224	C	1	H	3	6.2	6.2	3.06	x	1525.1
200	1224	C	1	H	3	41.1	41.1	3.41	x	1537.2
200	1224	C	1	H	3	89.4	89.4	3.89	x	1536.7
200	1224	C	1	H	3	125.4	125.4	4.25	x	1533.2
200	1224	C	1	H	4	14.0	14.0	4.64	x	1528.2
200	1224	C	1	H	4	77.5	77.5	5.28	x	1532.0
200	1224	C	1	H	5	6.2	6.2	5.76	x	1555.5
200	1224	C	1	H	5	31.0	31.0	6.01	x	1551.2
200	1224	D	1	R	1	45.0	47.0	25.95	x	5667.4
200	1224	D	1	R	1	45.0	47.0	25.95	y	5708.0
200	1224	D	1	R	1	45.0	47.0	25.95	z	5468.6
200	1224	D	1	R	2	86.0	88.0	27.50	x	5950.0
200	1224	D	1	R	2	86.0	88.0	27.50	y	5601.3
200	1224	D	1	R	2	86.0	88.0	27.50	z	5776.6
200	1224	D	1	R	3	47.0	49.0	28.57	x	6136.5
200	1224	D	1	R	3	47.0	49.0	28.57	y	5792.9
200	1224	D	1	R	3	47.0	49.0	28.57	z	5773.7
200	1224	D	1	R	4	56.0	58.0	29.55	x	5476.5
200	1224	D	1	R	4	56.0	58.0	29.55	y	5050.5
200	1224	D	1	R	4	56.0	58.0	29.55	z	5144.6
200	1224	D	2	R	1	13.0	15.0	35.23	y	5039.2
200	1224	D	2	R	2	98.0	100.0	37.37	x	5374.5
200	1224	D	2	R	2	98.0	100.0	37.37	y	5256.3
200	1224	D	2	R	2	98.0	100.0	37.37	z	5241.0
200	1224	D	2	R	3	68.0	70.0	38.39	x	5083.7
200	1224	D	2	R	3	68.0	70.0	38.39	y	4648.7
200	1224	D	2	R	3	68.0	70.0	38.39	z	4795.9
200	1224	D	2	R	4	104.0	106.0	40.07	x	5837.9
200	1224	D	2	R	4	104.0	106.0	40.07	y	5652.1
200	1224	D	2	R	4	104.0	106.0	40.07	z	5588.4
200	1224	D	3	R	1	47.0	49.0	45.17	x	6041.3
200	1224	D	3	R	1	47.0	49.0	45.17	y	6006.4
200	1224	D	3	R	1	47.0	49.0	45.17	z	5871.6
200	1224	D	3	R	2	80.0	82.0	46.50	x	5783.3
200	1224	D	3	R	2	80.0	82.0	46.50	y	5310.2
200	1224	D	3	R	2	80.0	82.0	46.50	z	5428.6
200	1224	D	3	R	3	42.0	44.0	47.56	x	5659.5
200	1224	D	3	R	3	42.0	44.0	47.56	y	5471.0
200	1224	D	3	R	3	42.0	44.0	47.56	z	5477.5
200	1224	D	4	R	1	78.0	80.0	50.08	x	5754.4
200	1224	D	4	R	1	78.0	80.0	50.08	y	5586.0
200	1224	D	4	R	1	78.0	80.0	50.08	z	5499.8
200	1224	D	4	R	2	34.0	36.0	50.96	x	5540.3
200	1224	D	4	R	2	34.0	36.0	50.96	y	5440.4
200	1224	D	4	R	2	34.0	36.0	50.96	z	5450.0
200	1224	D	5	R	1	63.0	65.0	51.93	x	5490.4
200	1224	D	5	R	1	63.0	65.0	51.93	y	5263.4
200	1224	D	5	R	1	63.0	65.0	51.93	z	5202.9
200	1224	E	2	R	3	44.2	44.2	20.94	x	1611.3
200	1224	E	2	R	3	91.8	91.8	21.42	x	1612.6
200	1224	E	2	R	4	131.4	131.4	23.31	x	1619.1

Note: Only a portion of this table appears here. The complete table is available in **ASCII.**